NAVAL POSTGRADUATE SCHOOL
MONTEREY, CALIFORNIA

19970313 073

DISSERTATION

OBSERVATIONS AND MODELING OF THE
INTERNAL TIDE IN A SUBMARINE CANYON
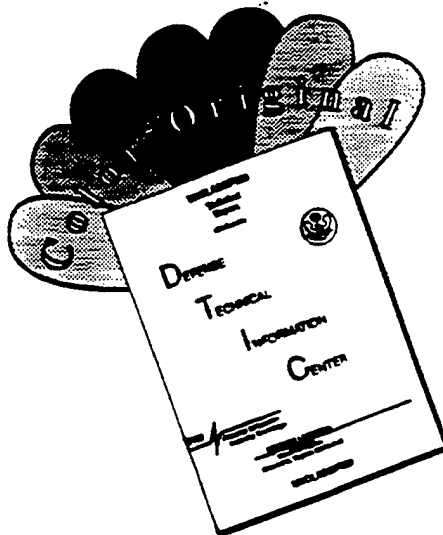
by

Emil T. Petruncio

September, 1996

Dissertation Supervisors: Jeffrey D. Paduan
                                   Leslie K. Rosenfeld

Approved for public release; distribution is unlimited.

DISCLAIMER NOTICE

REPORT DOCUMENTATION PAGE

Public reporting burden for this collection of information is estimated to average 1 hour per response, including the time for reviewing instruction, searching existing data sources, gathering and maintaining the data needed, and completing and reviewing the collection of information. Send comments regarding this burden estimate or any other aspect of this collection of information, including suggestions for reducing this burden, to Washington Headquarters Services, Directorate for Information Operations and Reports, 1215 Jefferson Davis Highway, Suite 1204, Arlington, VA 22202-4302, and to the Office of Management and Budget, Paperwork Reduction Project (0704-0188) Washington DC 20503.

1. AGENCY USE ONLY *(Leave blank)*	2. REPORT DATE September 1996.	3. REPORT TYPE AND DATES COVERED Doctoral Dissertation

4. TITLE AND SUBTITLE OBSERVATIONS AND MODELING OF THE INTERNAL TIDE IN A SUBMARINE CANYON	5. FUNDING NUMBERS
6. AUTHOR(S) Emil Thomas Petruncio	
7. PERFORMING ORGANIZATION NAME(S) AND ADDRESS(ES) Naval Postgraduate School Monterey CA 93943-5000	8. PERFORMING ORGANIZATION REPORT NUMBER
9. SPONSORING/MONITORING AGENCY NAME(S) AND ADDRESS(ES)	10. SPONSORING/MONITORING AGENCY REPORT NUMBER

11. SUPPLEMENTARY NOTES The views expressed in this thesis are those of the author and do not reflect the official policy or position of the Department of Defense or the U.S. Government.

12a. DISTRIBUTION/AVAILABILITY STATEMENT Approved for public release; distribution is unlimited.	12b. DISTRIBUTION CODE

13. ABSTRACT *(maximum 200 words)*

Shipboard ADCP and CTD measurements were conducted in Monterey Submarine Canyon in April and October 1994 to determine the propagation characteristics and energy levels of the semidiurnal internal tide. The measurements reveal a bottom-intensified internal tide propagating energy upcanyon. The region of strongest motion is in a beam 150-200 m thick, centered approximately 150 m above the Canyon floor. Along-canyon baroclinic M2 currents are typically 15-20 cm s^{-1}, an order of magnitude larger than the estimated barotropic tidal currents. In April 1994, the internal tidal beam is well described by a progressive wave, while in October 1994, the signal is standing along and perpendicular to the beam. The Princeton Ocean Model was used to study the generation and propagation of semidiurnal internal tides in submarine canyons and to investigate their sensitivity to canyon shape. Minor changes in floor slope are found to have a significant impact on the strength of internal tides in a canyon. The numerical experiments reproduce several features of the internal tide that are in qualitative agreement with the observations, including upcanyon energy propagation along the canyon floor, internal tide generation along the canyon rim, and tidal pumping of dense water up onto the shelf near the canyon head.

14. SUBJECT TERMS internal waves, tides, internal tides, Monterey Bay, Monterey Submarine Canyon, submarine canyons, coastal ocean currents, POM, ocean modeling			15. NUMBER OF PAGES 192
			16. PRICE CODE
17. SECURITY CLASSIFICATION OF REPORT Unclassified	18. SECURITY CLASSIFICATION OF THIS PAGE Unclassified	19. SECURITY CLASSIFICATION OF ABSTRACT Unclassified	20. LIMITATION OF ABSTRACT UL

OBSERVATIONS AND MODELING OF THE INTERNAL TIDE IN A SUBMARINE CANYON

Emil T. Petruncio
Lieutenant Commander, United States Navy
B.S., United States Naval Academy, 1985
M.S., Naval Postgraduate School, 1993

Submitted in partial fulfillment
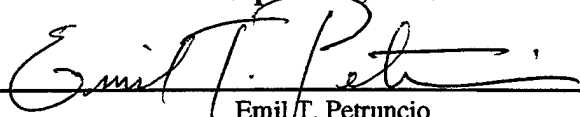of the requirements for the degree of

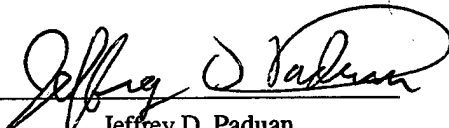**DOCTOR OF PHILOSOPHY IN PHYSICAL OCEANOGRAPHY**
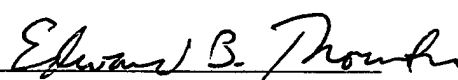
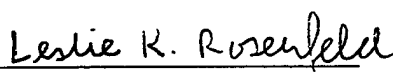from the

NAVAL POSTGRADUATE SCHOOL
September, 1996
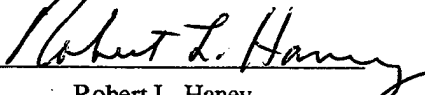
Author: _____
Emil T. Petruncio
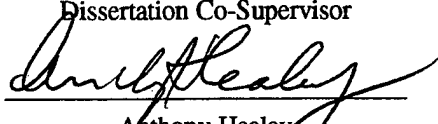
Approved by:

_____   _____
Jeffrey D. Paduan   Edward B. Thornton
Assistant Professor of Oceanography   Professor of Oceanography
Dissertation Co-Supervisor   Dissertation Committee Chair
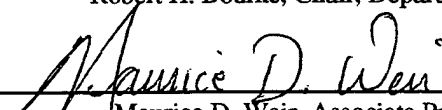
_____   _____
Leslie K. Rosenfeld   Robert L. Haney
Research Assistant Professor of Oceanography   Professor of Meteorology
Dissertation Co-Supervisor

_____
Anthony Healey
Professor of Mechanical Engineering

Approved by: _____
Robert H. Bourke, Chair, Department of Oceanography

Approved by: _____
Maurice D. Weir, Associate Provost for Instruction

iii

ABSTRACT

Shipboard ADCP and CTD measurements were conducted in Monterey Submarine Canyon in April and October 1994 to determine the propagation characteristics and energy levels of the semidiurnal internal tide. The measurements reveal a bottom-intensified internal tide propagating energy upcanyon. The region of strongest motion is in a beam 150-200 m thick, centered approximately 150 m above the Canyon floor. Along-canyon baroclinic M2 currents are typically 15-20 cm s^{-1}, an order of magnitude larger than the estimated barotropic tidal currents. In April 1994, the internal tidal beam is well described by a progressive wave, while in October 1994, the signal is standing along and perpendicular to the beam. The Princeton Ocean Model was used to study the generation and propagation of semidiurnal internal tides in submarine canyons and to investigate their sensitivity to canyon shape. Minor changes in floor slope are found to have a significant impact on the strength of internal tides in a canyon. The numerical experiments reproduce several features of the internal tide that are in qualitative agreement with the observations, including upcanyon energy propagation along the canyon floor, internal tide generation along the canyon rim, and tidal pumping of dense water up onto the shelf near the canyon head.

TABLE OF CONTENTS

ACKNOWLEDGEMENTS

I. INTRODUCTION

A. MOTIVATION

1. Coastal Tidal Current Prediction

It is well established that the interaction of the open ocean tides with the variable topography of the continental margins results in sea level and current oscillations of considerable magnitude. Given a month-long record from a well maintained tide gauge, the tidal component of sea level variations can be analyzed and subsequently predicted for long stretches of the coastline with reasonable accuracy. Forecasting coastal tidal currents however, is a problem which must be solved in three dimensions, with much finer spatial resolution. Godin (1991) notes that the distances over which tidal currents remain coherent in direction and strength may be as little as a few hundred meters in the horizontal, and only a few meters in the vertical.

The flow field associated with the barotropic tide is altered in the vicinity of large depth changes and alongshore topographic variations such as capes and headlands. Further complicating the task of tidal current analysis and prediction are internal waves of tidal frequency ("internal tides"), which can account for a significant portion of the total current variance in density-stratified coastal waters. At certain times and depths, baroclinic tidal currents oppose the barotropic tidal currents in direction and may exceed them in strength. Over the continental shelf, internal tides are characterized by typical current speeds of 5-20 cm s^{-1} and isopycnal displacement amplitudes of 20-50 m (Huthnance, 1989; Foreman, 1995). In certain locations, nonlinear developments such as soliton packets and bore-like surges may result in much larger current speeds and isopycnal displacements (Foreman, 1995).

Internal wave mixing affects sediment transport, nutrient distribution, acoustic propagation, and optical clarity in ocean regions where the internal wave field is locally intense. Additionally, the well mixed waters produced by internal wave action have been observed to spread laterally along isopycnals into deeper water (Gardner, 1989; Ivey and Nokes, 1989). This lateral spreading of water from the ocean boundaries has been proposed as a mechanism which might sufficiently weaken the stratification of the ocean interior to account for the large effective eddy diffusivities of $O(10^{-4} \text{ m}^2\text{s}^{-1})$ required to explain the mass and heat balances in abyssal basins (Eriksen, 1985; Garrett and Gilbert, 1988). In a review of processes affecting circulation on the

continental shelf, Huthnance (1995) notes the significant contribution of baroclinic tides to internal and near-bottom mixing, particularly in submarine canyons, and cites the need for current and temperature time series with high spatial resolution to test developing 3-D models of internal tides and waves.

2. Internal Tides In Monterey Bay

This study describes recent measurements of semidiurnal internal tides in Monterey Submarine Canyon (MSC) (Figure 1) and numerical simulations of internal tide propagation in idealized canyon shapes. As is the case in many submarine canyons, the internal tide in MSC is exceptionally energetic. Several Naval Postgraduate School (NPS) studies of near-bottom currents in the Canyon report semidiurnal and higher frequency oscillatory flow in the along-canyon direction, with bore-like upcanyon surges of up to 50 cm s^{-1} (Gatje and Pizinger, 1965; Njus, 1968; Dooley, 1968; Caster, 1969; Hollister, 1975). These current measurements were made within a few kilometers of the Canyon terminus or "head", near Moss Landing harbor. In the same vicinity, semidiurnal isopycnal displacements of 60-120 m have been observed in depths ranging from 120 to 220 m (Broenkow and McKain, 1972; Shea and Broenkow, 1982; Heard, 1992).

There is mounting evidence that these large amplitude internal tides have a considerable impact on the near-surface flow at the head of the Canyon. Several drift pole studies conducted in this area by Moss Landing Marine Laboratories in 1970 suggested current maxima on the order of 50 cm s^{-1} (Lazanoff, 1971). In most cases, the drift pole tracks appeared to follow bathymetric contours, and on one occasion the drift poles converged near the Canyon head during high tide (Broenkow, personal communication). McKay (1970) measured near-surface currents in Monterey Bay using a geomagnetic electro-kinetograph (GEK). Towing the GEK electrodes above the Canyon axis, McKay observed downcanyon/offshore flow during rising tide and upcanyon/onshore flow during falling tide. Near the Canyon head, he recorded current speeds as high as 50 cm s^{-1}, consistent with the drift pole studies. More recently, a breaking internal wave or bore-like surge at the Canyon head may have contributed to a mishap in which the propeller of a tanker became entangled with a buoy chain during a fuel transfer operation at Moss Landing. The incident, which is the subject of a cautionary notice issued in 1991 by the U.S. Coast Guard, was attributed to a hydraulic jump stemming from "strong currents moving landward through Monterey Canyon" (*NOS Tidal Current Tables 1995*).

2

Recent HF-radar measurements of current flow in the top meter of the Bay, recorded in hourly or two hour intervals, reveal semidiurnal currents with maximum amplitudes of 15 cm s^{-1} for the M2, or Principal Lunar Semidiurnal Component, and 6 cm s^{-1} for the S2, or Principal Solar Semidiurnal Component near the head of MSC (Petruncio, 1993; Paduan et al., 1995). The amplitudes were determined through harmonic analysis of 30-day time series. These relatively strong surface tidal currents appear to be directly influenced by the internal tide in the Canyon, as the M2 and S2 ellipses are oriented along bathymetric contours and are amplified over the head of the Canyon. Additionally, a comparison of the phases of the HF radar-derived M2 currents and the local M2 sea level signal confirms McKay's anecdotal reference to downcanyon (offshore) flow during rising tide and upcanyon (shoreward) flow during falling tide (Figure 2).

Petruncio (1993) hypothesized that a semidiurnal first mode interfacial wave, propagating along the axis in the shoreward direction and standing in the vertical, could explain the observed phase relationships between the M2 surface currents over the Canyon axis and the M2 sea level changes in the Bay. The hypothetical wave would need to have a wavelength of 20-30 km (typical for internal tides observed over the continental shelf (Baines, 1986) and a shoreward horizontal phase velocity of 45-70 cm s^{-1} (similar to the phase speeds observed by Holloway (1994) over the Australian Northwest Shelf). Additionally, the isopycnal displacements at the head of the canyon would need to be approximately in phase with the surface tide.

B.   OBJECTIVES

1.   The Field Study

Motivated by the apparent impact of the MSC internal tide on the surface circulation of the Bay, and aided by the availability of advanced technology with which to study this phenomenon, NPS conducted two shipboard experiments in April and October 1994 aboard the R/V *Point Sur*. Both cruises were sponsored by the Commander, Naval Meteorology and Oceanography Command in support of U.S. Navy Meteorology and Oceanography (METOC) Officer education. The objective of both experiments was to determine the propagation characteristics (i.e., the vertical and horizontal wavelengths and phase speeds) and energy levels of the internal tide in MSC. The experiments were therefore designed to obtain high spatial resolution hydrographic and velocity data which might reveal internal tides at multiple sites. Both

3

experiments involved repetitive Conductivity, Temperature, and Depth (CTD) casts over a 25 hour period (2 cycles of the M2 tide) at two stations on the Canyon axis, and continuous current measurement along the axis using a downward-looking Vessel Mounted Acoustic Doppler Current Profiler (VM-ADCP). The April experiment concluded with the deployment of 27 Expendable Bathythermographs (XBTs) along a 16 km track over the Canyon axis. The October experiment included 25 additional hours of cross-canyon CTD and VM-ADCP measurements. The resulting high-resolution "snapshots" of the internal tide are of interest as they reveal:

- large amplitude, bottom-intensified current and density oscillations along the Canyon axis,

- beam-like, shoreward propagation of energy along the Canyon floor in April, and

- a standing wave pattern in October.

To augment the field study, tide gauge data from the Monterey and Santa Cruz stations (Figure 1) were obtained from the National Ocean Service (NOS) of the National Oceanic and Atmospheric Administration (NOAA). The hourly sea level measurements were used to study the spatial variability of the tides across the Bay and to characterize the barotropic tides during each cruise. Additionally, near-bottom current and temperature records from a recent deployment of an S-4 mooring near the Canyon head were analyzed for the tidal signal. These records reveal strong semidiurnal current and temperature oscillations in a portion of the water column which could not be measured by the VM-ADCP and CTD probe, as well as significant diurnal and higher frequency (6-8 hour period) oscillations.

2.   The Modeling Study

The goal of the modeling study was to gain insight into how canyon geometry affects the generation, propagation, and dissipation of internal tides. In pursuit of this goal, the ocean circulation model of Blumberg and Mellor (1987), also known as the Princeton Ocean Model (POM), was used to conduct a process study involving tidal forcing, density stratification, and canyon geometry. The modeling studies reveal the highly focused nature of internal tides in canyons, as opposed to the weaker internal tides propagating over the continental slope and shelf. Additionally, these three-dimensional simulations serve to demonstrate the sensitivity of internal tide propagation to canyon floor slope and width. Several features of the internal tide in MSC are

4

reproduced in the idealized simulations, including shoreward propagation of internal tide energy along the canyon floor and bottom-intensified current and density oscillations.

This work is organized as follows: background information on internal wave theory and observations is presented in Chapter II. Chapter III discusses the design, execution, and results of the field experiments, and includes an estimate of the barotropic tidal currents in Monterey Bay. The modeling experiments are presented in Chapter IV, and conclusions and recommendations are discussed in Chapter V.

II. REVIEW OF INTERNAL TIDE THEORY AND OBSERVATIONS

Internal tides are recognized as significant sources of current shear in the vicinity of large bathymetric features such as seamounts, shelf banks, sills, and the continental slope. A comprehensive review of internal tide theory and observations is given by Wunsch (1975). A more general review of oceanic internal waves is given by Garrett and Munk (1979), while Baines (1986) and Huthnance (1989) focus on internal waves and tides on continental shelves. Foreman (1995), in a discussion of internal tide variability and its impact on de-tiding observational data, describes more recent observations. A brief summary of internal tide theory and observations follows.

A. INTERNAL TIDE GENERATION AND PROPAGATION

Internal tides are generated over sloping topography, where the vertical component of the barotropic tidal current forces oscillations in the density field. If the forcing frequency (i.e., the tidal frequency) is superinertial and below the Brunt-Väisälä (i.e., buoyancy) frequency, the oscillations may propagate away from the generation site as plane internal waves. In a two-layer medium, internal wave energy propagates horizontally along the interface of the two fluids. In a continuously stratified medium, the energy associated with a plane internal wave travels at an *angle* to the horizontal. This angle is a function of the radian wave frequency, ω, the local buoyancy frequency, N, and the inertial frequency, f. The slope c of the energy flux or group velocity vector (the wave characteristic), derived from the dispersion relation for linear inertial-internal waves, can be expressed as:

$$c = \tan\theta = (\omega^2 - f^2)^{\frac{1}{2}}(N^2 - \omega^2)^{-\frac{1}{2}} \tag{1}$$

where θ is the angle which the group velocity vector makes with the horizontal. The wave number vector $\kappa = (k_H, m)$, which corresponds to the direction of phase propagation, is perpendicular to the group velocity vector (Figure 3). The horizontal components of the group velocity and wavenumber vectors point in the same direction, and their vertical components point in opposite directions. By geometry then, c is also equal to $k_H m^{-1}$ (the ratio of the horizontal

7

component of the wavenumber vector to the vertical component), and θ is also the angle which κ makes with the *vertical*.

Internal wave generation is strongest where the bathymetric slope γ, is equal to c (i.e., where the bottom slope is "critical" for the given wave frequency). In this situation the plane of the forcing motion, which is dictated by the bottom slope, and the plane of the particle motion for the free internal wave coincide. When this form of resonance exists, even very weak barotropic tidal currents can generate strong internal tides. On the continental slope south of Cape Cod, Massachusetts, where the barotropic tidal currents are estimated to be less than 1 cm s^{-1}, Wunsch and Hendry (1972) found the flow field to be dominated by internal tide contributions near a portion of the slope which is critical for the semidiurnal period. The most obvious generation site for internal tides in the coastal ocean is at the continental shelf break, where over a distance of a few kilometers the bathymetric profile changes from supercritical ($c < \gamma$) on the continental slope to generally subcritical ($c > \gamma$) on the shelf.

1.   Beam-like Propagation Of Internal Tides

Lab experiments and theoretical models indicate that near a generation site (within a few tens of kilometers), internal tide energy is confined to beams propagating along characteristics in the cross-isobath direction. These beams can be represented by ray tracing techniques as well as by the superposition of numerous vertical modes which constructively interfere inside the beam and destructively interfere elsewhere. Prinsenberg et al. (1974) superpose solutions of 45 vertical modes to demonstrate internal wave generation by a long surface wave passing over an idealized continental shelf in a continuously stratified (constant N) ocean, and subsequent beam-like propagation of internal wave energy in the shoreward and seaward directions. The seaward moving beam propagates downward and reflects off of the abyssal plain. The theoretical vertical thickness of this beam, in the inviscid case, is twice the depth of the shelf break. Prinsenberg et al. (1975) show that the inclusion of vertical and horizontal eddy viscosity in the normal mode solution yields a much thicker (O(2 km)) oceanic beam. The shoreward beam is narrower and travels along a characteristic ray path which reflects between the surface and the subcritical floor of the continental shelf.

8

Despite numerous observations of oceanic internal waves through the years, reports of beam-like internal wave propagation in the ocean are exceedingly rare. The primary reasons for this are:

- the narrow nature of the shoreward beam (and the typically coarse vertical resolution of current meter moorings on the continental shelf),

- the logistical difficulty of measuring internal waves seaward of the shelf break, where the beam should be wider, and

- the rapid dissipation of higher modes through nonlinear effects such as frictional damping, thermal diffusion and wave breaking.

Torgrimson and Hickey (1979) report propagation of the internal tide in an 80 m thick beam over the continental slope and narrow shelf off Oregon, based on analysis of current meter and temperature sensor data obtained at four cross-shelf locations. Beam-like propagation was inferred from the occurrence of baroclinic current maxima (5-10 cm s^{-1}) at depths which corresponded to the location of theoretical characteristic rays reflecting between the sea surface and shelf floor. Much wider (500-2600 m thick) seaward propagating beams have been observed beyond the continental shelf break in the Bay of Biscay by Pingree and New (1989, 1991) and off the west coast of Vancouver Island by Drakopolous and Marsden (1993). The remaining evidence for beam-like propagation lies in observations of strong internal tide signals at a few locations which correspond to likely characteristic ray paths for seaward propagating energy (Regal and Wunsch, 1973; Barbee et al., 1975; Petrie, 1975; DeWitt et al., 1986; Konyaev et al., 1995).

Most internal tide field measurements have been made over the continental shelf in depths of approximately 100 m, and the majority of these reveal shoreward propagation in the lowest vertical mode, rather than in a beam composed of numerous modes (Baines, 1986 and Huthnance, 1989). Beam-like propagation over the shelf is inhibited not only by the bottom and surface reflections (which dampen the higher modes), but by the variable stratification in the ocean. An accurate description of oceanic stratification usually lies somewhere between the two-layer and continuously stratified approximations, and Baines (1986) asserts that most internal tide energy propagating over the shelf is concentrated along the thermocline, with some of it "leaking" into the weakly stratified continuum below. In the thermocline, where N is large, the group velocity vector for internal tides is nearly horizontal. As stratification decreases with depth, the angle of the group velocity vector with respect to the horizontal becomes steeper. Sherwin (1988) notes that the amount of internal tide energy that propagates shoreward in the continuously stratified portion of

9

the water column is highly dependent upon the slope of the shelf. A brief discussion of the effects of bottom slope on internal wave propagation follows.

2. Internal Wave Reflection From Sloping Bottoms

The internal wave energy density spectrum, which appears to be fairly constant in shape and magnitude in most of the world's deep ocean (Garrett and Munk, 1979), becomes distorted in the presence of rapidly changing bathymetry. Sloping bathymetry tends to filter out some internal wave frequencies and amplify others. Phillips (1977) applied linear wave theory to demonstrate that the direction in which a progressive internal wave reflects from a sloping bottom boundary varies with the relationship between c and γ. For $c < \gamma$ (supercritical bottom slope), the incident internal wave energy reflects back to deeper water. Unlike reflected optical or acoustic waves, which make the same angle with respect to the reflective surface as the incident wave, a reflected internal wave maintains its angle relative to the horizontal (thereby conserving its frequency). For $c > \gamma$ (subcritical bottom slope, which is often the case on the continental shelf), the reflected wave energy continues to shoal.

Wunsch (1969) notes that as a wave is focused by subcritical bathymetry into shallower water, the wavenumber and particle velocity amplitudes increase linearly, in inverse proportion to water depth. Phillips explains the increase in wavenumber as a consequence of the no normal-flow boundary condition and the ensuing requirement to match, on the plane of the bottom slope, the projections of the incident and reflected wavenumber vectors. These projections are depicted in Figure 3. Group velocity, which varies inversely with wavenumber, decreases upon subcritical reflection and energy density increases. Eriksen (1982) notes that the ratio of reflected to incident energy density is proportional to the square of the ratio of reflected to incident vertical wavenumbers. Eriksen (1982) and Gilbert (1993) discuss the reflection of waves which arrive from various azimuths or orientations to the bottom slope. These effects will be ignored in this discussion, except to note that bottom reflection deflects waves toward a direction more normal to the sloping boundary, due to amplification of the wavenumber component which is normal to the isobaths.

Flat-bottom, constant N solutions for the first vertical mode show that the vertical velocity maximum and the corresponding node in horizontal velocity occur at mid-depth (Figure 4).

10

Wunsch (1969) shows that these modal shapes are distorted over sloping bathymetry due to amplification of the wave exhibiting downward phase propagation. As a subcritical bottom slope approaches the critical angle, the vertical and horizontal velocity mode shapes become "nose-like", with the deeper maxima increasing in magnitude and moving closer to the bottom (Figure 4). These near-bottom velocity maxima imply significant current shear and mixing over a sloping bottom. The special case of $c = \gamma$, critical bottom slope, results in a singularity in the linear solution; the vertical wavenumber (and hence, energy density) goes to infinity and the group velocity vanishes. Wunsch suggests that strong bottom intensification of the baroclinic currents and the creation of an unstable bottom boundary layer occurs in this case. The lab experiments of Cacchione and Wunsch (1974) and Ivey and Nokes (1989), the numerical experiments of Slinn and Riley (1996), and the field measurements of Gilbert (1993) and White (1994) indicate that critical angle reflection does in fact result in vigorous bottom currents and the establishment of a turbulent boundary layer. In any case, the sloping bottom is a region of significant shear, and this shear increases as the ratio of internal wave characteristic to bottom slope approaches unity.

3.   Internal Waves And Tides In Canyons

In submarine canyons, the effects of steep walls on internal wave intensification must be considered in addition to the focusing effect of the sloping floor. Gordon and Marshall (1976) describe submarine canyons as internal wave "traps"; for most internal wave frequencies, energy incident from above the canyon will be reflected deeper into the canyon (toward the floor) by the supercritical walls. Hotchkiss and Wunsch (1982) note that in the case of internal waves propagating along the axis toward the canyon head, energy density should increase not only because of the depth change but because the walls tend to narrow as well; the energy density increase should be inversely proportional to the decrease in canyon cross-sectional area. Thus, for a finite frequency band (the band for which the floor slope is subcritical and the wall slopes are supercritical), submarine canyons may be viewed as conduits which focus and amplify internal wave energy, channeling it toward the canyon head.

In most canyons, internal tides appear to be included in the band of internal wave frequencies which are amplified. In a study of near-bottom currents in 27 different canyons (including MSC), Shepard et al. (1979) noted that with the exception of aperiodic turbidity flows,

11

the most energetic canyon currents were those of tidal period. At 3 and 30 m above the floors of the various canyons, currents attributed to internal tides regularly attained speeds of 20-30 cm s^{-1}. Shepard et al. used simultaneous current measurements from adjacent moorings to estimate the horizontal component of phase propagation. In most cases, phase velocities were 20-100 cm s^{-1} in the upcanyon direction.

Wunsch and Webb (1979) used Shepard's Hydrographer Canyon data to document a five-fold increase in the kinetic energy density (normalized by N) of the internal wave field, from a position near the canyon mouth to one well inside the canyon (a distance of approximately 30 km). In a Hudson Canyon study, Hotchkiss and Wunsch (1982) used the same approach with data from four moored instrument arrays to depict a greater than six-fold increase in the normalized kinetic energy density over an axial distance of 20 km. The energy density spectra of both the Hydrographer and Hudson Canyon studies show distinct peaks at the semidiurnal frequency. By comparison, internal tides propagating over the continental shelf appear to dissipate over distances of 20-40 km (Brink, 1988 and Rosenfeld, 1990). Observations of strong internal tides have also been made in Baltimore Canyon (Hunkins, 1988; Gardner, 1989), Monterey Canyon (Broenkow and McKain, 1972; Shea and Broenkow, 1982; Heard, 1992), and on the shelves adjacent to Trou-Sans-Fond (Park, 1986), and Cape Point Valley (Largier, 1994). These studies reveal the following attributes of internal waves in canyons:

- Internal wave energy spectra are dominated by the semidiurnal internal tide.
- Baroclinic tides are more energetic in the canyon than on the adjacent continental slope, and most energetic near the canyon head, and
- Baroclinic tides are anisotropic, with greater kinetic energy in the along canyon direction than in the cross canyon direction.

Although Wunsch and Webb discuss the Hydrographer Canyon measurements in the context of rare exceptions to the canonical Garrett-Munk (1975) spectrum of deep ocean internal waves, submarine canyons should be recognized as features which traverse both the deep ocean and littoral regions. Hunkins notes that more than two dozen major canyons incise the continental shelf and slope off the east coast of the U.S. between Maine and Cape Hatteras. Hickey (1995) estimates that canyon mouths occupy 20% of the eastern Pacific shelf edge between Alaska and the equator, and in some locations (such as the Washington-Oregon coast) this figure is closer to 50%. Amplified internal wave energy within these canyons may travel to within a few kilometers of the coast before it is dissipated or reflected from the canyon heads. Along their propagation path,

these energetic internal waves can be expected to affect nutrient distribution, sediment transport, and optical clarity.

4.   Internal Tides In Monterey Submarine Canyon

The canyons which incise the narrow continental shelf off the west coast of the U.S. lie much closer to shore than those off the east coast. In the case of MSC, the Canyon head lies within 100 m of Moss Landing harbor. Within the confines of Monterey Bay the axis of the Canyon lies, with some meandering, in the cross-shore direction (080°-260°T), bisecting the Bay (Figure 1). Between the mouth of the Bay and the Canyon head, a distance of approximately 20 km, the floor of the Canyon rises from 1000 m to 100 m with a slope that varies between .030-.045 (1.7-2.6°). Over the same distance, Canyon width (defined as the distance between the 150 m isobaths on the Canyon rims) decreases from approximately 11 km to nearly 2 km. The great size of the Canyon and its proximity to shore make MSC an especially interesting and accessible natural laboratory for studying internal tides.

In addition to the NPS studies mentioned previously, Shepard et al. included MSC in their worldwide survey of near-bottom canyon currents. Analyzing 3-4 days worth of measurements from Savonius rotor current meters moored at 3 and 30 m above the axis at depths ranging from 155 to 1445 m, Shepard et al. found current oscillations with average cycle lengths of 8-9 hours. These current records may have been dominated by harmonics, or "overtides" (perhaps due to nonlinear interaction of semidiurnal and diurnal components near the bottom) rather than by the semidiurnal internal tide. In order to estimate the along-canyon phase speed of the observed current oscillations, Shepard et al. performed manual cross-correlations by superimposing simultaneous velocity plots from current meters at adjacent stations, and shifting the top plot right or left until a subjective "best fit" was obtained. The resulting time shift was used to calculate the rate of advance up or down the canyon for the current oscillations. Comparing velocity plots from three axial moorings at depths of 384 m, 357 m, and 155 m, Shepard et al. estimated upcanyon phase speeds of 30-45 cm s^{-1}. Additionally, Shepard et al. report downcanyon propagation at 265 cm s^{-1} between 1061 m and 1445 m (near the mouth of the Bay). This would be consistent with generation of internal tides in the main body of the canyon, however the 265 cm s^{-1} downcanyon phase speed is questionable due to its unusually high magnitude. It is quite conceivable that the

13

internal waves measured at the two deeper stations have different sources, as the Canyon axis meanders significantly at the mouth of the Bay.

Broenkow and McKain (1972) were the first to systematically observe tidal-band density field oscillations throughout the water column in MSC, recording vertical profiles of temperature and salinity over a 25 hour period at axial locations with water depths of 120 m and 220 m. Their measurements reveal semidiurnal isopycnal oscillations with maximum vertical displacements of 80 m and 115 m (i.e., wave amplitudes of 40 m and 57.5 m). Based on an observed phase lag of 3-4 hours between the two stations, and a station separation of 3 km, they conclude that an internal tide was propagating shoreward in the Canyon at 20-30 cm s^{-1}. These phase speeds imply a horizontal wavelength of $L_H = 8.9 - 13.4$ km for the semidiurnal internal tide ($L_H = c_{P_H} \times T_{M2}$, $T_{M2} = 12.4206$ hr $= 44,714$ s).

Despite the numerous accounts of internal tide activity in MSC, the three dimensional propagation characteristics and the dynamics involved in producing the unusually large amplitudes remain unknown. Shea and Broenkow attribute the large amplitude of the internal tide at the Canyon head to the narrowing and shoaling of the Canyon (as did Hotchkiss and Wunsch in the case of Hudson Canyon), however the floor slope alone may contribute to much of the amplification. Average values of buoyancy frequency in Monterey Bay, based on data from 50 CTD casts made at 36.64°N, 122.14°W between November 1989 and December 1992, range from 2×10^{-3} s^{-1} at 1000 m to 3.5×10^{-3} s^{-1} at 200 m. Using these values for N in Equation 1, with $f = 8.7 \times 10^{-5}$ s^{-1} (the inertial frequency at 36.75°N), and $\omega = 1.4 \times 10^{-4}$ s^{-1} (the M2 frequency), the resulting characteristic slopes range from 0.055 (at 1000 m) to 0.032 (at 200 m). Thus, the slope of the Canyon floor between the mouth of the Bay and the Canyon head (0.035-0.40) may be nearly critical for the M2 frequency.

If the buoyancy frequency profile in the Canyon is such that the floor slope is critical for the M2 frequency, bottom intensification of the internal tide could occur due to both the trapping of energy associated with incident internal tides (of external origin) and the generation of internal tides along the floor. Prior to this study, the only time series of temperature profiles obtained over deeper parts of the Canyon with high enough temporal resolution to reveal internal tides were those of Coelho (1994) and Shea and Broenkow. Shea and Broenkow obtained a 20 hour time series at a mid-bay, axial location 13 km west of Moss Landing, while Coelho conducted a 3 day tow-yo CTD and VM-ADCP survey of the upper ocean in a 4 km^2 box near the mouth of the Bay. While

14

both studies revealed semidiurnal isotherm displacements of O(20 m) in the thermocline, neither study could shed light on the degree of internal tide bottom intensification since neither extended deeper than 250 m; less than half the total water depth was measured in both cases.

III. THE FIELD EXPERIMENTS

A. DATA COLLECTION AND PROCESSING

1. Shipboard Experiments

a) *Experiment Design And Execution*

Two field experiments were designed in order to determine the wavenumber, the phase and group velocities, and the potential and kinetic energy levels of the internal tide in MSC. These "Internal Tide Experiments", which exploited the capability of the R/V *Point Sur* to obtain simultaneous vertical profiles of hydrographic and velocity data, were conducted in Monterey Bay during NPS student cruises on April 23-24 (ITEX1) and October 29-31 1994 (ITEX2). Both experiments included repetitive CTD sampling at two axial stations; one near the Canyon head and one further seaward in the Canyon. By cycling between CTD stations with continuous ADCP operation over a 25 hour period, it was possible to construct density and velocity time series with sufficient temporal resolution to reveal the semidiurnal isopycnal and current oscillations at both sites. Spatial averaging of the ADCP data allowed reconstruction of horizontal velocity time series not only at the CTD stations but at several locations between the stations as well. Upon completion of the ITEX1 CTD casts the ship travelled a straight course for 16 km along a line which passed over the CTD stations (Figure 1). During this transit 27 Expendable Bathythermographs (XBTs) were launched over the stern at intervals of approximately 500 m (Figure 1). The XBT data were used to produce a high spatial resolution "snapshot" of the temperature field along the Canyon axis. In order to obtain an estimate of the internal tide energy flux through the Canyon and a description of the cross-canyon structure of the internal tide, the ITEX2 along-canyon measurements were followed by 25 hours of cross-canyon CTD and ADCP surveys. The locations of the CTD stations and the positions assigned to the spatially-averaged ADCP measurements are depicted in Figure 5.

The analysis plan for the hydrographic data included the use of temperature and salinity to compute density, and the phase differences between the semidiurnal isopycnal oscillations at the two axial stations would be used to compute the horizontal (along-canyon) component of internal tide phase velocity and wavenumber. In this sense, the analysis plan was

similar to that employed by Broenkow and McKain. Additionally, the high vertical resolution of the hydrographic surveys was expected to reveal whether the internal tide was standing or propagating in the vertical, a feature of internal tide propagation not addressed in previous MSC studies. The simultaneous measurements of current velocity, temperature, and conductivity (and hence, density) would reveal for the first time the kinetic and potential energy levels of the internal tide.

During ITEX1, the CTD stations were spaced 8.3 km apart, with the expectation that this distance would represent 1/4-1/2 of an internal tide wavelength. This station separation was deemed close enough to permit a sampling rate which would resolve the phase of the semidiurnal signal at each site (i.e., at least every 3 hours), yet far enough to ensure a significant horizontal phase *difference* between the internal tides measured at each site. To avoid degradation of the ADCP measurements and maintain good horizontal resolution, a ship speed of 7 kts was used to transit between CTD stations. In practice, the CTD stations were occupied every 1.5-2 hours. This along-canyon sampling strategy proved successful and was used again during ITEX2, however the stations were located closer together (5.6 km apart) and closer to shore. The ITEX2 CTD stations were positioned so that the deeper axial station would be common to both the along- and cross-canyon measurements, allowing construction of a time series 50 hours in length at that site. The remaining cross-canyon stations were located above the north and south Canyon walls and in the shallow water (60-90 m) on the north and south flanks of the Canyon.

In order to find suitable locations for the CTD casts and verify the charted depth, the first cast at each site was preceeded by a bathymetric survey using the ships fathometer. Once a suitable site was identified, the bottom depth, latitude and longitude were recorded. The goal was to lower the CTD probe to within 10 m of the bottom on each cast, but the casts were occasionally shortened due to the proximity of the Canyon walls. The position of the ship at the commencement of the CTD cast was chosen as the location assigned to the CTD data, and post-cruise analysis of these locations indicated that the casts for any given CTD station were clustered within 200 m of each other. The ship was able to reoccupy each CTD station with great accuracy through the use of Differential Global Positioning System (DGPS) navigation, however the effects of wind and swell sometimes made accurate station keeping during the CTD casts a challenge. The ship kept station and minimized roll during the casts by turning toward the direction of the swell and maintaining bare steerageway. Considerable swell during ITEX2 necessitated a change in plans for the locations of the cross-canyon CTD stations. The original sites formed a line perpendicular

18

to the along-canyon stations, but these positions were altered slightly so that the ship could head into the swell (toward the northwest) during the transit from station to station. Each cycle of cross-canyon CTD casts began at the southernmost station and ended at the northernmost station.

Upon completion of each CTD cast at the along canyon stations, the ship proceeded to the next station by executing a Williamson turn and accelerating so as to be near cruising speed when the turn was completed. This maneuver ensured ADCP operations at constant course and speed along the line between stations. Although the ADCP is capable of measuring to depths greater than 400 m, this range was reduced by interference created by reflections of the side lobes from the Canyon floor and walls. Typically, the ADCP could only obtain measurements in the upper 70-80% of the water column. The geographic coordinates of each CTD station position, the depth indicated by the fathometer, and the maximum depths of the density and horizontal velocity time series constructed for each site are listed in Table 1.

TABLE 1 ITEX1 AND ITEX2 CTD STATION POSITIONS AND DEPTHS

ITEX 1					
STATION	LATITUDE deg min N	LONGITUDE deg min W	BOTTOM DEPTH (m)	MAX CTD DEPTH (m)	MAX ADCP DEPTH (m)
A1	36 47.52	121 50.10	248	243	171
A2	36 47.10	121 55.68	640	555	387
ITEX 2					
B1	36 47.85	121 49.19	175	147	115
B2/C3	36 47.70	121 52.98	420	411	307
C1	36 46.50	121 51.96	75	67	59
C2	36 47.40	121 52.72	360	307	275
C4	36 48.00	121 53.23	230	227	227
C5	36 49.20	121 54.24	85	75	67

b)   *ADCP Data Processing*

The ADCP used on both cruises was a hull-mounted RD Instruments model VM0150, a four beam JANUS array with a 150 KHz operating frequency. The ADCP was configured to record data in one minute ensemble averages and 8 m vertical bins. The transducer head is located 3m below the water line, and a 4 m blanking interval was selected to avoid recording data contaminated by turbulence near the hull. The first bin of data is therefore centered at 11 m and represents velocities averaged over depths of 7-15 m. The raw data was collected

using the RD Instruments Data Acquisition Software (DAS), which was run on a PC in the ship's lab. The navigation information supplied to the DAS came from ADCP bottom tracking when the ship was in water depths of less than 600 m, and from the DGPS system otherwise. An ADCP calibration run was conducted with bottom tracking during each cruise, so that the raw data could be corrected for alignment, gyro compass, and beam geometry errors in accordance with Joyce (1989). The subsequent steps in ADCP post processing, which involved editing data contaminated by side lobe reflections from the Canyon walls and floor, computing the ship's speed made good, and converting the raw, relative velocities to absolute velocities, are discussed in the following paragraph.

The geographic positions recorded by the DAS at the end of each ensemble were checked for obviously bad points, and corrected by linear interpolation when necessary. These quality checked positions were then used to calculate the orthogonal components of the ship's velocity (u, positive eastward, and v, positive northward). The next step was to determine the depth (bin number) to which the data remained reliable for each ensemble. This depth is the shallower of either bottom depth, or the depth at which the cutoff value of Percent Good Return (PGR) is reached. PGR is based on a signal to noise threshold or error velocity, and a cutoff value of 50% was chosen. The depth of reliable data was further checked by visually inspecting each of the ensembles for unrealistically large shears, which indicate contamination by side lobe reflections from the Canyon floor and walls. Once the maximum depths of the reliable data were identified, a reference layer common to all ensembles was selected (bins 3-5), and the averages of the raw velocities in this layer were computed. The u and v components of ship velocity were then added to the raw velocities in the reference layer, canceling the apparent velocities introduced by ship motion. The resulting absolute reference layer velocities were then smoothed to remove high frequency noise (by applying a low pass Hamming window with a cutoff period of 25 minutes) and subtracted from the raw velocity profiles of each ensemble. The accuracies of the resulting velocity measurements are estimated to be ± 4 cm s^{-1} (Heard, 1992; Coelho, 1994).

The locations of the processed ADCP ensembles were plotted with respect to latitude and longitude, effectively displaying the ship's track. During both cruises, the tracks between CTD stations plotted within swaths no wider than 500 m. The velocity data were then spatially averaged by assigning the measurements to evenly spaced along-track geographic bins. The along-track length of the bins used for the ITEX1 data was 1.5 km. For the ITEX2 along-Canyon measurements, the bin length was 0.75 km, and for the cross-canyon transect data the bin

length was 0.67 km. The centerpoints of the ITEX1 and ITEX2 bins are indicated with dots in Figure 5. Since the ADCP ensembles were recorded each minute and the ship's speed was 7 kts, several ensembles fell within a given geographic bin during each transit between CTD stations. The one minute ensembles in each geographic bin were then temporally averaged so that the sampling interval at each de facto ADCP station was the same as that of the CTD stations, 1.5-2 hours.

c)   CTD Data Processing

Hydrographic data were collected using a Neil Brown Instrument Systems (NBIS) Mk IIIB CTD during the April cruise, and a Sea-Bird model SBE 9/11 CTD during the October cruise. Both CTDs were pre- and post-cruise calibrated to check conductivity and temperature against lab standards. Differences obtained were then averaged and fit to linear regression schemes to obtain the coefficients necessary to adjust the CTD measurements to the reference standards. A detailed description of the calibration process for the NBIS Mk IIIB CTD is given in Tisch (1990), and calibration of the SBE 9/11 CTD is described in Rosenfeld et al. (1995).

During the cruises, pressure offsets (i.e., the pressures recorded by the CTD while on deck) were recorded at the beginning of each cast. These offsets were used as checks against lab-measured historical instrument drift. Hydrographic data were acquired during downcasts using winch speeds of 30 m/min in the upper and lower 150 m and 60 m/min at intermediate depths. Water samples were taken at various depths during the upcasts for use in post-cruise calibration of the salinity data, and the conductivity probe was rinsed with fresh water and covered after each cast to help ensure accurate salinity measurements.

The processing of the raw CTD data obtained with the NBIS Mk III-B CTD was accomplished with "CTDPOST", a software program designed specifically for EG & G Marine Instruments CTD systems. The Sea Bird CTD data was processed with another tailored software program, "SEASOFT". Both programs accomplish the same basic tasks, including: removal of obviously bad data points (due to plankton ingestion, power spikes, etc...), filtering of pressure data to remove high frequency noise, time-shifting the conductivity data relative to temperature in order to minimize salinity spikes, applying a thermal mass correction for the conductivity cell, and averaging the data into evenly spaced depth bins (2 m for the NBIS Mk III-B and 1 m for the SBE 9/11). Salinity was calculated from conductivity and temperature using PSS-78, and salinity and temperature were used to compute density (σ_θ). The salinity and temperature obtained with both

CTDs are considered accurate to within ±0.005 psu and ±0.005°C, respectively. The pressure measurements are accurate to within ±0.1% of the depth.

2. Sea Level Data

NOS maintains a tide gauge in Monterey harbor as a permanent control station in the National Water Level Observation Network. Between 17 May and 1 December 1991, NOS maintained a temporary tide gauge in Santa Cruz harbor in order to update tidal datums following the 1989 Loma Prieta earthquake. After 1 December 1991 the Santa Cruz gauge was on loan to NPS for the purpose of acquiring additional sea level measurements. Data was still processed by NOS, however data obtained after 10 September 1992 is suspect due to tide gauge equipment malfunctions.

Hourly sea level measurements recorded at Monterey and Santa Cruz between 18 May 1991 and 18 May 1992 were obtained from NOS and used to analyze the spatial variability of the surface tide in the Bay. NOS also provided hourly sea level data recorded with the Monterey tide gauge during ITEX1 and ITEX2. Both the Monterey and Santa Cruz tide gauges are of the stilling well type. A stilling well gauge is basically a stand pipe which houses a float, the level of which represents sea level. Water enters the stilling well through a small orifice which is usually located approximately 2 m below Mean Lower Low Water (MLLW) (Lentz, 1993). The orifice serves to damp out higher frequency oscillations. The float is attached through a system of gears and a counterweight to an automatic recorder. The level of the float is sampled every 6 minutes and automatically recorded by the punching of a binary code on a paper tape.

Possible sources of error in tide gauge measurements include currents in the vicinity of the stilling well (strong currents will cause a lower sea level in the well due to the Bernoulli effect), wave induced errors, marine fouling, and density changes due to river discharge or the advection of cooler or warmer waters in the vicinity of the well. According to Shih and Baer (1991), these effects can introduce errors on the order of several centimeters. Lentz reports the rms errors associated with a stilling well tide gauge measurement to be on the order of 1.5 cm or less.

22

3. S-4 Current Meter and Thermistor

Between 16 May and 21 June 1991, the Monterey Bay Aquarium Research Institute (MBARI) deployed an S-4 mooring with a current meter and platinum temperature sensor near the head of MSC at approximately 370 m depth, at 36° 47.73' N, 121° 51.88' w (Figure 1). The instruments were located 1.5 m above bottom. The temperature sensor has a reported resolution of 0.003° C and an accuracy of ±0.02° C. During the deployment, sensors recorded data every two minutes for 10 minutes, then shut off for 10 minutes to conserve power. The u and v velocity components (referenced to magnetic north) recorded by the sensor therefore represent two minute averages, while the temperature is an instantaneous measurement made at the end of the two minute averaging interval. In order to obtain hourly values of velocity and temperature for conventional tidal analysis, the 2 minute data were averaged to 10 minute data, and these average values were then taken to represent data obtained with a 20 minute sampling rate (one data point every 20 minutes). The time assigned to each data point was the middle of the 10 minute data acquisition period. The 20 minute data were then smoothed with three moving box car filters recommended by Godin (1972); the first filter averaged three data points at a time, and the second two each averaged four data points at a time. The smoothed time series of hourly velocity data were then rotated into east-west and north-south components (i.e., referenced to true north), and the velocity and temperature data were then analysed with least squares harmonic analysis programs which are discussed in the next section.

B. OBSERVATIONS AND ANALYSIS

This section presents density profiles, time series of isopycnal depth and currents, and along- and cross-canyon "snapshots" of the internal tide, as constructed from data obtained during both shipboard experiments and the S-4 current meter and thermistor deployment. The amplitude and phase of the semidiurnal internal tide are determined through least-squares harmonic analysis. The organization of this section is as follows: a brief description of the least squares harmonic analysis program is given, and then analyses of the surface tide in Monterey Bay and the internal tide observed in the along-canyon (ITEX1 and ITEX2) and cross-canyon measurements (ITEX2) are presented. The discussion of along-canyon observations includes an estimate of the barotropic

23

tidal currents in the Bay, which shows this component of current flow to be negligible (< 1 cm s^{-1}) in strength. This section concludes with a discussion of the S-4 current meter and thermistor observations.

1.   Harmonic Analysis

The tidal analysis programs of Foreman (1977, 1978) were used to determine the amplitudes and phases of the semidiurnal oscillations in sea level, isopycnal depth, density at a given depth, and current velocity. The programs are based on the least squares method described by Godin (1972), and have been employed in other internal tide studies, including Holloway (1985) and Hunkins (1988). Among the desirable features of these programs are the permission of gaps within the data record and compensation for smoothing effects due to prefiltering of the data. A standard list of 69 constituents is used for the analysis, with 77 additional shallow water constituents available for inclusion. The program output lists the amplitudes and Greenwich Phases of each resolved constituent, as well as a time series of hourly tidal height or current values (in the same units and covering the same time period as the input) based on the analysis results. A more extensive discussion of harmonic tidal analysis is contained in Appendix A.

While the amplitudes and phases of the various gravitationally forced tidal constituents are constant over time, the determination of their values is not a trivial matter. Short time series may prevent the resolution of important constituents which are narrowly separated in frequency. Meteorological factors, such as seasonal changes in the direction of prevailing winds and diurnal changes due to land/sea breeze cycling cause periodic sea level and current oscillations with tidal-band frequencies. The tides themselves contribute to non-gravitational forcing of tidal-band currents through internal wave generation and nonlinear interaction among stronger constituents. Analyses of internal tides are more sensitive to non-tidal "noise" than sea level analyses. Wunsch (1975) notes that while some of the observed intermittency in internal tides is real, much of it may be due to random fluctuations of background noise which "bury" the signal that would otherwise be visible.

The number of frequencies which can be resolved through harmonic analysis is dependent upon the record length. As record length increases, the effect of random noise in the record is reduced, and the number of identifiable tidal constituents increases. Those constituents which are

expected to be strongest in the record, based on their representation in the Equilibrium Tide, are applied earliest in the least squares fit; the longer the record length, the greater the number of tidal constituents that will be applied to the least squares fit. A record length of 24 hours, for example, is sufficient to identify the presence of semidiurnal oscillations in sea level records, but is too short to resolve the amplitudes and phases of the various semidiurnal constituents (M2, (12.42 hrs), S2 (12.0 hrs), K2 (11.97 hrs), etc.). In this case, the tidal analysis program will attribute the dominant semidiurnal oscillation in the record to the M2 constituent, since in the Equilibrium Tide M2 is stronger than the other semidiurnal constituents. The effect of unresolved constituents is to produce amplitude and phase modulations of the resolved constituent. The frequencies of the modulations can be determined by the differences in frequencies between the resolved and unresolved constituents; thus, failure to resolve the S2 constituent will produce an apparent spring-neap modulation (14.8 day period) of the M2 amplitude and phase.

Analyses of Monterey Bay sea level data (Petruncio, 1993; Schomaker, 1983; Maixner, 1973) show that the mixed, predominantly semidiurnal tide is dominated by the M2 constituent (49 cm amplitude). The next strongest semidiurnal constituent, S2, has an amplitude of 13 cm, 26% as large as M2. Thus, in a short record, attributing semidiurnal oscillations solely to the M2 constituent is an appropriate simplification in Monterey Bay, with the understanding that the calculated amplitude and phase actually represents a band of frequencies around the M2 consituent. Using the standard Rayleigh comparison constant of 1, a record length of 355 hours would be required for inclusion of both M2 and S2 in the least squares harmonic analysis (Foreman, 1977).

2.   Monterey Bay Tidal Heights Analyses

In order to analyze the spatial variability of the surface tide in the Bay, least squares harmonic analyses were performed on 366-day time series of sea level recorded at the Monterey and Santa Cruz tide gauges from 18 May 1991 through 18 May 1992. Sixty seven tidal constituents were resolved in the analyses, however the eight strongest constituents (four diurnal and four semidiurnal) account for 95% of the observed sea level variance. The periods and amplitudes of these components are listed in Table 2. The amplitudes are also depicted in a bar graph in Figure 6. In general, the results for Monterey and Santa Cruz are very similar. Both

locations are characterized by a mixed, predominantly semidiurnal tide, which is typical for the central California coast.

TABLE 2 DOMINANT TIDAL CONSTITUENTS IN SEA LEVEL

	Monterey		Santa Cruz	
	Amplitude (cm)	Greenwich Phase (deg)	Amplitude (cm)	Greenwich Phase (deg)
M2	48.9 ± .1	181.9 ± .3	49.5 ± .3	180.9 ± .4
K1	36.4 ± .1	219.5 ± .2	36.0 ± .2	220.3 ± .3
O1	22.8 ± .1	203.1 ± .3	22.8 ± .2	203.9 ± .5
S2	13.0 ± .1	180.7 ± .6	13.1 ± .3	179.6 ±1.4
P1	11.5 ± .1	216.4 ± .6	11.4 ± .2	218.5 ± .9
N2	11.2 ± .1	155.9 ± .6	11.2 ± .3	154.2 ±1.7
Q1	4.1 ± .1	197.3 ± 1.6	4.1 ± .2	196.8 ±2.5
K2	3.6 ± .1	172.6 ± 2.0	3.9 ± .3	169.2 ±4.8

In addition to the tide gauge errors discussed in the previous section, sea level fluctuations associated with periodic atmospheric pressure changes, wind forcing, and unresolved tidal constituents will contribute to errors in the tidal analysis. The errors associated with the analyzed amplitude and phases for the major constituents were determined by calculating the variance in residual sea level within the constituent frequency bands and then computing the propagation of this uncertainty in the subsequent amplitude and phase calculations. This error analysis method follows Filloux and Snyder (1979), and is a more rigorous treatment than that of Godin (1972), which assumes that the noise is spread equally across all frequencies. The frequency bands used to measure the residual variance in the vicinity of the major constituents were .036-.042 cycles per hour for the diurnal constituents and .077-.084 cycles per hour for the semidiurnal. Equations used to calculate the standard deviations of amplitude and phase may be found in Appendix B.

As expected for a year-long time series of sea level, the calculated amplitude and phase errors for the major constituents are quite small (less than 0.4 cm and 5°). The differences in amplitude for the major constituents at Monterey and Santa Cruz are within the estimated 1.5 cm

accuracy of the tide gauges. The phases in Table 2 suggest that the diurnal and semidiurnal components of the tidal signal arrive nearly simultaneously in Santa Cruz and Monterey; the Bay essentially co-oscillates. Between Monterey and Santa Cruz, the difference in phase for the M2 constituent, for example, is 0.3-1.7° (using the error bounds in Table 2); applying $\Delta t = \Delta G \times \dfrac{T_{M2}}{360°}$, where T_{M2} = 12.42 hours, this phase difference indicates an arrival of the M2 signal 1-3 minutes earlier in Santa Cruz than in Monterey. The phase differences for the other major constituents are either smaller than this, or insignificant compared to the calculated phase errors.

Differences between the phases of the various semidiurnal and diurnal constituents at Monterey and their corresponding constituents in Santa Cruz are most likely due to differences in the mechanical response of the tide gauges or the influences of bathymetry and harbor geometry in the immediate vicinity of the gauges, rather than propagation of a gravity wave in the Bay. The shallow water gravity wave phase speed for the Bay is about 30 m s^{-1} ($c = \sqrt{gh_o}$, h_o = 100 m), and such a wave would require about 20 minutes to travel from Santa Cruz to Monterey (as opposed to the 1-3 minute delay indicated by the M2 phase differences). Tidal period barotropic Kelvin wave propagation in embayments is expected only in cases where the width of the bay is much greater than the barotropic Rossby radius ($W << \sqrt{gh} \ f^{-1}$) (Werner, 1992). In such cases the tides propagate along the shores of the bay, rotating counterclockwise (in the Northern Hemisphere) about a nodal point in the center of the bay. The width of Monterey Bay, as measured between Point Pinos (on the northern tip of the Monterey Peninsula) and Point Santa Cruz (just west of Santa Cruz harbor) is approximately 36 km, while the barotropic Rossby radius within the Bay is approximately 360 km (using h = 100 m). Thus, little if any horizontal propagation of the surface tides is expected within the Bay.

3. Along-canyon Observations Of The Density Field

a) M2 Fit To Isopycnal Oscillations

Time series of isopycnal depths were constructed by searching through the profiles of σ_θ for a given value and recording its depth in each profile. In the event a given σ_θ value was

found at multiple depths in one profile, the shallowest depth was chosen if the isopycnal was ascending (based on its depth in the previous cast), and the deepest depth was chosen if the isopycnal was descending. Time series of isopycnal depths for the axial CTD stations, the concurrently observed sea level variations (as recorded at the Monterey tide gauge station), and the M2 amplitudes and phases resulting from harmonic analyses of the time series are presented in Figures 7 (ITEX1) and 8 (ITEX2). The de-meaned sea surface heights are represented by a dashed line which oscillates above and below $z = 0$ m. The vertical scale of the sea surface heights is exaggerated by a factor of 10; the actual range from higher high water to lower low water is approximately 2 m. Isopycnals are depicted at their observed depths (i.e., without exaggeration of the vertical scale) for every .02 kg m^{-3} increase in density. The isopycnal depths are linearly interpolated from nearly two-hourly to hourly for ease of display. Although the isopycnal depth variations are plotted with solid lines, the reader should bear in mind that significant depth variations due to shorter period oscillations may have been unobserved and/or aliased by the chosen sampling scheme.

In both experiments, large amplitude (>10m) internal tides are apparent throughout the water column at the shallow stations and below 100 m at the deep stations. The M2 amplitudes and phases of the isopycnal oscillations are depicted at the mean depths of the corresponding isopycnals. The maximum M2 displacement amplitudes are 39 m in ITEX1 and 35 m in ITEX2 (i.e., total crest-to-trough displacements of 78 m and 70 m, respectively). Due to the short record lengths, it is difficult to place "error bars" on the amplitude and phase plots. Conventional error estimate techniques (Filloux and Snyder, 1979, and Tee, 1982) use the assumptions that the covariances of the sine and cosine terms resulting from the least squares fit are equal to zero, and that their variances are equal to each other (see Appendix B). These assumptions may not hold true for short records. As a relative measure of the confidence in the analysis, the percent variance accounted for by the M2 fit is depicted below the time series of isopycnal depths. In lieu of a more rigorous error analysis, it will suffice to say that the time-varying signal based on the analyzed M2 amplitudes and phases accounts for 50-90% of the variance in the observed density field.

b) *Isopycnal Displacement Phase Variations - ITEX1*

The M2 phases in Figures 7 and 8 are plotted in hours, relative to the phase of the M2 sea level signal. A positive phase value indicates the length of time that passes between high

tide for the M2 component of sea level and the cresting of an isopycnal displacement caused by the semidiurnal internal tide; since the M2 period is 12.4 hours, a phase lag of 6.2 hours would indicate a 180° phase difference between the baroclinic and barotropic tides. The ITEX1 phases (Figure 7) generally increase with depth, which indicates downward phase propagation of the internal tide. The phase increases nearly linearly between 125-400 m at the deep station, over which a 2.5 hour increase in phase occurs, and between 50-175 m at the shallow station, where a 2 hour increase occurs. At a given depth, the phases at the shallow station lag those at the deep station, which indicates an eastward component of phase propagation.

On continental shelves, internal tides are commonly observed to be standing in the vertical due to superposition of upward and downward propagating waves. The linear phase increase with depth in the ITEX1 measurements is indicative of beam-like behavior, and the slope of the beam can be determined by finding the depths at which a given phase value is found at both stations (since phase is theoretically constant along the beam). A phase lag of 5 hours, for example, occurs at 410 m at the deep station and 75 m at the shallow station. Since the station separation is 8.3 km, the slope of the beam is $(.41-.075)/8.3 = .04$, which corresponds to an angle of 2.3°. Since the horizontal components of phase and energy propagation share a common direction, the energy must be propagating eastward and upward from the deep station to the shallow station at an angle of about 2.3°.

This slope estimate can be checked by calculating the horizontal and vertical components of phase velocity (c_{p_x} and c_{p_z}), and using them to determine the wave characteristic slope, since $\tan \theta = k_h m^{-1} = L_z L_x^{-1} = c_{p_z} c_{p_x}^{-1}$. The method of least squares is used to fit a straight line to the portion of the phase plots which indicate a linear increase in phase with depth. The slope of this line, $\Delta z (\Delta G)^{-1}$, is taken to be c_{p_z} at each station. c_{p_x} is calculated by dividing the distance between the two stations by the phase difference between stations ($\Delta x (\Delta G)^{-1}$) at those depths over which $\Delta z (\Delta G)^{-1}$ is linear. Using this method, c_{p_z} equals 2.7 cm s^{-1} downward at the deep station (which corresponds to a vertical wavelength of $L_z = c_{p_z} (2\pi) \omega^{-1} = 1.2$ km) and 1.7 cm s^{-1} downward at the shallow station ($L_z = 0.76$ km). Since c_{p_z} is slightly different at each station, c_{p_x} varies slightly with depth, from 62.2 cm s^{-1} at 125 m to 57.4 cm s^{-1} at 175 m, with an average value of 59.6 cm s^{-1} ($L_x = 26.65$ km). Using the average value of c_{p_x} and the

values of c_{p_z} determined at each station, $\theta = 2.6°$ at the deep station and $1.6°$ at the shallow station. This change in propagation angle for the group velocity is consistent with the flatter trajectories expected in shallower depths, where N is higher. The average of these two angles is $2.1°$, close to the $2.3°$ estimate obtained by comparing the depths of equal phases.

A further check on these calculations is to use the density profiles from each station to compute N profiles, and use appropriate values of N to solve Equation 1, $c = \tan \theta = (\omega^2 - f^2)^{\frac{1}{2}}(N^2 - \omega^2)^{-\frac{1}{2}}$. The temporally averaged density profiles and the corresponding N profiles for the two stations are depicted in Figure 9. The average values of N, calculated over the depths of the linear phase increases, are $N = 3.63 \times 10^{-3}$ s^{-1} between 125-395 m at the deep station and $N = 5.19 \times 10^{-3}$ s^{-1} between 50-180 m at the shallow station. Using these values in Equation 1, we obtain propagation angles of $1.7°$ and $1.2°$ at the deep and shallow stations, respectively. These are 25-35% smaller than the angles computed by the other methods, but qualitatively similar in that the steeper angle to the horizontal is found at the deeper station. It is found that better agreement with the previous estimates is obtained if f in Equation 1 is set equal to zero. The equation then yields energy propagation angles of $2.2°$ (deep station) and $1.6°$ (shallow station). The dispersion relation for internal waves (Equation 1) does not account for the presence of lateral boundaries, and these results indicate that the angle of internal tide energy propagation is altered by canyon geometry. This effect will be discussed further in the section on the along-canyon current field observations.

The wave group velocity at the two stations can be calculated using the equation for waves in the "rotating wave regime" (Gill, 1982), appropriate for waves with $\omega = O(f)$ but $\omega \geq f$:

$$c_{g_H} = \frac{N(\omega^2 - f^2)^{\frac{1}{2}}}{\omega\, m} \qquad c_{g_z} = -\frac{(\omega^2 - f^2)^{\frac{3}{2}}}{\omega\, N\, k_H}.$$

Using the buoyancy frequencies and wavenumber components discussed above, these equations yield upcanyon group velocities of 54.9 cm s^{-1} and 49.2 cm s^{-1} at the deep and shallow stations, respectively. These group velocities indicate that 55 cm s^{-1} may be the upper bound on current speeds associated with the internal tide in MSC (50 cm s^{-1} near the Canyon head), except perhaps in turbulent bores, since the particle velocity in a linear wave cannot exceed the wave group velocity. This upper limit is consistent with the maximum tidal current velocities of 50 cm s^{-1}

observed in and above MSC by Dooley (1968) and McKay (1970). If rotational effects are considered negligible (i.e., $f = 0$), these group velocities are reduced by 2 cm s^{-1} at the deep station and by 1 cm s^{-1} at the shallow station.

c)   Isopycnal Displacement Phase Variations - ITEX2

Although the internal tide is of similar amplitude in ITEX1 and ITEX2, the vertical and horizontal phase variations in the two experiments are quite different. The variations in phase of the ITEX2 isopycnal displacements (Figure 8) are indicative of a standing wave pattern, as opposed to a progressive wave as in ITEX1. Between 90-250 m at the deep station and between 20-110 m at the shallow station, phase is nearly constant at approximately 2 hours (relative to M2 sea level). In the upper and lower 100 m of the deep station, the phase changes approximately 180° (6 hours). The 180° phase shift in the lower 100 m corresponds to a node in vertical displacement, which is represented by the M2 amplitude minima at 350 m. The 180° phase shift near the surface may also coincide with a node, but the near surface minimum in vertical displacement does not necessarily verify the presence of an internal wave node since displacements are expected to be minimal in the region of strong stratification. Further evidence of a standing wave pattern will be presented in the discussion of the baroclinic tidal currents observed in ITEX2.

4.   Along-canyon Observations Of The Current Field

In order to describe baroclinic tidal currents, it is sometimes necessary to separate the barotropic and baroclinic components of velocity since they may have comparable magnitudes. In field measurements of internal tides over the shelf, this separation is usually accomplished by assuming that the depth integral of the horizontal baroclinic tidal currents is equal to zero. The barotropic tidal current at a given location can thus be approximated by performing a tidal analysis of the depth-averaged current, if the water column is well sampled in the vertical (i.e., by moored current meter strings). The barotropic tidal currents can then be subtracted from the original time series, and a tidal analysis can be performed on the residual current to determine the baroclinic tidal currents, as in Rosenfeld (1990) and Holloway (1994). Although the ITEX ADCP measurements feature better vertical resolution than typical current meter strings, they did not

reach the bottom 20-30% of the water column over the Canyon axis. Since the baroclinic tidal currents are expected to be bottom-intensified when the bottom slope is near-critical, as appears to be the case in MSC, the depth integral of the ADCP measurements can be expected to retain a significant contribution from baroclinic currents. An alternate approach to separating the barotropic and baroclinic tidal currents is to consider a theoretical model of the barotropic tide, as in Huthnance and Baines (1982). An estimate of the east-west (along-canyon) component of the barotropic tidal currents in Monterey Bay, based on both the spatial variability of tidal heights across the Bay and previous studies of barotropic tides in the eastern Pacific, is presented in the following paragraphs.

a)   *Barotropic Tidal Current Estimate*

Given that the Bay co-oscillates at tidal frequencies, simple mass conservation arguments can be used to calculate the strength of the barotropic tidal currents expected at the mouth of the Bay. The volume which flows into the mouth of the Bay during the flood tide should roughly equal the change in volume of the Bay that occurs between low and high tide. We can use this approximation to calculate a temporally averaged, barotropic flood current as follows:

$$u = \frac{\eta\, A}{t\, h\, w}$$

where

u = average flood current across the Bay mouth

η = typical tidal excursion (1.5 m)

A = surface area of the Bay (500 km^2)

t = duration of flood tide (6 hr)

h = average depth across the Bay mouth (175 m)

w = width of the Bay at the mouth, defined by a line connecting Pt. Santa Cruz and Pt. Pinos (36 km).

The above equation yields an average current speed of 0.55 cm/s flowing shoreward across the mouth of the Bay during the six hours between typical low and high tides. For the M2 component of this current, we substitute 1 m (twice the M2 tidal amplitude of 50 cm) for η and 6.2 hours for t in the above equation, which yields an average semidiurnal flood current of 0.37 cm s^{-1}. Assuming the current varies sinusoidally, its maximum amplitude would be 0.58 cm s^{-1} ($\pi/2$ times the mean

32

value taken over half a cycle). This amplitude is consistent with the weak cross-shore current expected of the very long wavelength (≈ 8000 km) Kelvin-like wave of M2 frequency propagating northward along the California coast, modelled by Munk et al. (1970) and further discussed by Miles (1972). It is also in very close agreement with the Battisti and Clark (1982) estimate of 0.2-0.5 cm s^{-1} for the cross-shore M2 currents over the narrow shelf off central California (Figure 10) and the barotropic M2 currents observed off northern California by Rosenfeld and Beardsley (1987).

Breaker and Broenkow (1994) arrive at a much larger estimate of 18 cm s^{-1} for the semidiurnal flood current flowing northeastward into the Bay. However, their methodology has a number of problems associated with it, the primary one being that they calculate the current associated with a shallow water wave propagating with a shoreward component, as opposed to the actual semidiurnal tide which propagates alongshore. They neglect the effect of a reflected wave, as well as rotational and frictional effects. For the purposes of this study, the barotropic M2 current in MSC is assumed to be negligible, and the results of the tidal analyses performed on the ADCP measurements will be taken to represent the baroclinic tidal currents.

b) Along-canyon Baroclinic Currents

As in the case of the isopycnal analyses, the ADCP-derived u and v components of velocity were linearly interpolated to hourly values and subjected to harmonic analysis. In general, the u component of velocity was much stronger than the v component and increased in strength with depth. Due to the meandering of the Canyon axis (Figure 1), no attempt was made to rotate the orthogonal velocity components into along- and cross-canyon directions, although in general u is nearly along-canyon. The variance of each hourly-interpolated time series of u for the along-canyon measurements is depicted in the top graphs in Figure 11. Variance is plotted with respect to ADCP bin depth and the distance of the geographic bin from the Canyon head (defined as 121.8° W, 36.8° N). The wedge in each graph depicts the approximate slope and depth of the canyon floor. The graphs at the bottom of Figure 11 indicate the percentage of u variance accounted for by fitting (via harmonic analysis) a tidal (M2) period wave to the data. These percentages were determined by calculating the ratio of the M2 u variance to the variance of the hourly interpolated u time series, and multiplying by 100.

Maximum values of u variance were similar in both experiments: 145 cm^2 s^{-2} (ITEX1) and 141 cm^2 s^{-2} (ITEX2). The variances of the v component of velocity (not depicted)

were generally less than 25 cm^2 s^{-2} at most depths, although values as high as 56 cm^2 s^{-2} (ITEX1) and 64 cm^2 s^{-2} (ITEX2) were observed at a few scattered locations. Except for portions of the water column where the u variance is weak (< 20 cm^2 s^{-2}), the variance of the M2 u accounts for 50-90 % of the total variance in u. This simplified presentation of the ADCP measurements demonstrates that at those Canyon locations in which strong currents were observed, most of the current activity is attributable to semidiurnal oscillations. Consistent with beam-like propagation, the depths at which the M2 currents stand out against background noise correspond to the depths of strong M2 isopycnal oscillations. It should be noted that some of the regions of weak current variance correspond to those portions of the ships track which leave the Canyon axis and pass over portions of the Canyon walls. This is especially true for the ITEX2 data, which shows an abrupt change from strong to weak variance at approximately 4 km from the Canyon head. This region corresponds to that part of the track which carried the ship over a portion of the north wall, just west of CTD station B1 near the Canyon head (Figure 5).

The steering effect of the Canyon walls can be seen in the orientation of the M2 tidal ellipses, which are presented in Figures 12 and 13. Each ellipse is plotted in an x-y plane, however the center of each ellipse is plotted at the depth appropriate to the ADCP bin from which the ellipse was calculated. Over those bottom depths at which strong M2 currents are found, ellipse orientation is uniform and aligned with the Canyon axis. The maximum M2 currents are approximately 20 cm s^{-1} in the along-canyon direction, which corresponds to an along-canyon particle excursion of 2.8 km before current reversal. Some rotation of the ellipse orientation occurs in the upper part of the water column, above and below the depths of the weakest M2 currents. This rotation is likely due to vertical shear stresses (Prandle, 1982). The near-surface M2 current maxima may be due to the presence of internal tides at the base of the surface mixed layer, or near-surface beams of internal tide energy, which will be discussed further in Section C.

Theoretically, the ratio of the semimajor axis to the semiminor axis for an internal gravity wave is equal to the ratio of ω to f, which for the M2 frequency and the latitude of Monterey Bay and is 1.6:1. The observed ratios in the nearly rectilinear ellipses are considerably greater, most likely due to the presence of the Canyon walls. For a 20 cm s^{-1} semimajor axis, the theoretical semiminor axis would be 12.5 cm s^{-1}, which corresponds to a particle excursion of 1.8 km in the cross-canyon direction over 6 hours (1/2 of the semidiurnal period). In the vicinity of

ITEX1 CTD station A2, the walls narrow from roughly 3 km at the rim (defined as the 100 m isobath) to less than 1 km along the floor.

The observed u velocities (interpolated to hourly data), the tidal fits to these observations, and the concurrent isopycnal displacements at the ITEX1 CTD stations are plotted together versus depth and time in Figure 14. The magnitude and direction of u is represented in color, with eastward flow represented in red, westward in blue. Superimposed on the u field are white lines indicating the depth excursions of selected isopycnals (plotted for each 0.1 kg m^{-3} increase in density). At the top of each graph, the observed sea level variations (exaggerated by a factor of 10) are indicated with dashed black lines. Between 200-400 m at the deep station and throughout the water column at the shallow station, maximum shoreward flow occurs approximately 1/4 cycle (three hours) before the isopycnal reaches its maximum upward displacement, i.e. u leads ξ (and ρ') by approximately 90°. This phase relationship is consistent with an internal wave propagating in the horizontal and vertical directions (i.e., in a beam-like manner), with $k_H > 0$ and $m > 0$. A description of the expected phase relationships for beam-like propagation follows.

In a continuously stratified, incompressible fluid, the perturbation velocities and density associated with a small disturbance can be related to the perturbation pressure by the following equations (Gill, 1982):

$$\frac{\partial^2 u}{\partial t^2} + f^2 u = -\frac{1}{\rho_o}\frac{\partial^2 p'}{\partial x \partial t} - \frac{f}{\rho_o}\frac{\partial p'}{\partial y}$$

$$\frac{\partial^2 v}{\partial t^2} + f^2 v = -\frac{1}{\rho_o}\frac{\partial^2 p'}{\partial y \partial t} + \frac{f}{\rho_o}\frac{\partial p'}{\partial x}$$

$$\frac{\partial^2 w}{\partial t^2} + N^2 w = -\frac{1}{\rho_o}\frac{\partial^2 p'}{\partial z \partial t}$$

$$\frac{\rho'}{\rho_o} = -\frac{i\,N^2 m}{g(N^2 - \omega^2)}\frac{p'}{\rho_o}$$

The polarization relations for plane progressive internal waves are obtained by substituting the wave form solution (i.e., $p' = p'_o\,[\cos(kx + mz - \omega t) + i\,\sin(kx + mz - \omega t)]$) for each of the variables in the above equations. Defining the x axis as the direction of the horizontal component of the wave number vector, and expressing the variables in terms of p', these substitutions yield:

35

$$u = \frac{k\omega}{(\omega^2 - f^2)} \frac{p'}{\rho_o}, \qquad\qquad v = -\frac{i f k}{(\omega^2 - f^2)} \frac{p'}{\rho_o}$$

$$w = -\frac{\omega m}{(N^2 - \omega^2)} \frac{p'}{\rho_o}, \qquad\qquad \rho' = -\frac{i N^2 m}{g(N^2 - \omega^2)} \frac{p'}{\rho_o}$$

To observe the phase relationships with respect to time at a given point in the water column, we can set ($kx + mz$) in the p' term equal to zero. We then find that for a wave which exhibits downward phase propagation ($m < 0$), u,w, and p' vary as $\cos(\omega t)$, v varies as $-\sin(\omega t)$, and ρ' varies as $\sin(\omega t)$. These relationships are depicted in Figure 15. In such a case, u and w are in phase and lead ρ' by 90°, as observed in ITEX1. Theoretically, v is 180° out of phase with ρ'; thus maximum northward (southward) flow occurs at the troughs (crests) of the isopycnals, and at a given point in space, the velocity vector rotates anticyclonically in time. The ellipses calculated from the ITEX1 data exhibited anticyclonic rotation at most depths, however the v component of velocity was generally insignificant (due to topographic constraints), compared to the estimated accuracy (± 4 cm s^{-1}) of the ADCP measurements. The robust results of the harmonic analysis of the currents are the ellipse orientation and the amplitude and phase of the along-canyon component of velocity.

Since u and w are in phase, the particle motion should lie in the plane of the wave characteristic. The amplitudes of u (or more appropriately, the amplitude of the ellipse semi-major axis) and w (which is computed from $w_o = \xi_o \omega = \frac{\rho_o'}{\partial \rho_o / \partial z} \omega$) inside the beam can thus be used as another check on the previously calculated slope of the wave characteristic, since $w_o / u_o = \tan \theta$. Using the depths at which u leads ρ' by approximately 90° as a criteria for identifying the location of the beam, the range of values for θ calculated from $\tan^{-1}(w_o / u_o)$ is 1.83°-2.94° between 250-387 m at the deep station and 1.31°-2.73° between 51-171 m at the shallow station. These angles and depths are in reasonable agreement with the calculations based on the isopycnal phases (i.e., 2.6° and 1.6° at the deep and shallow stations respectively).

The above polarization relations were used to calculate the perturbation density and velocity fields for a theoretical M2 internal tide (with $f = 8.7 \times 10^{-5}$ s^{-1}, appropriate for 36.75°N) for comparison to the ITEX1 observations. The theoretical velocity and density fields were based on an internal tide with $m = 5.2 \times 10^{-3}$ m^{-1} and $k = 2.1 \times 10^{-4}$ m^{-1} (consistent with

36

$L_z = 1.2$ km and $L_x = 30$ km, as computed from the ITEX1 CTD data). A buoyancy frequency of $N = 3.5 \times 10^{-3}$ s^{-1} was used, consistent with the mean value observed below 250 m at the ITEX1 deep CTD station. The theoretical mean density was a function of depth, increasing from $\rho_o = 1026$ kg m^{-3} at the surface to $\rho_o = 1027.5405$ kg m^{-3} at $z = -1200$ m, with a vertical gradient consistent with the chosen buoyancy frequency value. Having specified these values, it was possible to use typical values of u (based on the ITEX observations) to solve for the perturbation pressure amplitude p'_o, and p' was then used to solve for the remaining variables. The theoretical and observed u and ρ' fields are compared in Figure 16. The observed fields are the M2 u and ρ' time series at ITEX1 Station A2, from the shallowest depth at which a buoyancy frequency of 3.5×10^{-3} s^{-1} is appropriate, to the maximum depth at which current measurements were obtained. Over these depths, the amplitude of u increases from 6.8 to 14.4 cm s^{-1}. For this comparison, a theoretical u_o of 10 cm s^{-1} was used to solve for the remaining variables. Better agreement with the observed fields is found by setting $f = 0$ in the polarization equations. The theoretical vertical displacements are 35% smaller than observed if rotational effects are included.

A theoretical ρ' field is compared to the snapshot of the temperature field obtained with the XBT drops at the conclusion of ITEX1 (Figure 17). The temperature field was assembled from XBTs dropped over a 56 minute time span as the ship cruised westward along the Canyon axis. The last XBT was dropped at 1818 (GMT), one minute prior to the predicted high tide at Monterey. Of the 27 XBTs dropped, the first two and last one indicated abnormally high temperatures (above 11° C) throughout the water column and were considered unreliable. Another XBT profile obtained 6 km from the Canyon head indicated abnormally high temperatures below 100 m, and only part of the profile was used. For this comparison, which spans depths of 50 to 450 m, a u_o of 15 cm s^{-1} is used to calculate ρ' (with $f = 0$); this velocity gives a slightly better fit of the the theoretical ρ' field to the large isotherm excursions observed below 300 m than the choice of 10 cm s^{-1}.

Only the upper 1/3 ($0 \leq mz \leq 2\pi/3$) and the eastern 1/2 ($\pi \leq kx \leq 2\pi$) of the theoretical density field are depicted in Figure 17, at time $\omega t = 0$. Below 200 m, where the actual buoyancy frequency is fairly constant, the slope of the isotherms (60 m depth change over 9-10 km) is in excellent agreement with the sinusoidal shape of the theoretical density field. Superimposed on the mesoscale internal tide oscillations are microscale (O(1 km)) oscillations of

37

considerable amplitude. These smaller scale oscillations are barely resolved by the XBT sampling scheme, but are consistent with the hydraulic jumps associated with the internal tides observed by Holloway (1991) on the Australian NW Shelf. Similar small scale features may have been aliased in the ITEX CTD and ADCP measurements, and are considered a possible source of error in fitting an M2 wave to the observations.

The ITEX2 u velocity component and concurrent isopycnal oscillations are depicted in Figure 18. Unlike the ITEX1 observations, the ITEX2 currents and isopycnals reveal a standing wave pattern. Abrupt 180° phase shifts in u occur between 50-100 m at Station B2 and above 50 m at Station B1. A 180° phase shift also occurs in ρ' above 50 m at B2, but is more easily seen in the phase plot of Figure 8. Below these depths, the phase of u and ρ' at both stations is essentially constant with depth. Internal tides on the continental shelf are typically observed to propagate in the first mode, i.e. standing in z and propagating shoreward (Baines, 1986). In such a case, u and ρ' are 180° out of phase in the upper half of the water column (above the thermocline) and in phase in the lower half, due to a 180° phase shift in u at mid-depth (across the thermocline). The mid-depth node in u in such a case corresponds to a maximum in w and ρ'. In the ITEX2 observations, u leads ρ' by 90°. This phase relationship can exist along certain portions of an internal wave which is standing in both z and x. Unlike progressive waves, the phase relationships between u, v, w, and ρ' in standing waves have spatial dependence.

The behavior of the first mode, flat bottom internal seiche (i.e., an internal wave standing in two dimensions) is useful for a general description of how the phase relationships between u, w, and ρ' differ in progressive and standing waves. In the case of a wave standing in z and propagating in x (the typical continental shelf case), the applicable polarization equations can be derived by making substitutions of the form:

$$p' = p_o[\cos(mz)\cos(kx - \omega t) + i\,\cos(mz)\sin(kx - \omega t)]$$

which represents the sum of upward and downward propagating waves. In the case of a wave standing in both x and z, substitutions of the form:

$$p' = p'_o[\cos(kx)\cos(mz)\cos(-\omega t) + i\,\cos(kx)\cos(mz)\sin(-\omega t)]$$

are made, which results in the following polarization equations:

$$u = \frac{k\omega}{(\omega^2 - f^2)}\frac{p_o}{\rho_o}\sin(kx)\cos(mz)\sin(\omega t) \ , \qquad v = \frac{kf}{(\omega^2 - f^2)}\frac{p_o}{\rho_o}\sin(kx)\cos(mz)\cos(\omega t)$$

38

$$w = -\frac{m\omega}{(N^2 - \omega^2)}\frac{p_o}{\rho_o}\cos(kx)\sin(mz)\sin(\omega t), \quad \rho' = \frac{N^2 m p_o}{g(N^2 - \omega^2)}\cos(kx)\sin(mz)\cos(\omega t).$$

The spatial dependence of the phase relationships between these variables can be seen in Figure 19, which depicts a first mode ($L_z = 2H$, where H is the bottom depth), flat bottom internal seiche. There is no vertical component of flow at any point along the wave at times $\omega t = 0$ and $\omega t = \pi$, when the isopycnals are at their maximum deflection, and the only horizontal flow is due to v (not depicted). Maximum u and w velocities occur one quarter of a cycle later. In the quadrants bounded by $0 < kx < \pi/4$ and $\pi/2 < kx < 3\pi/4$ in the upper half of the water column and by $\pi/4 < kx < \pi/2$ and $3\pi/4 < kx < 2\pi$ in the lower half, u leads ρ' by 90° as observed in ITEX2. Additionally, nodes in u and w (or ξ) are colocated as appears to be the case in ITEX2.

The fact that the observed 180° phase shifts in u occur at different depths at each ITEX2 along-canyon station suggests that the internal tide during this period is standing *along and perpendicular to the characteristic* (in the manner of the basin internal seiches depicted in Maas and Lam (1995)), rather than in the horizontal and vertical planes. This pattern is seen clearly in Figure 20, which depicts the phases of the M2 u oscillations observed at each along-canyon geographic bin in ITEX1 and ITEX2. The phases are plotted in color, in hours relative the maximum M2 sea level displacement. The dashed lines superimposed on the figure represent M2 characteristics calculated from the N profiles observed at the deep and shallow ITEX2 CTD stations. The source regions for these characteristics (i.e., the internal tide generation sites) are discussed in Section C of this chapter.

While the ITEX1 u phases in Figure 20 show a steady increase from -2 hours (leading the M2 sea level oscillations) to +2 hours (lagging sea level) with depth, the ITEX2 phases show an abrupt shift from ±6 hours (180° out of phase with sea level) to values between 0 and -2 hours (nearly in phase with sea level). The depth of the abrupt phase shift, which corresponds to the depth of the nodes in the M2 ellipse plots (Figure 13), decreases towards the Canyon head at a rate that matches the slope of the M2 characteristics. A modal description of the observed standing wave pattern is presented in Section C.

5. Cross Canyon Observations

a) Density Field

The cross-canyon CTD and ADCP measurements were conducted during the second half of ITEX2. These measurements, like the ITEX2 along-canyon measurements, revealed large amplitude isopycnal and current oscillations with little vertical phase propagation at depths greater than 90 m. The observed isopycnal oscillations, M2 amplitudes and phases, and the percentage of total variance accounted for by the M2 wave fit are depicted for three of the five cross-canyon CTD stations in Figure 21. The isopycnal oscillations observed at the mid-canyon site (C3) during this time period are depicted in Figure 8, and data from the CTD station on the northern rim (C5) is not displayed, since the internal tide at that site was very weak (< 4 m in amplitude). Isopycnals for every .02 kg m^{-3} increase in σ_θ at the north wall (C4), south wall (C2), and southern rim (C1) are plotted at their observed depths. The percent variance accounted for by the M2 fit, as well as the M2 amplitudes and phases are plotted versus depth. The values for Station C3 are depicted with a black dotted line. The observed oscillations are well represented by the M2 wave fit, which accounts for up to 90% of the observed variance in isopycnal depth. M2 amplitudes are somewhat stronger on the southern side of the Canyon (Station C2), with maximum values of nearly 40 m. The 12 m amplitude oscillations over the southern rim are the strongest observed at that depth range (50-60 m). Below 90 m, the M2 phase of the isopycnals is nearly constant, lagging the M2 sea level oscillations by approximately two hours. The constant phase with depth is consistent with the ITEX2 along-canyon observations of the density field.

Snapshots of the isopycnal displacements at two points in the tidal cycle, based upon the harmonic analysis results, are depicted in Figure 22. Isopycnals are depicted for every 0.1 kg m^{-3} increase in σ_θ, between 25.68 and 26.48 kg m^{-3}. The corresponding range in temperature is 10.85-8.24 C. At 0500 (GMT) 31 October, two hours after the high tide recorded at the Monterey tide gauge, the isopycnals are at their maximum upward displacement. Six hours (half of a tidal cycle) later, they are at their lowest depths. The depth excursions are much greater on the south side of the Canyon than on the north side, and the "tidal pumping" (Shea and Broenkow, 1982) of cooler, denser water over the southern rim of the Canyon is readily apparent in the depth change of the 25.78 kg m^{-3} isopycnal (10.47 C isotherm). Very little change in isopycnal depth is seen on the north side of the Canyon.

b) Current Field

The variance of the currents observed during the cross-canyon transects (Figure 23) shows that the u velocity component is much more energetic than the v component. The u variance ranges from 120-140 $cm^2 s^{-2}$ over a cross sectional area measuring roughly 0.2 km^2. The variance of the v component is generally less than 25 $cm^2 s^{-2}$. The energetic along-canyon currents can be attributed to the internal tide, as evidenced by the large portion of variance (80-90 %) accounted for by the M2 fit. There is no obvious pattern in the percent variance accounted for by the M2 fit to the relatively weak v velocity component, except that the highest values (80-90 %) occur over the southern rim, where the large isopycnal displacements were observed.

The M2 tidal ellipses (Figure 24) are nearly rectilinear, and those representing the stronger currents (20 cm s^{-1}) are almost uniformly oriented in the along-canyon direction. An exception to this pattern exists over the southern rim, where the near-bottom currents are oriented in the north-south direction, normal to the isobaths. The relatively strong isopycnal oscillations and the cross-isobath orientation of the ellipses over the southern rim suggest that internal tide generation is occurring along this portion of the Canyon. At most ADCP "stations", a minimum in M2 horizontal velocity exists at depths of 50-60 m. A phase shift of approximately 180° or 6.2 hours in the u velocity component also occurs over this depth range (Figure 25), which is consistent with a node in a standing wave, and with the pattern of the M2 ellipses (Figure 13) and M2 u phases (Figure 20) derived from the ITEX2 along-canyon measurements.

6.   Near Bottom Current And Temperature Oscillations

Time series of hourly predicted sea level at Monterey and the hourly, smoothed S-4 velocity and temperature data for the time period 2000 16 May to 1300 21 June 1991 are depicted in Figure 26. The S-4 mooring was located 2 m above the bottom, at an approximate depth of 370 m. Current velocity is depicted with stick vectors which point from the horizontal axis toward the direction of current flow. Strong semidiurnal and diurnal oscillations are apparent throughout the velocity and temperature records, and a low frequency modulation (with a period of roughly 10 days) is present in the temperature record. The spring-neap cycle of June 6-21 (hours 480-840) is well represented in both velocity and temperature, although with a slight lag relative to sea level. The currents regularly attained speeds of 20-30 cm s^{-1}, and the maximum recorded velocity was

41

41.2 cm s^{-1}. Examination of temperature and velocity spectral densities revealed strong diurnal and semidiurnal peaks, and lesser peaks in the terdiurnal (8 hour period) and quarterdiurnal (6 hour period) bands. The results of least squares harmonic analysis of the temperature and velocity records are presented in Tables 3 and 4. Thirty-six constituents were resolved in the analyses, however only those constituents which figured prominently in both the temperature and velocity analyses are listed. In order to reduce errors due to unresolved constituents, the P1 and K2 constituents were inferred from K1 and S2, based on their amplitude and phase relationships in the year-long tidal heights analysis. The method for determining the standard deviations associated with the tidal analysis results are discussed in Appendices B and C.

a) *Temperature Perturbations*

The amplitudes of the temperature perturbations (T') listed in Table 3 represent deviations from the mean temperature of 6.965° C. The strongest temperature oscillations occurred at the M2, K1, and O1 frequencies, which are also the strongest constituents in the surface tide. Significant amplitudes were also attributed to three other semidiurnal frequencies (N2, L2, and S2) and to the quarterdiurnal constituent SN4. The amplitudes of the terdiurnal oscillations were 0.03° C or less. If the background stratification is assumed to be stable, T' can be assumed to be 180° out of phase with the vertical displacement of the 6.96° C isotherm. This relationship can be used to compare the phases of the internal tide isotherm displacements to the phases of the corresponding constituents in sea level.

A comparison of the Greenwich Phases of the M2 internal tide (as inferred from the phase of T'_{M2}, 146.5° + 180° = 326.5°) and the M2 surface tide measured at Monterey (181.9°) suggests that the near-bottom M2 internal tide during this period lagged the surface tide by 144.6°. Taking into account the error bounds on the phase of T'_{M2}, this phase lag is equal to 4.7 - 5.3 hours, consistent with the phase values observed in the lower part of the water column during ITEX1 (Figure 7). Similar phase lags exist for the N2 and L2 internal tides (relative to the N2 and L2 surface tides), however the inferred lag between the S2 surface and internal tides is somewhat less, at 1.3-3.3 hours. The relative proportions of the N2, M2, and S2 T' amplitudes are roughly the same as in sea level ($T'_{M2} : T'_{N2}$ = 2.8:1, versus 4.4:1 in sea level, and $T'_{M2} : T'_{S2}$ = 3.4:1, versus 3.7:1 in sea level). The amplitude of the L2 temperature perturbation is disproportionately strong (compared to the relatively small L2 sea level amplitude of 3.1 cm), and may indicate a

42

spread of M2 energy to this neighboring frequency due to variability in the generation and propagation of the M2 internal tide.

TABLE 3. S-4 TIDAL TEMPERATURE PERTURBATIONS 16 MAY - 21 JUNE 1991

Tidal Constituent	Frequency (cyc/hr)	Period (solar hrs)	Amplitude (deg C)	Greenwich Phase (deg)
O1	.03873065	25.8193446	.126 ± .03	263.2 ± 13.6
P1	.04155259	24.0658886	.048 ± .03	330.1 ± 36.2
K1	.04178075	23.9344674	.152 ± .03	332.4 ± 11.3
N2	.07899925	12.6583480	.058 ± .03	122.3 ± 25.6
M2	.08051140	12.4206013	.168 ± .03	146.5 ± 8.9
L2	.08202355	12.1916206	.060 ± .03	156.1 ± 24.8
S2	.08333333	12.0000000	.049 ± .03	69.3 ± 30.6
SN4	.16233258	6.1601929	.037 ± .01	178.6 ± 13.8

TABLE 4 S-4 TIDAL CURRENTS 16 MAY - 21 JUNE 1991

Const.	Semi-Major (cm/s)	Semi-Minor (cm/s)	Greenwich Phase (deg)	Inclination (deg ccw from 090°T)
O1	4.8 ± 0.6	-0.9 ± 0.7	13.0 ± 6.7	50.4 ± 7.8
P1	2.5 ± 0.7	0.1 ± 0.5	66.5 ± 24.9	46.2 ± 16.9
K1	8.3 ± 0.6	0.3 ± 0.6	70.1 ± 4.1	46.2 ± 4.3
N2	5.4 ± 0.9	0.2 ± 0.9	224.6 ± 4.4	46.3 ± 10.6
M2	13.9 ± 1.0	2.4 ± 0.9	266.1 ± 4.4	40.2 ± 3.9
L2	5.2 ± 1.0	-0.1 ± 0.9	265.6 ± 9.0	41.3 ± 8.0
S2	5.7 ± 1.1	0.4 ± 0.7	191.0 ± 11.4	32.2 ± 7.9
SN4	2.4 ± 0.2	0.2 ± 0.7	333.4 ± 36.2	29.4 ± 82.5

Since the diurnal frequencies are subinertial at this latitude, the relatively strong K1 and O1 oscillations most likely represent bottom-trapped disturbances which are generated along the floor and walls of the Canyon by the diurnal barotropic tides. The Greenwich Phases of

the K1 and O1 surface tides are 220.3° and 203.9°, respectively. The phases of the K1 and O1 internal tide displacements (inferred from their respective T' phases) indicate that the diurnal internal tides lead their surface tide displacements by approximately 1/5 (K1) and 1/3 (O1) of a cycle. This phase relationship supports the idea of local generation of the diurnal internal tides; the two-dimensional scenario presented by Baines (1982) shows that the isotherms in the generation region lead sea level by 1/4 cycle.

The SN4 constituent, which is theoretically a higher harmonic resulting from nonlinear interaction of the S2 and N2 constituents, was the strongest quarterdiurnal constituent in both the temperature and velocity analyses. Parker (1991) discusses the various nonlinear interactions that result in "overtides", or higher harmonics, as opposed to the wave beat that results from linear superposition of tidal constituents. Given that S2 and N2 interact to create the SN4 signal, the phase of SN4 should be equal to the sum of the S2 and N2 phases. This phase relationship holds for the temperature analysis (SN4 phase = 178° ± 13.8°, and the S2 phase + N2 phase = 191.6° ± 56.2°), but not for the currents analysis. If in fact strong interaction is occurring between S2 and N2, one might expect a difference-frequency harmonic to be present. The period of the theoretical low frequency harmonic would be 9.6 days, and it is tempting to consider this as a potential explanation for the roughly 10 day modulation of the temperature record. It is not clear however, why the S2-N2 interaction should be favored over interactions involving the strong M2 constituent.

b)   *Tidal Currents Analysis*

The lengths of the semi-major and semi-minor axes, the Greenwich Phases, and the inclinations of the tidal current ellipses (in degrees counter-clockwise from due East) are presented in Table 4. There are several qualities of the tidal currents analysis results that are similar to the analysis of the temperature perturbations. The M2 constituent is strongest in both analyses, and the ratio of the M2 semimajor axis length to those of the N2, L2, and S2 constituents is nearly identical to the ratios of the respective T' amplitudes (2.4-2.7:1). The M2, N2, and L2 currents *lag* their respective high tides by 2-3 hours (1/6 - 1/4 cycle), and *lead* their respective isotherm displacements (as inferred from the T' analysis) by 2-3 hours, consistent with progressive internal waves. The S2 currents lead the S2 isotherm displacements by nearly 2 hours, and are nearly in phase with S2 sea level. A possible explanation for the shorter phase lag between the S2

44

internal and surface tides is that the generation site for the S2 internal tide is closer to the mooring than the sites at which the other semidiurnal constituents are generated. In contrast to the semidiurnal current oscillations, the diurnal currents (K1 and O1) lag their respective isotherm displacements by 6.5 and 8 hours (1/4 and 1/3 cycle), and are 180° out of phase with their corresponding sea level constituents.

As in the T' analysis, the L2 constituent is disproportionately strong. The fact that the L2 ellipse inclination and phase are not significantly different from those of the M2 constituent is further evidence that the L2 signal is a result of energy spread from the M2 constituent. Godin (1991) notes that the power spectrum of a current record (as opposed to a sea level record) is likely to be contaminated due to bathymetric steering of the flow and spatial changes in current flow during large and small tides; individual spectral lines may be broadened due to asymmetric flow reversals.

Indeed, the current reversals depicted in Figure 26 are asymmetric, flowing toward 210°T in the downcanyon direction and toward 040°T in the upcanyon direction. A scatter plot representing the observed currents (Figure 27) shows that strong upcanyon flow tends to be aligned with the Canyon axis, while strong downcanyon currents tend to flow toward the south-southwest (210°T), with a cross-canyon component. This asymmetric flow resulted in a mean flow of 5.0 cm s^{-1} due southward. Similar bimodal patterns in current flow were observed in the near-bottom current measurements made in MSC by Shepard et al. The asymmetric flow may be simply a result of local bathymetric effects. Nevertheless an alternate explanation for the asymmetric flow, based on progressive internal tides in a V-shaped canyon, is presented in the following paragraph.

During the ITEX1 period, measurements indicate that the internal tide existed as a progressive internal wave, with eastward and downward phase velocities ($k > 0$ and $m < 0$). In such a case, the along-canyon horizontal velocity is in phase with the vertical velocity. The maximum eastward/upcanyon flow leads the internal wave crest by 1/4 cycle, and the westward/downcanyon flow leads the wave trough by 1/4 cycle. The time series depicted in Figure 26 are consistent with this model of the internal tide; the strong downcanyon flow is associated with increasing temperatures (falling isotherms) and the upcanyon flow is associated with temperature decreases. The falling internal tide in a V-shaped canyon such as MSC seems more likely to be affected by the proximity of the canyon walls than the rising internal tide; since the

45

water is sinking into a region of decreasing volume, some of the downward vertical velocity must be converted to cross-canyon flow. The S-4 mooring was located on the northern side of the Canyon floor, so the southwestward flow may be a result of downslope flow from the northern wall, which would have a southward component. The slope of the northern wall in the vicinity of the mooring site is approximately 11°. The vertical velocity associated with a vertical displacement of 40 m (typical for the semidiurnal internal tide in MSC) would be 40 m / 6 hr = .185 cm s^{-1}. A sinusoidal current with this average velocity (i.e., averaged over 1/2 cycle) would have an amplitude of .29 cm s^{-1}. If this vertical component of velocity is maintained while the current flows down an 11° slope, a horizontal (cross-slope) velocity component with an amplitude of 1.49 cm s^{-1} would be imparted to the flow. Since this horizontal component would be imparted during the time of downcanyon flow, the downcanyon flow would be deflected away from the wall. Assuming a typical along-canyon flow (based on the S-4 measurements) of 20 cm s^{-1}, and an orientation of the Canyon axis along 040-220°T (appropriate to the S-4 site), the direction of downcanyon flow would be deflected from 220° to 215.7° T.

The temperature record indicates that increases in temperature occur much more rapidly than temperature drops. If these temperature changes are largely the result of progressive internal tides, then by inference the internal waves have gradually rising wave fronts and steepened trailing edges. For the typical 40 m isotherm displacement, the average vertical velocities associated with the steep trailing edge of the internal tide would be greater than the estimated average value of .185 cm s^{-1}, and the resulting cross-slope deflection of the downcanyon flow would be greater as well. It is therefore conceivable that much of the asymmetry in the near-bottom current measurements is due to the proximity of the mooring to the north wall of the Canyon.

7. Energetics

The energy density of an internal wave is defined as the mean perturbation energy per unit volume (Gill, 1982), i.e., by

$$E = \frac{1}{2}\rho_o \overline{(u^2 + v^2 + w^2)} + \frac{1}{2}\frac{g^2 \overline{\rho'^2}}{\rho_o N^2}$$

46

where u, v, and w are the perturbation velocities associated with the internal wave, ρ' is the perturbation density, and the overbars denote the mean over one wavelength. The first term represents the mean perturbation kinetic energy (KE), and the second represents the mean perturbation potential energy (PE). If a variable A changes sinusoidally over time, the mean value of A^2 over one wavelength can be expressed as

$$\overline{A^2} = \overline{(A_o \cos(t))^2} = A_o{}^2 \ \frac{\displaystyle\int_0^{2\pi} \cos^2 t \ dt}{2\pi} = A_o{}^2 \ \frac{\displaystyle\int_0^{2\pi} \frac{1}{2}(1+\cos 2t) \ dt}{2\pi} = A_o{}^2 (\frac{\pi}{2\pi}) = \frac{A_o{}^2}{2}$$

where A_o represents the amplitude (1/2 the waveheight) of the variable. Thus, the amplitudes of the semidiurnal velocity and density perturbations at a given depth (determined through harmonic analysis) can be used in an expression for the mean perturbation energy per unit volume for the internal tide:

$$E = \frac{1}{4}\rho_o(u_o{}^2 + v_o{}^2 + w_o{}^2) + \frac{1}{4}\frac{g^2 \rho'_o{}^2}{\rho_o N^2}$$

where u_o, v_o, and w_o are the M2 velocity amplitudes and ρ'_o is the amplitude of the M2 density perturbation (not to be confused with ρ_o, the average density at a given depth).

The values of mean perturbation PE and KE calculated from the ITEX1 and ITEX2 along-Canyon measurements are plotted versus depth in Figure 28. The semimajor and semiminor axes of the M2 ellipses were used for u_o and v_o in the KE calculation. The contribution to KE from w_o was neglected, since w_o (estimated from ρ' at the CTD stations) was an order of magnitude smaller than u_o and v_o. KE values for each ADCP bin are plotted versus depth, on an x axis which ranges from 0 to 7.5 J m^{-3}. The positions of the zero lines on the x axes correspond to the middle of the along-track geographic bins. The dashed lines represent the potential energy calculated from the CTD data. PE was calculated every 8 m in depth, at the mid-depth of each ADCP bin.

The data from both cruises reveal energy maxima in the lower half of the water column which shoal toward the Canyon head at nearly the same angle as the Canyon floor. Near-surface maxima are also present, most noticeably in the ITEX1 data. The near surface maxima may be a result of internal wave energy propagating shoreward in a narrow near-surface beam, and will be discussed further in Section C.

At the ITEX1 stations, the energy is nearly equally partitioned between KE and PE. The theoretical ratio of energy distribution in internal gravity waves is (Gill, 1982):

47

$$\frac{KE}{PE} = \frac{\omega^2 + f^2 \sin^2 \phi'}{\omega^2 - f^2 \sin^2 \phi'} \quad , \quad \phi' = 90° - \theta$$

but since the observed value of ϕ' for the internal tide is nearly 90°, the equation simplifies to the ratio for Poincare waves, namely

$$\frac{KE}{PE} = \frac{\omega^2 + f^2}{\omega^2 - f^2} \quad .$$

This equation yields a ratio of 2.26, which was rarely observed in the ITEX data. The equal partitioning of energy between KE and PE suggests (as did the comparison of the theoretical and observed ITEX1 u and ρ' fields) that due to topographic constraints on north-south (cross-canyon) motion, the APE of the internal tide in the Canyon is proportionately stronger with respect to KE than would otherwise be the case. The ITEX2 energy values were similar to those observed in ITEX1, and the focusing of energy along an M2 characteristic is easier to see in these more closely spaced measurements. The apparent drop in energy at the three ITEX2 stations located 2-3.5 km from the Canyon head is attributable to the departure of the ship's track from the Canyon axis (Figure 5). Both cruises revealed greater PE than KE at the shallow CTD stations, where departure from linear theory is expected due to interaction of the waves with the bottom and sides of the Canyon.

Depth-integrated values of energy density were calculated by summing the mean perturbation KE and PE values to obtain total energy (TE), multiplying each of the TE values by 8 m (the size of the ADCP bins), and summing over the water column. The resulting energy density values for ITEX1 are 2519 and 1580 J m^{-2} at the deep and shallow stations, respectively. Somewhat smaller values of 1052 and 1112 J m^{-2} are obtained for the ITEX2 deep and shallow stations. The ITEX1 and ITEX2 energy densities are comparable to those reported by Petrie (1975) for an internal tide propagating seaward from a generation site at the Scotian shelfbreak (1700 J m^{-2}).

The higher energy densities during ITEX1 are most likely due to greater barotropic forcing during that period, compared to ITEX2. The tidal heights recorded at the Monterey tide gauge during ITEX1 and ITEX2 are displayed in Figure 29. The sea level excursions from high to low tide just prior to and during ITEX1 are 1.5-2 times greater than those prior to and during ITEX2. The amplitudes of the M2 and S2 sea level constituents (which are constant in time) constructively

48

interfere during spring tides and destructively interfere during neap tides. The semidiurnal u_o, v_o, and ρ' amplitudes used for the energy calculations are based on analyses of short (25-50 hour) record lengths, and therefore most likely include contributions from both the M2 and S2 internal tides (as well as from other weaker semidiurnal internal tides that may be present). Thus, the semidiurnal internal tides are expected to be more energetic during the spring tides (represented by ITEX1 conditions) than during the neap tides (ITEX2). This explanation implies that the internal tide is a result of linear superposition of semidiurnal internal tides with slightly different frequencies, and the near-bottom S-4 current meter and thermistor records support this idea. It was observed in the near-bottom measurements that the ratios of the M2 semimajor axis length and temperature perturbation to those of the S2 and N2 constituents were nearly the same as the corresponding ratios of sea level amplitudes.

Energy flux estimates for ITEX1 were obtained by multiplying the energy density values by the group velocities (54.9 and 49.2 cm s^{-1}) calculated at Stations A1 and A2. This yields energy fluxes of 1383 and 777 W m^{-1} at the deep and shallow stations, respectively. Since most of the energy is contained in the bottom half of the water column, most of the dissipation between the two stations probably occurs through turbulent mixing in the bottom boundary layer along the floor and walls of the Canyon. If the difference in energy flux between the two stations is due solely to dissipation, the dissipation per unit volume can be calculated by dividing the difference in energy fluxes by the area of a cross-shore (along canyon) slice between the two stations. The area of this slice is approximately 3.4×10^6 m^2, and the dissipation is estimated to be 1.65×10^{-4} W m^{-3}, which is comparable to the value of 1.42×10^{-4} W m^{-3} calculated by Holloway (1984) for the internal tide on the North West Australian shelf. The 766 W m^{-1} flux at the shallow station must dissipate along the final 3 km of the Canyon length, over a cross-sectional area of approximately 5×10^5 m^2. The resulting value of dissipation over that part of the Canyon is 1.5×10^{-3} W m^{-3}. It is likely that a significant portion of the dissipation at the head of the Canyon can be attributed to the pumping of cool water onto the flanks of the Canyon, discussed by Shea and Broenkow (1982).

This two dimensional methodology yields a conservative estimate of the dissipation between the deep and shallow axial stations, since it neglects the expected increase in energy density at the shallow station due to the narrowing of the Canyon walls. The cross sectional area of the Canyon decreases between the two stations by a factor of roughly 7.5. Ignoring dissipation as well as generation of internal tides along the floor between the stations, the energy density at the

shallow station would be approximately 18,750 J m^{-2} (area-integrated energy at the deep station divided by the cross sectional area at the shallow station). Using the same value of group velocity used in the previous calculation, the energy flux at the shallow station would be 9225 W m^{-2}. An upper limit on the rate of dissipation between the two stations can then be estimated by taking the difference between the "V-shape" and "2-D" energy flux estimates for the shallow station (9225 − 777 = 8448 J m^{-2}) and dividing by the area of the along-canyon slice (3.4 × 10^6 m^2). This estimate yields a dissipation rate of 2.5 × 10^3 W m^{-1}, an order of magnitude greater than the 2-D estimate.

C.   DISCUSSION

1.   Possible Internal Tide Generation Sites

In order to assess the potential variability of the internal tide, it is necessary to identify the generation site. The effect of mean currents and stratification changes at the generation site and along the propagation path between the generation site and the region of interest can then be addressed. The beam-like propagation of internal tide energy upward and eastward through the water column in ITEX1 suggests that the internal tide observed in this part of MSC is generated in deep water, somewhere west of (further downcanyon from) the ITEX CTD sites. Although the internal tide appears to be "funnelled" by the Canyon walls, as evidenced by the orientation of the tidal current ellipses inside the beam, it seems doubtful that the internal tide could be steered around the sharp (greater than 90°) meander of the Canyon axis at the mouth of the Bay (Figure 30) without significant dissipation. Rather than searching for bathymetric conditions favorable for internal tide generation along the Canyon floor (i.e., a change in floor slope from supercritical to subcritical), a more straightforward approach to identifying the generation site is to assume that the energy propagates directly from some bathymetric feature beyond the mouth of the Bay, following an east-northeasterly course until it enters the portion of MSC which lies within the confines of the Bay. Using the north and south walls of the Canyon as limits, a wedge of possible propagation paths is depicted in Figure 30. The eastward end point or apex of the wedge is the head of the Canyon, defined as 36.8° N, 121.8° W. The bathymetric profile encountered along the center of the wedge (indicated with a dashed line in Figure 30) is depicted in Figure 31. Two prominent

bathymetric features along the wedge are the large rise in the sea floor referred to by USGS and MBARI geologists as "Smooth Ridge" (labelled "A" in Figures 30 and 31) and a steeper feature (labelled "B") which for the purposes of this study will be dubbed Steep Ridge.

Assuming generation is likely at these two sites, the characteristic ray paths emanating shoreward (010° T) and seaward (260° T) from these two sites were calculated for ITEX1 and ITEX2 stratification conditions. These ray paths are depicted in Figure 31. The buoyancy frequency profile used for the ray path calculations in water deeper than 400 m was computed from the average density profile from 50 CTD casts conducted by MBARI at 36.64° N, 122.14° W between November 1989 and December 1992. For rays propagating in depths shallower than 400 m, the buoyancy frequency profiles calculated from the average density profiles obtained at the ITEX1 and ITEX2 deep CTD stations (Figure 9) were used.

The ray traces reveal that along much of Smooth Ridge, the bottom slope is near-critical for the M2 frequency and thus favorable for internal tide generation. Additionally, the general shape of Smooth Ridge is concave downward, which Baines (1974) and Gilbert and Garrett (1989) show to be a more favorable bathymetric shape for critical frequency energy enhancement and internal tide generation than flat or concave upward slopes. The narrow beam of rays emanating shoreward from Smooth Ridge is seen to reflect from the sea surface prior to encountering the head of the Canyon (backward reflected rays from the Canyon head are not depicted). This surface reflection would cause near-surface intensification of the currents, and might explain the relatively strong tidal currents observed near the head of the Canyon with HF radar (Figure 2) and the higher near-surface values of KE observed in ITEX1 (Figure 28). The reflection would cause a 180° phase shift in w and vertical displacement, but the phase of the horizontal currents would be unaffected. The energy propagating eastward from the tip of Steep Ridge enters the Canyon at greater depth than the energy from Smooth Ridge, and does not encounter the sea surface until very near the Canyon head. In order to keep Figure 31 uncluttered, rays emanating downward from the tips of the two ridges are not drawn, however the presence of downward propagating energy would be expected. Energy propagating eastward and downward from Steep ridge would be expected to reach the floor of MSC somewhere between 122.0-121.9° W, and could contribute to bottom intensification of the baroclinic tidal currents. Energy propagating downward and eastward from Smooth Ridge would encounter the western side of Steep Ridge and reflect backward and further downward, and would thus not have an effect on currents inside the Bay.

51

The characteristics calculated with the ITEX2 buoyancy frequency profile are flatter than the ITEX1 characteristics due to increased stratification. The rays from Smooth Ridge therefore travel further before reflecting from the surface, and the ray propagating eastward from Steep Ridge encounters a steep bump near 121.83° W which is actually a portion of the north wall near the Canyon head. The ray path corresponding to the theoretical backward (supercritical) reflection from this feature is depicted with a dashed line. This backward reflection would cause a 180° phase shift in the u component of velocity. The superposition of shoreward and seaward propagating energy would result in a standing wave (standing in x', the along-characteristic direction), which is consistent with the ITEX2 observations. The ITEX2 observations indicate the internal tide was also standing in z' (perpendicular to the characteristic), which would require superposition of upward and downward propagating energy. The source of the downward propagating energy is not clear from this ray tracing exercise, but the sea surface near the Canyon head is a likely source. It is clear that the energy travelling up the Canyon follows a flatter path in ITEX2, and it is likely that more energy is available for reflection back down the Canyon from the head.

Superposition of the ray paths from Smooth Ridge and Steep Ridge with the M2 u phases observed during ITEX1 and ITEX2 is depicted in Figure 20. Ray paths are indicated by dashed lines. Remarkable agreement is seen between the observed isophase lines (areas of similar color) and the theoretical ray paths. The ITEX1 u phases vary smoothly in x and z, with phase lag increasing toward the Canyon floor from -2 hours (green) to +2 hours (dark blue). The downward phase propagation is consistent with upcanyon energy propagation. The isophase lines clearly lie along characteristics, nearly parallel to the Canyon floor. In their analyses of CTD and thermistor chain measurements at several sites seaward of the Bay of Biscay, Pingree and New (1989, 1991) documented a linear increase in displacement phase of 2-3 hours across a well defined beam which they observed propagating offshore. Additionally, they observed phase to be constant along the beam, with a mean value of approximately -3 hours (i.e., leading the predicted high tide by 3 hours).

The ITEX2 phase lags, by contrast, rapidly change from their near-surface values of ±6 hours (≈180° out of phase with sea level) to values between 0 and +2 hours (nearly in phase with sea level). The depth at which this phase shift occurs changes gradually from approximately 90 m at the westernmost station to approximately 25 m at the easternmost station. These are the same

depths at which the current ellipses are at minimum strength (Figure 13). The colocation of these two lines indicates the presence of a node in horizontal velocity, and the ray paths superimposed on the ITEX2 phases show that this node lies along the characteristic calculated from the average ITEX2 density profile. This is further evidence that the internal tide was standing in both the along- and cross-characteristic directions.

Internal seiches in basins have been the subject of recent studies (Maas and Lam, 1995, and Münnich, 1996), but they have rarely been observed in the ocean. Niiler (1968) discusses a seiching internal tide in the Florida Straits, Winant and Bratkovich (1981) identify internal tides standing in the cross-shelf plane on the narrow Southern California Shelf, and Griffin and Middleton (1992) discuss standing internal wave patterns in the nearshore region of Sydney, Australia. A common factor in the oceanic observations is the presence of a narrow continental shelf, which implies that little dissipation occurs between the internal tide generation area (most likely the shelf break) and the reflecting boundary (the coast).

2. Comparison To Wunsch's Modal Solutions For Standing Waves

Wunsch (1968) derived analytic solutions for internal waves over a linear wedge in an inviscid, Boussinesq fluid of constant buoyancy frequency. The resulting pattern of standing waves indicated a linear decrease of wavelength and an increase in amplitude of the velocity field as the intersection of the bottom and surface is approached. Furthermore, a region of high shear was shown to exist along the floor of the wedge. In view of the few oceanic observations available at the time, and having failed to reproduce the predicted line of high shear in laboratory experiments, Wunsch (1969) considered a subsequent set of propagating solutions as more appropriate. The ITEX2 observations are considered a good opportunity to test Wunsch's earlier standing wave results.

Wunsch introduces the stream function $\hat{\psi}$ which describes two dimensional motion in a stably stratified, Boussinesq fluid such that $u = \hat{\psi}_z$, $w = \hat{\psi}_x$, and

$$\nabla^2 \hat{\psi}_{tt} + N^2 \hat{\psi}_{zz} = 0. \qquad (2)$$

Considering periodic internal wave motion of radian frequency ω, such that $\hat{\psi} = \psi\, e^{-i\omega t}$, then (2) becomes

53

$$\psi_{zz} - \frac{1}{c^2}\psi_{xx} = 0, \quad c^2 = \frac{\omega^2}{N^2 - \omega^2}. \tag{3}$$

The motion described by (3) is linear, inviscid, hydrostatic, independent of the longshore coordinate, and irrotational. Rotational effects can easily be incorporated, and are generally important for internal tides, but the irrotational case appears to be more applicable to internal tide propagation in MSC.

In a wedge with bottom depth defined by $z = -\gamma\, x$, the general solution to (3) is

$$\psi = F(cx - z) + G(cx + z).$$

In polar coordinates, with $x = r \cos\beta$, $z = r \sin\beta$, ($\beta = \tan^{-1}\gamma$, the angle of the bottom slope):

$$\psi = F[r(1+c^2)^{\frac{1}{2}}\cos(\beta + \alpha)] + G[r(1+c^2)^{\frac{1}{2}}\cos(\beta - \alpha)], \quad \alpha = \tan^{-1}\frac{1}{c}.$$

Wunsch then considers the solutions $F = \sin[p\ln(cx - z)]$, $G = -\sin[p\ln(cx + z)]$ which give velocity fields of :

$$u(x,z) = -\psi_z(x,z) = \frac{p}{cx-z}\cos[p\ln(cx-z)] + \frac{p}{cx+z}\cos[p\ln(cx+z)]$$

$$w(x,z) = -\psi_x(x,z) = \frac{pc}{cx-z}\cos[p\ln(cx-z)] - \frac{pc}{cx+z}\cos[p\ln(cx+z)],$$

with $p = \dfrac{2n\pi}{\ln(\dfrac{c+\gamma}{c-\gamma})}$, where n is the mode number. The best match of these velocity fields to the ITEX2 observations was obtained by summing the first two modes with $\gamma = .035$ (appropriate for the Canyon floor) and $N = 3.0 \times 10^{-3}\ s^{-1}$ (consistent with the N profile computed from the ITEX2 deep station CTD casts). For comparison to ITEX2 Station B2/C3 measurements, a bottom depth of 420 m was used to determine the appropriate location on the idealized wedge. For a wedge slope of .035, the depth of 420 m corresponds to a distance from the wedge apex of $x = 12$ km. The distance from the apex was then decreased by 740 m (based on the approximate distance between the centers of the geographic bins) for comparison to each subsequent ADCP geographical bin along the Canyon axis. The theoretical and observed u and w fields at ITEX2 station B2/C3 are depicted in Figure 32. The observed u field is given by

$$u_{M2} = \frac{u_{MAJ}\ \cos(G - G_{MAX})}{u_{MAX}}$$

where u_{MAJ} is the M2 semi-major axis length resulting from the harmonic analysis, u_{MAX} is the largest u_{MAJ} in the water column, and G_{MAX} is the Greenwich Phase corresponding to the u_{MAX} ellipse. The u field therefore shows the distribution of the currents when u_{MAX} is at its maximum upcanyon value. The observed w field is similar, with w estimated from $\xi_o \omega$ and normalized by w_{MAX}. Likewise, the theoretical fields are normalized by the maximum u and w values.

The "Wunsch Modes" correctly describe the depth of the u and w maxima, as well as the near surface node in u and the near bottom node in w. Also depicted in Figure 32 are the theoretical and observed u fields corresponding to the three deepest ADCP geographic bins in the ITEX2 along-canyon measurements. The observed shoaling of the near surface nodes and the depths of the current maxima are well described by the theoretical mode shapes. The constant N assumption for the theoretical modes necessitated choosing higher N values for comparison to the shallower station u fields (not depicted), but no satisfactory fit could be found for the observations closest to the Canyon head. The failure of linear theory near the Canyon head is anticipated, since the reflection of energy from the narrow walls and the floor is expected to cause complex phase shifts in u and w.

The u profiles suggest zones of high shear in the vicinity of the nodes and the sea floor. Although the depths of the theoretical near-bottom nodes and phase reversals in u were beyond the view of the downward-looking ADCP (or, in the shallower end of the Canyon, unmeasurable due to side lobe reflections from the Canyon walls), the relatively large amplitudes of the observed baroclinic velocities at mid-depth imply their existence, since the amplitude of the depth-averaged current is required to be close or equal to the estimated barotropic u amplitude of 0.58 cm s^{-1}. In order to estimate the amplitude of the near-bottom M2 currents in MSC, the hourly u and v velocities from the three cross-canyon geographic bins located over the deeper portions of the Canyon (those which were co-located with CTD stations C2, C3, and C4) were averaged over depth, and the depth-averaged values were then rotated 10° counterclockwise into along- and cross-canyon components. The amplitude of the depth-averaged, along-canyon M2 current flowing across the 5.49×10^5 m^2 cross-sectional area of these three geographic bins was approximately 6 cm s^{-1}, with maximum shoreward flow occurring approximately one hour before high tide. The

area of that portion of the water column not measured by the ADCP in these three geographic bins was roughly 1.3×10^5 m², including 1.4×10^4 m² in the top 7 m of the water column. In order to obtain a depth-averaged velocity of zero (since the barotropic u amplitude of 0.58 cm s⁻¹ is essentially zero, to the accuracy of the ADCP measurements), the amplitude of the M2 currents in the unmeasured portion of the water column must be equal to 24.8 cm s⁻¹, with maximum *downcanyon* flow occurring approximately one hour before high tide (i.e., balancing the baroclinic shoreward flow).

It is a reasonable assumption that the M2 currents in the top ADCP bin (7-15 m) is also representative of the flow in the top 7 m. The average amplitude of the M2 currents derived from the top ADCP bin at the 3 mid-canyon ADCP stations is 11 cm s⁻¹, and the maximum downcanyon flow does in fact occur approximately one hour prior to high tide. The estimate for the amplitude of the near-bottom currents is then:

$$\frac{(24.8 \text{ cm s}^{-1})(1.3 \times 10^5 \text{ m}^2) - (11 \text{ cm s}^{-1})(1.4 \times 10^4 \text{ m}^2)}{(1.3 \times 10^5 - 1.4 \times 10^4) \text{ m}^2} = 26.5 \text{ cm s}^{-1}.$$

The magnitude of this estimated current velocity is reasonable, based on the observations of Shepard et al. (1976) and on the S-4 mooring observations presented in this study, although it cannot be determined whether the internal tide existed in the form of a standing wave during those periods.

D.   SUMMARY

Shipboard ADCP measurements conducted above the axis of MSC in April (ITEX1) and October (ITEX2) 1994 show the along-canyon component of current velocity to be much stronger than the cross-canyon component, and most of the variance of the along-canyon velocity component (up to 90%) is accounted for by the semidiurnal internal tide. Although the amplitude of the along-canyon barotropic tidal current is estimated to be less than 1 cm s⁻¹, the focusing of internal tide energy within the Canyon results in bottom-intensified, along-canyon baroclinic tidal currents with speeds of over 20 cm s⁻¹. The group velocity of the semidiurnal internal tide, which represents an upper bound on the current speeds associated with the internal tide in MSC, is estimated to be 50-55 cm s⁻¹. The currents associated with the internal tide in MSC are thus not

expected to exceed 55 cm s^{-1}, except perhaps in turbulent bores as the internal waves break down at the Canyon head.

The along-canyon phase differences between isopycnal oscillations at a given depth during ITEX1 suggest an internal tide horizontal wavelength of approximately 30 km. A similar wavelength is evident in the high resolution, along canyon XBT survey conducted during ITEX1 (Figure 17). This horizontal wavelength is greater than the more typical value of 20 km observed over continental shelves (Rosenfeld, 1990) but less than the 42 km wavelength computed by Petrie (1975) for the internal tide over the Scotian slope. During ITEX1, maximum shoreward flow associated with the internal tide is observed to occur later with depth, with the highest shoreward velocities occurring in the lower half of the water column (in the beam), 2-3 hours after high tide (Figure 20). During ITEX2, the along-canyon velocity component is essentially in phase throughout the middle of the water column, with maximum shoreward flow occurring 1-2 hours before high tide, while near the surface, maximum shoreward flow occurs close to the time of low tide (Figure 17). The relatively weak near-surface currents and the stronger currents in the middle of the water column are approximately 180° out of phase and are separated by a node in horizontal velocity. The near-bottom currents were not observed during the ITEXes, due to limitations in the range of the downward-looking VM-ADCP over deeper portions of the Canyon, and due to noise associated with reflection of the ADCP transmissions from the walls and floor of the Canyon over shallower portions.

There are numerous indications that the energy associated with the internal tide propagates shoreward in a beam-like manner, nearly parallel to the Canyon floor, at an angle of approximately 2.3° to the horizontal. The orientation of the M2 characteristic (the path along which internal tide energy propagates) and the direction of internal tide energy propagation along this path are determined by:

- Direct calculation of the M2 characteristic slope c (from the dispersion relation for internal waves), using buoyancy frequency values computed from observed density fields,

- Calculation of c from the ratio of the horizontal wavenumber component (computed between CTD stations from the phase difference in the isopycnal oscillations at a given depth) to the vertical wavenumber component (computed at a given CTD station from the phase increase with depth in the isopycnal oscillations)

- Calculation of c from the ratio of the vertical component of velocity (estimated from the isopycnal oscillations) to the east-west (along-canyon) component,

- The alignment of isophase lines, for semidiurnal isopycnal oscillations as well as semidiurnal east-west velocity component oscillations, along the characteristic paths,

- The phase relationships between the semidiurnal isopycnal oscillations and along-canyon (east-west) velocity component, which are consistent with a plane wave propagating with $k_H > 0$, $m < 0$ (i.e., phase propagation eastward and downward, consistent with energy propagation eastward and upward),

- Alignment of kinetic and potential energy maxima along characteristic ray paths.

- Alignment of 180° phase shifts in the along-canyon velocity component, as well as the location of velocity minima (nodes), with the characteristic paths in the case of the standing wave pattern (ITEX2).

The alignment of the characteristic rays with the slope of the Canyon floor results in the focusing of internal tide potential and kinetic energy into a 150-200 m thick beam which is centered approximately 150 m above the Canyon floor. Typical along-canyon M2 current amplitudes inside the beam are 15-20 cm s^{-1}, roughly 3 times the strength of the currents outside of the beam. Near the Canyon head, in depths of 250 m or less, strong internal tide current and density oscillations are observed throughout the water column.

The vertical profiles of both the along-canyon velocity component and the vertical velocity component (inferred from the isopycnal displacements) during ITEX2 are well described by modal solutions (Wunsch, 1968) for a standing wave over a sloping bottom (Figure 32). In the portion of the water column not measured by the VM-ADCP, the modal solutions suggest another 180° phase shift in the along-canyon velocity component, with a node located approximately 100 m above bottom. A near-bottom 180° phase shift in the isopycnal displacements (hence, the vertical component of velocity) is observed and predicted by the Wunsch modes.

The fate of the internal tide upon reaching the Canyon head appears to be governed by changes in the buoyancy frequency profile within the Canyon. Presumably, the internal tide energy which propagates upward toward the Canyon head during ITEX1 is dissipated in the vicinity of the head and/or along the Canyon rim. The standing wave pattern observed during ITEX2 indicates the superposition of upward and downward propagating energy, which implies significant reflection of internal tide energy from the Canyon head. The presence of reflected energy in

58

ITEX2, and its apparent absence in ITEX1, can be attributed to increased stratification during ITEX2 and hence, flatter ray paths. The flatter ray paths would cause a greater percentage of the internal tide energy to encounter (and be reflected by) the Canyon walls and head.

Better agreement exists between linear wave theory and the ITEX observations when rotational effects are considered "negligible", i.e., when f in the polarization relations and the internal wave dispersion relation is set equal to zero. This is also true in the comparison of the magnitudes of internal tide potential and kinetic energy, which are nearly equal in deeper parts of the canyon, and in the comparison of Wunsch's modal solutions for standing waves to the ITEX2 observations (the Wunsch modes were solved with the assumption that rotational effects are negligible). In the absence of lateral boundaries, better agreement between theory and observations would probably be found by including rotational effects in the calculations of characteristic ray paths and theoretical density fields, since at this latitude the semidiurnal period is close to the inertial period. The presence of walls however, appears to affect the propagation path of the internal tide and the partitioning of energy between kinetic and potential, perhaps by deflecting cross-canyon motion into vertical motion. The nearly rectilinear tidal ellipses observed during both shipboard experiments indicate that the amplitude of the cross-canyon component of velocity is reduced by the presence of the walls. The conversion of the cross-canyon particle motion to vertical motion through interaction with the canyon walls would explain the relatively high levels of potential energy observed during both cruises, as well as the closer agreement between the amplitudes of the theoretical and observed isopycnal displacements when f is set equal to zero (which results in greater isopycnal displacements for a given along-canyon velocity amplitude). It would therefore seem more physically correct to say that rotational effects on internal tides are *modified*, rather than negligible, in submarine canyons.

Observations of enhanced isopycnal displacements over the southern rim of the canyon during ITEX2, and cross-canyon orientation of tidal ellipses in the same location, indicates that internal tide generation occurs over the southern rim. The "tidal pumping" of denser water onto the shelf at this location, which lies several kilometers further seaward than previous internal tide measurements, suggests that previous estimates of the amount of water transported out of the canyon due to this process (Broenkow and McKain, 1972; Shea and Broenkow, 1982; Heard, 1992) are conservative estimates. The relative lack of internal tide energy over the northern rim may be due to local bathymetric effects, and is not necessarily the case along other portions of the Canyon.

Month-long records of near-bottom current and temperature measurements approximately 5 km from the Canyon head reveal strong current and temperature oscillations 2 m above the floor of the Canyon. Harmonic analysis reveals that the current and temperature oscillations have significant diurnal and semidiurnal components. Additionally, the relative proportions of the M2, S2, and N2 semi-major axis lengths and perturbation temperature amplitudes are nearly the same as the relative proportions of the corresponding sea level amplitudes. This finding, and the observation of higher energy levels during ITEX1 (spring tide conditions) versus ITEX2 (neap tide conditions), suggests that the internal tides in this portion of MSC are coherent (or "phase-locked") with the spring-neap cycle. Sandstrom (1991) notes that phase-locking between internal tides on the continental shelf and the surface tide is rare, due to the inherent variability of stratification and mean flow in the vicinity of the shelf break. However, Sherwin (1988) observed a clear spring-neap cycle in the internal tides near Rockall Trough north of Ireland, and Pineda (1995) hypothesizes that fortnightly variations in nearshore surface water temperature anomalies along most of the west coast of North America are due to spring-neap variations in internal tide energy. Additionally, Noble et al. (1987) state that the semidiurnal internal tide over the continental slope off northern California can have a stable phase over several months. In general, phase-locking between internal tides and surface tides may be more common on narrow shelves, close to the internal tide generation site. In any case, it appears that the internal tide propagating shoreward in MSC is generated at a depth greater than 500 m, where the primary factor in the variability of the internal tide would be the spring-neap cycle in the barotropic forcing, rather than variations in the density field.

Two offshore locations are identified as likely generation sites for the internal tides propagating in MSC (Figure 30). One location is a large topographic feature commonly referred to as Smooth Ridge, which lies approximately 35 km due west of the Canyon head. The other location is a smaller, steeper topographic feature which lies approximately 20 km from the Canyon head (at the mouth of the Bay), and is referred to in this study as Steep Ridge. M2 ray traces, based on the average buoyancy frequency profile in deeper portions of the water column and the ITEX buoyancy frequency profiles in shallower depths, demonstrate the potential for internal tides to propagate shoreward into MSC from these two ridges (Figure 31). Within MSC, the M2 characteristics are nearly parallel to the Canyon floor. Reflection of these rays from the sea surface near the head of MSC may explain near-surface kinetic energy maxima observed during ITEX1.

IV.   THE MODELING EXPERIMENTS

A.   MOTIVATION

The major goal of the numerical modeling efforts presented here is to gain insight into how canyon geometry affects the generation, propagation, and dissipation of internal tides. Hotchkiss and Wunsch (1982) note that existing theory does not permit a quantitative study of the full complexity of internal waves propagating within canyon geometry. Huthnance (1989) states that for irregular shelf-edge topography (of which canyons represent the extreme case), 3-D models are needed. More recently, Foreman (1995) notes:

> *Numerical models of internal tides are in their infancy. We are unaware of any XYZT numerical models that have been systematically compared to data.*

The high resolution field observations obtained in Monterey Bay present a unique opportunity to validate the performance of a 3-D numerical model in simulating internal tide propagation in a canyon.

Some insight into internal wave propagation in a canyon may be gained from the wave tank experiments conducted by Baines (1983), although his experiments were specifically designed to study motion in a "narrow" canyon, i.e., one in which rotational effects are negligible. Using a tank measuring 22.9 cm in width and 183 cm in length, Baines simulated continental shelf/slope bathymetry with a flat "shelf" 30.8 cm above the tank floor and a plane slope extending downward from the edge of the shelf at an angle of 33° to the tank floor. Canyon bathymetry was simulated by making an incision along the length of the slope, from the shelf edge to the tank floor. The horizontal length of the slit (the "breadth" of the canyon) was constant (16.7 cm) with height, so that the canyon floor slope was the same as that of the continental slope ($\gamma = \tan 33° = 0.65$). The canyon walls were slightly tapered, measuring 2.5 cm in width at the canyon floor and widening to 3.5 cm at the the edges of the incision (the "mouth"). The tank was filled to a height of 4.5 cm above the shelf with a stratified fluid and wave motion was forced by a plunger located at the end of the tank opposite the sloping bathymetry. A glass sidewall of the tank served as one of the canyon walls, allowing Baines to photograph the oscillatory motion (made visible with dye) in the canyon. Baines varied c, the slope of the internal wave characteristic (defined in the absence of

rotation as $c = \omega / (N^2 - \omega^2)^{\frac{1}{2}}$) by varying the forcing frequency (ω) of the plunger. The periods of the forced wave motion ranged from 0.19 s to 0.56 s. In general, Baines observed large amplitude displacements in the canyon, compared to the continental slope at the same depths, and the spatial structure of these displacements varied with the ratio γ / c. Motion in the canyon was found to be essentially barotropic for $\gamma / c < 0.4$. For frequencies higher than the critical frequency ($0.4 < \gamma / c < 1$), large amplitude internal waves were confined to an area near the head of the canyon. For the critical frequency ($\gamma / c = 1$), Baines found that the wave motion in the canyon generally had "the same amplitude and phase at all depths," with outward phase propagation and downward energy propagation. When frequencies below the critical frequency were used ($\gamma / c > 1$), wave energy propagated to the foot of the canyon, where Baines states it was reflected into "a number of upward-energy propagating modes, most of which decayed rapidly in the vertical." Baines compared this process to the reflection of sound waves from the open end of an organ pipe, and considered it a potentially important mechanism for the enhancement of internal wave energy near the foot of a narrow canyon (one in which the Coriolis force is expected to have a small effect on the motions inside the canyon).

Baines' experiments represent a significant first step toward understanding the effects of canyon geometry on internal waves. In addition to demonstrating that the results of earlier 2-D wave tank experiments (such as those of Cacchione and Wunsch, 1974) may have application to internal wave reflection in canyons, they raise the possibility of an additional mechanism for internal wave intensification (reflection from the open end of a canyon) which could not have been studied with 2-D bathymetry. His results may have limited application to the study of internal tides in MSC and other large canyons however, for several reasons:

- Baines' use of a steep (33°) canyon floor slope resulted in barotropic motion that was strongest at the canyon head. Internal wave generation was therefore strongest near the canyon head. Baines noted that if the flow were hydrostatic, as would be expected in the case of a more gently sloping canyon floor, the largest barotropic velocities are found at the point corresponding to the shelf break outside the canyon.

- Baines' experiments were non-rotating, and thus could not simulate the potential effects of internal edge waves and associated cross canyon variations which could occur at tidal frequencies.

- Baines noted that his experiments were appropriate to canyons of approximately uniform horizontal cross section and width, and that internal wave propagation in canyons with V-shaped cross sections (and hence, wide mouths) may be significantly different. MSC is V-shaped, with walls that narrow from as wide as 11 km at the rim (defined by the distance between 150 m isobaths on either side of the canyon) to less than 1 km at the floor of the canyon. Additionally, the rim width of MSC decreases significantly toward the canyon head.

Shea and Broenkow attributed the large internal wave energy in MSC to the narrowing and shoaling of the canyon (as did Hotchkiss and Wunsch in the case of Hudson Canyon), however Breaker and Broenkow (1994) suggest that Baines' experimental results for a supercritical slope ($\gamma / c > 1$) may apply to internal tides propagating in the deeper part of the canyon that lies beyond the mouth of the Bay.

The use of numerical models to study internal wave propagation offers several obvious advantages over wave tank studies, including easier incorporation of realistic bathymetry (i.e., shallow slopes) and rotational effects, and easier measurement and visualization of the velocity and density fields. Perhaps most importantly, tidal frequencies can be incorporated into the study. Gill (1982) notes that the energy of the deep ocean internal wave spectrum is dominated by low frequencies, and Huthnance (1989) notes that internal tidal currents may account for a significant portion of the total current field near the continental shelf edge. The numerical modeling experiment described in the following section, is designed to determine the relative importance of canyon bottom slope versus the cross-sectional shape of realistically-sized canyons in producing large amplitude internal tides.

B. MODEL DESCRIPTION

The coastal ocean circulation model developed by Blumberg and Mellor (1987), also known as the Princeton Ocean Model (POM), is used here to study the process of internal tide generation, propagation, and dissipation in submarine canyons. This model was chosen due to its inclusion of the physics likely to be important in this process, such as a free surface and sub-grid scale mixing parameterizations. The model was originally designed to address mesoscale phenomena with time scales ranging from tidal to monthly, depending on domain size and grid

resolution (Blumberg and Mellor, 1987). Also, the model employs a σ (sigma) coordinate system in the vertical dimension which results in "terrain following" vertical levels and allows high resolution of surface and bottom boundary layers over variable bathymetry. The σ-coordinate transformation scales the z-level according to the water depth, such that at the free surface ($z = 0$), $\sigma = 0$, and at the bottom ($z = -H$), $\sigma = -1$. In discussing advantages of sigma coordinate models, Kowalik and Murty (1993) note:

> *The resolution of the vertical processes by a constant layer thickness often fails to reproduce the processes in the region of abrupt topography variations or in the surface or bottom boundary layers.*

Huthnance (1989) notes the importance of appropriately representing the buoyancy frequency profile and the internal wave characteristic in numerical simulations of internal tides, and points out that these can be described better by levels or spectra in z than by layers. Additionally, Huthnance states that vertically stretched coordinates offer the advantage of "more easily describing ∇H" (bottom slope), which is important due to the sensitivity of internal wave reflections to the ratio γ / c. σ coordinate models do, however, have their own limitations in the presence of steep topography as pointed out by Haney (1991) and Kowalik and Murty. This error source is discussed in detail below, in the section on model initialization.

POM is well documented and in wide use by the research community. A version of the model is currently used by the U.S. Navy for analysis and forecasting of circulation in semi-enclosed seas, and is being considered for future use in littoral applications (Durham, 1994). A brief description of the model and a discussion of previous POM tidal applications follows. This 3-dimensional, non-linear, time-stepping model employs finite difference techniques to solve the primitive equations for the three components of the velocity field, temperature, salinity, and two quantities which characterize the turbulence, the turbulence kinetic energy and the turbulence macroscale. The Boussinesq and hydrostatic assumptions are used in the formulation of the primitive equations. *In-situ* density is calculated from potential temperature and salinity using the equation of state given by Mellor (1991). Horizontal eddy viscosity is calculated using the formulation of Smagorinsky (1963), whereby the viscosity is dependent upon horizontal resolution, local vertical shear, and deformation. The Smagorinsky formulation allows for vertical variation

of horizontal diffusion and produces the desired effect of zero viscosity (a parameterization of sub-grid scale turbulence) in the absence of current flow. Mellor and Blumberg (1985) report that the incorporation of this horizontal diffusion calculation into their 3-D ocean model resulted in more realistic bottom boundary layers on sloping bottoms. The model's imbedded turbulence closure scheme (Mellor and Yamada, 1982) calculates vertical mixing coefficients (eddy viscosity and diffusion) using analytically derived relations between vertical shear, buoyancy frequency, vertical density gradient, turbulent kinetic energy, and turbulent mixing length.

The model may be run in a simple 2-D, external mode, in which the 3-D calculations are skipped and only barotropic solutions are computed. In this case, the bottom stress, which would otherwise result from the 3-D calculation and the turbulence mixing coefficient, is replaced by a quadratic friction relation. 3-D simulations can be performed in either the diagnostic mode (in order to assess the current field associated with a specified density field) or the prognostic mode (in order to assess the evolution of the density and current fields). In the case of 3-D simulations, split time-stepping is employed; the "external mode" portion of the model uses short time steps determined by the Courant-Frederich-Levy (CFL) stability criterion (Courant et al., 1928, cited in Roache, 1972) applicable to the external wave speed, and the "internal mode" uses longer time steps based on the CFL condition applicable to internal wave speeds. Bottom stress and vertically-integrated velocities are calculated and passed from the internal mode to the external mode for subsequent surface elevation and velocity transport calculations.

1.   Previous Tidal Applications

POM has been used to simulate the barotropic tides in the Middle Atlantic Bight (Blumberg and Kantha, 1985), the Delaware Bay (Galperin and Mellor, 1990), the Rio de la Plata Estuary off the Atlantic coast of South America (O'Connor, 1991), and the North-Central Gulf of Mexico (Lewis, Hsu, and Blumberg, 1993). In all cases, tidal forcing was accomplished by specifying the tidal heights (from local tide gauges or global tide models) at the open boundaries. While these modeling efforts reproduced observed coastal sea level variations with reasonable accuracy (modeled and observed amplitudes were generally within 10 centimeters, and phases within approximately 0.5 hour), the current fields associated with barotropic tide simulations can be expected to match observed currents only in shallow, well mixed seas and estuaries. Foreman

(1995) notes that it is essential to account for stratification in numerical simulations of tidal currents.

Oey et al. (1985) used the model to study tidal sea level variations and the tidal advection of salinity fronts in the Hudson-Raritan Estuary. While their study included variation of the salinity field, temperature was assumed to be constant in the vertical. As a consequence, their modeled currents compared well to current measurements obtained in shallow areas during spring tides (when the water column was well mixed), but were stronger than observed during neap tides. Oey et al. note that although salinity variations generally dominate temperature variations in the determination of density in the Hudson-Raritan Estuary, temperature stratification makes an important contribution to vertical stability and should be included in future modeling efforts.

Even if density stratification is properly represented, numerical simulations may fail to accurately represent observed tidal currents unless they properly resolve bathymetric variations as well. In a study of baroclinic circulation in the northeast Atlantic shelves and seas (Oey and Chen, 1992; Oey et al. 1992), tidal forcing was employed primarily to contribute to realistic bottom friction for the study of subtidal currents. While mean currents were accurately reproduced, the model tidal current fields were generally weaker than observed, and Oey et al. (1992) attribute this discrepancy to insufficient vertical resolution and smoothing of bathymetric regions with significant variation, such as trenches and ridges.

Important to this study, Holloway (1996) used POM specifically to simulate the internal tides over cross sections of the Australian North West Shelf, using the M2 sea level constituent for forcing. Holloway's simulations were three-dimensional and incorporated real topography in the cross-shore direction, however they neglected the effects of alongshore bathymetric variation. The model domain extended approximately 300 km in the cross-shore direction, with 2.5 km horizontal resolution. In the alongshore direction, the domain extended 70 km, with 10 km resolution. The maximum bottom depth was 1600 m, and 31 sigma levels were used, with closer spacing (higher vertical resolution) in the bottom boundary layer. Holloway's simulations reproduced a number of features of the internal tide that are consistent with his field measurements, including onshore propagation from the shelf break of a predominantly first mode wave, and little energy reaching the inner portion of a 150-200 km wide shelf. Bottom-intensified currents near critically-sloping bathymetry were in qualitative agreement with observations, but the amplitude of the isopycnal oscillations near the generation site were much weaker than observed (2m vs. 10m). Holloway's simulations ignored the effects of alongshore bathymetric variation, and he attributes some of the

66

disparity between the modeled and observed internal tides to his 2-D simplification of the actual bathymetry.

2. Internal Tides Process Study

This study marks the first application of POM, or any primitive equation model, to the study of internal tide generation and propagation in the presence of alongshore bathymetric variations. The bathymetry used for the simulations is idealized in order to facilitate a study of the effects of various canyon shapes and floor slopes on internal tide propagation and dissipation, but the basic features are representative of the relatively steep continental slope and narrow shelf typical of the Central California coast. The domain includes a 2500 m deep basin, a continental slope with a maximum gradient of 0.125 (7.15°), and a 20 km wide shelf, 100 m in depth (Figure 33). The shelf and slope are incised by a single canyon which is perpendicular to the coast. The eastern boundary of the domain, which represents the coast, is the only closed boundary. Early model testing employed a 100 km x 100 km domain, however it was found that the domain could be reduced to 70 km x 70 km (moving both the north and south boundaries in 15 km, and moving the western boundary in 30 km) without adversely affecting the solution. The values of f specified in the 70 km x 70 km model domain are appropriate for latitudes between 36° 18.6′ N and 36° 55.6′ N. The relative simplicity of the model bathymetry, as compared to the actual Monterey Bay bathymetry (Figure 33), permits easier identification of internal tide generation sites and propagation paths. Additionally, the performance of boundary conditions in transmitting baroclinic energy out of the domain can be monitored more precisely than would be the case if multiple internal wave generation sites were present.

The model is initialized with an *in situ* temperature and salinity profile which represents the average of 50 CTD casts made near the mouth of Monterey Bay at 36.64° N, 122.14°W (Rosenfeld et al., 1994). The profiles (Figure 34) indicate a very shallow surface mixed layer, and are typical of summertime stratification conditions in the vicinity of Monterey Bay. The same T and S profile is linearly interpolated onto the sigma coordinates of each grid cell, thus density is initially horizontally homogeneous throughout the domain. Although the equation of state used in POM (described by Mellor, 1991) uses potential temperature to calculate *in situ* density, the

difference between *in situ* and potential temperature at 2500 m is negligible for the purposes of this study.

a) Horizontal and Vertical Resolution and Model Time Steps

Horizontal resolution of 1 km x 1 km is used throughout the domain. The high horizontal resolution is desirable in order to resolve the motion in the vicinity of the internal tide generation sites and across the realistically shaped canyons, which are as narrow as 3 km near the coast. The high horizontal resolution enables the use of very small values for horizontal viscosity. Using a Smagorinsky coefficient, equal to 0.01, typical values of horizontal viscosity are 1 to 10 m^2s^{-1}. The model is also run with zero horizontal eddy viscosity, however values between 1 and 10 m^2s^{-1} appear to be more appropriate for 1 km resolution, based on the summary of turbulent diffusion experiments reviewed by Bowden (1962). The use of high resolution over the deep basin permits clear identification of regions associated with seaward propagating internal tide energy, however it also necessitates a very short time step in order to ensure model stability. The two-dimensional, advective form of the CFL criterion for computational stability is (Blumberg and Mellor, 1987):

$$\Delta t_E \le C^{-1}(\Delta x^{-2} + \Delta y^{-2})^{-\frac{1}{2}}$$

where $C = 2(gH_{MAX})^{\frac{1}{2}} + U_{MAX}$, and U_{MAX} is the expected maximum velocity. This constraint, with $H_{MAX} = 2500$ m and $\Delta x = \Delta y = 1$ km, necessitates an external time step of $\Delta t_E = 2$ s (U_{MAX} is assumed to be on the order of 1 cm s^{-1}, and is thus negligble in the calculation).

The equation for the less restrictive internal time step is similar, however in this case $C \approx 2(g'H_{MAX})^{\frac{1}{2}} + u_{ADV}$, where $g' = g\dfrac{\Delta \rho}{\rho_o}$ and u is the maximum advective current speed expected. This formulation uses the "reduced gravity" approximation for the phase speed of a first mode internal wave, which is two orders of magnitude slower than the shallow water surface gravity wave speed. Oey et al. (1985), in their Hudson-Raritan Estuary study, define $\Delta \rho$ as the top-to-bottom density difference. That definition is suitable for a shallow estuary, but in the domain used for this study, a more appropriate definition of $\Delta \rho$ is the density perturbation expected to be caused by an internal wave propagating along the thermocline, where the vertical density gradient is 1.5 x 10^{-2} kg m^{-3} per meter. Assuming an internal wave amplitude of 10 m (typical for

those observed propagating along thermoclines), $\Delta\rho \approx 0.15$ kg m^{-3}. No steady currents are specified in the domain, however the possibility of interaction between internal waves propagating from separate generation sites is considered, and u_{ADV} is estimated to be approximately 0.1 m s^{-1}. The constraint on the internal time step is therefore approximately 180 s, however a shorter time step of 120 s is chosen, since it divides nearly evenly into the forcing period of 12.4206 hr and allows sampling the model output at evenly spaced intervals over the tidal cycle.

High vertical resolution is also used throughout the model (Figure 35). Thirty sigma levels are used, with logarithmic distribution of the sigma levels near the surface and bottom. In the middle of the water column (between sigma levels 5 and 26), vertical resolution ranges from 107.5 m over the basin to 4.3 m over the shelf. As internal tides intensify in the vicinity of surface and bottom reflections (especially in the case of reflection from a critically sloping bottom), it is desirable to increase resolution in the surface and bottom boundary layers. Vertical resolution in the boundary layers ranged from 12.5 m over the basin to 0.5 m over the shelf.

C.   MODEL INITIALIZATION, FORCING, AND BOUNDARY CONDITIONS

Numerical simulations of ocean processes, especially coastal ocean processes, often necessitate ending the computational grid at an artificial (non-coastal) boundary. In such instances, the modeler must either specify a physically realistic value for one or more of the model variables, or use a mathematically well-posed condition which will allow disturbances from within the computational domain to leave the domain without disrupting the interior solution. Reviews on open boundary conditions are given by Chapman (1985) and Roed and Cooper (1986). The following section discusses open boundary conditions used in these experiments.

1.   External Mode Boundary Conditions

a)   Surface Elevation

In many tidal simulation studies, the tidal sea level oscillations are specified at the open boundaries by interpolating amplitude and phase values from global tide models onto the model grid points. In this process study, the model was forced at the seaward (western) boundary,

69

by specifying the free surface elevation as a cosine wave with a period of 12.4206 hours (the M2 period) and an amplitude of 0.5 m. This amplitude is representative of the M2 tide in Monterey Bay (Petruncio, 1993), thus the internal tides generated by propagation of the model barotropic tide are expected to be representative of the M2 internal tides generated by the cross-shore barotropic tidal currents in the vicinity of Monterey Bay.

The M2 tide in the eastern Pacific propagates northward (Figure 10) with the maximum amplitude at the coast, in a manner similar to a barotropic Kelvin wave. Analytical solutions (Munk et al., 1970; Battisti and Clarke, 1982) and field studies (Winant and Bratkovich, 1981; Rosenfeld and Beardsley, 1987) of the barotropic M2 tidal currents in the eastern Pacific are consistent with the Kelvin-like wave comparison, revealing maximum flow parallel to the coast at local high tide and very weak (approximately 1 cm s^{-1} or less) cross-shore flow. The model forcing used in this study has constant phase in the north-south direction, and so does not represent alongshore propagation of the barotropic tide. The specified tide is a shallow water gravity wave with a cross-shore wavelength of nearly 7000 km ((gH)$^{1/2}$ x 12.42 hr)). This wavelength is approximately 100 times the distance between the seaward open boundary and the coast, and so conditions within the model domain are representative of those in the vicinity of a node. The reflected wave is approximately 180° out of phase with the incoming tide and has a slightly reduced amplitude due to bottom friction (Clarke, 1991) and dissipation through internal tide generation, and thus nearly cancels the currents associated with the shoreward propagating wave. It will be demonstrated that this forcing does produce similarly weak (0.5-1.5 cm s^{-1}) barotropic cross-shore currents however, due to reflection of the tide from the continental slope and the coastal boundary.

The sea level forcing at the western boundary is accomplished by specifying the surface elevation at the boundary as:

$$\eta^{t+1} = R(t) A_{M2} \cos(\omega_{M2} t)$$

where η^{t+1} is the surface elevation at the forward time step, $R(t)$ is a "ramping" function which increases linearly over each external mode time step from 0 to 1 over an inertial period (and remains equal to 1 thereafter), A_{M2} is the amplitude of the M2 tide (0.5 m), ω_{M2} is the M2 radian frequency (1.4052 x 10^{-4} s), and t is the model time, which is incremented each external mode time step. The ramping function is used to reduce the transient oscillations which are generated by starting the model from rest.

In an effort to make the northern and southern boundaries transparent to surface gravity waves, the following form of the Orlanski (1976) radiation condition is used:

$$\eta_{i,j}^{t+1} = \eta_{i,j}^{t-1} - \mu \ (\eta_{i,j}^{t-1} - 2\eta_{i,j\pm1}^{t})(1+\mu)^{-1} \ ,$$

where t, $t+1$, and $t-1$ denote the present, forward, and backward time steps, i and j are the grid point coordinates along the boundary (i and j increasing to the east and north, respectively), $j\pm1$ is the first interior gridpoint in the model, and $\mu = (gH_{i,j})^{\frac{1}{2}} \dfrac{\Delta t_E}{\Delta y_{i,j}}$. This form, which was used by Oey and Chen (1992) in their simulation of tidal circulation in the Northeast Atlantic shelf (Chen, personal communication), is similar to the explicit form of Orlanski radiation discussed by Chapman (1985). However, the shallow water gravity wave speed is specified rather than calculated from information within the model domain. This simplification is appropriate for use in this study, since the only forcing present is that due to the imposed tide at the western boundary.

b) External Mode (Depth Averaged) Velocities

The vertically averaged current velocity associated with a linear, progressive wave can be expressed as:

$$U = \pm\eta \ (g \ / \ H)^{\frac{1}{2}}$$

where u represents the velocity component normal to the wave crest (Roed and Cooper, 1986). Applying this equation to the situation in which a wave is propagating from an open boundary (with the wave crest parallel to the boundary) toward the interior of the computational domain, the expression is positive at southern and western boundaries and negative at northern and eastern boundaries (Lewis et al., 1993). Assuming superposition of incoming and outgoing waves at the boundary, with the incoming wave (the specified tide) represented by the elevation at the open boundary (η_B) and the outgoing (reflected) wave represented by the surface elevation at the first model gridpoint inside the boundary ($\eta_{B\pm1}$), the velocity can be expressed as

$$U = \pm(\eta_{B\pm1} - \eta_B)(g \ / \ H)^{\frac{1}{2}}$$

where the expression is now positive for northern and eastern open boundaries and negative for southern and western boundaries. This expression is similar to the Reid and Bodine (1968) boundary condition discussed by Lewis et al., although in that study the Reid and Bodine boundary condition is actually used to force the model. In this application, the above expression amounts to

71

a calculation of the velocity component normal to the open boundary based on the slope of the sea surface, and was used to calculate appropriate normal velocities at the three open boundaries.

Model calculations are generally less sensitive to the velocity component tangential to the boundary (Mellor, 1996). In this application, upstream advection was used to compute the tangential velocity component as follows:

$$U_B^{t+1} = U_B^t - \frac{\Delta t_E}{\Delta x} \left[V_1 (U_B^t - U_{B\pm1}^t) + V_2 (-U_B^t) \right]$$

where u is the tangential component of velocity, v is the normal component, $V_1 = 0.5(V_B + |V_B|)$, and $V_2 = 0.5(V_B - |V_B|)$. Applying this equation to the northern boundary, we see that when the normal component of flow at the boundary is positive (toward the boundary), $V_2 = 0$. The magnitude of the tangential velocity at the forward time step is then slightly reduced (increased) if $U_B - U_{B\pm1}$ is positive (negative). If the normal component of flow is away from the boundary, $V_1 = 0$, and the magnitude of the tangential velocity at the boundary is decreased. The above equation is applicable to the northern boundary. At the southern boundary, the equation is:

$$U_B^{t+1} = U_B^t - \frac{\Delta t_E}{\Delta x} \left[V_1 (U_B^t) + V_2 (U_{B\pm1}^t - U_B^t) \right]$$

The equation at the western boundary is similar to that used at the southern, except that the positions of u and v are swapped.

2.   Internal Mode Boundary Conditions

The formulation of boundary conditions for internal waves is an area of active research. The simplest approach is to apply a sponge boundary condition in which the velocity is gradually reduced to zero over a number of model gridpoints. Chapman (1985) and Martinsen and Engedahl (1987) have demonstrated the suitability of sponge boundary conditions for surface gravity wave simulations, and a sponge layer (the "flow relaxation zone" of Martinsen and Engedahl) was used successfully in the internal tide simulations of Holloway (1996). There are a number of drawbacks to sponge boundaries, however, including greater computational expense (as compared to a radiation condition) due to the requirement for a larger domain, and the prevention of two-way information flow that is desirable in nested grid systems. Chapman (1985) found that the use of a sponge boundary condition in an alongshelf wind stress problem resulted in incorrect steady state currents, due to the limited amount of geostrophic flow which can pass through the open boundary.

A more physically correct, but computationally complex approach is to decompose the baroclinic mode velocities into a set of internal orthogonal modes and prescribe boundary conditions for each mode (Shulman and Lewis, 1995). If the internal waves in the model domain are propagating mainly in the first baroclinic mode however, a simplified radiation condition can be formulated based on the approximate phase speed of the first mode wave. The phase speed approximation has already been introduced in the discussion of the stability criterion for the internal time step, i.e., $c_i \approx (g \frac{\Delta \rho}{\rho_o} H)^{\frac{1}{2}}$. This approximation can be incorporated into the explicit gravity wave radiation condition (Chapman, 1985):

$$U_B^{t+1} = \mu U_{B\pm1} + (1-\mu)U_B^t,$$

where $\mu = c_i \Delta t / \Delta x$. Mellor (1996) points out, however, that if Δt_i and Δx are chosen such that

$$c_{i\,MAX} \approx (g'H_{MAX})^{\frac{1}{2}} \approx \frac{\Delta x}{\Delta t_i}, \text{ then } \mu_{MAX} \approx 1, \text{ and } \mu \text{ can be approximated by:}$$

$$\mu \approx \sqrt{\frac{H}{H_{MAX}}}.$$

The above approximation also relies on the rough assumption that c_i is proportional to $(H)^{\frac{1}{2}}$.

In this application of the model however, the desired high horizontal resolution and the CFL criterion on the internal mode prevents the use of a Δt_i which would yield $\mu_{MAX} \approx 1$. Rather, the choice of $\Delta x = 1$ km, $\Delta t_i = 120$ s, and the estimated maximum internal phase speed of $c_i \approx (9.8 \times \frac{.15}{1027} \times 2500)^{\frac{1}{2}} = 1.89$ m s^{-1} results in $\mu_{MAX} = 0.227$. Therefore, μ is approximated by .

$$\mu \approx 0.227 \sqrt{\frac{H}{H_{MAX}}}.$$

This approximation was successfully applied on the north and south boundaries of the domain, where it will be shown that the internal tides propagating along the shelf exist mostly in the first mode by the time they reach the boundary.

This approximation was not suitable at the western boundary, where the internal tide was propagating in a beam-like manner (i.e., in many modes). A sponge boundary condition was therefore employed at the western boundary. The internal velocity components are gradually

reduced to zero at the western boundary through multiplication with the sponge, which is defined as:

$$SP = 1 - [1 - \left(\frac{i-2}{N}\right)]^2$$

where i is the gridpoint number (increasing in the eastward direction from 1 to i_{MAX}) and N is the total number of gridpoints used for the sponge, which in this case was 10. The sponge was applied not only to the internal velocities, but to the baroclinic pressure gradient which drives the velocities as well. The values of SP are plotted versus the east-west gridpoint number in Figure 36.

3.   Pressure Gradient Truncation Error Analysis

High horizontal and vertical resolutions are used in order to conduct a careful study of internal tide generation and propagation, but they would also be required in other studies using this bathymetry, in order to reduce truncation errors in pressure gradient calculations. In models with stretched vertical coordinates (such as the sigma coordinates), these errors can be severe if proper resolution is not used (Haney, 1991, Kowalik and Murty, 1993, Mellor et al., 1994). A brief review of the sources of this truncation error follows.

The pressure gradient force in a sigma coordinate model is calculated by summing two terms, one involving the gradient of pressure along a constant σ surface (where σ represents a fraction of the total depth) and the other involving the gradient of bottom topography. Haney (1991) notes:

> *The potential for truncation error arises from the fact that these two terms become, in the presence of steep topography, large, comparable in magnitude, and opposite in sign. Thus a small error in the calculation of either term near steep topography can lead to a significant error in the total pressure gradient force.*

Truncation errors in the numerical computation of the pressure gradient force over steep topography produce false currents which, upon geostrophic adjustment, flow parallel to the isobaths. The direction of flow along the isobaths depends on the distribution of the sigma levels and the position in the water column (Haney, 1991). Gary (1973, cited in Haney 1991) found that

74

the truncation error could be significantly reduced by subtracting a horizontally uniform reference state density field before computing the individual pressure gradient terms. Haney notes that the error can be further reduced by increasing vertical resolution. In calculations of the first three baroclinic Rossby modes associated with a buoyancy frequency profile typical of the California Current region (in a 2000 m deep ocean), these techniques were shown to reduce the errors in the calculation of 1st and 2nd mode disturbance temperature profiles (and hence, baroclinic pressure gradient and velocity profiles), but did not reduce the errors in mode 3 profiles. Mellor et al. (1994) note that subtracting a reference state density field to reduce truncation error has been standard practice within their modeling group for regional modeling studies, and the technique was employed in this study as well.

Another source of pressure gradient error, "hydrostatic inconsistency" (Mesinger and Janjic, 1985, cited in Haney (1991)), is believed to exist when a sigma surface which lies immediately below a sigma surface of depth z in one cell rises above depth z within a horizontal distance of one grid interval. In such a case, the finite difference scheme is purportedly nonconvergent, and any subsequent increase in vertical resolution will theoretically worsen the truncation error. The only way to reduce the error would be through finer horizontal resolution, such that

$$\left|\frac{\sigma}{H}\frac{\delta H}{\delta x}\right|\delta x < \delta\sigma \text{ , or more simply, } \frac{\delta H}{H} < \frac{\delta\sigma}{\sigma}$$

is satisfied. In this equation, σ is the value of the vertical coordinate midway between a given sigma surface and the one immediately above it ($\sigma = (\sigma_1 + \sigma_2)/2)$), H is the average depth between the adjacent grid cells of interest, δH is the change in depth between adjacent grid cells, δx is the horizontal grid cell size, and $\delta\sigma$ is the vertical cell size. In a model with evenly spaced sigma levels, this criterion is most restrictive at the bottom, where $|\sigma|$ is highest. Mellor et al. (1994) assert that the criteria for hydrostatic consistency is severely restrictive and contend that the pressure gradient error in POM is not numerically divergent; rather, the pressure gradient error decreases with the square of the vertical and horizontal grid size. Given the sigma level spacing of $\delta\sigma = 0.005$ used for the surface and bottom boundary layers in this study, the horizontal resolution would need to be as fine as 13 m above the canyon walls (which slope as steeply as 9° at an average depth of 423 m between grid points) in order to satisfy the Mesinger and Janjic criterion for hydrostatic consistency. This scale of resolution would be

75

unattainable without reducing the domain size (due to computational memory constraints) or using an advanced grid generation technique.

In order to make a rough estimate of the potential error currents in the model domain, the model was initialized with temperature and salinity values dependent only on z (i.e., horizontally uniform), and run in the prognostic mode for four days (the length of the model runs used for the internal tides studies) with no external forcing and zero surface heat flux. The model current, temperature, and salinity fields were sampled daily, and an algorithm was used to search all sigma levels for the maximum currents at each model grid point. The maximum velocities at the end of day 1 (after geostrophic adjustment has occurred), which are entirely erroneous because of the horizontally uniform density field, are depicted in Figure 37. As expected, the maximum velocities are found in the areas of steep topography and are flowing alongshore. The maximum current speed in the domain at this point is less than 0.9 mm s^{-1}. Since the truncation errors result in erroneous advection of temperature and salinity across isobaths, the T-S distributions should be monitored in "unforced" control runs. Temperature-salinity curves representing the initial conditions and conditions at the end of day 1 (Figure 38) are essentially identical, indicating that the density field has not been noticeably perturbed at this point. The error velocities were found to steadily grow over the four day test but were no greater than 2.1 mm s^{-1}.

The above errors are considered acceptable, however they represent the errors associated with the unperturbed density field, as opposed to those associated with the internal tide. The internal tide density perturbations are expected to exhibit smaller vertical scales than the unperturbed profile, and it has been noted (Haney, 1991; Sundqvist, 1975) that errors associated with higher mode (smaller vertical scale) buoyancy profiles are more severe than those associated with low mode profiles. These errors are difficult to assess however, since the pressure gradients associated with the internal tide are constantly changing, and the currents produced by these oscillations do not geostrophically adjust.

In order to make a conservative estimate of the errors associated with the internal tide density perturbations, profiles of density, temperature and salinity were obtained from a model run which included tidal forcing. The profiles were obtained at the foot of the canyon (I=39, J=35) during rising tide (three hours prior to high tide). It will be shown that the internal tides at this location and time are relatively energetic. The perturbation density, ρ', is defined as the difference between the density profile during rising tide and the initial density profile. The vertical scale of

the density perturbations was examined by computing, via centered differencing between sigma levels, the vertical gradient of ρ'. The vertical gradient of the perturbation density at this location and time is observed to be less than 8.2×10^{-5} kg m^{-4} at all depths. The vertical gradient of the initial density profile is much greater, exhibiting a maximum of 1.7×10^{-2} at a depth of approximately 30 m, and a minimum of 5.1×10^{-3} at the bottom (910 m).

Since the pressure gradient force error scales with this vertical density gradient (Haney, 1991), the error associated with the internal tide is (in terms of a false geostrophic current, V_g'):

$$V_g' = (2 \text{ mm s}^{-1}) \times \frac{8.2 \times 10^{-5}}{1.7 \times 10^{-2}} \approx 10^{-3} \text{ cm s}^{-1}.$$

The false acceleration (a') produced by this error is therefore

$$a' = fV_g' \approx 10^{-4} \text{ s}^{-1} \times 10^{-3} \text{ cm s}^{-1} \approx 10^{-7} \text{ cm s}^{-2}.$$

Three hours prior to high tide, the magnitude of the acceleration of the internal tide at the foot of the model canyon is observed to be:

$$\left| \frac{\partial u}{\partial t} \right| = \left| \frac{\partial (u_o \cos \omega t)}{\partial t} \right| = \left| \omega u_o \sin \omega t \right| = \left| (1.4 \times 10^{-4} \text{ s}^{-1})(2 \text{ cm s}^{-1})(\sin \frac{3\pi}{2}) \right| \approx 10^{-4} \text{ cm s}^{-2}.$$

This analysis shows that the error is 3 orders of magnitude smaller than the signal. To corroborate the above analysis, the T and S profiles obtained at this location were gradually merged with the original (unperturbed) T and S profiles at depths greater than 910 m and used as the initial profiles at each grid point for another unforced trial. The merged profiles were interpolated onto the sigma levels at each grid point, resulting in a horizontally homogeneous density field, and the model was run in the prognostic mode for four days as in the previous test. The error currents exhibited a similar pattern to that observed in the first trial, and were only slightly greater in amplitude. Maximum currents of 0.94 mm s^{-1} were observed at the end of day 1, and the maximum current after 4 days was again equal to 2.1 mm s^{-1}. Since the currents associated with the internal tide do not geostrophically adjust, these currents do not actually represent the errors caused by the truncation error associated with the calculation of the internal tide pressure gradient. This exercise demonstrates however, that although the vertical density gradient associated with the internal tide exhibits smaller vertical scales, the amplitudes of the density perturbations are so small that the truncation error associated with the calculation of the internal tide pressure gradient is not expected to have a significant impact on this study.

Another factor which could change the density field is the model's use of a "no normal heat flux" bottom boundary condition. Since the isotherms in this horizontally homogeneous case are not perpendicular to the sloping bottom, downward heat diffusion will tend to bow the isotherms downward near the sloping boundary until they are perpendicular to the bottom, resulting in geostrophic flow along the boundary (Schwab et al., 1995). In order to explore this possibility, the original unforced test was repeated with the coefficient of vertical diffusion set to zero, however the error velocities were not noticeably changed at the end of the four day period. It is expected that the effects of downward heat flux along the sloping bottom would eventually perturb the density field and cause current spin-up, but the currents observed in this short simulation are apparently due to pressure gradient truncation error. In any case, the "unforced" currents are at least an order of magnitude smaller than the baroclinic currents observed in the tidal simulations, and are not considered to detract from the findings of this process study.

D.   RESULTS

1.   Overview Of Experiments

This section discusses the results of eight experiments involving internal tide generation and propagation. Two of the experiments involve continental slope/shelf bathymetry with no alongshore variation, and six involve canyons of various shape. The cases without alongshore variation were conducted in order to assess the generation of internal tides along the continental slope and shelf break, and propagation across a narrow shelf, in the absence of canyons. In addition to confirming previous analytical solutions for internal tide generation, they serve to contrast the results obtained with various canyon shapes incising the continental slope and shelf. The cases involving canyon geometry were specifically designed to investigate the sensitivity of internal tides to canyon floor slope and canyon width. Three different floor slopes were investigated, including one which shoals at an angle that is critical or near-critical for the M2 frequency along much of its extent. The critically sloping canyon floor is of prime interest, due its apparent importance in the case of MSC and the failure of linear theory to adequately describe critical bottom reflection. Therefore, the critical floor slope was used with four different canyon widths in order to examine the effect of side boundaries on a bottom-intensified internal tide.

The organization of this section is as follows. The results of the experiments using simple continental slope/shelf bathymetry are discussed, and are then contrasted with the canyon case which most closely resembles MSC in size and shape. Results of the canyon floor slope investigation are then presented, followed by results of the experiments involving various canyon wall and floor widths. The section concludes with a summary of the major findings.

2. Internal Tide Generation On the Continental Slope and Shelf Break

The steep continental slope typical of the eastern Pacific was approximated with two different geometric shapes: a linear, 6.62° rise with an abrupt shelf break, and a cosine function with an amplitude of 1200 m and wavelength of 60 km (Figure 39). The cosine amplitude of 1200 m was chosen so that the trough of the wave shape would correspond to the onset of the continental rise at a depth of 2500 m, and the crest would occur at the 100 m deep shelf break. The maximum slope resulting from the cosine function was 7.15°, occurring at a depth of 1300 m (the inflection point of the cosine shape). The two shapes are useful in demonstrating the sensitivity of internal tide generation to the rate at which the bathymetry in the generation region transitions from supercritical to subcritical.

The model was run in the prognostic mode with tidal forcing for 4 days, and the final 3 tidal cycles were used for analysis. As expected for a wave that is nearly standing in the cross-shelf direction, the barotropic tidal currents (as represented by the depth-averaged currents) are weak. Maximum shoreward flow of approximately 1.5 cm s^{-1} occurs, as expected, at the shelf break during rising tide. The increase in barotropic current speed at the shelf break is a result of the rapid depth change from basin to shelf. The vertical component of the barotropic current over the slope is the driving force which produces internal tide generation.

A cross-shelf slice of the current field during rising tide (Figure 39) reveals the relatively strong baroclinic currents resulting from internal tide generation at the shelf break. As discussed by Prinsenberg et al. (1974), the discontinuity in the barotropic cross-shelf velocity at the shelf break results in the generation of two beams of internal waves propagating seaward, and a narrow beam of waves propagating shoreward. Superimposed on the velocity plots are rays indicating the M2 characteristics emanating from the shelf break. The ray positions were calculated using Equation 1 of Chapter II and the buoyancy frequencies computed from the temperature and salinity

79

profiles used to initialize the model fields. This ray-tracing technique is an effective means of defining the path of internal tide energy propagation. As described by Prinsenberg et al., the two characteristics emanating seaward describe the boundaries of the in-phase currents associated with the seaward propagating energy. The lower half of the seaward beam is enhanced by weaker internal tide generation along the continental slope, as discussed in Prinsenberg and Rattray (1975). The presence of several additional beams emanating downward along the continental slope in the case of the cosine-shaped bathymetry can be attributed to the broader area available for internal tide generation, as compared to the linear slope case which represents an abrupt change from supercritical to subcritical bottom slope at the continental shelf break. This feature is in agreement with the study of Baines (1974), who found that bathymetric features with concave downward shapes were especially efficient generators of internal tides. The narrow shelf beam is well described by a single characteristic reflecting between the sea surface and shelf break.

Although not very noticeable in the particular phase of the tide depicted in Figure 39, the base of the 6.62° linear continental slope was also found to be an internal tide generation site. Generation occurred at a depth of approximately 2200 m (where the slope of the M2 characteristic is, over a short depth range, equal to 6.62°) and resulted in a beam of internal tide energy propagating upward and seaward from the generation site. Use of the concave-upward shape at the base of the continental slope was found to nearly eliminate internal tide generation in that portion of the domain. Since internal tide generation at the foot of the continental slope was considered unimportant to this study, the cosine-shaped continental slope was used for each of the model runs involving canyon bathymetry.

Figure 40 provides a closeup view of the currents between the shelf break and the coast at four points in the tidal cycle. In the case of the abrupt shelf break, the most intense currents are found during rising and falling tide, where the beam reflects from the surface and bottom. This was also generally true in the case of internal tides generated at the rounded shelf break, although the beam was slightly more diffuse due to the wider area available for generation. When a beam of internal wave energy reflects from a supercritical boundary such as the straight wall at the model coast, the horizontal velocities undergo a 180° phase shift. This phase shift is evident in the near-surface currents within 10 km of the coast, which flow seaward (shoreward) during rising (falling) tide, in opposition to the near-bottom currents in this region. Prinsenberg et al. found that if the shoreward beam reflects from the coast, as would occur in the case of a narrow continental shelf

terminating with a steep wall at the coast, the 180° phase shift causes horizontal velocities to cancel at intersections of the shoreward and seaward (reflected) beam. These velocity minima can be seen in the current fields at high and low tide, where the beams intersect each other near mid-depth at distances of approximately 9 and 19 km from the coast. Prinsenberg et al. found that 45 modes were necessary to properly represent the current field seaward of the shelf break, while 5 were sufficient to represent important features of the narrow shoreward beam. Modal decomposition of the model current fields is not attempted in this study, however it is pointed out that the features described by the modal solutions of Prinsenberg et al. are reproduced in this 3-D simulation.

3.   Canyon Case 1

This section discusses the results of a simulation involving a canyon fairly similar to MSC in its shape, size, and proximity to the coast. This simulation will be referred to as Case 1. The bathymetry for this simulation is depicted in Figure 41. In Chapter II, it was noted that the floor of MSC rises from a depth of 1000 m to 100 m over a distance of approximately 20 km, and the canyon head terminates within 1 km of the coast. The average floor slope in MSC (2.6°) is critical with respect to the M2 frequency for typical buoyancy frequencies in the 600-800 m depth range. In order to construct a model canyon with its head located near the shore, and ensure realistic width and depth while limiting the steepness of the sides, a canyon with 1.5° bottom slope was used. The model canyon head is located 1 km from the closed eastern boundary, and the floor increases in depth from 100 m to 937 m (where it intersects the continental slope) over a distance of 31 km. For the initial density profile and the M2 frequency, the floor slope is critical at a depth of about 300 m. The canyon was designed to resemble MSC not only in bottom slope, but in width as well; the canyon is 11 km wide at the shelf break, and narrows to 3 km at the head.

Unlike MSC, there are no features seaward of the model canyon which could generate internal tides (such as "Smooth Ridge", which lies west of Monterey Bay). The only internal tides entering the model canyon are those generated at the foot, along the floor, and on the rims. The M2 internal tides in the model canyon are thus expected to be weaker than those propagating in MSC, but qualitatively similar, in that energy should propagate shoreward and upward from a

deep generation site (the canyon foot), travelling along the model canyon floor and reaching the canyon head with relatively little dissipation.

a)   Along-canyon Variations

As in the cases without a canyon, the barotropic currents (represented by the depth-averaged currents) were found to be strongest at the 100 m deep shelf break, with amplitudes of less than 1.5 cm s^{-1} (Figure 42). The variance ellipses representing the depth-averaged currents in the canyon have semi-major axes nearly as large as those at the same x location (I grid point) outside the canyon, but the canyon ellipses are nearly rectilinear. The barotropic currents in the vicinity of the canyon foot are weaker than those at the 100 m deep shelf break, thus internal tide generation at the foot of the canyon is expected to be weaker than at the shelf break. The currents associated with the internal tides propagating along the floor of the canyon however, were found to be 3-4 times stronger than those propagating across the shelf. Maximum cross-shore current speeds of 8 cm s^{-1} were found to occur during rising tide, near the critical region of the canyon floor at 300 m depth. Snapshots of the cross-shore currents at four points in the tidal cycle are depicted in Figure 43. (Note that the velocity scale in Figure 43 has been expanded to ±6 cm s^{-1}, vice the ±2 cm s^{-1} scale used for the shelf currents in Figure 40.)

As was observed to be the case in MSC during ITEX1, internal tide energy in the model canyon propagates shoreward nearly parallel to the canyon floor, and downward phase propagation results in maximum shoreward flow occurring later with depth. The characteristic emanating from the foot of the canyon defines the upper boundary of the strongest currents. The phase lag between the model currents and sea level is within ¼ cycle of that observed in ITEX1; near the head of the canyon, maximum shoreward flow occurs in the lower half of the water column, close to the time of high tide. Figure 44 depicts snapshots of the ITEX1 semidiurnal currents and the model M2 currents. Although the model currents are 50% weaker than observed, the structure of the observed and modeled current fields are qualitatively similar, with strong shoreward flow along the floor and offshore flow near the surface. The isophase lines are nearly parallel to the canyon floor.

As mentioned previously, the model currents are expected to be weaker than the baroclinic tidal currents observed in MSC due to the simplified model bathymetry. Internal tides in the model are generated at the canyon foot, which represents an abrupt change from supercritical to subcritical floor slope. "Smooth Ridge", a likely site for internal tide generation seaward of MSC,

features a concave downward shape which appears to be nearly critical for the M2 frequency over a horizontal distance of nearly 10 km (see Chapter III, Section C, and Figure 31). Some of the disparity between the strength of the modeled and observed internal tides can also be attributed to the use of only one tidal constituent in the model. The "M2" least squares fits to the observational data most likely contain contributions from other semidiurnal tidal constituents. The use of a tidal amplitude of 1 m, vice 0.5 m in this simulation, approximates the range of the spring tides along the Central California coast (and the tidal range observed during ITEX1), and results in a model current field with similar vertical structure but with maximum amplitudes of 15 cm s^{-1}, much closer to 20 cm s^{-1} internal tide velocities observed in MSC.

The region of strongest current activity in the model simulation lies in the bottom boundary layer, at floor depths of 200 to 300 m. Inspection of the density field in this boundary layer (Figure 45) reveals the presence of bore-like surges along the canyon floor. Densities ranging from 1027.35 to 1027.95 kg m^{-3} are contoured at intervals of 0.05 kg m^{-3}. At these depths, the vertical resolution in the bottom three sigma levels is between 1 and 1.5 m. A thin layer of dense water is seen to surge up the floor during rising tide, resulting in isopycnal displacements of 5-10 m. This boundary layer activity is consistent with the 2-D numerical simulations of Slinn and Riley (1996), who observed that critical angle internal wave reflection on floors with shallow slopes (3.4°-9°) resulted in the upslope propagation of thermal fronts in the bottom boundary layer.

b)   Energetics

In order to investigate energetics associated with the internal tide, mean perturbation kinetic and potential energy calculations are performed on along- and cross-canyon slices of velocity and density data. The vertical velocity component is converted from sigma coordinates to z coordinates before including it in the kinetic energy calculations. This is accomplished by using the formula given by Blumberg and Mellor (1987):

$$w = w_\sigma + U\sigma\frac{\partial D}{\partial x} - \frac{\partial \eta}{\partial x} + V\sigma\frac{\partial D}{\partial y} - \frac{\partial \eta}{\partial y} + \left(\sigma\frac{\partial D}{\partial t} + \frac{\partial \eta}{\partial t}\right),$$

where w_σ is the vertical velocity referenced to sigma coordinates, σ is the value of the sigma coordinate for the grid cell of interest, D is the total depth (bathymetric depth plus free surface elevation) and η is the free surface elevation. In this application however, the horizontal gradients of η are considered negligible and are not included in the calculations.

83

Since the specified tide is monochromatic, the amplitude of the M2 tidal currents are estimated by determining the amplitude of the perturbation velocities. Although nonlinear interactions can give rise to other frequencies, it is assumed that most of the energy is in the semidiurnal band. The u, v, and w velocity fields, sampled at a rate of 3720 s (12 points per tidal cycle) are de-meaned to obtain perturbation velocities, and the perturbation velocities are squared and temporally averaged over three tidal cycles. As discussed in Section B.7 of Chapter III, the amplitude of a sinusoidally varying signal can be calculated as $A_o = (2\overline{A'^2})^{\frac{1}{2}}$, where the overbar denotes the mean over one cycle. This method was compared to the conventional least squares harmonic analysis method (using the M2 frequency to perform the least squares fit), and the amplitudes of the tidal currents were essentially identical. Since the perturbation method is less computationally intensive, it is used to calculate the amplitudes of the M2 current and density oscillations in each of the modeling experiments. The velocity and density amplitudes are used to calculate mean perturbation kinetic energy (KE) and potential energy (PE), respectively (as described in the previous Chapter). The buoyancy frequency used in the PE calculations is computed from the vertical gradient of the model mean density field (the mean field is calculated over 3 tidal cycles), using centered differencing between sigma levels. KE and PE are summed to obtain the mean perturbation total energy per unit volume (E), and this quantity is converted to mean perturbation energy density (ED) by multiplying by the average vertical thickness of the sigma cell. Since the vertical resolution of the model varies, ED is a more meaningful quantity for comparing the model internal tide to the internal tide field observations.

Perturbation $\dot{u}$ amplitude and energy density in an along canyon slice are depicted in Figure 46. Maximum u and ED values occur close to the canyon head, near the floor. A "shadow zone" of minimal internal tide energy exists between the M2 characteristic rays emanating shoreward from the foot of the canyon and the reflected ray (drawn with dashed lines) descending from the canyon head to the floor of the basin. The increase in ED with depth is consistent with the ED profiles calculated from the ITEX1 and ITEX2 measurements, however the maximum value of 15.8 J m^{-2} is 25-50% of the magnitudes observed in MSC during the ITEXes. Qualitative agreement with the ITEX measurements was also found in the ratio of PE to KE. PE was found to be greater than KE near the head of the model canyon, as was the case in the ITEX measurements. Linear theory predicts a ratio of KE to PE of 2.26:1 for the M2 frequency at this latitude, so the

skewing of the energy distribution (such that a greater percentage is contained in PE) demonstrates the nonlinearity of the internal tide as it steepens near the canyon head.

Thus far, the discussion has focused on the motion in the x-z (along-canyon) plane, normal to the coast. The energy calculations show that ED increases toward the canyon head, and the region of highest energy density is bounded by the canyon floor and the characteristic ray emanating from the generation site at the foot of the canyon. The next section discusses the cross-canyon structure of the internal tide, which is shown to be affected by trapping of its energy along the southern wall of the canyon due to rotational effects. Analysis of the model fields is preceded by a short discussion of theories governing internal wave trapping.

c)   *Cross-canyon Variation*

Refractive trapping of obliquely incident internal waves has been discussed in theoretical terms by Wunsch (1969) and Chapman (1982). Wunsch showed that for internal waves obliquely incident to a sloping beach with $\gamma / c < 1$ (subcritical bottom slope), growth of the cross-shore wave number causes the wavecrests to refract, becoming parallel to the beach. The waves then propagate as edge waves trapped along the coast. Wunsch's study showed that observation of cross-shelf propagation of internal waves does not necessarily prove that generation occurs at the continental shelf break. Chapman demonstrated refractive trapping of internal waves obliquely incident on a step shelf. Trapping was shown to depend on the angle of incidence, the deep sea mode of the incident wave, and the depth of the shelf. Both studies neglected rotational effects, which are important for internal tides.

The only theoretical treatment of inertia-gravity wave propagation which includes the combined effects of stratification, rotation, and topography appears to be that of Rhines (1970), who presents solutions of linearized, Boussinesq equations for wave motion in a rotating, stratified fluid bounded by a single wall. Choosing a coordinate system such that the bottom of the inclined wall is at $x_3 = 0$, and x_1 and x_2 represent cartesian coordinates rotated through an angle φ from the alongslope and upslope directions respectively, Rhines shows that edge waves may occur for all frequencies less than $N \sin \gamma$, where γ is the angle of the wall from the horizontal. Rotational effects cause the waves to propagate with shallow water to the right, however the maximum trapping frequency is independent of f. The frequency of the trapped waves and their angle of propagation are related to the inclination angle by

85

$$\omega = N \sin \gamma \sin \phi .$$

The degree of trapping (i.e., the proximity to the wall of significant motion) is shown to be strongly dependent on γ, and the relation of γ to a trapping coefficient S, defined as $S = N/f$. In the limiting case of a vertical wall, the edge wave is simply an internal Kelvin wave, with motion decaying exponentially away from the wall. For relatively small slopes ($\gamma \sim S^{-1}$) and $\omega \sim f$, the case most applicable to internal tide propagation, strong trapping occurs, with motion penetrating about one wavelength into the fluid. In this case, the "wall" is more appropriately described as the bottom, and the waves are referred to as "bottom-trapped" waves. As in the case of simple 2-D propagation of internal tides (i.e., free waves propagating normal to the depth contours), planes of constant phase for the bottom-trapped waves are almost parallel to the boundary. Rhines speculates that the semidiurnal barotropic tide incident on the continental rise could produce strong trapped motions, as well as the more commonly discussed free waves.

The effect of canyon walls on internal tide propagation has been discussed in traditional 2-D terms, i.e. as either subcritical or supercritical for internal waves incident from above (Gordon and Marshall, 1976, Hotchkiss and Wunsch, 1982). Hotchkiss and Wunsch state that the effect of sloping walls in a V-shaped canyon is to enhance the focal properties of canyons so that energy entering the canyon from above will tend to be concentrated near the floor. Hotchkiss and Wunsch also consider the effect of internal tide generation at the rim of a canyon, noting that beams of energy should radiate toward both the shallow and deep water (i.e., up onto the shelf, and down into the canyon). Another possible effect which has not received attention in the literature is that energy propagating shoreward in a canyon can become trapped along the right side of the canyon (facing shoreward), if the conditions outlined by Rhines (1970) are met. Within the Case 1 model canyon, conditions are favorable ($\omega_{M2} < N \sin \gamma_w$, where γ_w is the slope of the canyon wall) for trapping the internal tide along the southern wall in the middle and deeper parts of the canyon. Examination of perturbation energy in cross-canyon slices of the model data does in fact reveal asymmetric energy distribution, with greater energy density existing along the southern wall of the canyon. It is also found that generation of internal tides at the rim of the canyon is asymmetric, with stronger generation occurring along the southern rim.

Cross-canyon slices of velocity and density are used to compute KE and PE, and these terms are summed and multiplied by the average vertical thickness of the grid cell to obtain ED. The energy density values at 5 cross canyon slices are depicted in Figure 47. The distance in

kilometers of each slice from the canyon head can be computed by subtracting the "I" grid cell coordinate from 69, the I grid cell coordinate at the canyon head. The slices are obtained every 6 km, between 25 and 1 km from the canyon head. Progressing shoreward from the deepest slice at I = 44, ED is seen to be focused near the floor (as was found to be the case in the along canyon slices), but is asymmetrically distributed in the cross-canyon direction, with a greater percentage lying along the southern wall. Contributions to perturbation energy can be expected from internal tide generation along the canyon floor, which should occur where the floor slope is critical for the M2 frequency. The floor slope is critical at a depth of about 300 m, near I = 62. Indeed, the internal tide appears to be much more energetic in the final 2 slices (I = 62 and I = 68). The energy near the floor in the final 2 slices is more symmetrically distributed, however asymmetric generation of internal tides is seen to occur at the rim of the canyon.

Generation of internal tides at the rim of a canyon could be caused by the vertical components of both the barotropic and baroclinic tidal currents, however the vertical component of the baroclinic tides encountering the rim of this model canyon would be an order of magnitude stronger than that of the barotropic tide. The horizontal components of the barotropic tidal currents near the head of the canyon are only a few milimeters per second, and the vertical component induced by the sloping sides of the canyon would be even smaller. The fact that internal tide generation is stronger on the southern rim of the model canyon is in accordance with the increased baroclinic energy already present along the southern wall due to trapping of shoreward propagating internal tides. It is noted however, that in regions where the barotropic tidal currents have a significant longshore (hence, cross-canyon) component, as is the case in the Eastern Pacific, the barotropic tidal currents could generate significant internal tides along the rims.

In order to observe changes in total internal tide energy in the cross-canyon slices, it is a simple matter to sum the ED values in a given slice, and then multiply by the cross-shore and along-shore dimensions of the slice (the vertical height of the slice is already accounted for in the conversion of total energy, KE+PE, to ED). It appears to be important to include the energy associated with the waves generated along the rims, since they may represent a transfer of energy from internal tides propagating along canyon to those propagating along the coast. A slice length of 31 km (J grid points 20 through 50) was therefore chosen, so that the contributions from the rim-generated waves would be included in the calculation. The total energy in each slice is depicted in Figure 48.

87

The total perturbation energy in the vicinity of the canyon is seen to decrease almost linearly from I = 44 to I = 56. The energy decrease most likely represents turbulent dissipation of the internal tide due to shear along the canyon walls. The total energy present in the vicinity of the canyon nearly doubles however, between I = 56 and I = 62, indicating that contributions from internal tide generation on the floor of the canyon far outweigh the losses incurred along the walls. It should be noted that if the critical floor slope served only to focus the energy associated with the shoreward propagating internal tide into a decreasing cross-sectional area, the total baroclinic energy present would either remain constant, or decrease due to turbulent losses in the bottom boundary layer. However, the critical floor slope also provides a generation site for internal tides; energy is therefore transferred from the barotropic tide to the baroclinic tide not only at the foot of the canyon but along the floor in the upper reaches of the canyon as well. An additional increase in total energy at I = 68 most likely indicates the effects of continued internal tide generation on the floor of the canyon, which is only slightly subcritical at this location.

Significant isopycnal displacements were observed at the head of the model canyon (Figure 49). As the strong shoreward flow encounters the head of the canyon, isopycnal displacements of 5 to 10 m move water from beneath the canyon rim up onto the shelf. The densities depicted in Figure 49 are contoured in intervals of 0.03 kg m^{-3}, and range from 26.335 kg m^{-3} to 26.635 kg m^{-3}. As the isopycnals sink back down below the rim, lenses of dense water pinch off and remain on the shelf, in the manner suggested by Shea and Broenkow (1982). Shea and Broenkow consider this process a potentially significant source of nutrient enrichment for the Bay in the absence of wind driven upwelling.

d)   *Alongshore Propagation*

The "tidal pumping" observed at the head of the model canyon was found to be a source of alongshore-propagating internal tides. A snapshot of the alongshore velocity component in a north-south slice at the head of the canyon is depicted in Figure 50. The slice used for this figure was taken from an early model run which featured the 100 km x 100 km domain. The larger domain provides a better view of the gradual change of the alongshore internal tide, from beam-like near the generation site (the canyon rims) to basically 1st mode near the model boundaries. Beams of internal tide energy are seen emanating from the north and south rims of the canyon. The surface and bottom reflections of the beams on the north side of the canyon are regularly spaced, and after the 2nd surface reflection visual inspection reveals that most of the higher modes have

been damped out, with the internal tide propagating mainly as a 1st mode wave. These waves were found to be propagating as internal Kelvin waves. The signature of these trapped waves could be seen in surface current patterns as well as in small (3-4 mm) deflections of the sea surface which decayed exponentially offshore over a distance of approximately 4 km (one internal Rossby radius of deformation, computed as $a_i = (g'H)^{\frac{1}{2}} f^{-1}$). By observing successive plots of free surface elevation, the sea level disturbances were easily tracked as they propagated towards and through the northern boundary. The rate of travel of the sea level disturbances implied an alongshore phase speed for the Kelvin waves of roughly 35 cm s^{-1}. Calculation of $c_i = (g'H)^{\frac{1}{2}}$ with $g' = g\dfrac{\Delta\rho}{\rho}$ yields a phase speed of 37.8 cm s^{-1}, very close to the estimated value. The beams projecting southward from the canyon rims are slightly more intense and appear less regularly spaced. The irregular spacing appears to be due to the fact that the waves on the south side of the canyon are not propagating along the coast, but are propagating seaward across the shelf as ordinary internal Poincare waves. The sea surface signature of these waves was much broader and indicated a radial spread of internal wave energy away from the canyon. It was found that running the model with the Coriolis parameter set to zero (i.e., no rotation) resulted in symmetric generation of internal waves along the rims of the canyon and radial spread of internal wave energy away from the canyon head, with regularly spaced wave trains propagating both southward and northward along the coast. In the absence of rotation, the waves have no preferential direction of propagation.

The presence of the internal Kelvin waves provided a good opportunity to test the radiation boundary condition used for the internal velocities at the north and south open boundaries. It was found that if the phase speed of the internal waves was improperly specified (via the μ term in the radiation boundary condition), only partial transmission of the internal waves through the boundary occurred. Imperfect transmission was inferred from animations of sea level, which depicted the Kelvin waves turning the corner (as if the open boundary were closed) and propagating westward toward the basin with a slightly reduced amplitude. The model domain size was therefore chosen such that the internal Kelvin waves would be propagating in the first mode by the time they encountered the open boundary, and the phase speed of a first mode wave was used in the formulation of the radiation boundary condition. This model domain and forcing could be used for a more advanced study of radiation boundary conditions for internal waves.

e)   *Near-Surface and Near-Bottom Currents*

In order to observe the effects of the internal tide on the near-surface and near-bottom currents, current variance ellipses are calculated for sigma levels 1 and 29 (Figures 51 and 52). The model currents are actually calculated midway between sigma levels, so the "level 1" currents lie not on the free surface but slightly below, at average depths ranging from 0.27 m on the shelf to 6.75 m over the basin (the actual depths vary as the free surface varies). The currents nearest the bottom are calculated midway between levels 29 and 30, and are situated (on the average) 0.27 m above the floor of the shelf and 6.75 m above the floor of the basin (the "level 30" currents would lie below the bottom, and are thus not calculated). The near-surface (level 1) ellipses are amplified 5 to 10 km south of the canyon, where the beams emanating from the southern canyon rim reflect from the surface. This pattern is in general agreement with HF radar-derived tidal ellipses for Monterey Bay, which show amplification of semidiurnal surface currents near the head of MSC (Figure 2). Although the largest ellipses in Figure 2 lie on the north side of the Canyon head which terminates near Moss Landing, they lie to the south of a slumping region which can be viewed as a second head.

The variance ellipses from level 29 represent the currents in the bottom boundary layer, and reveal the bottom intensification of the internal tide. Depths are contoured in 50 m intervals (starting at 100 m), and it is seen that the near-bottom currents become significantly stronger at a depth of 300-350 m (I = 60-62), in the critically sloping region. The near-bottom currents are also intensified over the southern rim of the canyon, where significant internal tide generation is observed to occur.

4.   Summary of Canyon Case 1 Experiment

It is observed that internal tide energy density increases in the upper reaches of the Case 1 canyon due to both the focusing of internal tide energy propagating from the canyon foot into a smaller-cross sectional area, as well as internal tide generation along the critically sloping section of the canyon floor. Shoreward propagation in the form of a "bottom-trapped" wave (Rhines, 1970) along the southern wall of the canyon is evidenced by higher perturbation energy densities on the south side of the canyon. Internal tide generation is observed to occur on the rim of the canyon,

90

with stronger generation observed on the southern rim. Generation at the canyon rim results in alongshore (northward) propagation of the internal tide as an internal Kelvin wave.

In order to further investigate the effects of canyon shape on internal tide propagation, additional experiments were conducted with various canyon floor slopes, rim widths, and floor widths. The experimental results will be discussed in terms of floor slope variations (Case 2) and width variations (Case 3).

5.   Canyon Case 2 - Floor Slope Variations

Floor slope effects were investigated with V-shaped canyons of constant width. Floor width and rim width were constant along the length of the canyon, measuring 3 km and 11 km respectively. Floor slopes of 0.013 (0.74°), 0.027 (1.5°), and 0.04 (2.29°) were investigated (Figure 53). The two steepest model floor slopes cannot be strictly defined as either subcritical, critical, or supercritical, since the use of a realistic density profile (thus, a non-constant N) causes γ and c to be related differently along the length of their floors. The 0.74° floor slope however, is subcritical along its entire length.

Mean perturbation energy density was calculated for along-canyon and cross-canyon slices as described in the previous section. The along canyon slices are presented in Figure 54, with the depths of the neighboring continental slope and shelf indicated with dashed lines. The internal tides in the case of the 2.29° floor slope are significantly more energetic than in the other two cases. The foot of the canyon represents an abrupt change from supercritical to subcritical bathymetry for both the 1.5° and 0.74° floor slopes, but in the case of the 2.29° slope the change is from supercritical to critical bathymetry. The transfer of energy from the barotropic tide to the baroclinic tide is therefore accomplished more efficiently with the 2.29° floor slope, since the barotropic motion (guided by the floor slope), and the baroclinic motion (guided by the frequency of the forcing and the degree of stratification) lie in the same plane. However, little of the energy generated at the foot of the 2.29° canyon floor reaches the shelf, since the floor is supercritical for the M2 frequency at shallower depths. Although not apparent in Figure 54, some internal tide generation was observed to occur at the head of this canyon, with subsequent shoreward propagation of the energy.

The ED pattern associated with the 1.55° floor slope is nearly identical to the Case 1 canyon which had an identical floor slope, but walls which narrowed from 11 km to 3 km (as measured at the canyon rim). The 0.74° floor slope results in relatively low ED values since it is subcritical with respect to the M2 frequency along its entire length.

ED in three cross-canyon slices are presented for each of the Case 2 canyons in Figure 55. In order to illustrate the difference in floor slopes, the vertical scale used to depict the slice at a given "I grid point" location is kept the same for each of the three canyons, although the scale changes between gridpoints. Due to the short length of the canyon with the 2.29° floor slope, the "I68" slice actually represents the portion of the continental shelf which lies shoreward of that canyon, and is included in the figure to illustrate the minor amount of baroclinic energy reaching the shelf in that case. The distribution of ED in each of the three canyons shows some evidence of trapping along the south wall, however the dramatic result from this experiment remains the significantly higher ED levels associated with the 2.29° sloping canyon floor. The total energy in each of the cross-canyon slices (Figure 56) shows that the amount of energy present near the foot of the canyon with the 2.29° floor slope is more than twice that present in the other two canyons, but that little of that energy reaches the inner shelf. The increase in energy that occurs between I = 56 and I = 68 (13 km and 1 km from the canyon head) with the 0.74° floor slope most likely indicates some contribution from generation along the canyon rim. The contribution of energy from that process is apparently sufficient to offset turbulent losses in the bottom boundary layer. The energy in the 1.55° floor slope case also increases between 13 km and 1 km from the head, however this increase is larger than in the subcritical case, due to an additional contribution from generation along the critically sloping floor in the vicinity of I=62, 7 km from the canyon head.

6.   Canyon Case 3 - Width Variations

The experiments discussed thus far include two canyons with floor slopes of 1.55°; one with walls of constant width (11 km) and one with walls which narrow from 11 km to 3 km, which is representative of the shape of MSC. The total energy levels in the cross-canyon slices of these canyons are very similar. The canyon with the narrowing width has approximately 10% more energy in the slice taken near the canyon head than does the constant width canyon. The effects of varying canyon width were further explored by comparing the constant width canyon with two

additional canyon shapes (Figure 57), each having a floor slope of 1.55°. In one canyon, the width of the floor is a constant 3 km, and the walls narrow from 21 km to 3 km. Another canyon features narrowing of both the floor and walls, with the floor narrowing from 11 km to 3 km, and the walls narrowing from 21 km to 3 km.

The perturbation ED levels in the along-canyon slices for these three canyons are nearly identical (Figure 58). (The along-canyon slice for the Case 1 canyon is show in Figure 46, and is also similar to these ED fields.) One would expect higher energy density levels to be present in the canyons with decreasing cross-sectional area, but the highest ED value for the slice along the canyon axis is found in the canyon with constant width. If more energy is present in the narrowing canyons, it must be contained closer to the canyon walls. The cross-canyon ED calculations (Figure 59) confirm that this is the case. Each of the canyons show increased ED levels on the southern side, suggesting the presence of bottom-trapping along the southern wall.

The cross-canyon slices at I = 56 are convenient for comparing the energy levels present in each of the canyons, since the cross-sectional areas are the same at this location. The most energetic internal tides are found in the canyon which has both a narrowing floor and narrowing walls. This simply illustrates that a wider area available for internal tide generation (i.e., a wider floor at the canyon foot) results in more internal tide energy propagating shoreward in the canyon. Comparing the two canyons with constant 3 km floor width, the one with narrowing walls (i.e., a wider rim at the generation site) is seen to have less energy density at I = 56. This suggests that, given the same floor width, steeper canyon walls result in more energetic internal tides. This idea is supported by comparing the same two canyons at I = 68. In this slice, the constant width canyon has a wider rim (less steep walls), and it is found to have lower energy levels than the narrowing canyon. Steeper walls most likely contribute to higher energy levels by facilitating stronger internal tide generation at the rim of the canyon. Given the same cross-canyon component of velocity v, a stronger vertical component will be induced in the flow as it encounters a steeper wall,

if it is assumed that $w = v\dfrac{\partial h}{\partial y}$ (where h is the depth and y is the cross-canyon direction).

The ideas discussed above are supported by the plots of total perturbation energy (Figure 60), which show the highest energy levels in the canyon with the widest floor at the generation site, and higher energy levels at a given location for canyons with steeper walls.

93

E.   SUMMARY

This process study demonstrates that internal tide generation can occur at the foot, floor, and rims of a submarine canyon, and that certain canyon geometries result in exceptionally energetic internal tides. The model used in this study is the Princeton Ocean Model, with 30 sigma levels in the vertical and 1 km x 1 km horizontal resolution. The model is forced with 0.5 m amplitude semidiurnal sea level oscillations along the offshore (western) boundary. This choice of model forcing simulates the weak cross-shore barotropic tidal currents typical of the central California coast and other coastal regions with narrow continental shelves. The model current fields are therefore dominated by baroclinic currents associated with semidiurnal internal tides.

Tidal forcing in the presence of a continuously stratified density field results in internal tide energy propagation along paths which are well described by the characteristic slopes given by the dispersion relation for internal waves. Beams of energy are observed to propagate shoreward and seaward from the shelf break and from the canyon foot. The strength of the internal tides propagating shoreward in the model canyons and the amount of internal tide energy reaching the canyon head are found to be very sensitive to canyon floor slope. Specification of a 1.55° floor slope, which is slightly subcritical for the M2 frequency near the foot of the canyon and critical in the upper reaches of the canyon, results in a bottom-intensified internal tide which propagates energy along the length of the canyon, from the foot to the head (Figure 43). In this case, internal tide generation is observed to occur not only at the canyon foot but along the critically sloping portion of the canyon floor, and on the rims of the canyon near the canyon head as well. Generation along the floor results in a significant contribution to total perturbation energy within the model canyon, however the strong currents associated with generation along the floor appear to be confined to a thin bottom boundary layer. The importance of internal tide generation along the floors of real canyons, which are not as straight and smooth as the model canyon floor, remains to be observed.

A minor reduction in floor slope (from 1.55° to 0.74°), such that the canyon floor is subcritical for the M2 frequency along its entire length, results in much weaker canyon currents (1.5 cm s^{-1} vice 8 cm s^{-1}) and virtually no generation of internal tides along the canyon rims. A minor increase in floor slope (from 1.55° to 2.29°), such that the canyon floor is initially critical at the foot and then supercritical near the canyon head, results in much stronger currents near the

94

foot, but much weaker currents shoreward of the canyon head due to backward reflection of the internal tide energy in the upper reaches of the canyon (Figure 54).

The 1.55° floor slope is used to investigate the effects of canyon width on the internal tides. Widening the canyon floor toward the canyon foot, which increases the area available for internal tide generation, results in a significant increase in the amount of internal tide energy which propagates up the canyon (Figure 59). For a given floor width, canyons with steeper walls are observed to have more energetic internal tides, perhaps due to the conversion of cross-canyon motion to vertical motion.

The vertical motions associated with the internal tide near the head of the model canyon result in "tidal pumping" of cold water from the canyon onto the shelf (Figure 49), as suggested by Shea and Broenkow (1982). Relatively strong internal tide generation is observed to occur along the canyon rims near the head, with subsequent propagation of internal tides in the alongshore direction (Figure 50). Upward propagation of internal tide energy from the canyon rims, and the subsequent reflection of this energy from the sea surface, results in amplification of surface currents near the canyon head. This mechanism for enhancement of surface tidal currents may explain observations of stronger semidiurnal surface currents above the head of MSC (Petruncio, 1993; Paduan et al., 1995).

Intensification of internal tide energy along the southern wall of the model canyons lends support to the theory of bottom-trapped internal waves (Rhines, 1970). In this case, the sloping bottom against which the internal tides are trapped is the southern wall of the canyon. This south-side intensification of the internal tide appears to result in stronger generation of internal tides along the southern rim near the canyon head. Trapping due to rotational effects was also observed in the alongshore-propagating internal tides, which propagate as internal Kelvin waves north of the canyon but are more diffuse on the south side.

V.   CONCLUSIONS AND RECOMMENDATIONS

In the portion of Monterey Submarine Canyon which lies inside Monterey Bay, internal tide energy propagates upward and shoreward, nearly parallel to the Canyon floor. The region of strongest motion is defined as a beam approximately 150-200 m thick, centered approximately 150 m above the canyon floor. Current oscillations within the beam are anisotropic, with much greater variance in the along-canyon direction than in the cross-canyon direction. Typical amplitudes associated with the along-canyon semidiurnal current oscillations in the beam are 15-20 cm s^{-1}, and are not expected to exceed the calculated group velocity of 55 cm s^{-1}.

Internal tide propagation in MSC is reasonably well described by linear theory in deeper parts of the canyon. Modification of rotational effects due to the presence of the Canyon walls can be accounted for by setting the Coriolis term in the dispersion relation and polarization relations to zero. This practice results in good agreement between theoretical and observed density and velocity fields, and between theoretical and observed energy propagation paths. Near the Canyon head, the internal tide becomes nonlinear, with strong isopycnal and current oscillations present throughout the water column and greater potential energy than kinetic energy.

The fact that the average slope of the Canyon floor is critical for the M2 frequency suggests that internal tide generation may occur along the Canyon floor. Observations of near-bottom currents were limited by the range of the downward-looking VM-ADCP over deeper parts of the Canyon, and by noise attributed to side-lobe reflections from the narrow canyon walls closer to the Canyon head. However, moored current meter measurements reveal strong (20-30 cm s^{-1}) current oscillations approximately 2 m above the Canyon floor. The near bottom current oscillations have significant semidiurnal and diurnal components. Further knowledge about the vertical structure of the internal tide in MSC is desirable, especially in the lower half of the water column where the internal tide is most energetic.

A process study of semidiurnal (M2) internal tide propagation in submarine canyons is conducted with the Princeton Ocean Model. The experiments indicate realistic internal tide generation, including shoreward and seaward propagation of energy along M2 characteristics emanating from the shelf break and the foot of an idealized submarine canyon. Idealized bathymetry is used in order to study of the effects of various canyon shapes on the strength of canyon internal tides. Minor changes in floor slope are observed to have a significant impact on the strength of the internal tides propagating shoreward in the canyon. Baroclinic tidal currents in

the canyon are strongest with a canyon floor slope that is subcritical for the forcing frequency (M2) near the canyon foot and critical near the canyon head. The width of the canyon floor at the foot of the canyon is also important. In the absence of other topographic features seaward of the canyon, the width of the floor at the canyon foot determines the area available for the generation of internal tides. A wider foot facilitates a greater transfer of energy from the barotropic to the baroclinic tides, hence more internal tide energy propagating up the canyon.

Despite the use of simplified bathymetry and tidal forcing, the numerical simulations reproduce several features of the internal tide which are in qualitative agreement with observations in MSC, including upcanyon energy propagation, bottom-intensified currents above the canyon floor, internal tide generation along the rim of the canyon, and "tidal pumping" of dense water up onto the shelf near the canyon head. The fact that these features are observed in the presence of simplified bathymetry and forcing is encouraging, and lends hope to the future use of this model to simulate internal tide propagation with more realistic bathymetry and forcing.

The baroclinic tidal currents in the model canyon are roughly 50% weaker than those observed in MSC, but this is expected for several reasons:

- Only one tidal constituent, M2, is used in the specification of the model barotropic tide. The use of other semidiurnal constituents would presumably result in a spring-neap cycle in the strength of the internal tides propagating shoreward in the canyon. Since the values of the Coriolis parameter specified in the model result in inertial periods of 20.2- 19.9 hours, the use of diurnal constituents would not be expected to affect the strength of the freely propagating internal tides (since the diurnal constituents would be subinertial), but could contribute to stronger currents near the floor and rims of the model canyon.

- Seaward of MSC, there are multiple sites available for internal tide generation by the cross-shore component of the barotropic tide (Figures 30 and 31). The amount of internal tide energy entering MSC is therefore probably greater than the amount entering the model canyon. The use of simplified model bathymetry facilitates a sensitivity study of various canyon shapes, but results in fewer sites available for internal tide generation.

- The strength of the internal tides generated at a given site is affected by the depth of the generation site, since the depth affects the strength of the barotropic forcing. For a given cross-shelf barotropic mass flux, the barotropic current speeds will be greater above a shallow shelf break than a deeper one. The complicated shape of the shelf break in the

vicinity of Monterey Bay may result in propagation of internal tide energy into MSC from shallower generation sites. These internal tides would be more energetic than the internal tides generated at the foot of the model canyon.

- The barotropic semidiurnal tidal currents seaward of Monterey Bay are expected to have a significant alongshore component (Figure 10). The internal tides generated by the alongshore component are expected to be more energetic than those generated by the cross shore component, and could make a significant contribution to the internal tide energy levels within MSC.

- The density field in the model domain is simplified, in that it is horizontally homogeneous. The presence of upwelling plumes, fronts, and eddies near Monterey Bay are expected to modify the propagation paths of internal tide energy, and could serve to focus additional energy into MSC.

Modeling studies of tidal circulation in Monterey Bay will require accurate representation of the barotropic forcing, vertical and horizontal variations in density, and bathymetry. The steep bathymetry in the vicinity of the Bay will probably require some smoothing, but the Canyon floor slope, the depth of the shelf break, and the shapes of the likely offshore generation sites (Smooth Ridge and Steep Ridge) should be reproduced as accurately as possible. Accurate resolution of the bathymetric features in the vicinity of Monterey Bay will probably require horizontal resolution of 0.5-1.0 km. If POM or other models with vertically stretched coordinates are used, the horizontal and vertical resolution will need to be very fine in order to prevent excessive errors caused by pressure gradient truncation error. Sensitivity studies will need to be conducted in order to investigate the effect of varying bottom friction and sub-grid scale mixing parameterizations, such as horizontal and vertical kinematic viscosity and diffusion, on the strength of the modeled internal tides.

Monterey Bay is an ideal location for the continued study of internal tide generation, propagation, and dissipation. There remains a need for the collection of hydrographic and velocity data with high spatial and temporal resolution, and the direct measurement of dissipation in the energetic regions along the Canyon floor, walls, and rim. These measurements are required to improve our understanding of tidal hydrodynamics in the presence of complex bathymetry, and to test the performance of ocean circulation models in forecasting tidal circulation in the littoral.
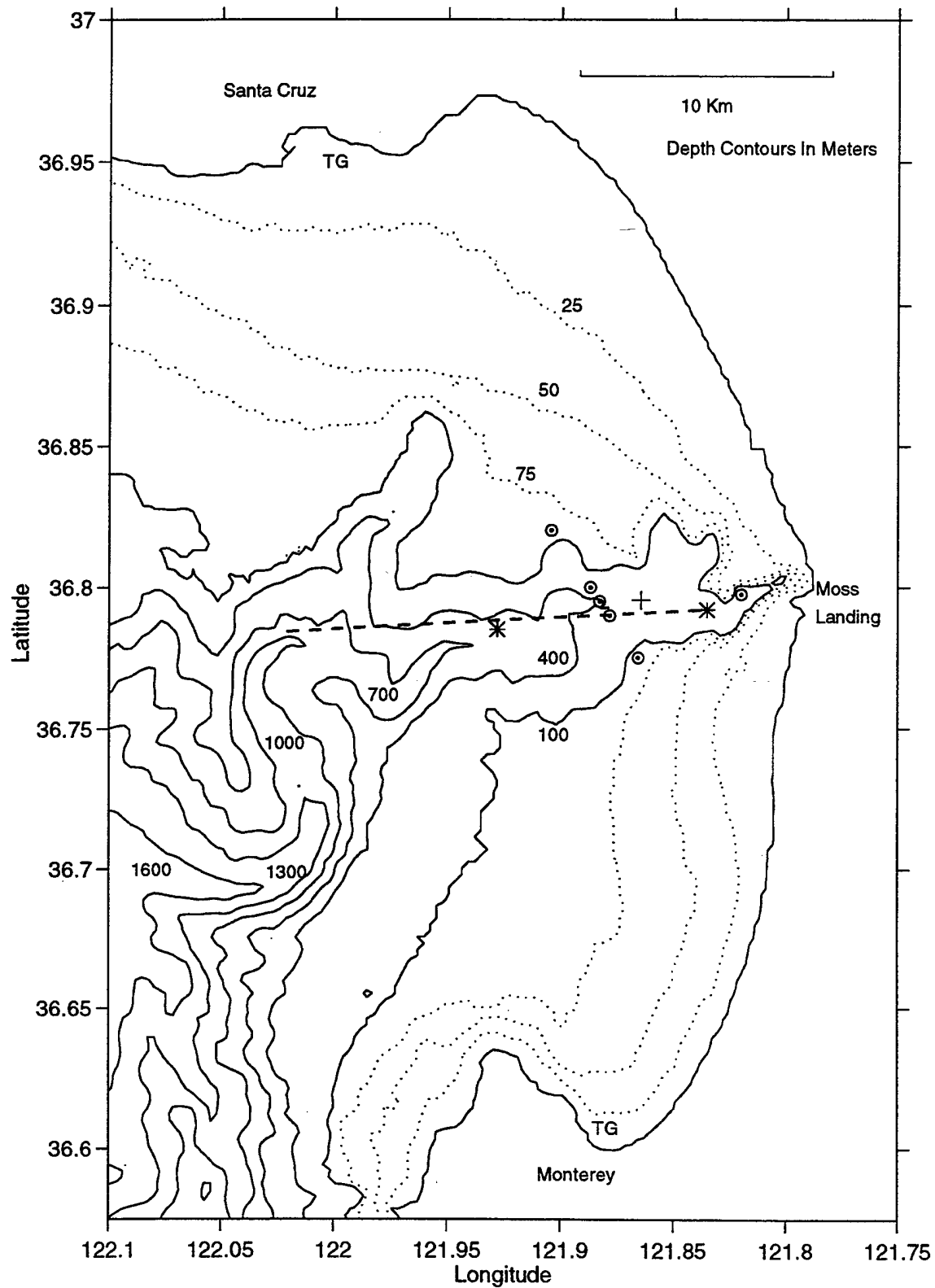
Figure 1. Monterey Bay Bathymetry and ITEX Data Sources. Symbols denote CTD stations for ITEX1 (*) and ITEX2 (o), the S-4 mooring (+), and tide gauges (TG). The dashed line shows the ITEX1 XBT track, and bathymetric contours are shown as dotted and solid lines.
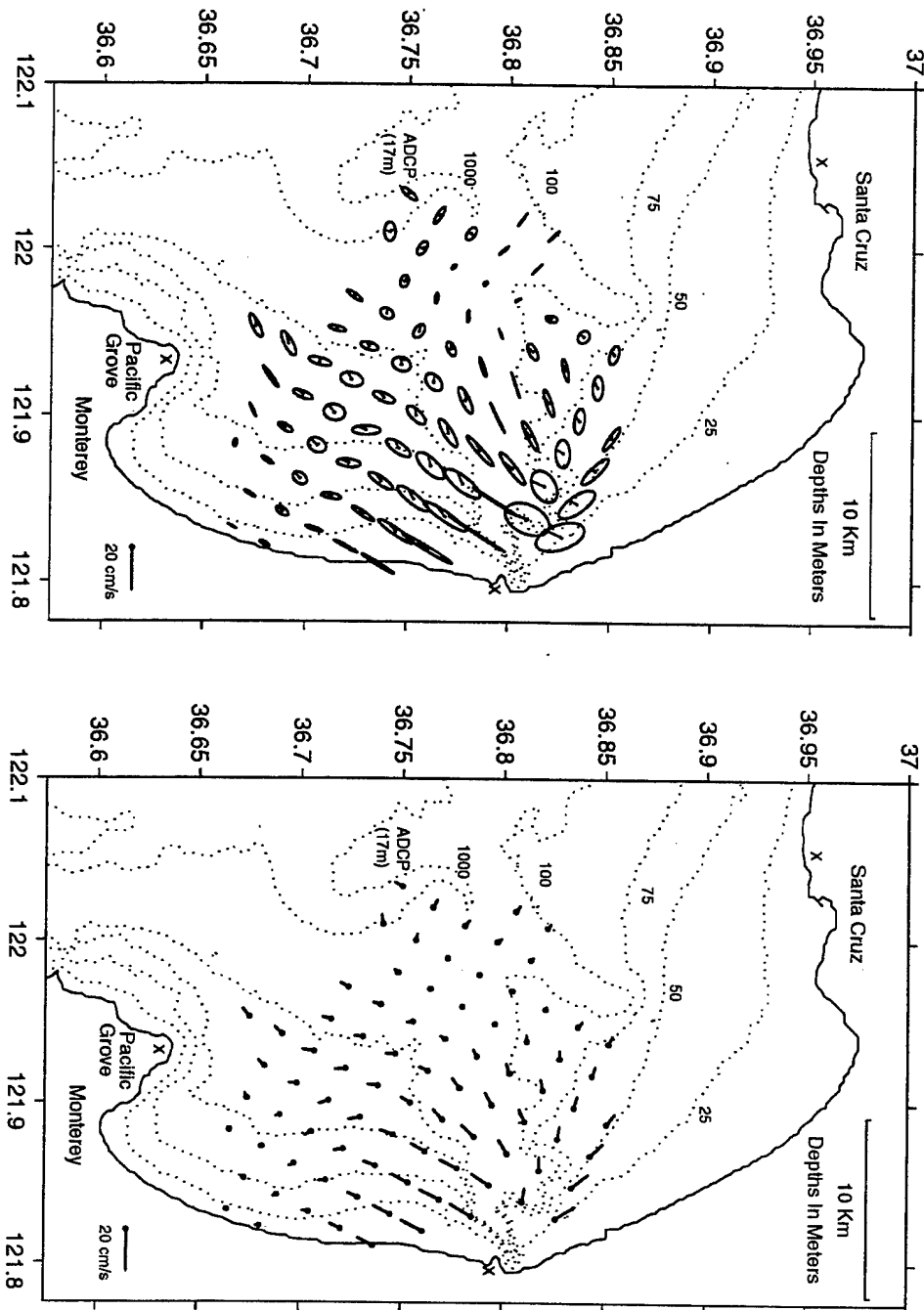
Figure 2. HF-radar Derived Semidiurnal Tidal Currents. M2 tidal current ellipses for September 1992 (left panel) are shown with lines extending out from the center to represent the direction towards which the current flows and its speed at the time of high M2 sea level. Current flow 3 hours prior to high M2 sea level (right panel) is also shown with flow directed away from the dots, which mark the centers of the HF radar bins.

102

Figure 3. Internal Wave Propagation and Subcritical Bottom Reflection. The downward directed group velocity vector, c_g, and an upward directed wavenumber vector, κ, associated with an internal wave (a) and the same vectors after subcritical bottom reflection (b), during which wavenumber enhancement ($\kappa' > \kappa$) and group velocity decrease ($c_g' < c_g$) take place with equal projections of κ and κ' onto the plane of the bottom slope (After Phillips, 1977).

103

Figure 4. First Vertical Modes Over Flat and Sloping Bottoms. The panels on the left depict the vertical structure of a 1st mode internal wave, with constant N, over a flat bottom. Horizontal velocity maxima exist at the surface and bottom, and are 180° out of phase. Vertical velocity is maximum at mid-depth. Solutions for the 1st vertical mode over a subcritical bottom slope ($\gamma = 0.03$, $c = 0.037$, $\omega = 1.405 \times 10^{-4}$ s^{-1}, $f = 8.726 \times 10^{-5}$ s^{-1}, $N = 3 \times 10^{-3}$ s^{-1}) at a location 20 km from the apex of the wedge (right panels; Wunsch, 1969) are also shown with amplification of the wavenumber after reflection from the bottom resulting in bottom-intensified horizontal and vertical velocities.

104
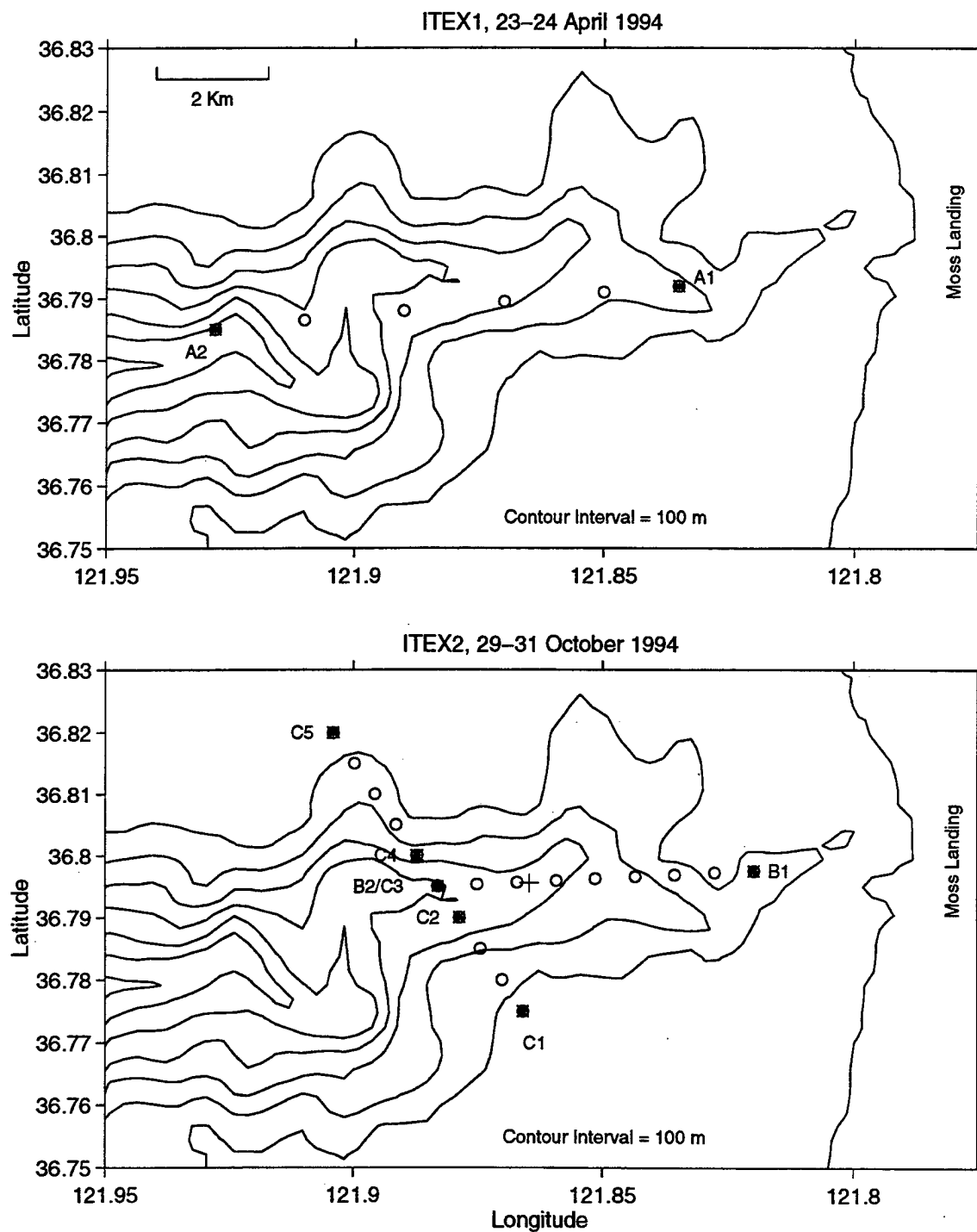
Figure 5. ITEX1 and ITEX2 CTD Stations and VM-ADCP Geographic Bin Locations. Symbols denote CTD stations (*), S-4 mooring location (+), and centers of the geographic bins used to average ADCP currents (o) for ITEX1 (upper panel) and ITEX2 (lower panel).

105
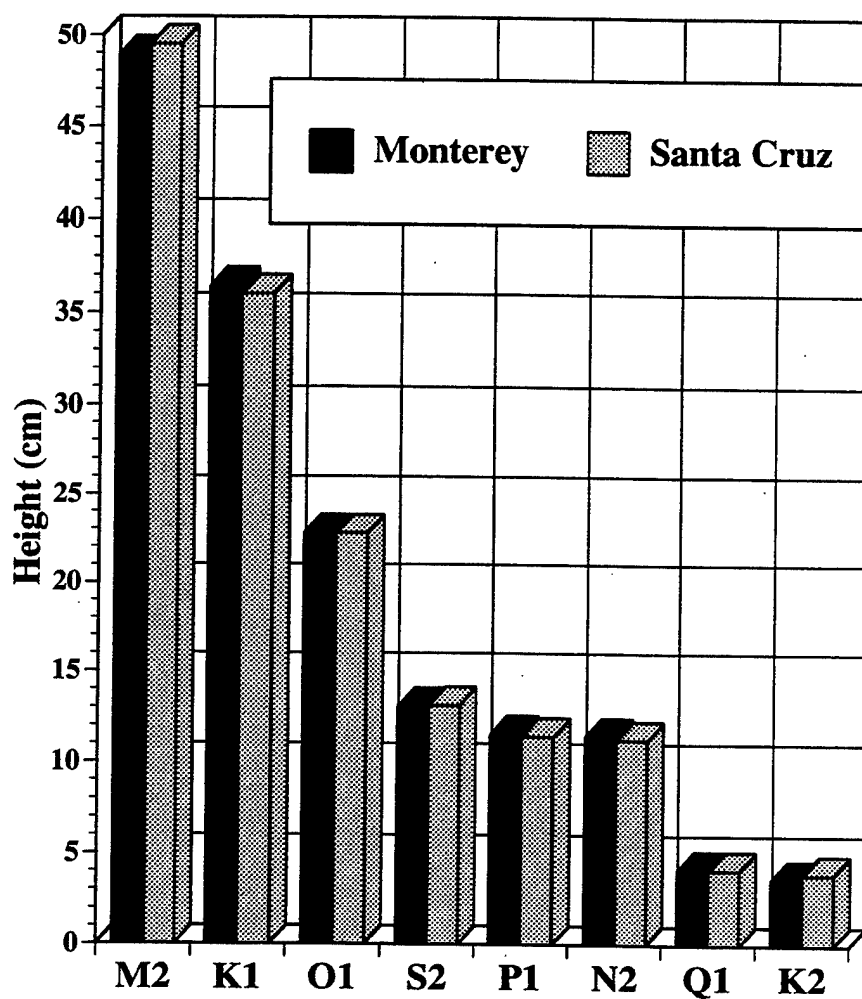
Figure 6. Tidal Height Amplitudes For Monterey and Santa Cruz. Amplitudes of the eight strongest constituents in tidal sea level variations observed in Monterey and Santa Cruz.

106
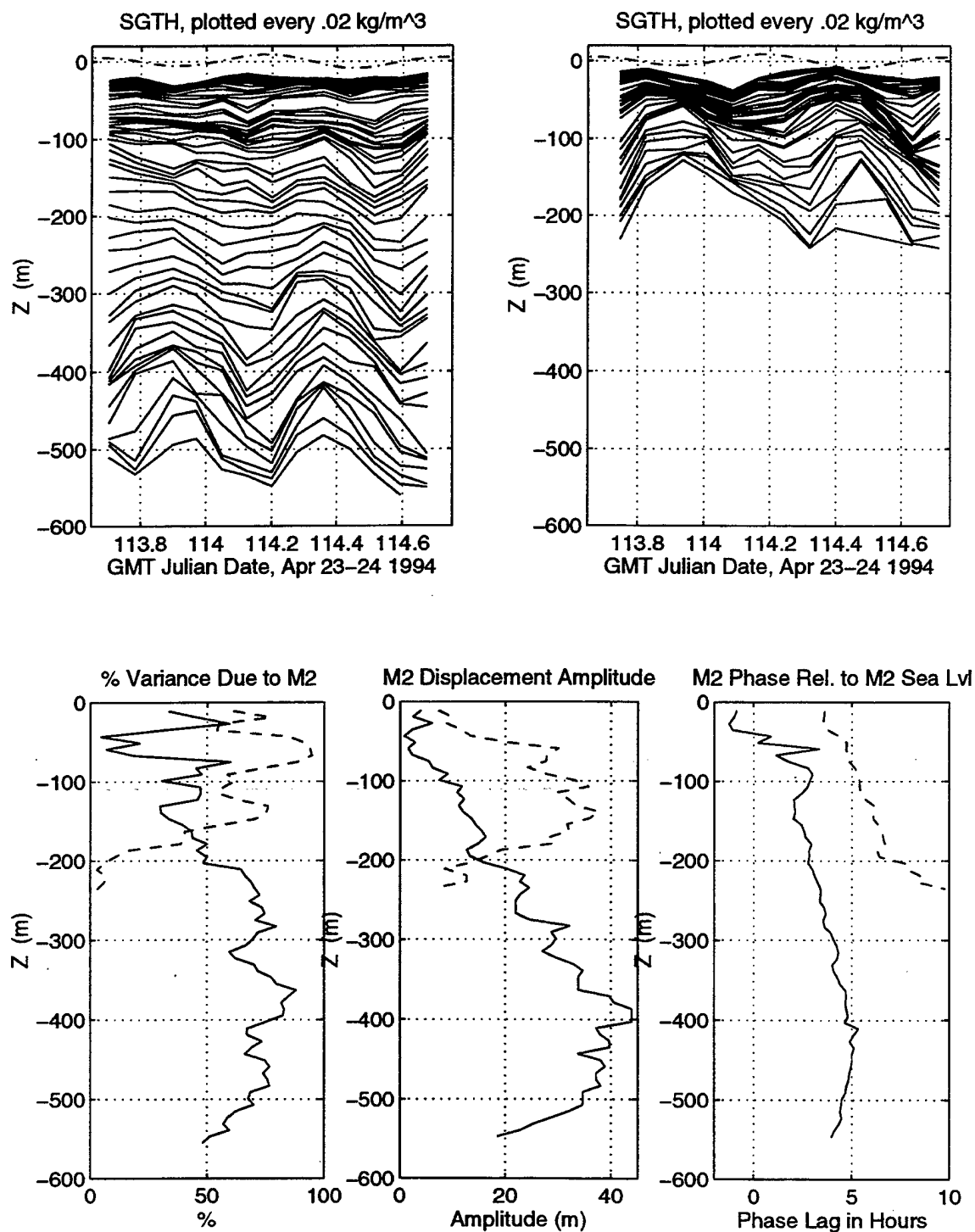
Figure 7. ITEX1 Isopycnal Oscillations and M2 Amplitudes and Phases. Time series of isopycnal depths (solid) and sea level (dashed) during ITEX1 at the deep (upper left) and shallow (upper right) CTD stations. Sea level oscillations were demeaned and exaggerated by a factor of 10. Percent variance described (left), amplitude (center), and phase (right) for the fit of an M2 wave to the data are shown in the lower panels as a function of depth at the deep (solid) and shallow (dashed) stations.

107
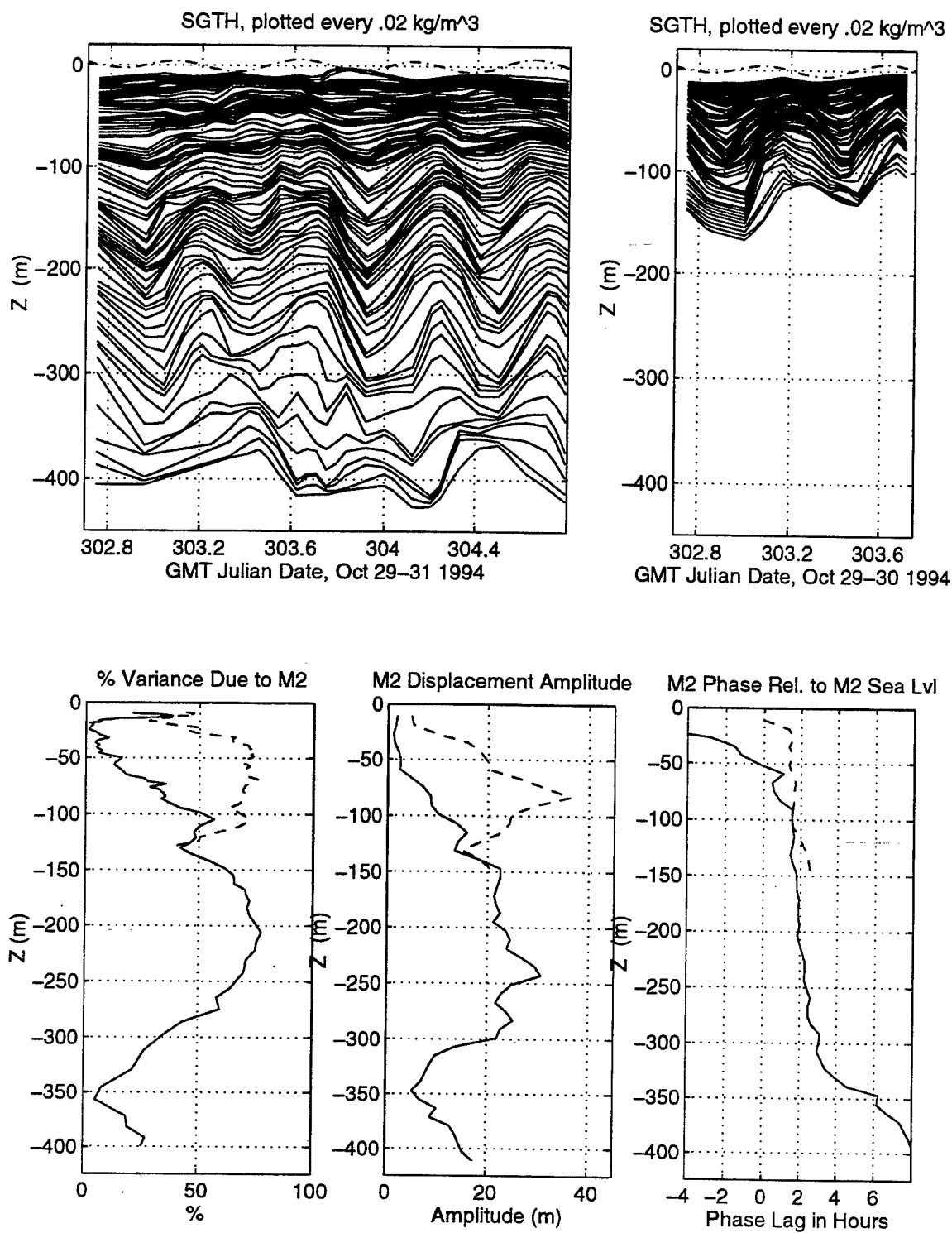
Figure 8. ITEX2 Isopycnal Oscillations and M2 Amplitudes and Phases. Time series of isopycnal depths, sea level, and harmonic analysis results (as in Figure 7) for ITEX2.

108
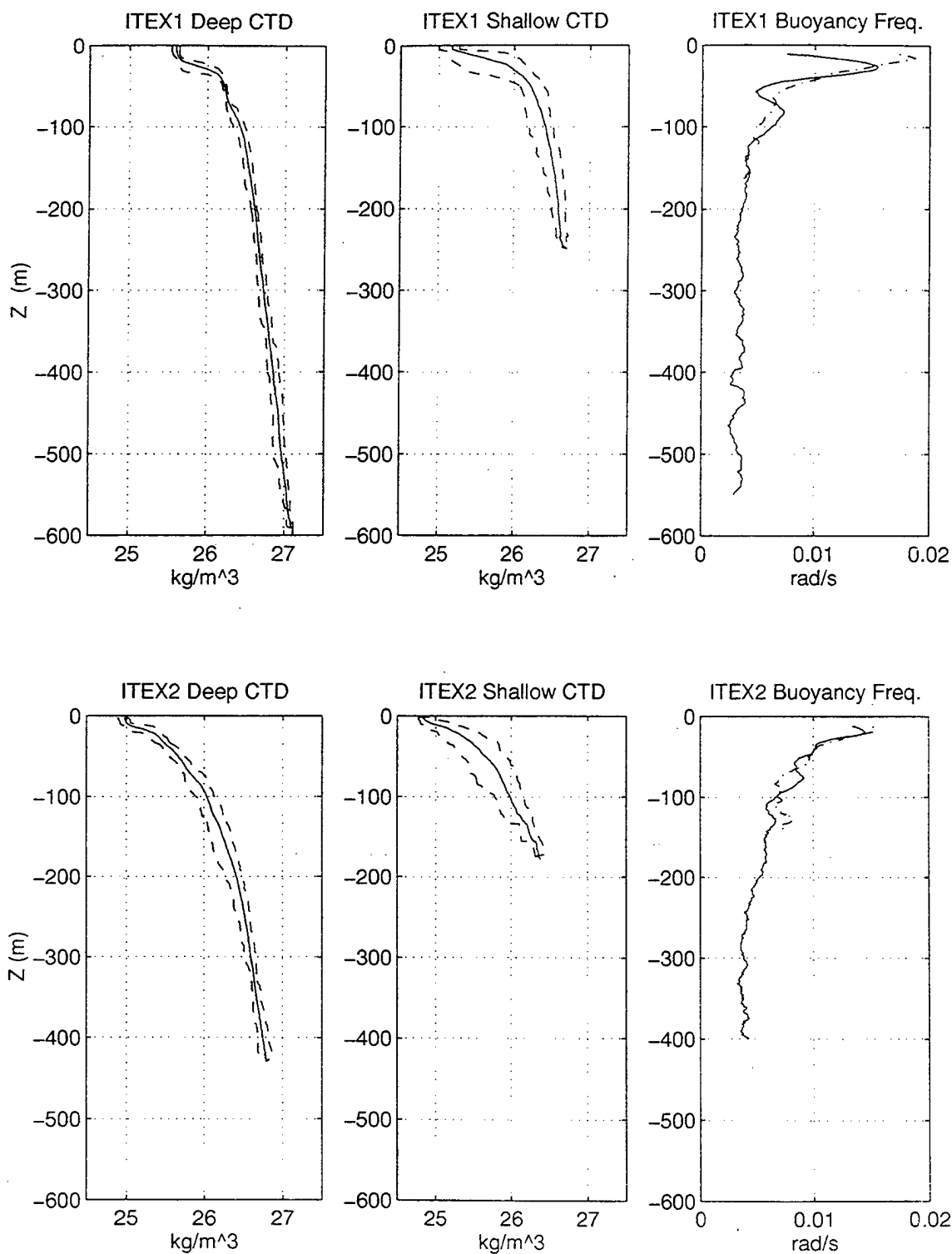
Figure 9. ITEX1 and ITEX2 Density and Buoyancy Frequency Profiles. Average density profiles (solid) and ranges (dashed) from ITEX1 (upper panels) and ITEX2 (lower panels) at the deep (left) and shallow (middle) stations. Right panels depict the average buoyancy profiles at the deep (solid) and shallow (dashed) stations.

109
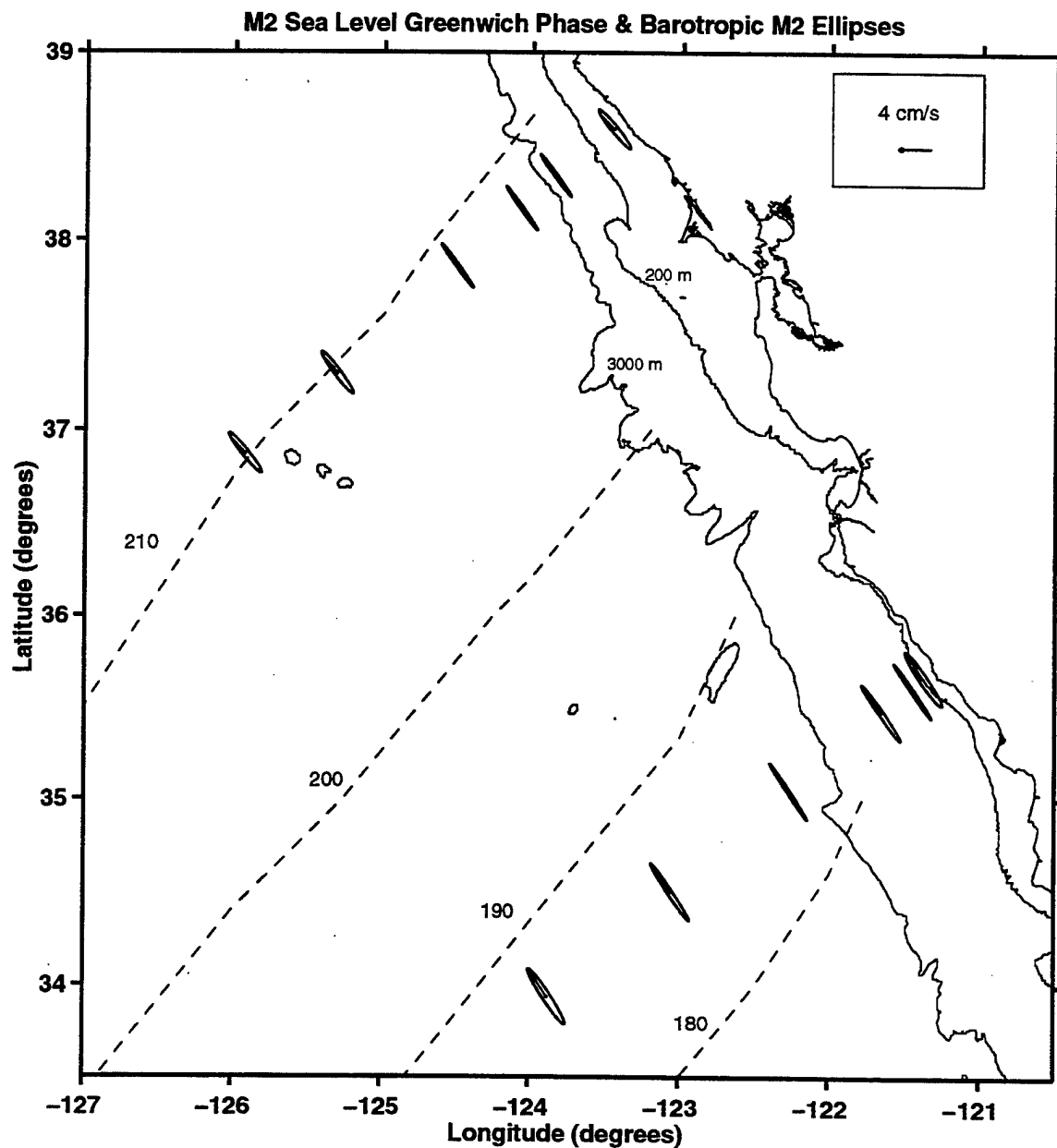
Figure 10. M2 Sea Level Greenwich Phase and Barotropic M2 Tidal Ellipses Off Central California. Dashed lines represent the co-phase lines for M2 sea level, as computed by Schwiderski (1979). The M2 tide propagates northward along the coast. The ellipses represent the barotropic M2 tidal currents modeled by Battisti and Clarke (1982), with phase corresponding to high M2 sea level.

110
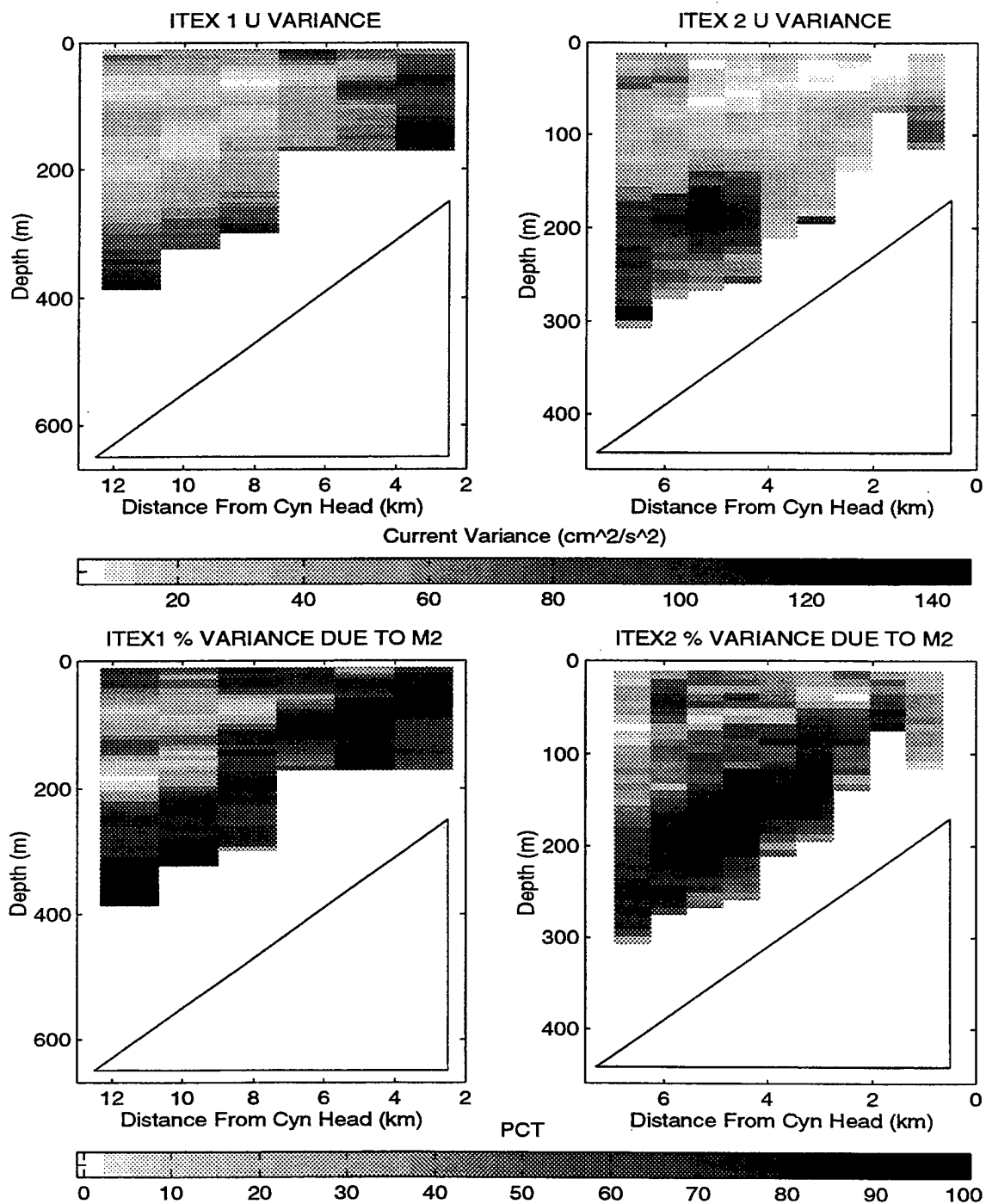
Figure 11. East-West Current Variance and Percent Variance Accounted for by the M2 Wave Fit. Variance of the east-west velocity (upper panels) and the percent variance accounted for by the M2 wave fit (lower panels) computed every 8 m in depth from along-canyon ADCP measurements during ITEX1 (left) and ITEX2 (right). The wedge in each panel represents the approximate depth and slope of the Canyon floor. Variance decrease 2-4 km from the Canyon head in ITEX2 corresponds to the portion of the ship's track that departed from the Canyon axis and passed over the north wall (see Figure 5).

111
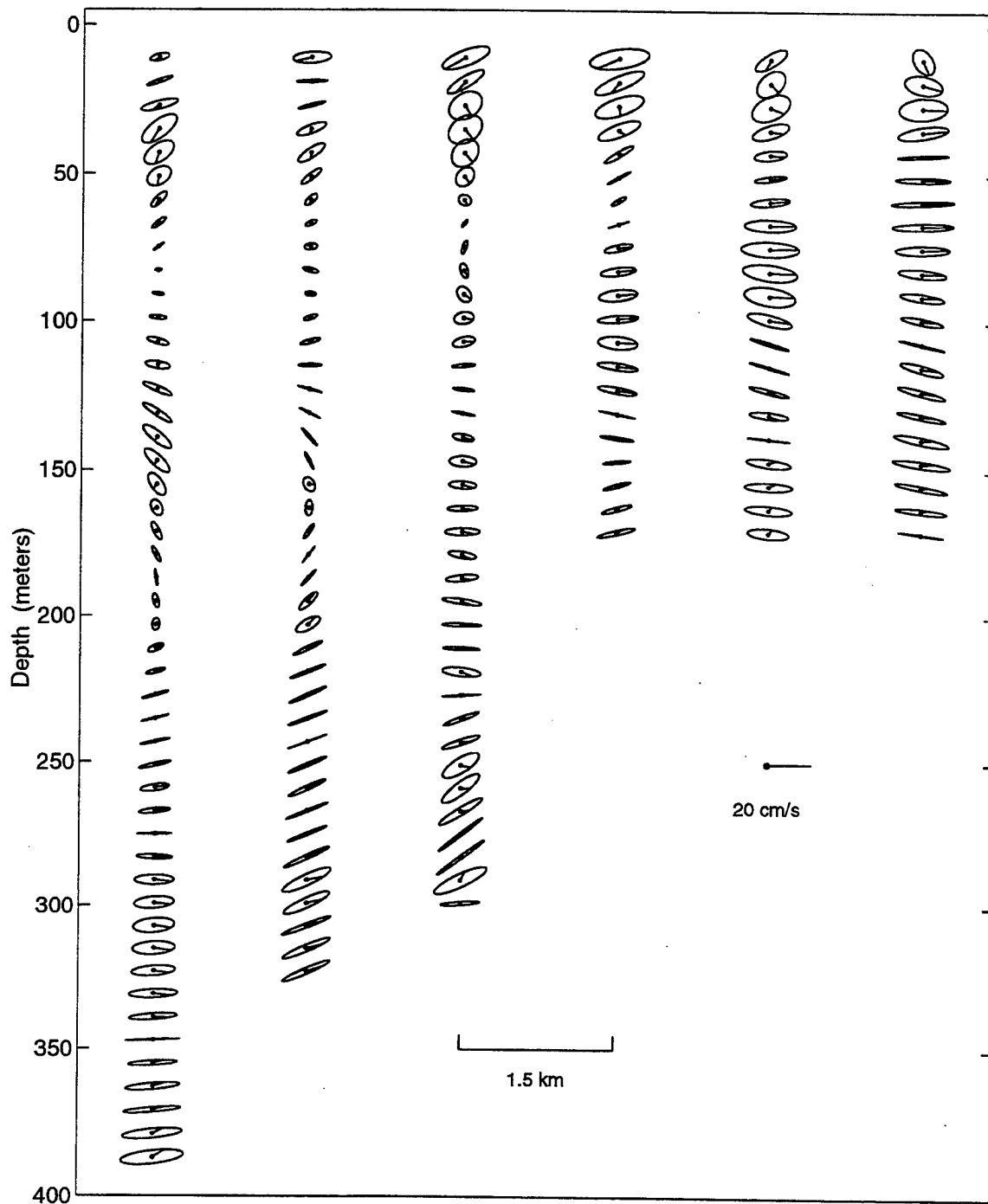
Figure 12. M2 Tidal Ellipses Along-Canyon during ITEX1. *x-z* section of M2 current ellipses (for horizontal velocity) during ITEX1. Ellipses are centered on the ADCP bins and the line extending from the center of each ellipse represents the current direction and speed at the time of high M2 sea level.

112
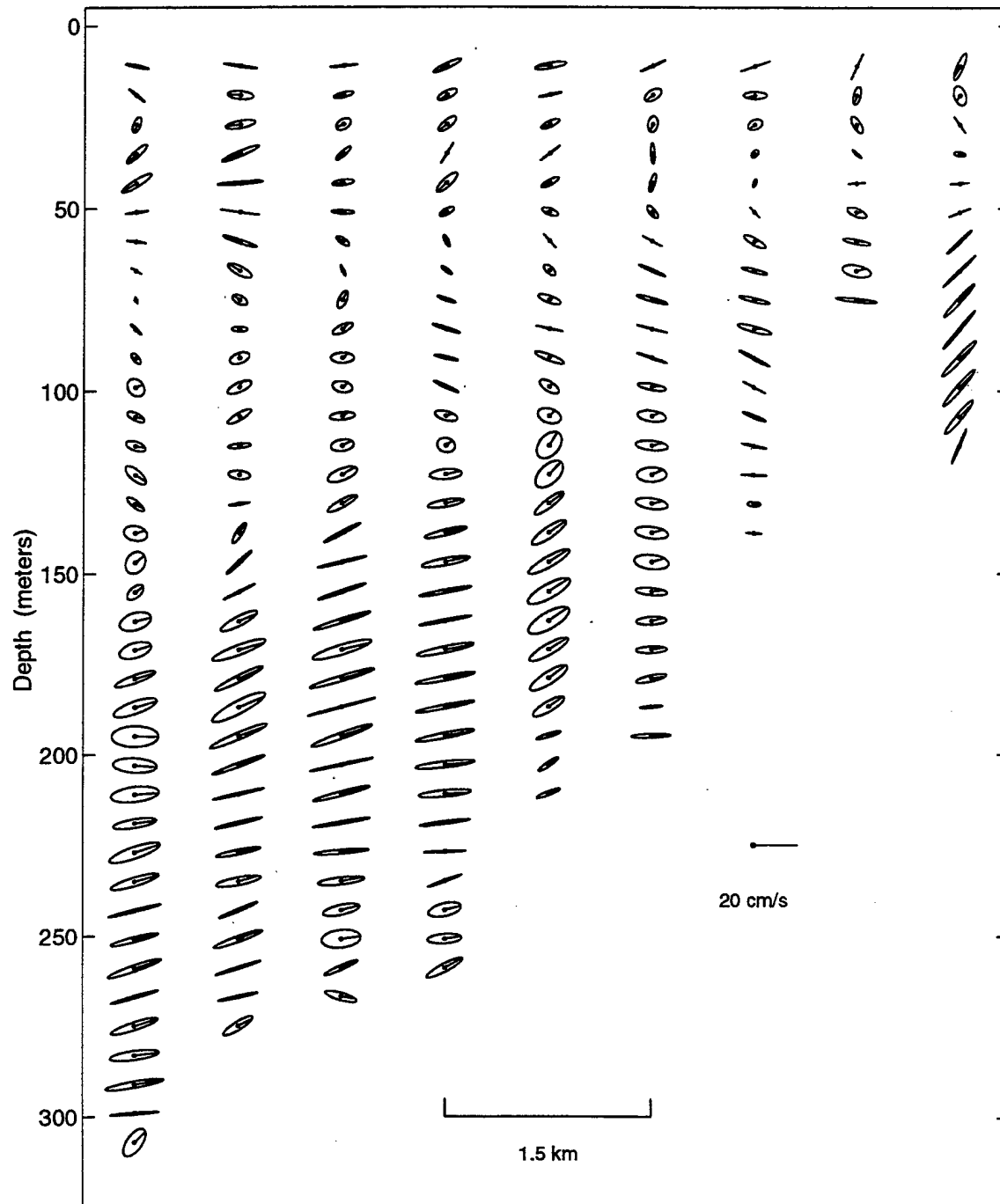
Figure 13. M2 Tidal Ellipses Along-Canyon during ITEX2. As in Figure 12, during ITEX2.

113
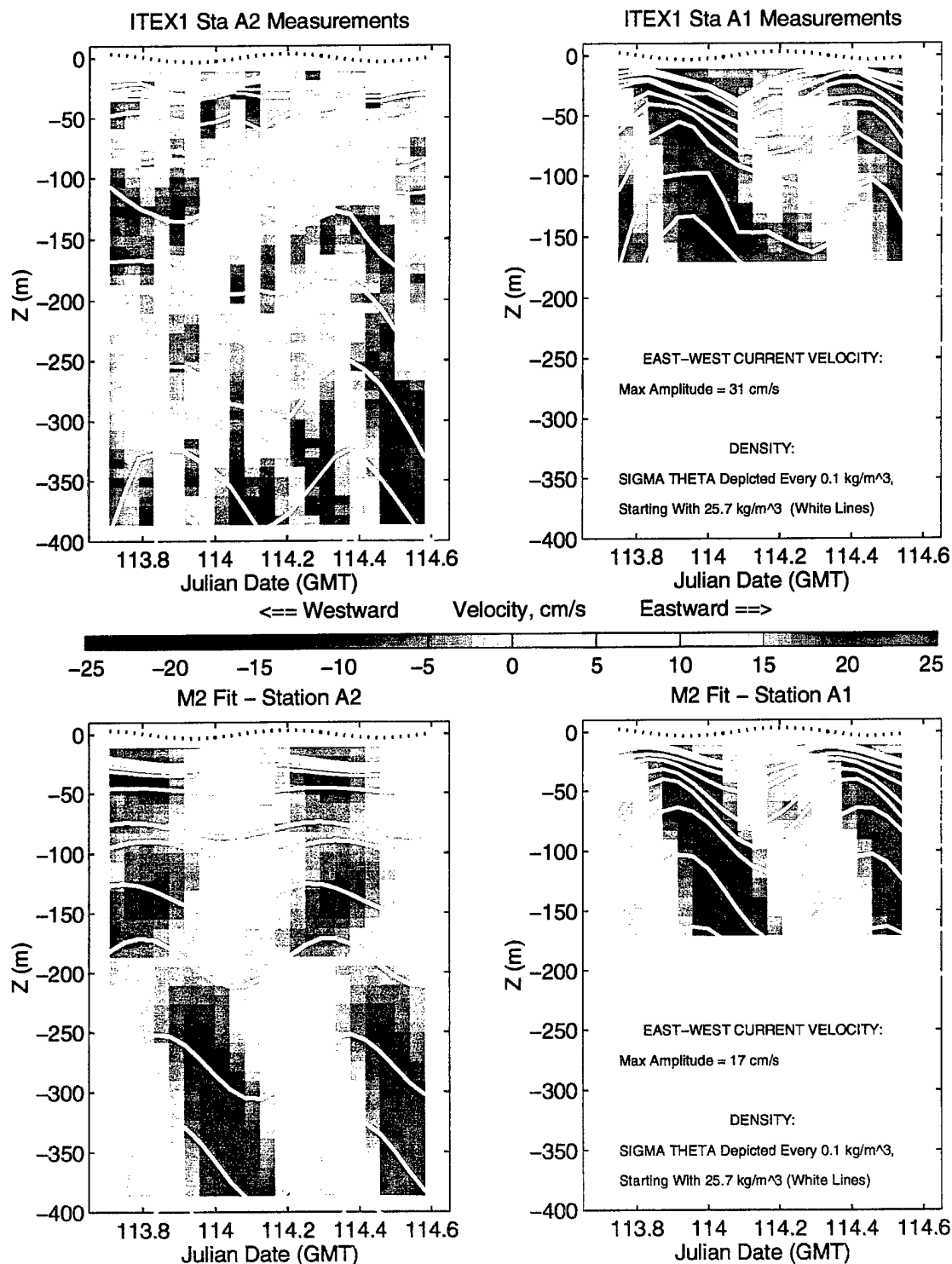
Figure 14. Observed Current and Isopycnal Oscillations and M2 Wave Fits during ITEX1. Time series of the observed (upper panels) and M2-fit (lower panels) east-west velocity component and isopycnal displacements for deep (left) and shallow (right) stations during ITEX1. Demeaned M2 sea level oscillations exaggerated by a factor of 10 (dashed lines) are also shown.

114

Phase Relations For m<0, k>0
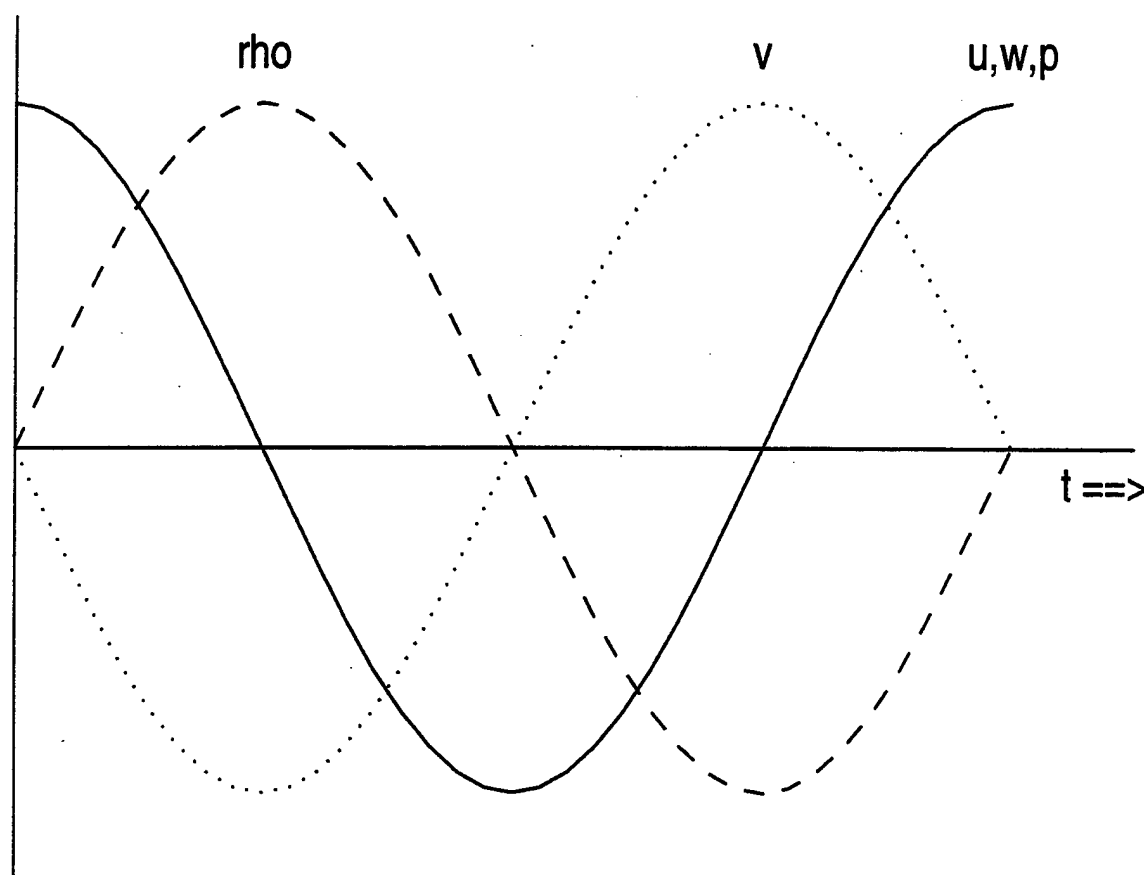
Figure 15. Phase Relationships Between Velocity, Pressure, and Density for a Linear Internal Wave Exhibiting Eastward and Downward Phase Propagation.
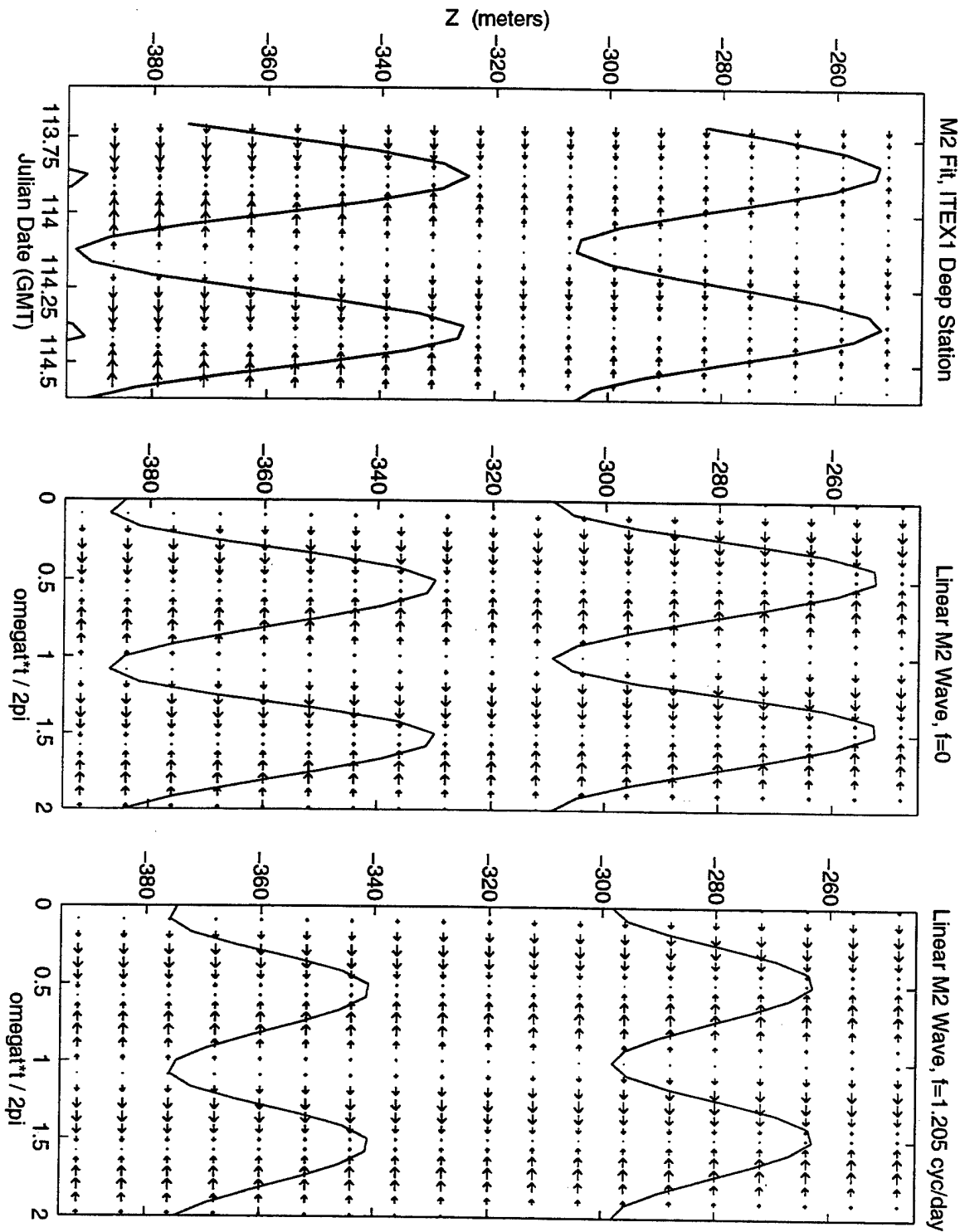
Figure 16. Observed and Theoretical Density and Velocity Fields. Time series of east-west velocity and isopycnal oscillations during ITEX1 at the deep CTD station (left) compared to theoretical fields computed from the polarization relations for internal waves using $L_x = 30$ km, $L_z = 1.2$ km, $N = 3.5\times10^{-3}$ s^{-1}, and $u_o = 10$ cm s^{-1}, with $f = 0$ (middle) and $f = 8.726\times10^{-5}$ s^{-1} (right).
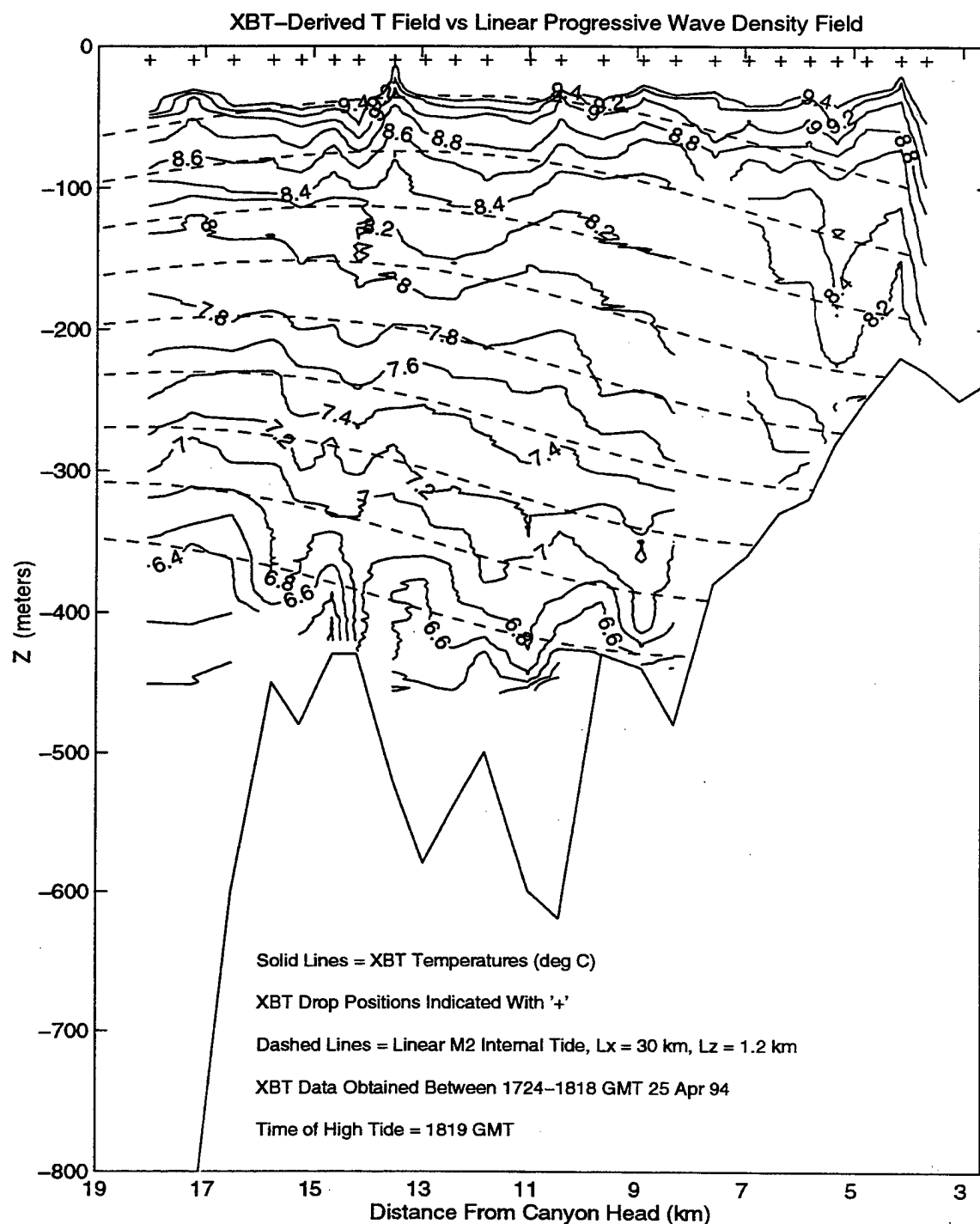
Figure 17. Along-Canyon Temperature Section and Theoretical Isopycnals during ITEX1. Along-canyon isotherms (solid) during ITEX1 from 24 XBT drops compared with theoretical isopycnals computed from the polarization equations for internal waves, using the same wavenumber and buoyancy frequency as in Figure 16, but with $u_o = 15$ cm s^{-1}. The higher u_o amplitude ($u_o = 10$ cm s^{-1} in Figure 16) gives better agreement below 300 m.

117
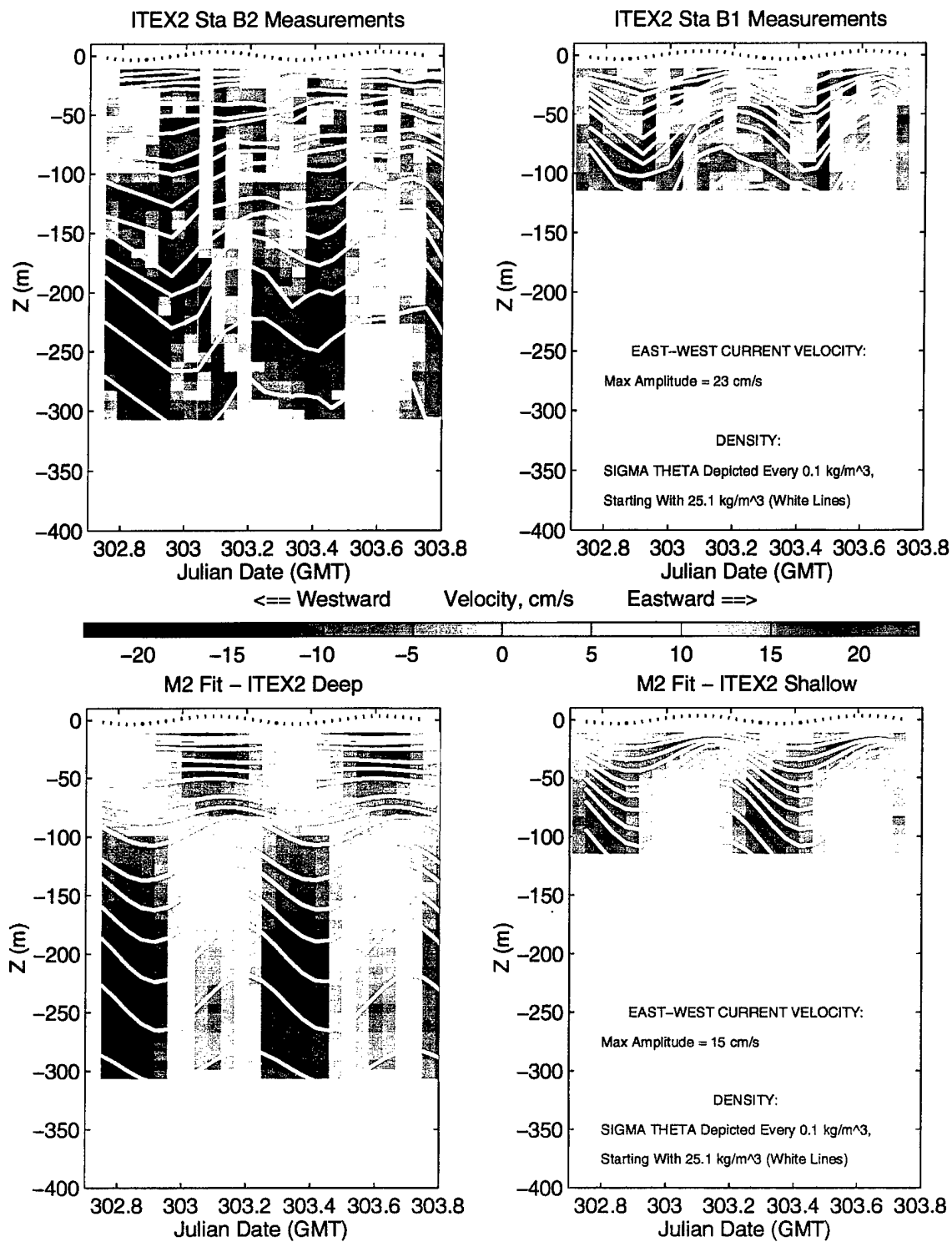
Figure 18. Observed Current and Isopycnal Oscillations and M2 Wave Fits during ITEX2. As in Figure 14 during ITEX2.

118
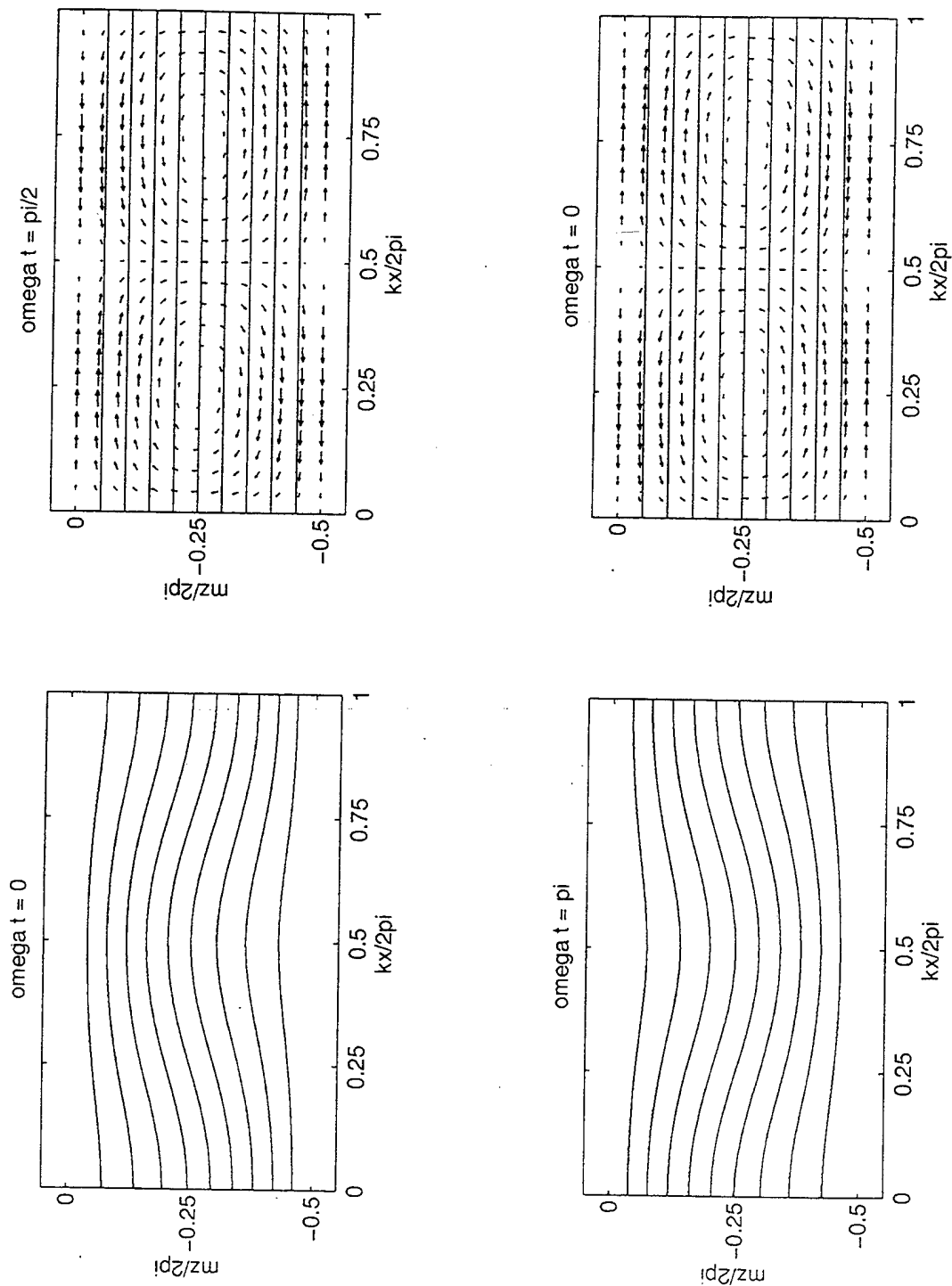
Figure 19. Snapshots of a First Mode, Flat Bottom Internal Seiche. Isopycnals (lines) and east-west velocity (arrows) for an internal wave standing in x and z at four phases of the wave period. Unlike a progressive wave, phase relationships between density perturbations and velocity in a standing wave are spatially dependent.

119
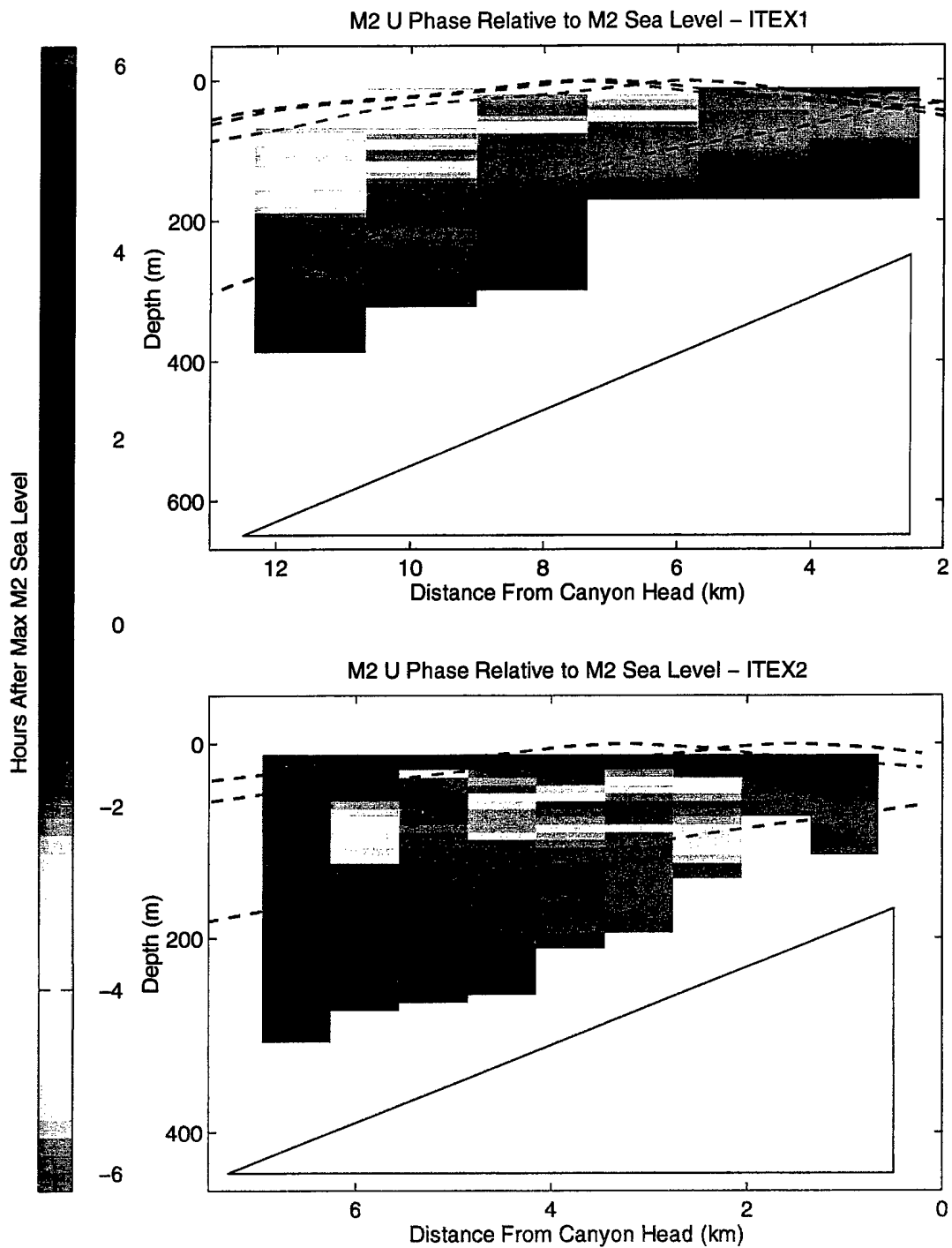
Figure 20. Phase of East-West M2 Velocity Versus Depth at Along-Canyon Geographic Bins. Phase of east-west M2 velocity relative to the phase of M2 sea level for each ADCP bin during ITEX1 (upper) and ITEX2 (lower) with the theoretical M2 characteristics from Figure 31 (dashed lines). Positive phase indicates that maximum shoreward flow occurs after high M2 surface tide.
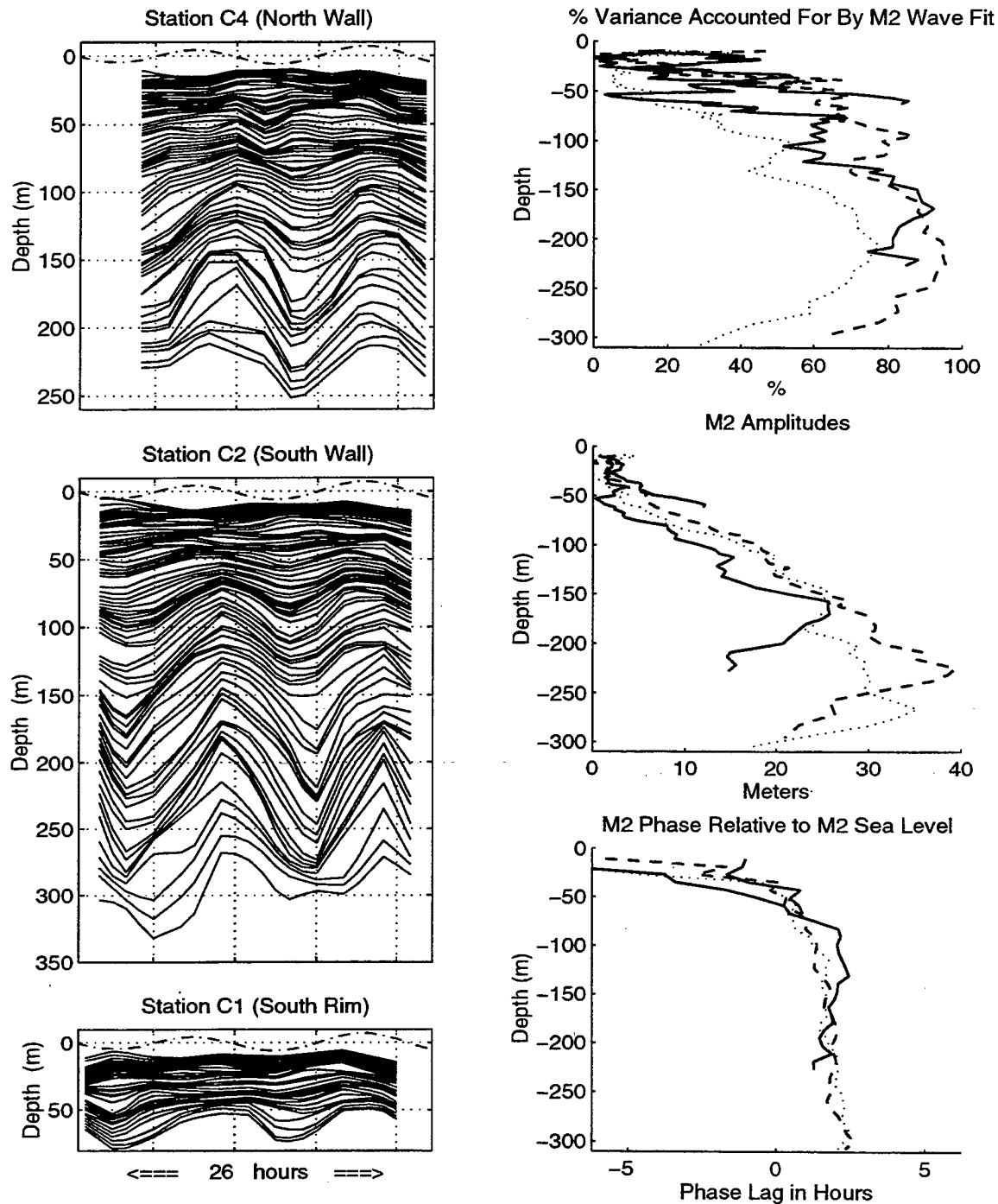
Figure 21. ITEX2 Isopycnal Oscillations and M2 Amplitudes and Phases at Cross-Canyon Stations. Time series of isopycnal depths (solid) and sea level (dashed) during ITEX2 at the north wall (upper left), south wall (middle left), and south rim (lower left) CTD stations during ITEX2. Sea level oscillations were demeaned and exaggerated by a factor of 10. Percent variance described (upper), amplitude (center), and phase (lower) for the fit of an M2 wave are shown in the right panels as a function of depth at the north wall (solid), south wall (dashed), and south rim (dotted) stations. Mid-axis results are depicted in Figure 8.

121
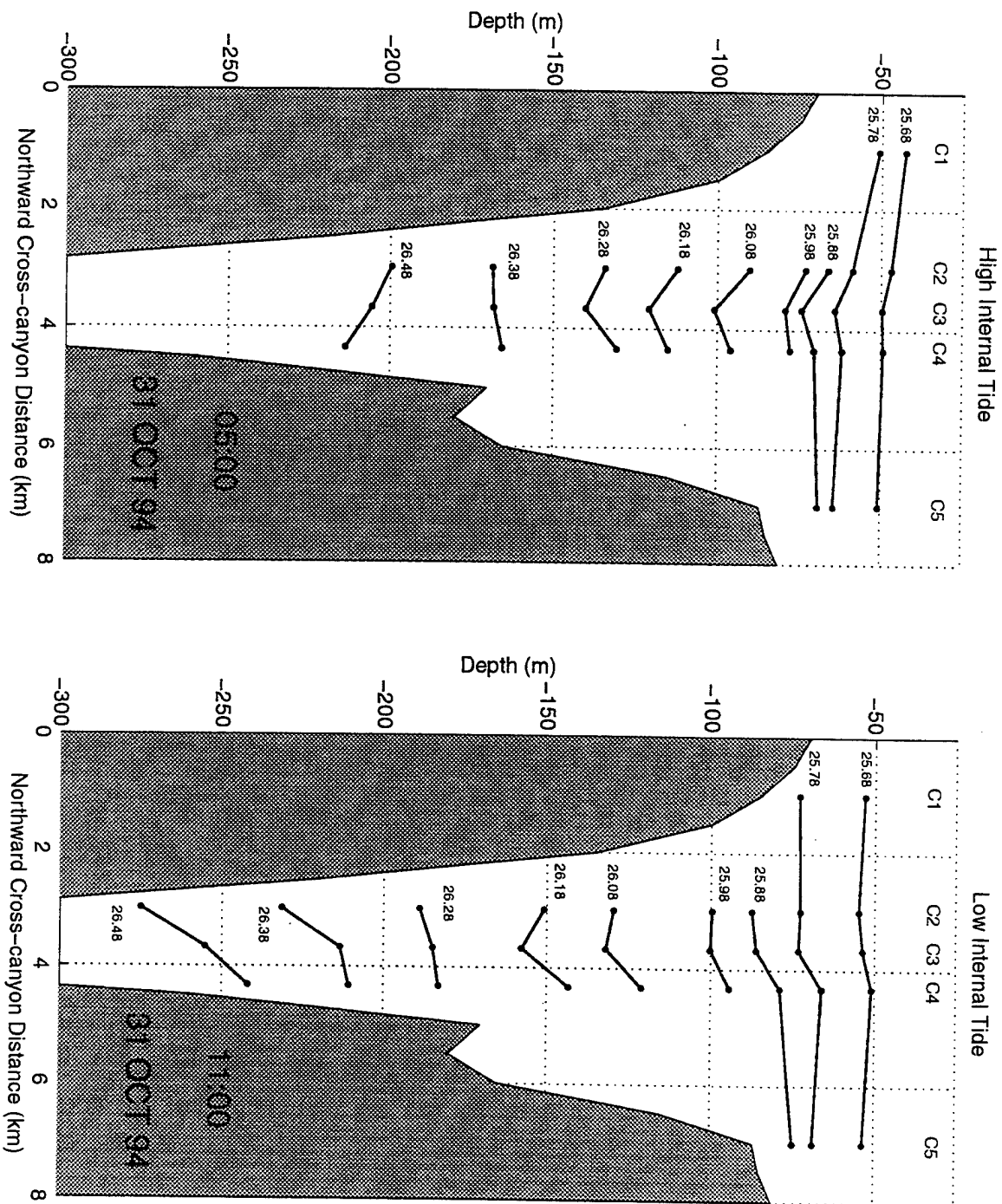
Figure 22. Snapshots of Cross-Canyon Density Field (σ_θ) during ITEX2.

122
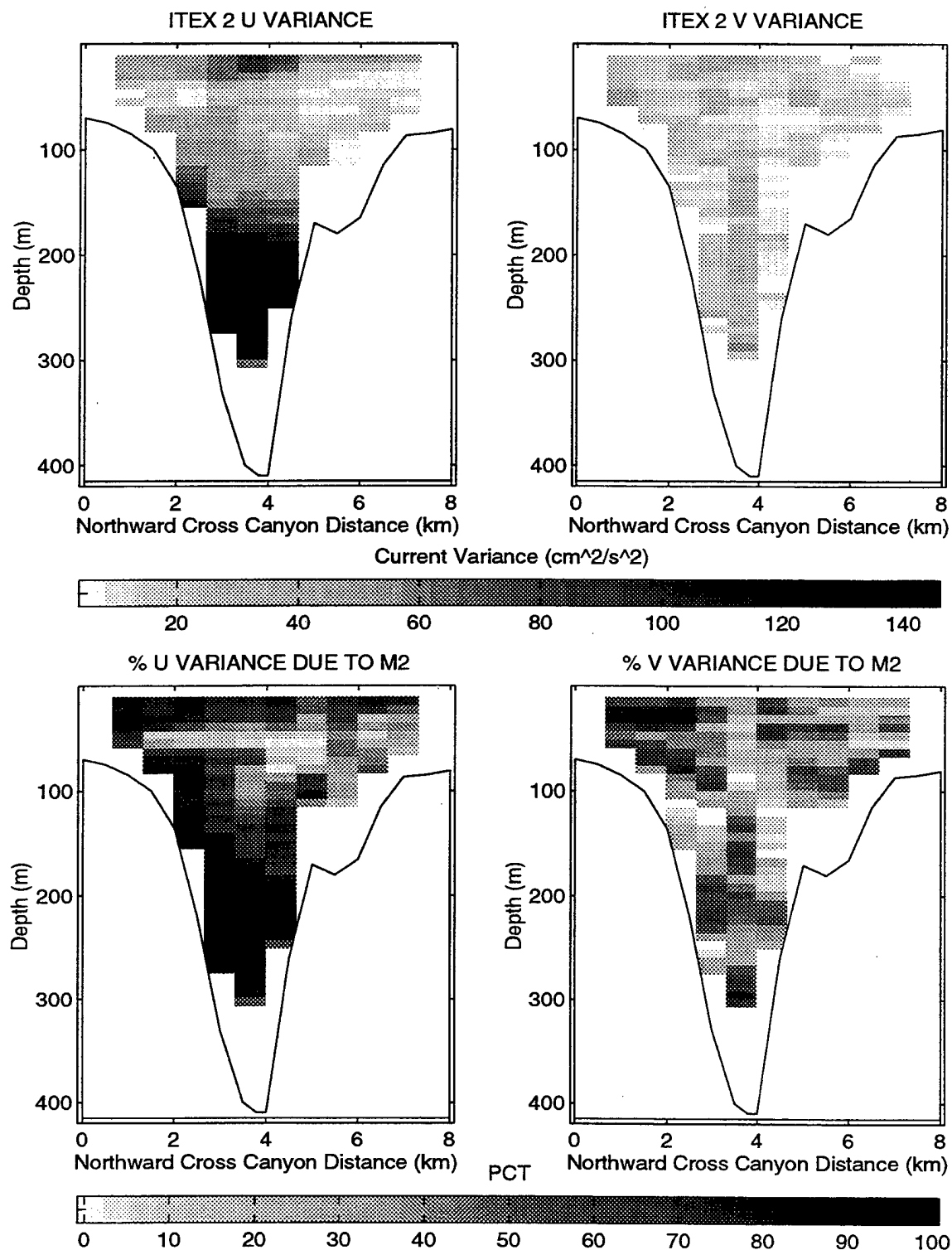
Figure 23. Current Variance and Percent Variance Accounted for by the M2 Wave Fit at Cross-Canyon Geographic Bins. Variance (upper panels) and the percent variance accounted for by the M2 wave fit (lower panels) for east-west (left) and north-south (right) velocity computed every 8 m in depth from cross-canyon ADCP measurements during ITEX2.

123
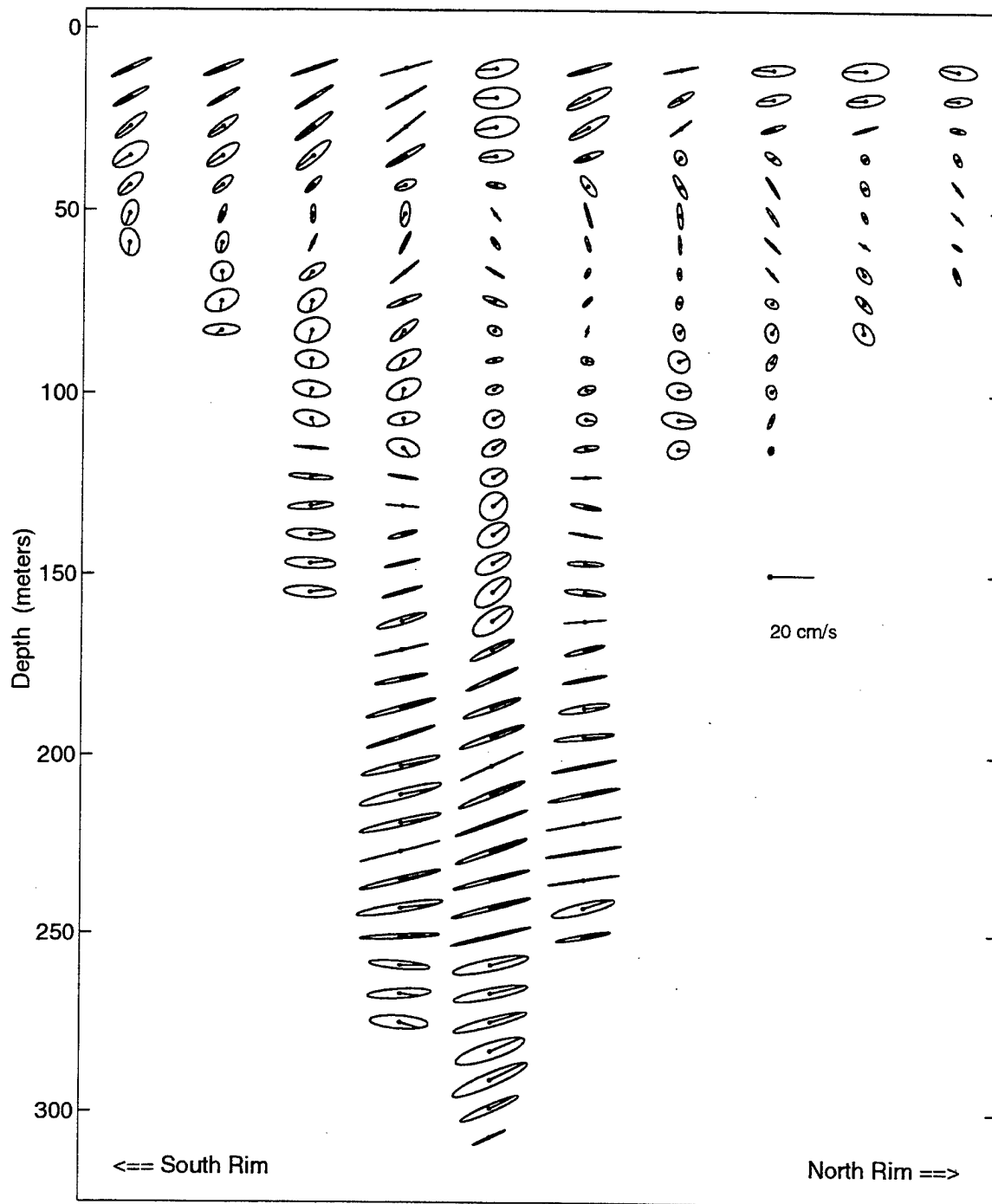
Figure 24. M2 Tidal Ellipses Cross-Canyon during ITEX2. *y-z* section of M2 current ellipses during ITEX2. Ellipses for horizontal velocity are centered on the ADCP bins and the line extending from the center of each ellipse represents the current speed and the direction towards which current flows at the time of high M2 sea level.

124
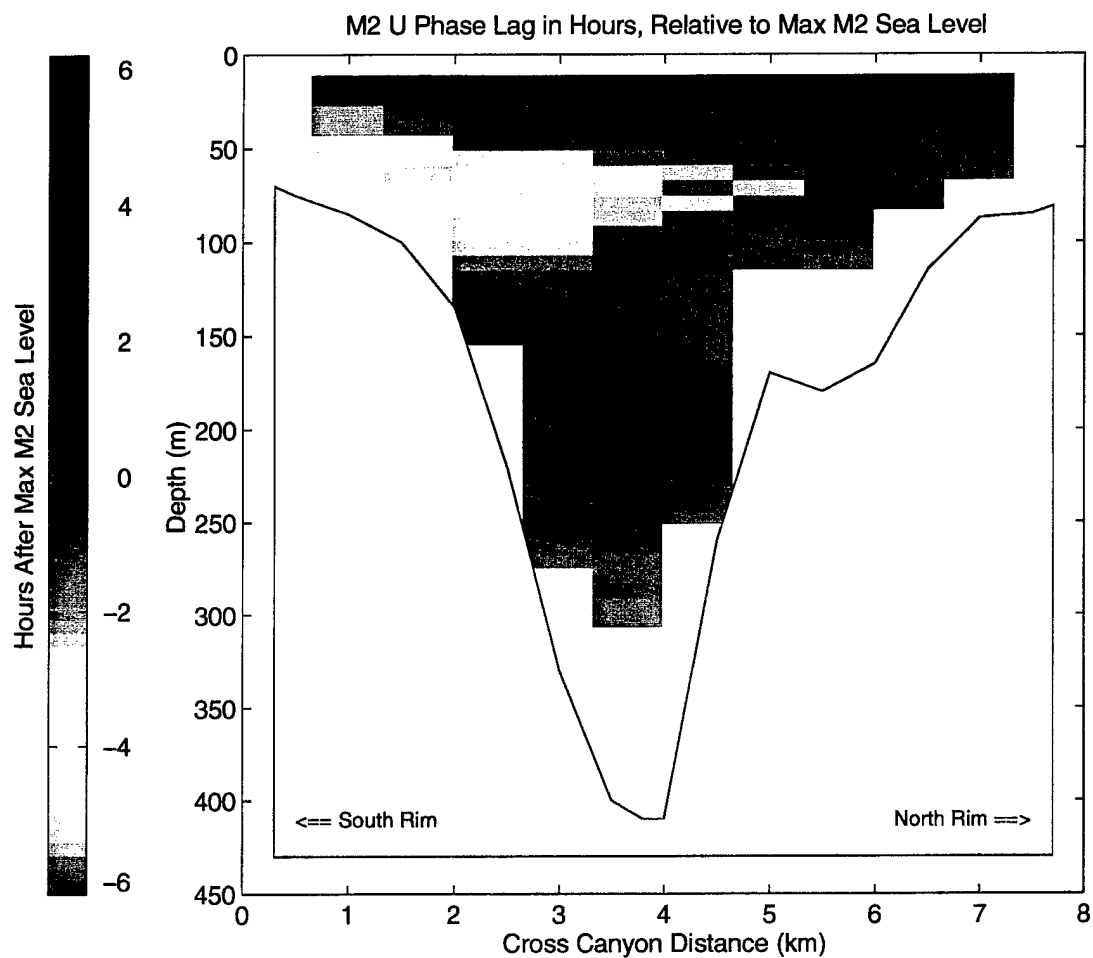
Figure 25. Cross-Canyon Phase of East-West M2 Velocity Versus Depth at Cross-Canyon Geographic Bins. Phase of east-west M2 velocity relative to the phase of M2 sea level for each cross-canyon ADCP bin during ITEX2. Positive phase indicates that maximum shoreward flow occurs after high M2 surface tide.

125
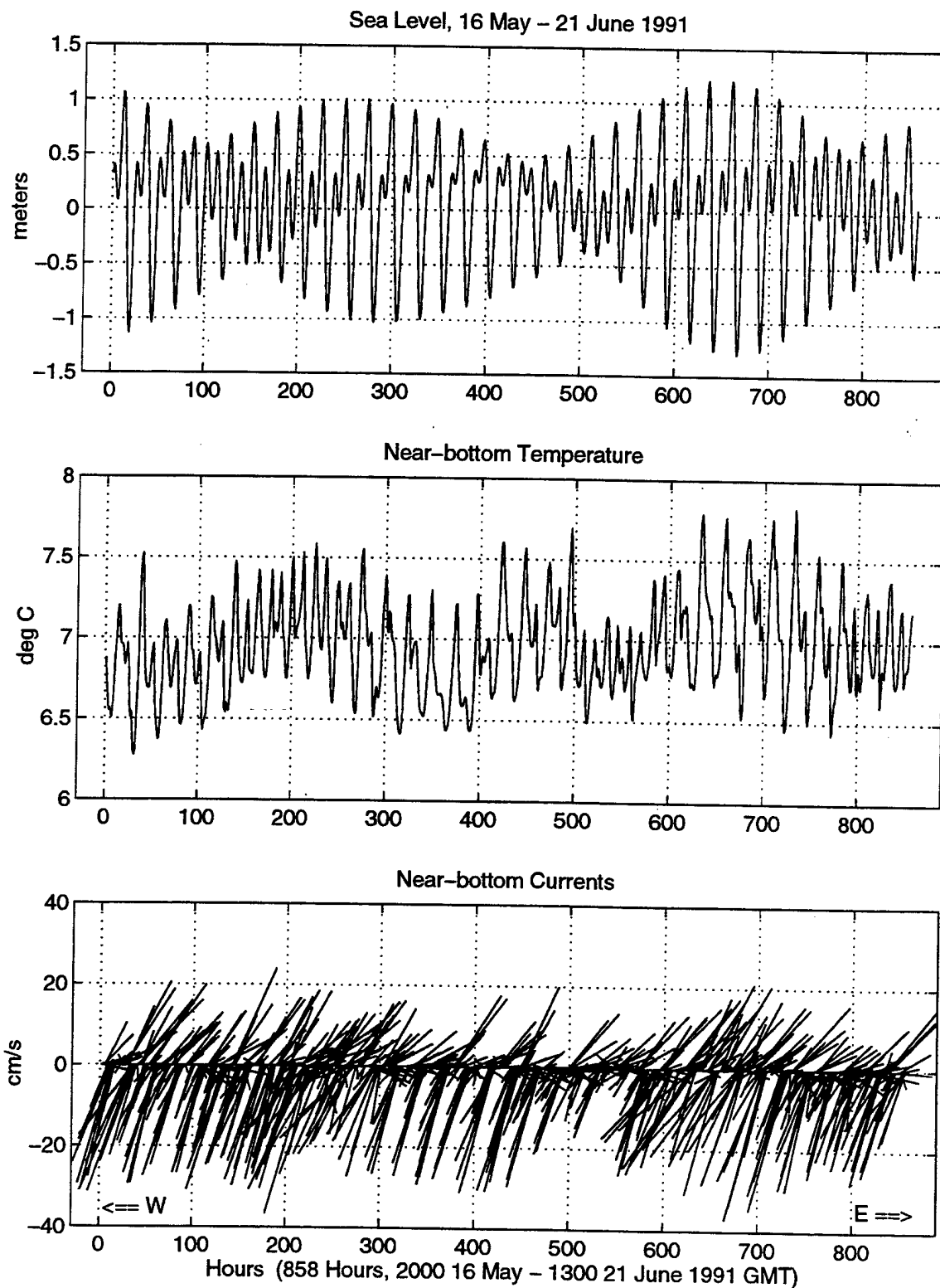
Figure 26. Sea Level and Near-Bottom Temperature and Currents. Demeaned sea level from the Monterey tide gauge (upper) with temperature (middle) and velocity (bottom) from the S-4 mooring 2 m above the bottom for 16 May–21 June, 1991.

126
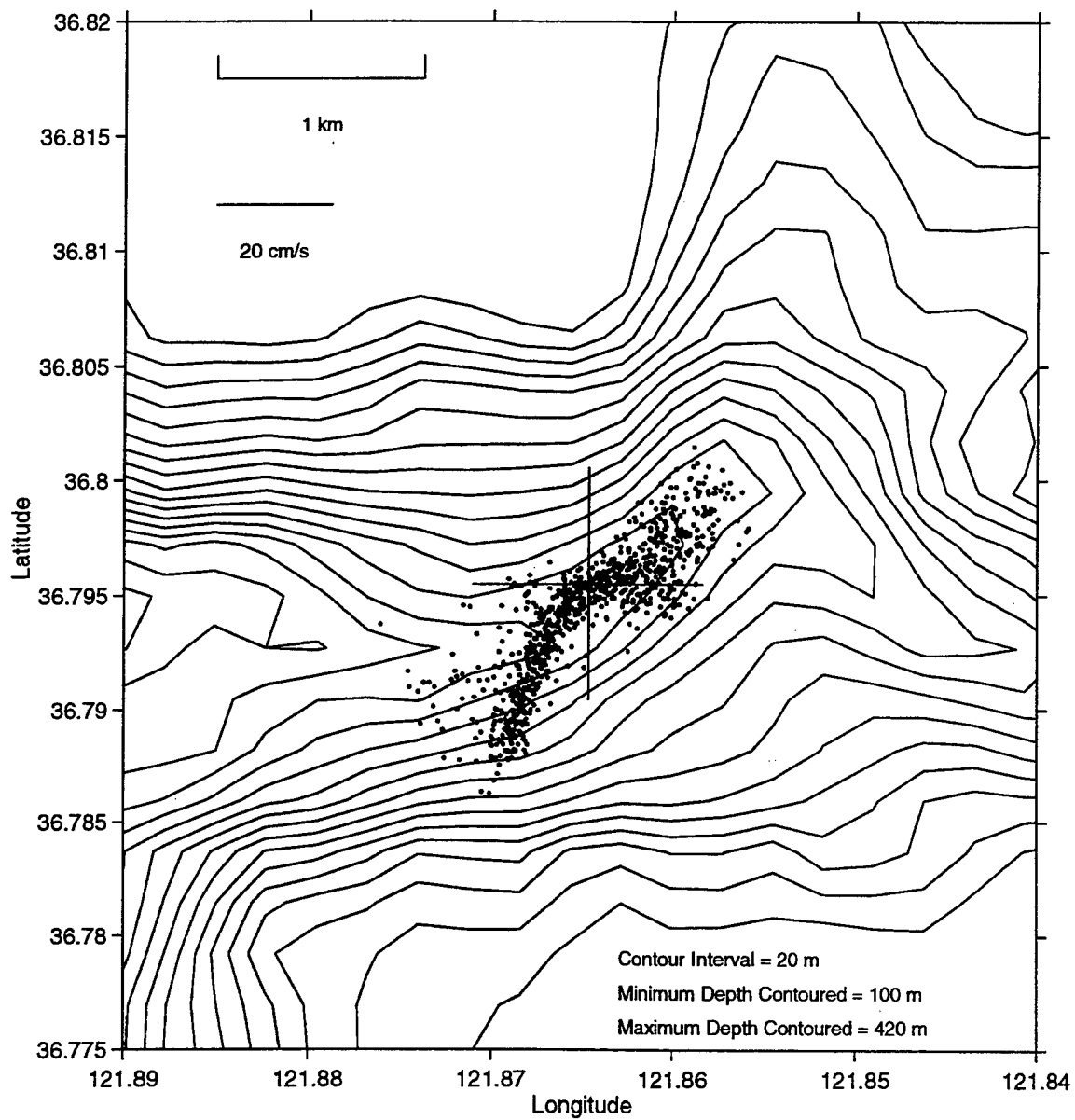
Figure 27. Near-Bottom Currents. Scatterplot of velocity from the S-4 mooring 2 m above the bottom during 16 May–21 June, 1991, together with nearby depth contours.
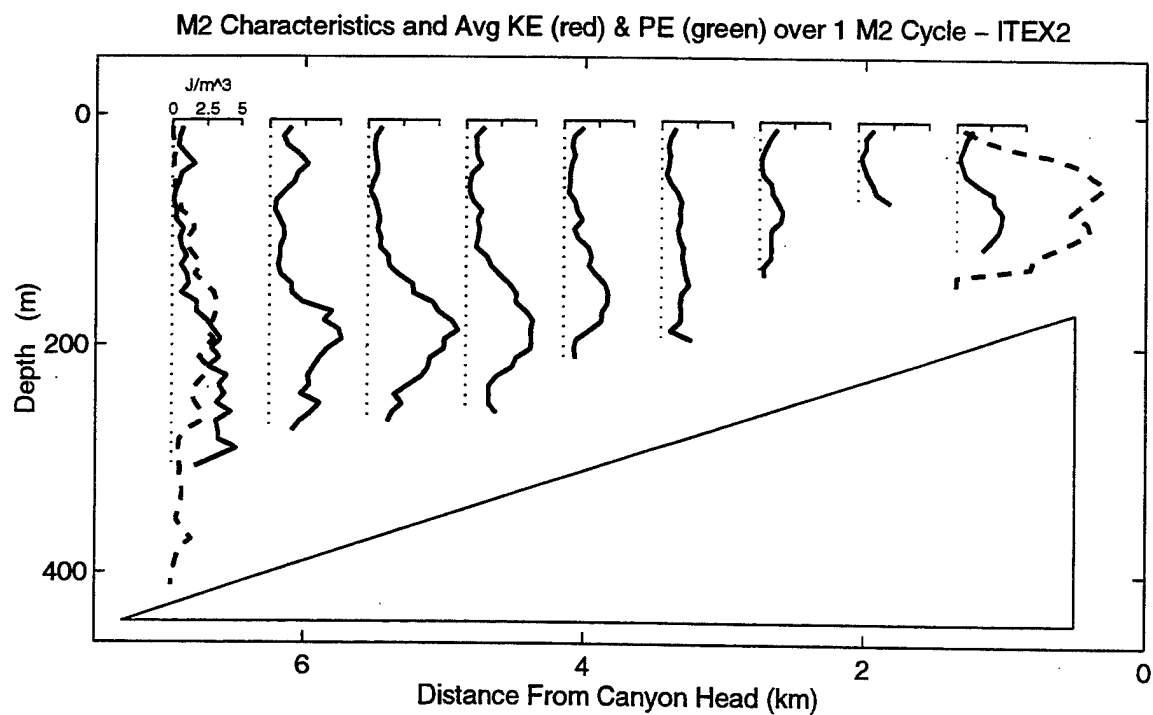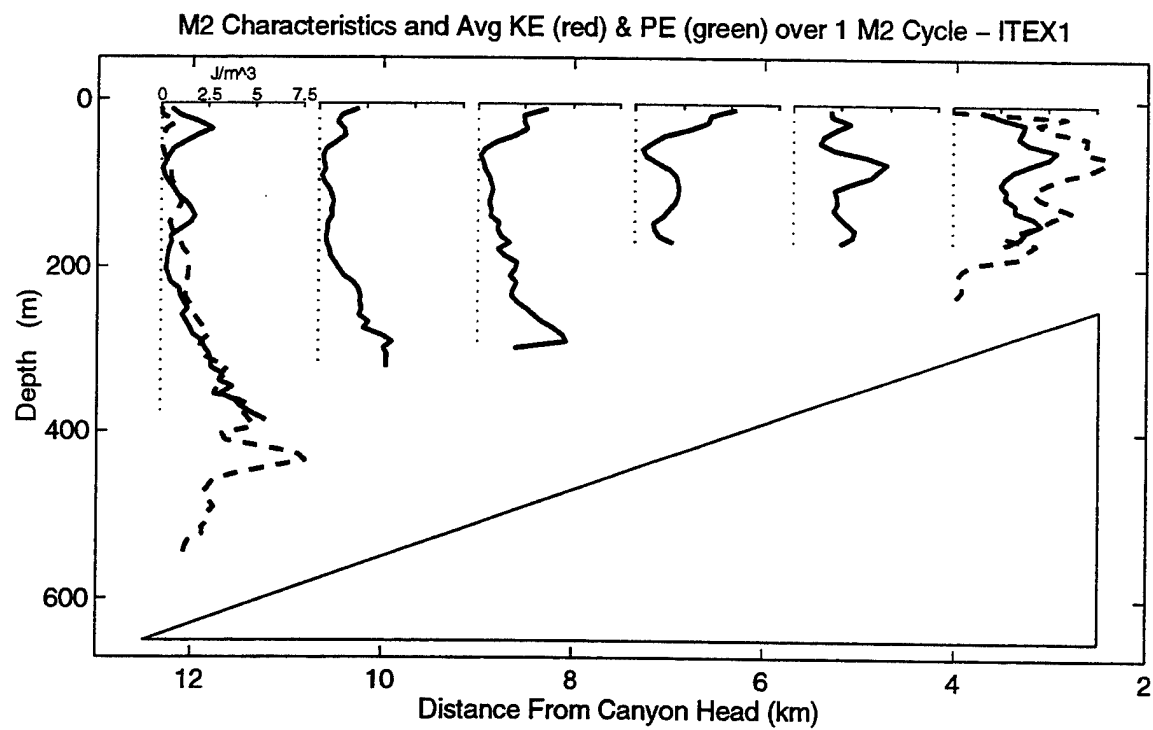
Figure 28. M2 Kinetic and Potential Energy Along-Canyon. Kinetic (solid) and potential (dashed) energy for the M2 wave fits versus depth during ITEX1 (upper) and ITEX2 (lower).

Demeaned Tidal Heights – ITEX1

Demeaned Tidal Heights – ITEX2
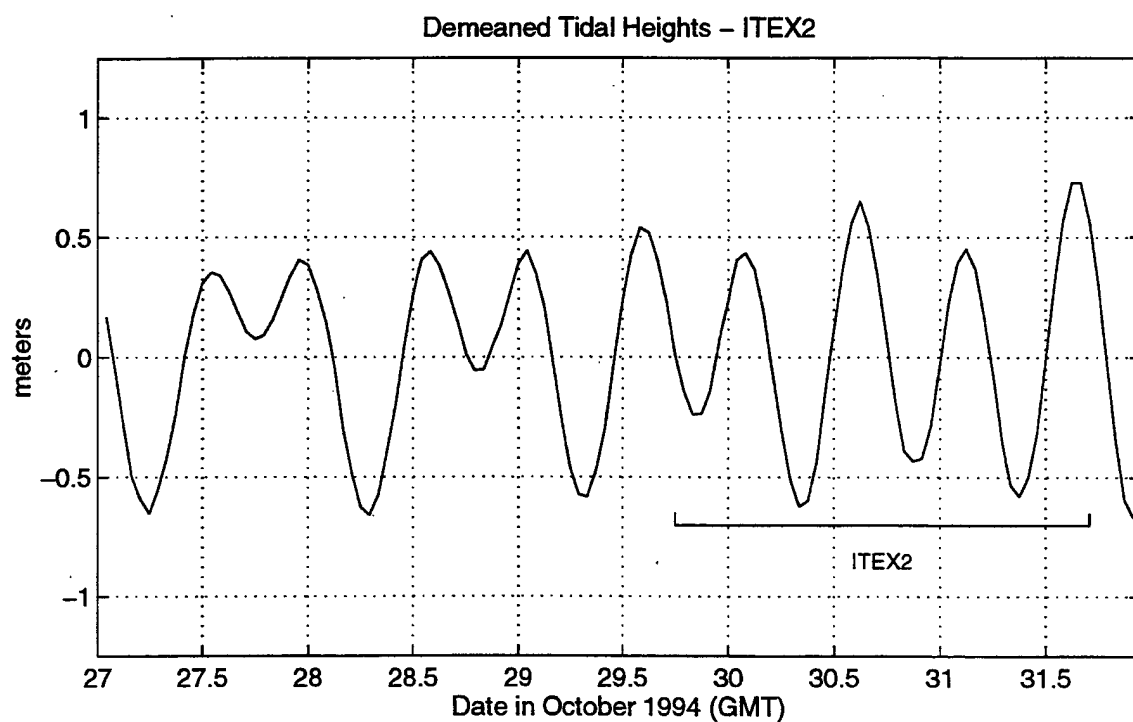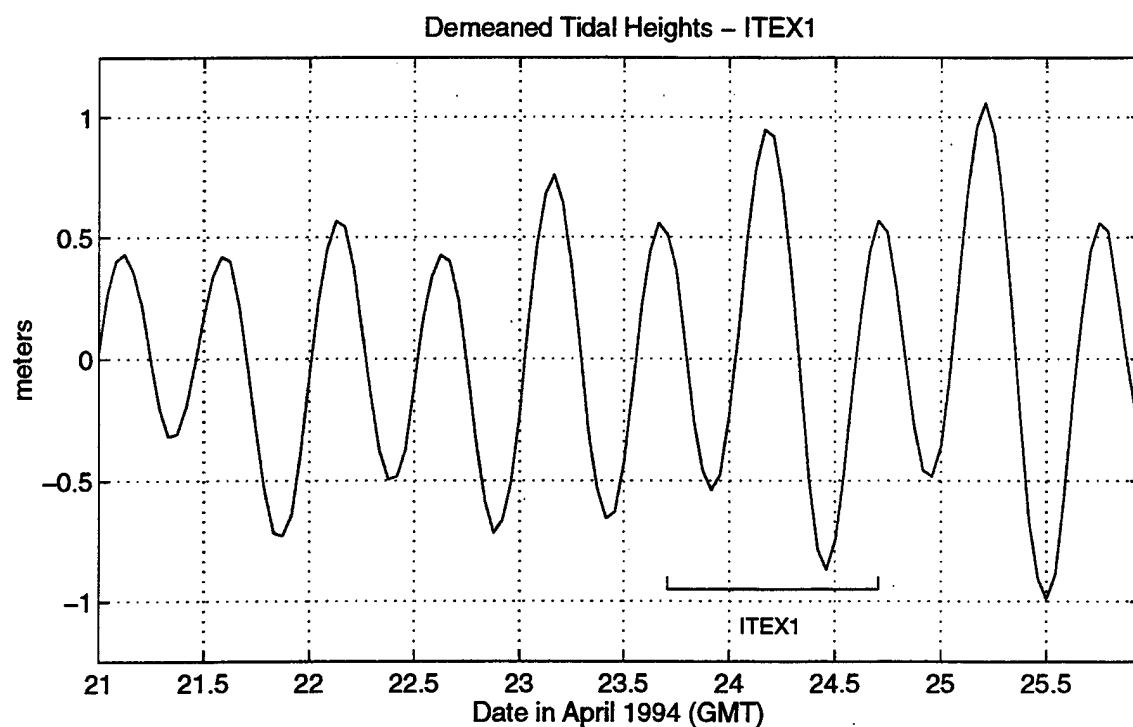
Figure 29. Demeaned Sea Level at Monterey during ITEX1 and ITEX2.

129
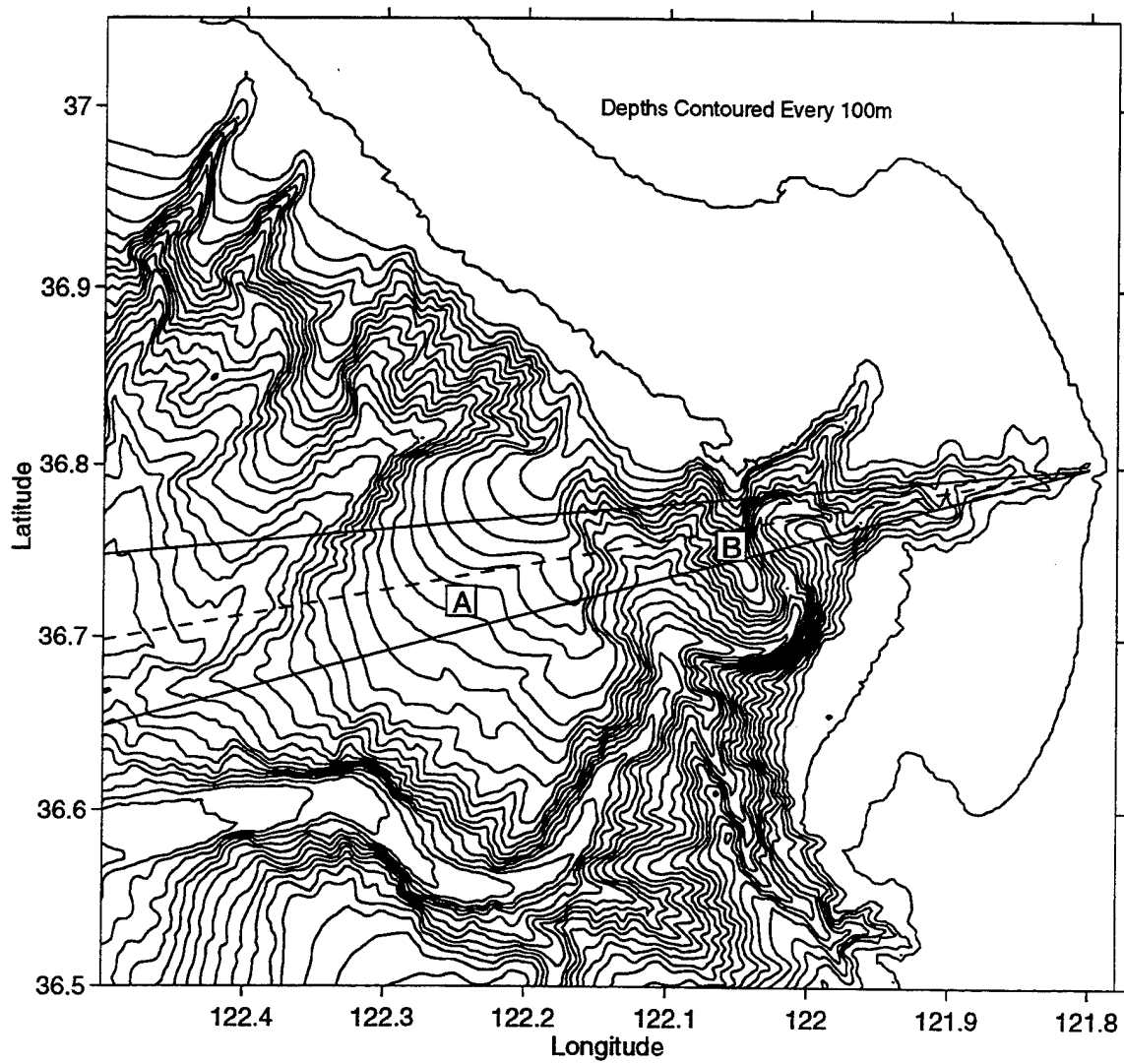
Figure 30. Possible Internal Tide Generation Sites. Likely locations of internal tide generation for MSC at "Smooth Ridge" (A) and "Steep Ridge" (B) based on M2 characteristic ray tracing.
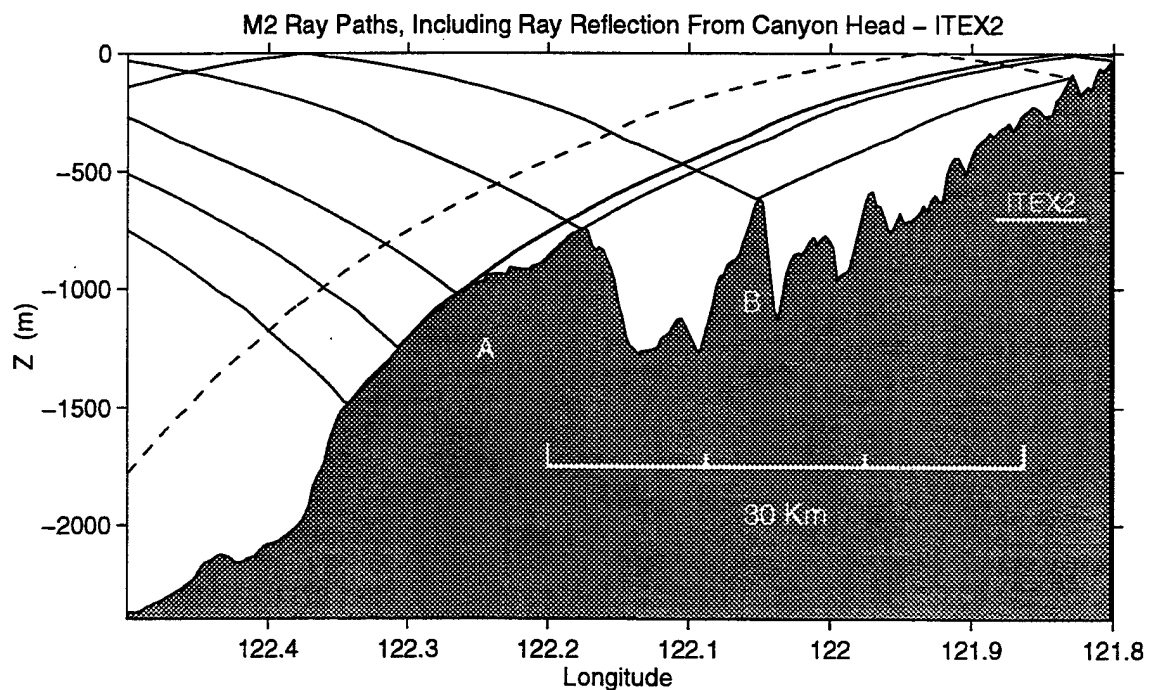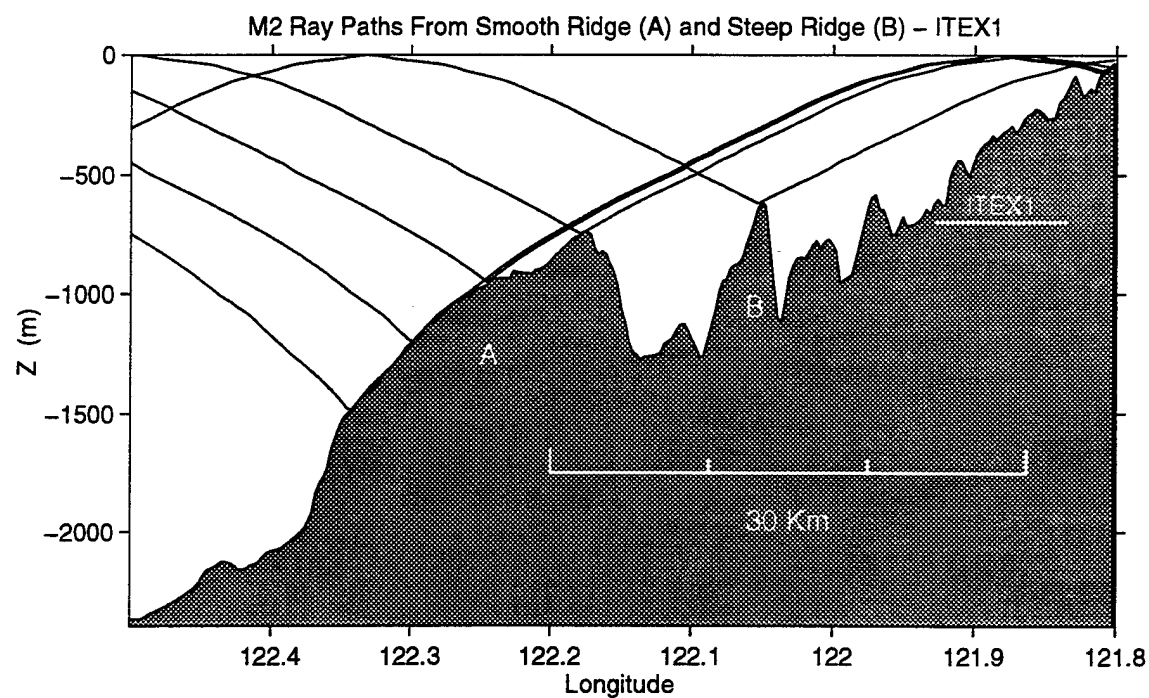
Figure 31. M2 Ray Traces from Smooth Ridge and Steep Ridge. M2 characteristics calculated from the internal wave dispersion relation (with $f = 8.726 \times 10^{-5}$ s^{-1}) showing possible paths of energy propagation from two offshore ridges into MSC. The dashed line represents a reflected ray.
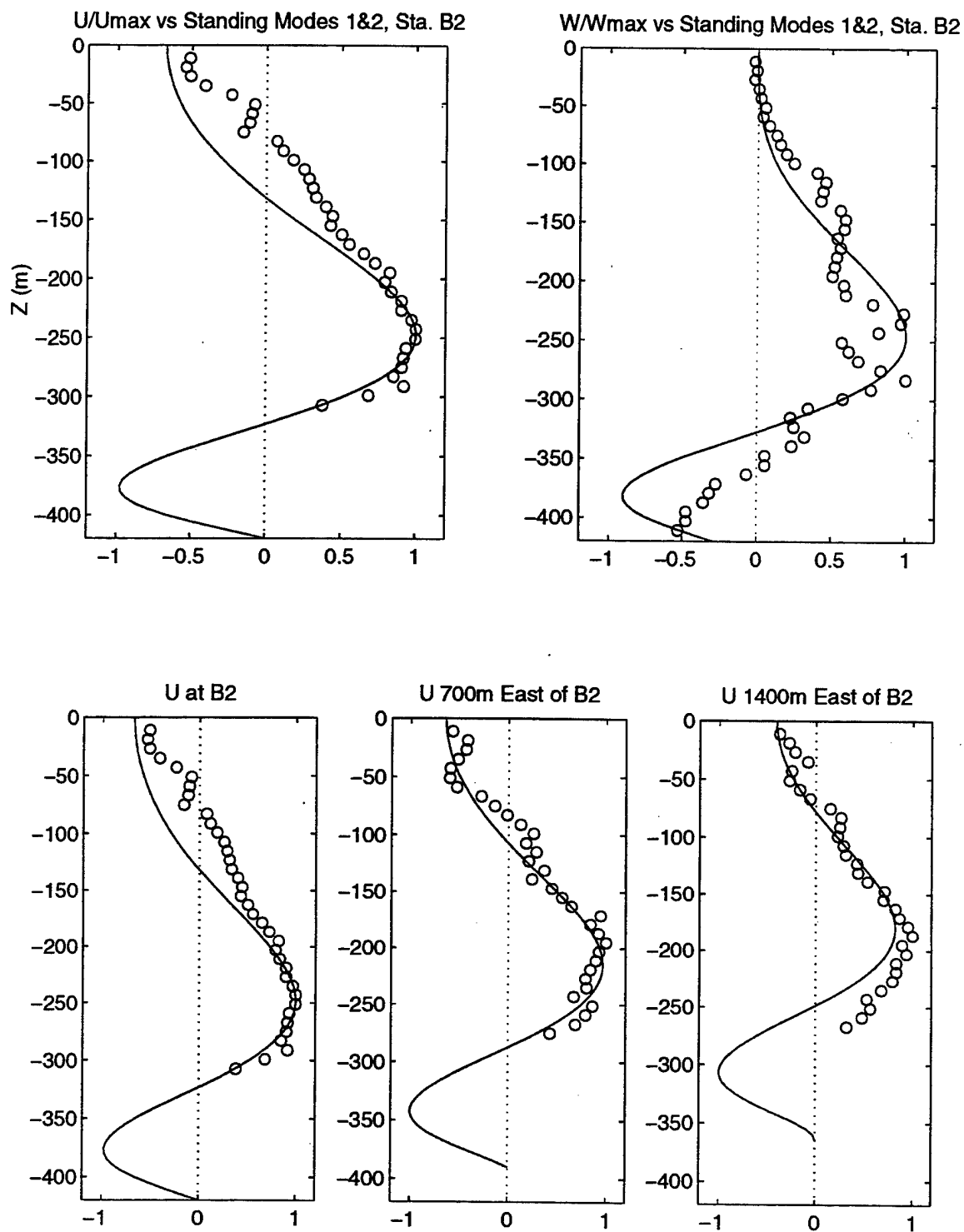
Figure 32. Observed and Theoretical Vertical Current Structure during ITEX2. Normalized east-west and vertical (upper right) velocity profiles (o) compared with theoretical solutions (solid lines) for the first 2 standing wave modes of Wunsch (1968) at stations shown in Figure 5. Vertical velocities are inferred from observed isopycnal displacements.
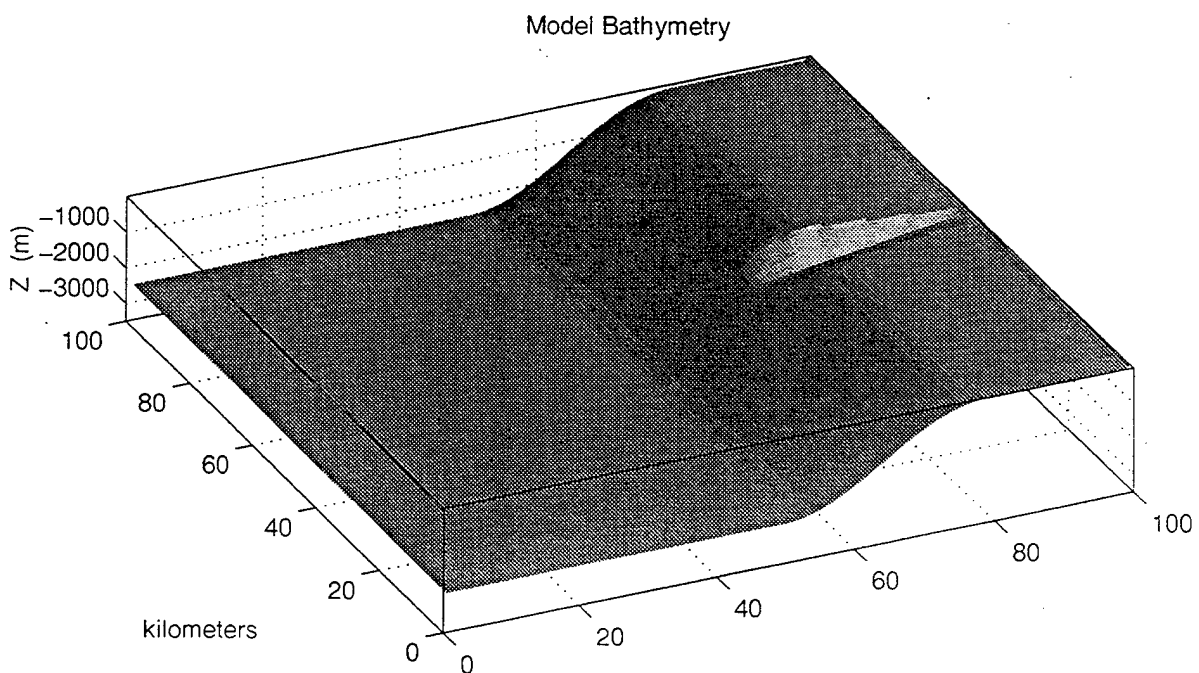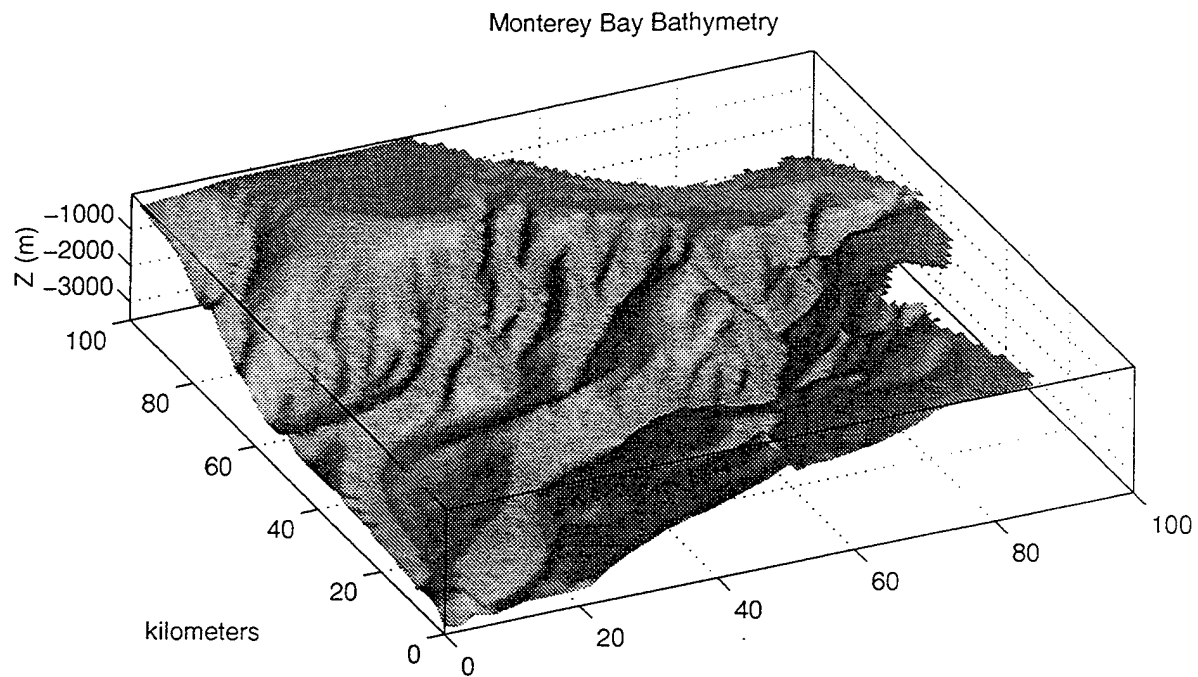
Figure 33. Monterey Bay Bathymetry and a Sample Model Bathymetry. Observed Monterey Bay bathymetry and model bathymetry that incorporates a relatively narrow shelf, a steep (7°) continental slope, a deep basin, and a canyon head lying close to shore.

133
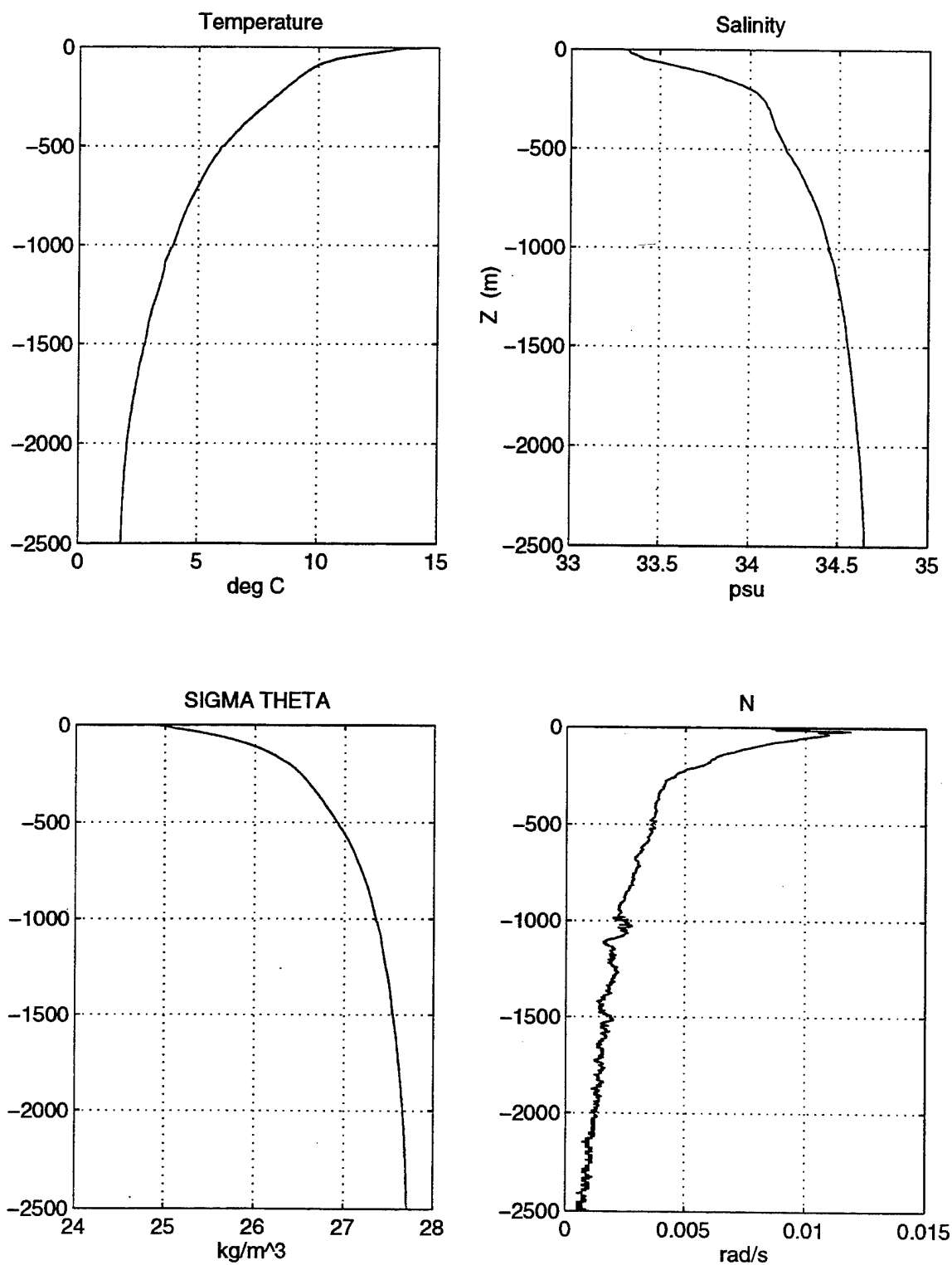
Figure 34. Temperature and Salinity Profiles Used for Model Initialization. Average temperature and salinity profiles from over 50 CTD casts ~15 km west of the Monterey Peninsula and the corresponding density (σ_θ) and buoyancy frequency (*N*) profiles.
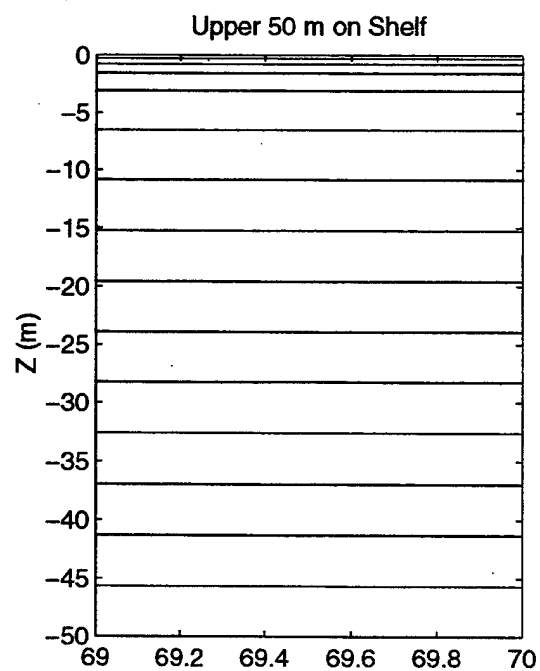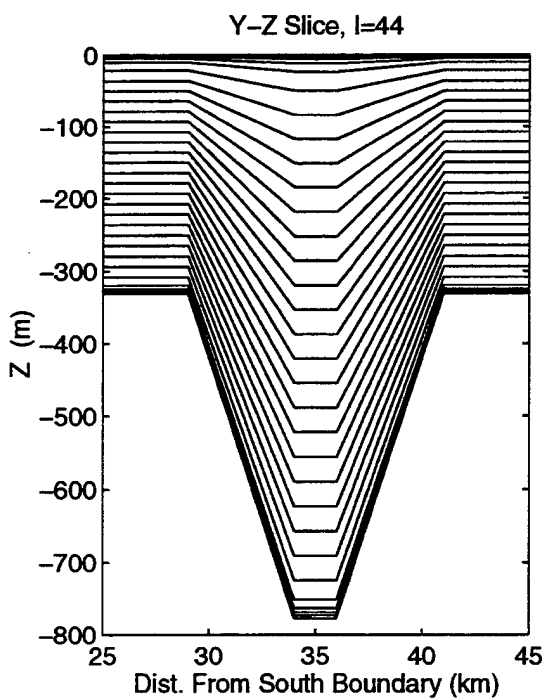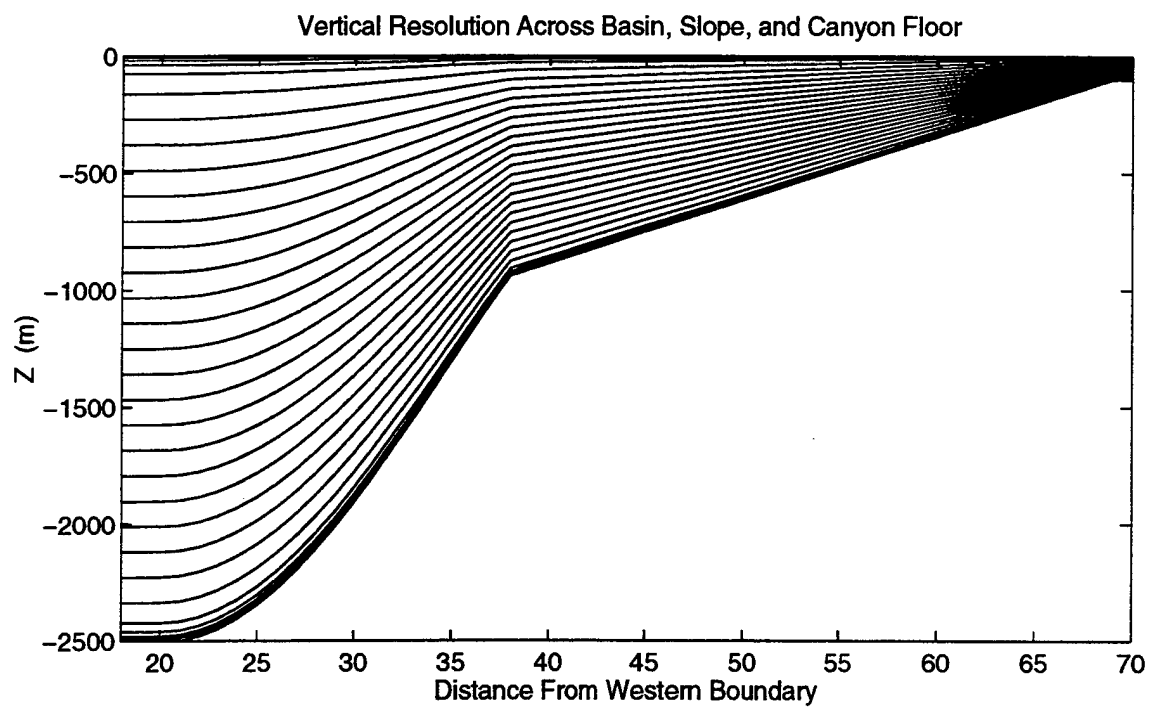
Figure 35. Vertical Resolution in the Model Domain. Along-canyon (upper), cross-canyon (lower left), and cross-shelf (lower right) sections through the model domain showing vertical distributions of 30 sigma levels.

135
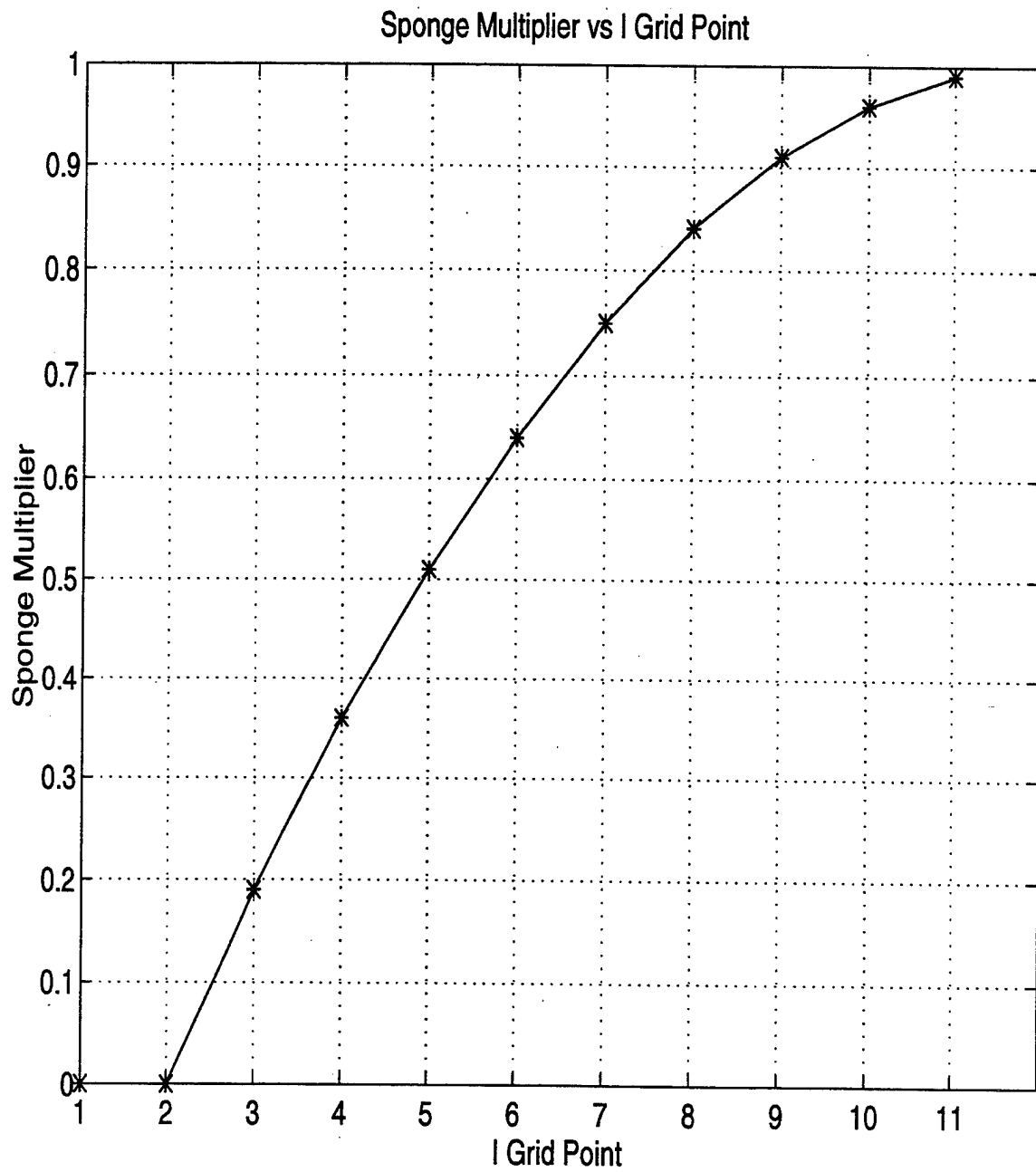
Figure 36. Sponge Multiplier at the Seaward Model Boundary. Multiplication factors for internal velocities and baroclinic pressure gradients over 10 grid points at the western model boundary.

136
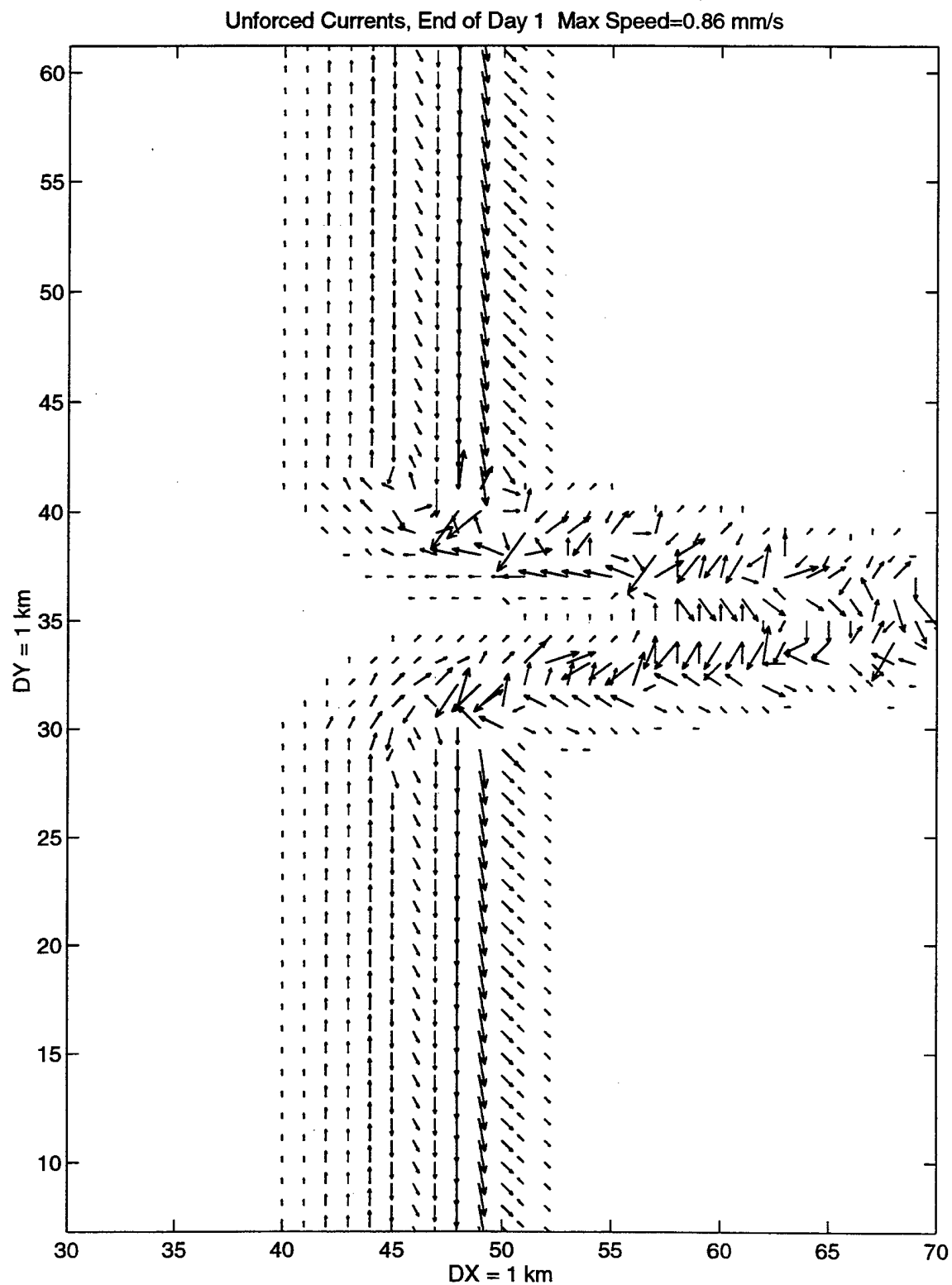
Figure 37. Unforced Currents at Day One. Plan view of maximum horizontal currents after one day in an unforced simulation.

137
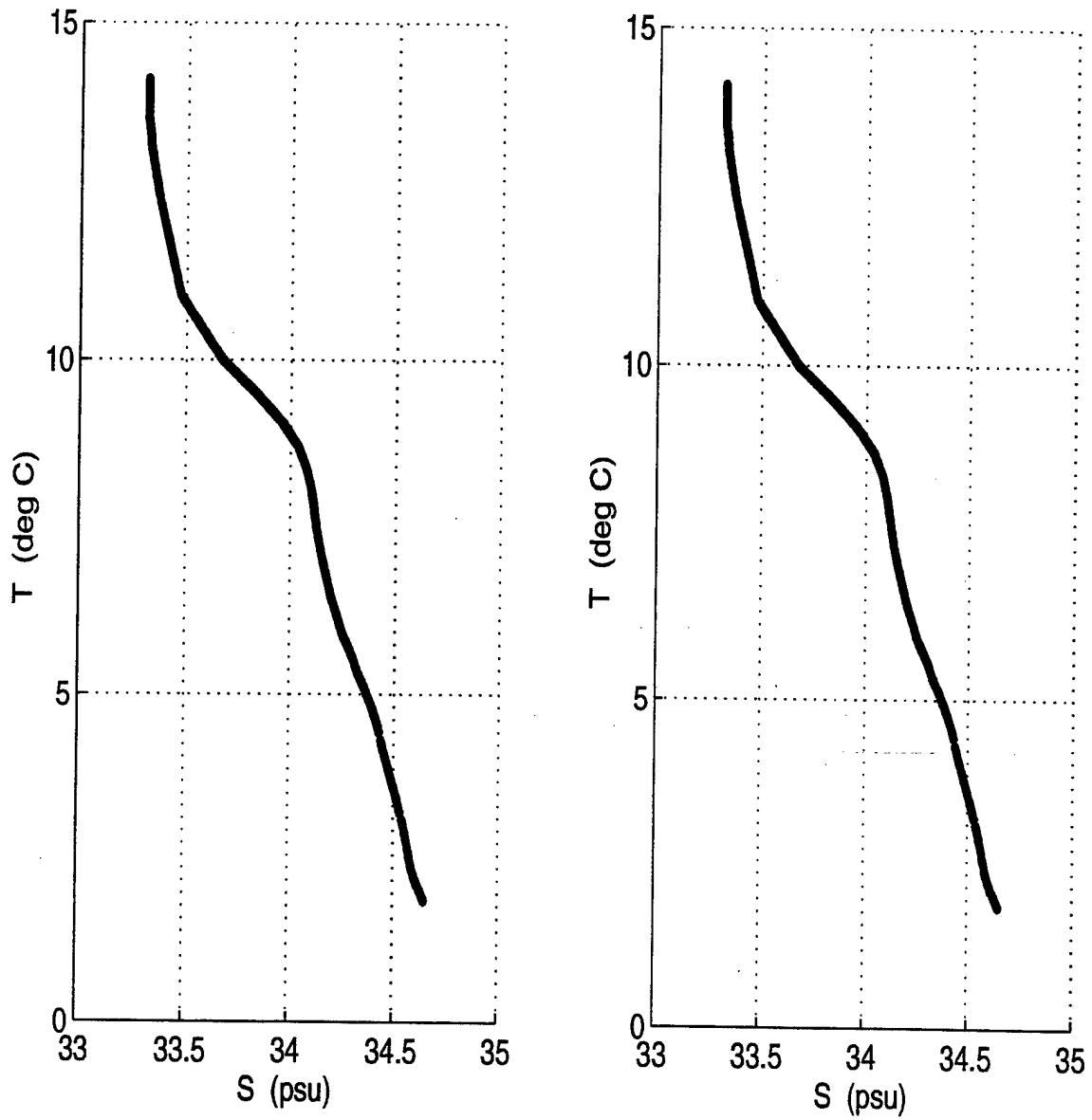
Figure 38. Initial T-S Curve (left) and T-S Curve (right) after One Day of Unforced Model Simulation.
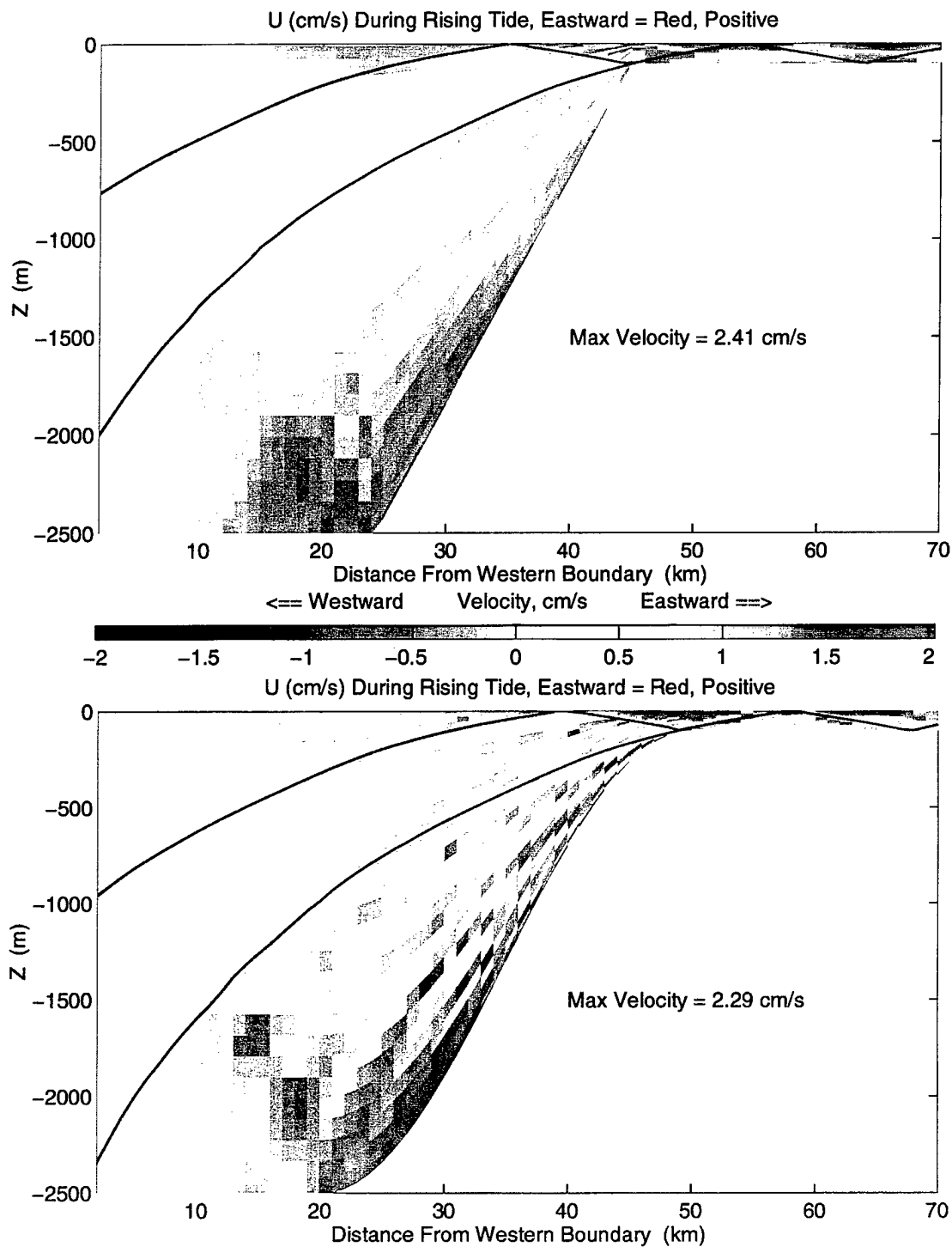
Figure 39. East-West Velocity in the X-Z Plane during Rising Tide. Cross-shelf sections of east-west model velocity during rising sea level for a sharp (upper) and cosine-shaped (lower) continental shelf break together with characteristics (solid lines) from the internal wave dispersion relation.
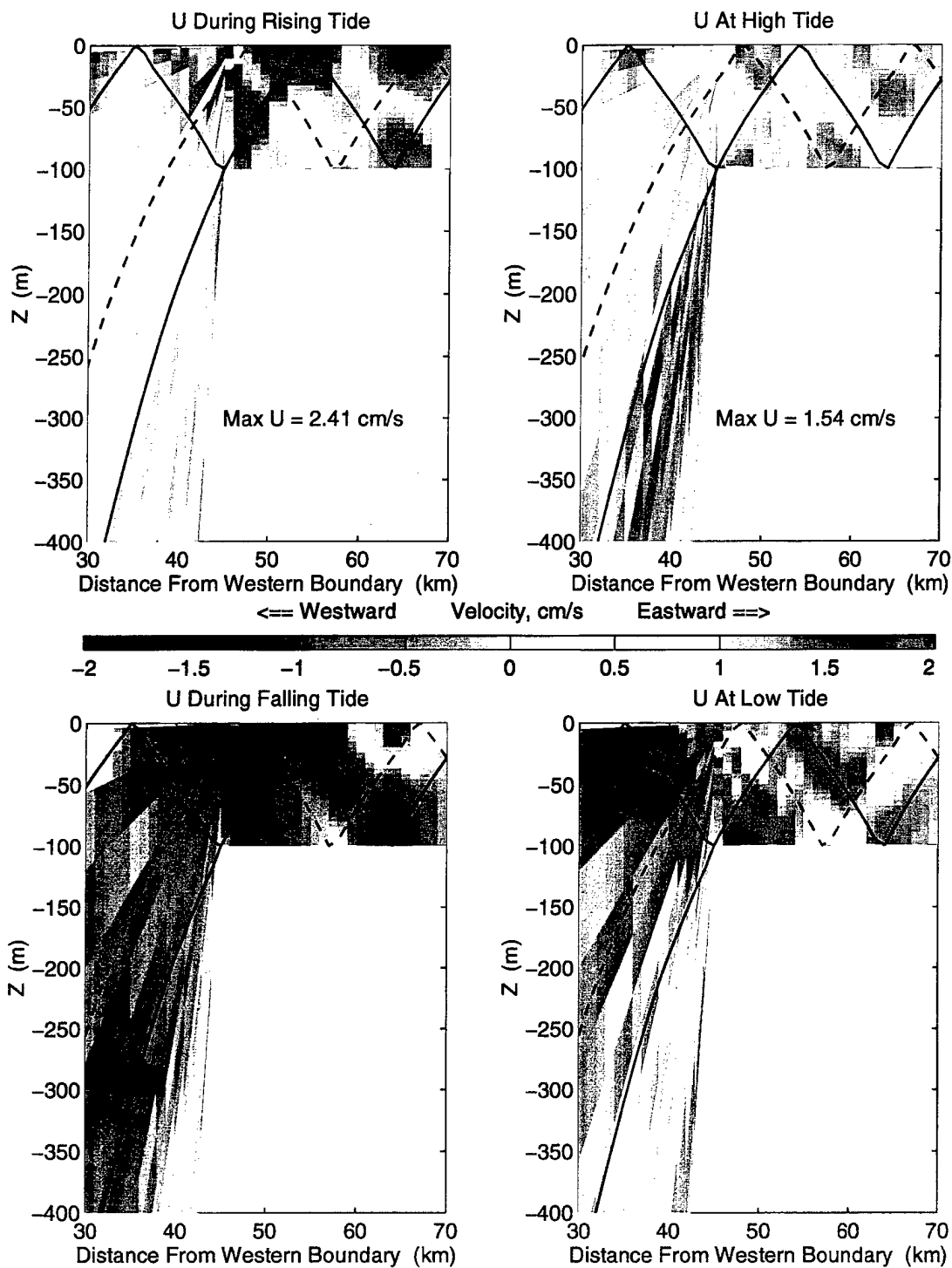
Figure 40. East-West Velocity Across the Continental Shelf. Cross-shelf sections of east-west model velocity during four phases of sea level together with characteristics emanating from the shelf break (solid lines) and reflecting from the coastal boundary (dashed lines). Note the 180° phase shift in horizontal velocity after reflection from the vertical boundary.

140
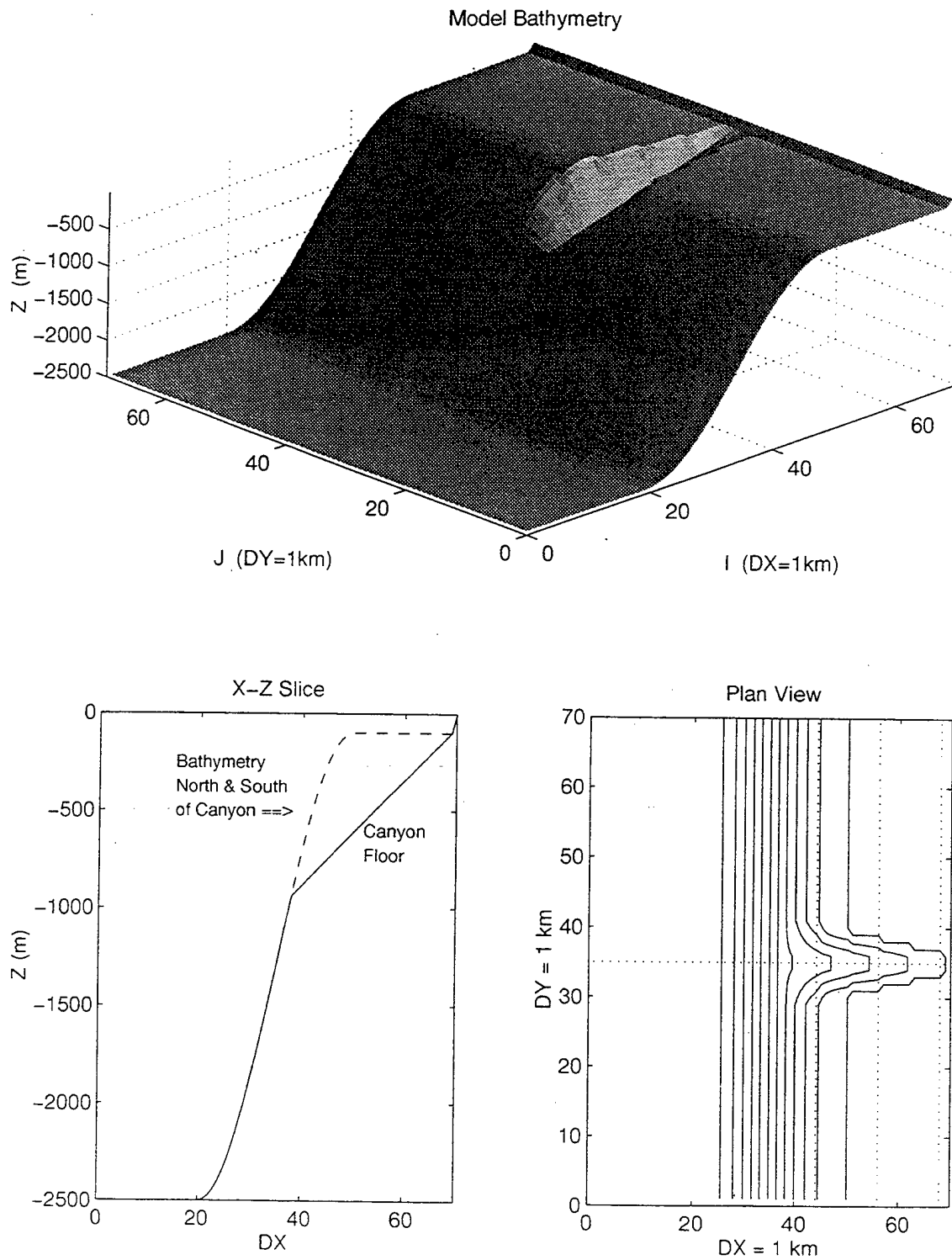
Figure 41. Case 1 Model Bathymetry. In plan view, depth is contoured every 200 m (between 100 m and 2500 m), and dotted lines indicate locations of x-z and y-z slices used for data analysis.

141
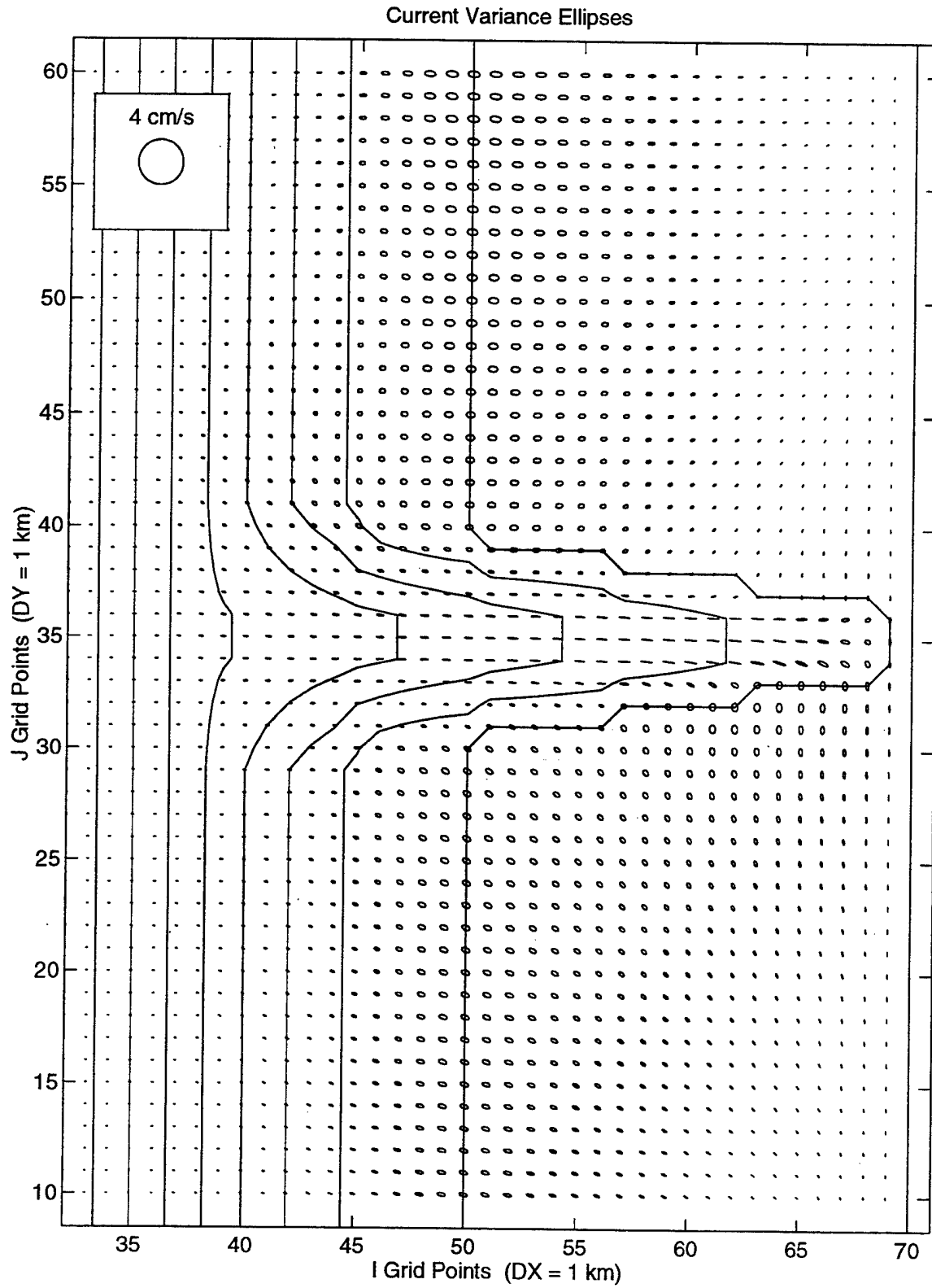
Figure 42. Depth-Averaged Current Variance Ellipses.

142
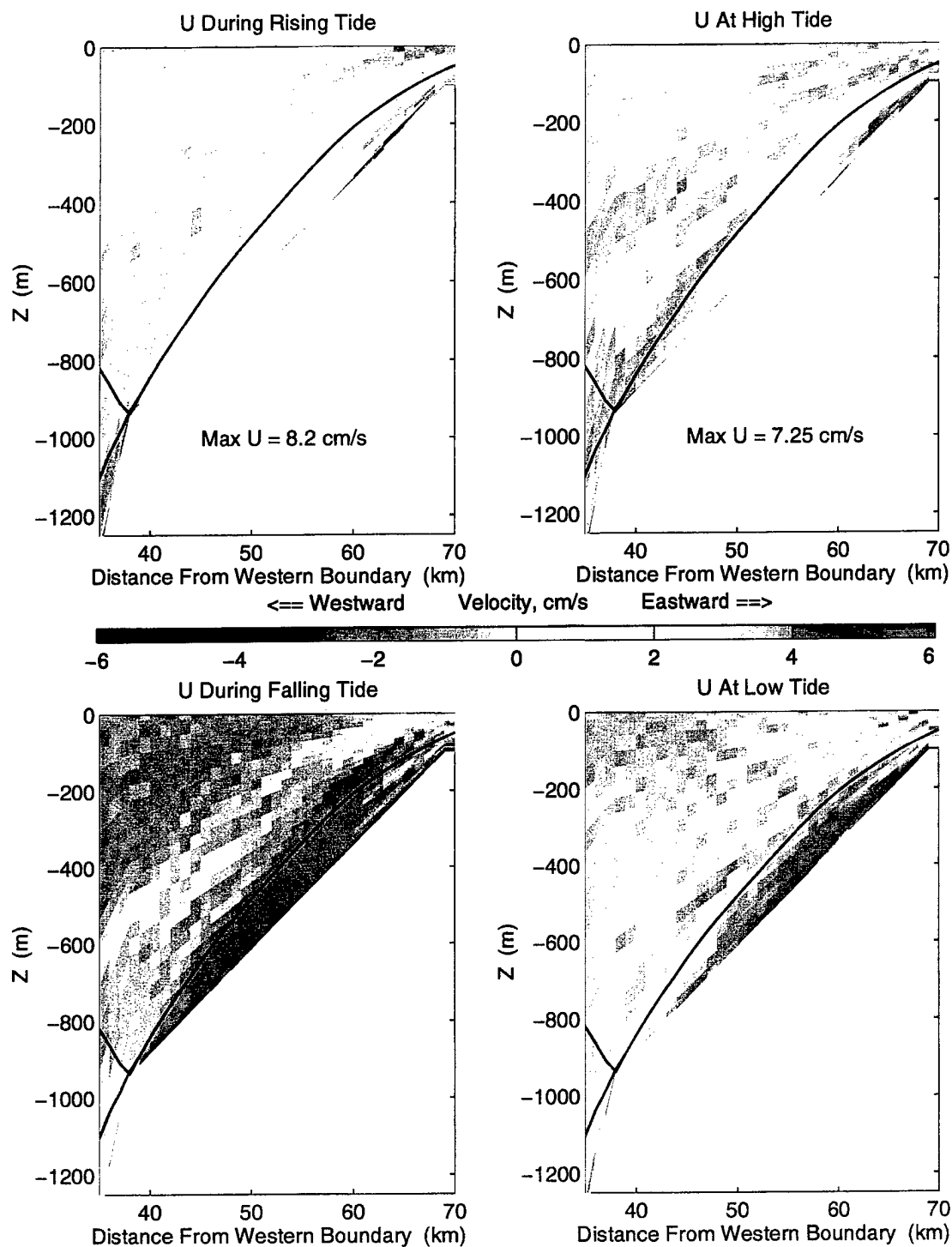
Figure 43. East-West Velocity Along-Canyon. Along-canyon sections of east-west model velocity during four phases of sea level together with characteristics emanating from the canyon foot (solid lines).

143
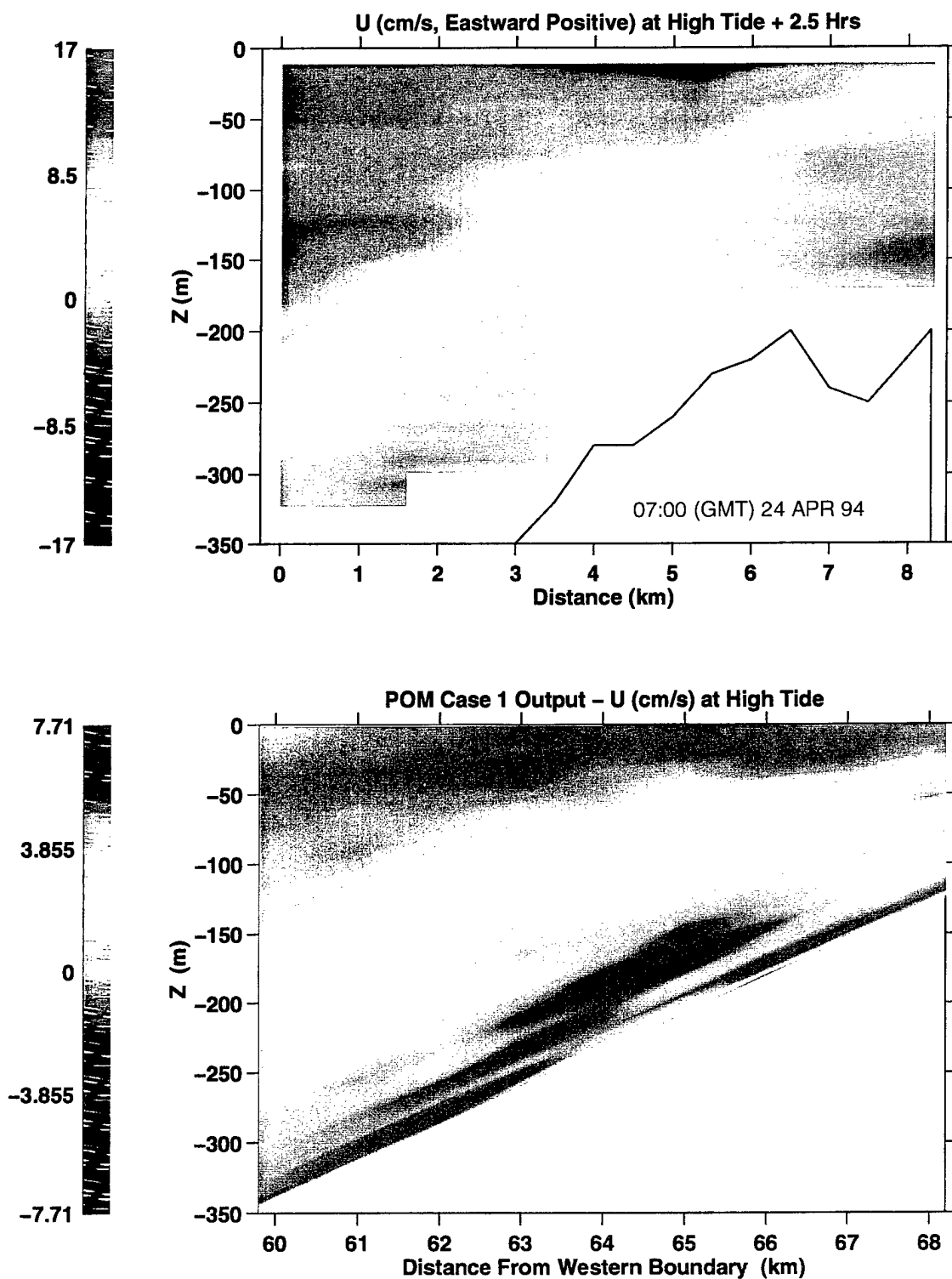
Figure 44. Observed and Modeled East-West M2 Currents in MSC. Along-canyon sections of east-west M2 velocity from ITEX1 (upper) and model simulations (lower).

144
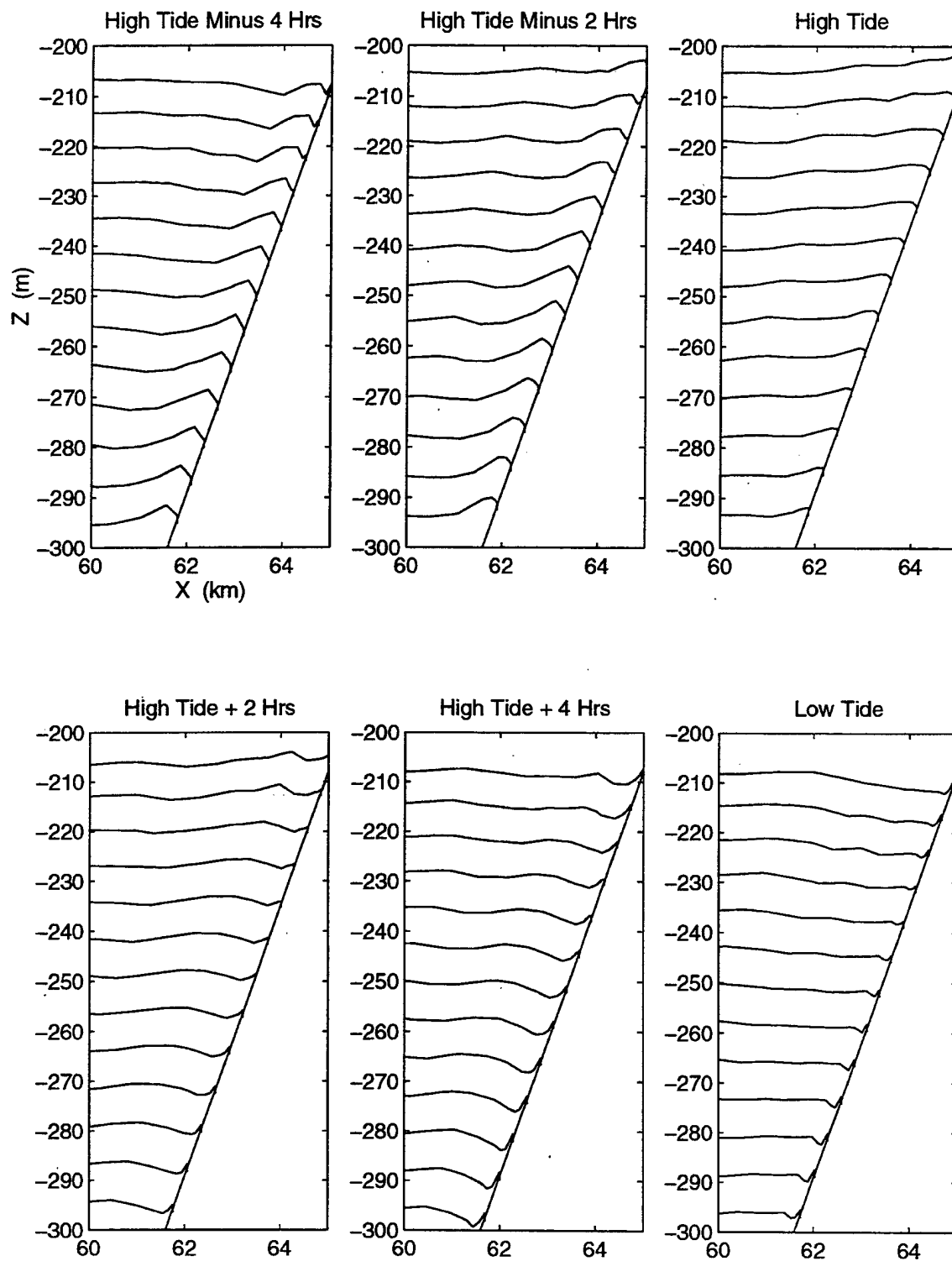
Figure 45. Along-Canyon Density Sections throughout the Tidal Cycle. Isopycnals contoured at intervals of 0.05 kg m^{-3} along the critically sloping portion of the model canyon during several phases of M2 sea level.

145
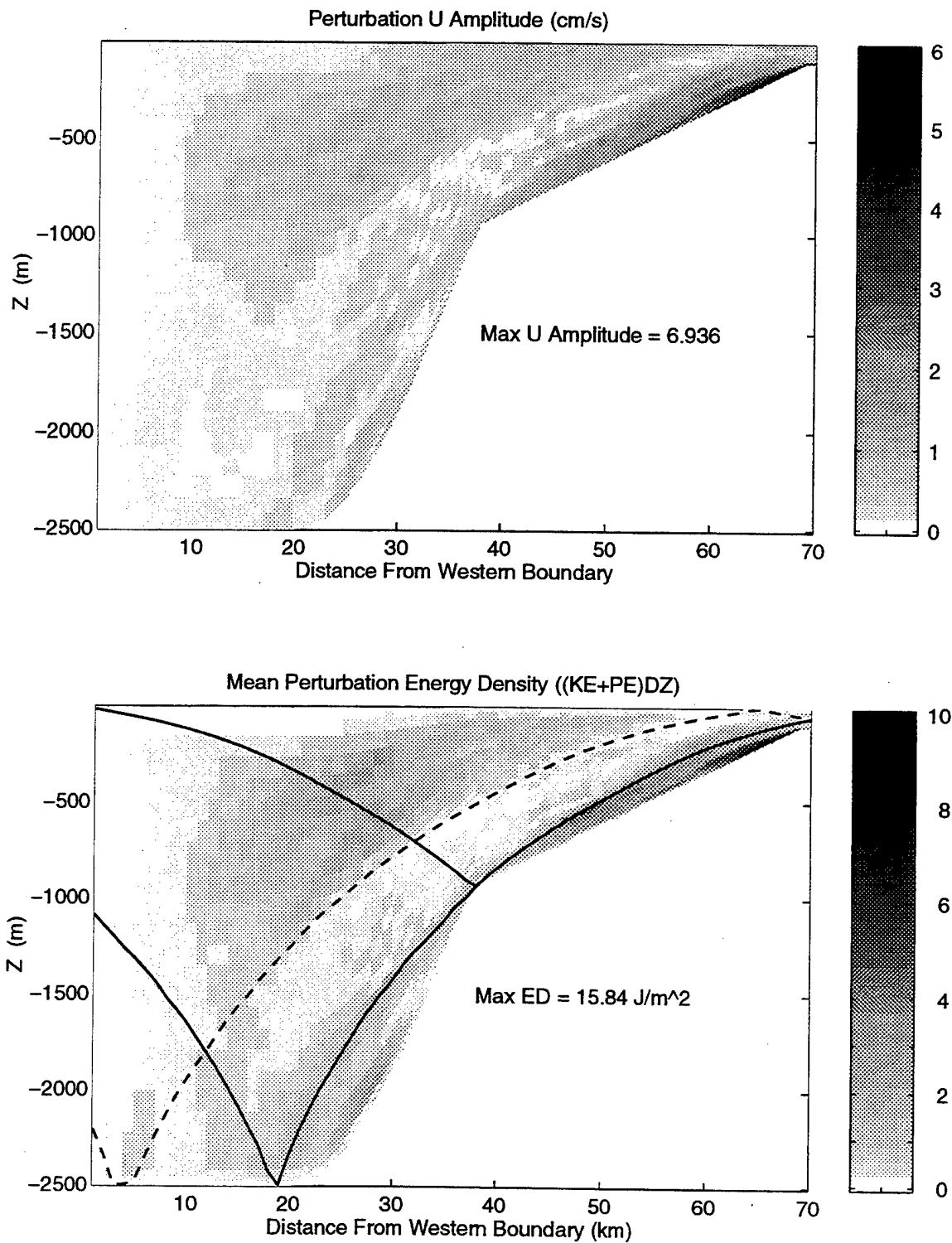
Figure 46. M2 Current Amplitude and Mean Perturbation Energy Density Along-Canyon. Along-canyon sections of east-west M2 current amplitude (upper) and kinetic plus potential energy density (lower) with characteristics emanating from the shelf break (solid lines) and reflecting from the coastal boundary (dashed lines).

146
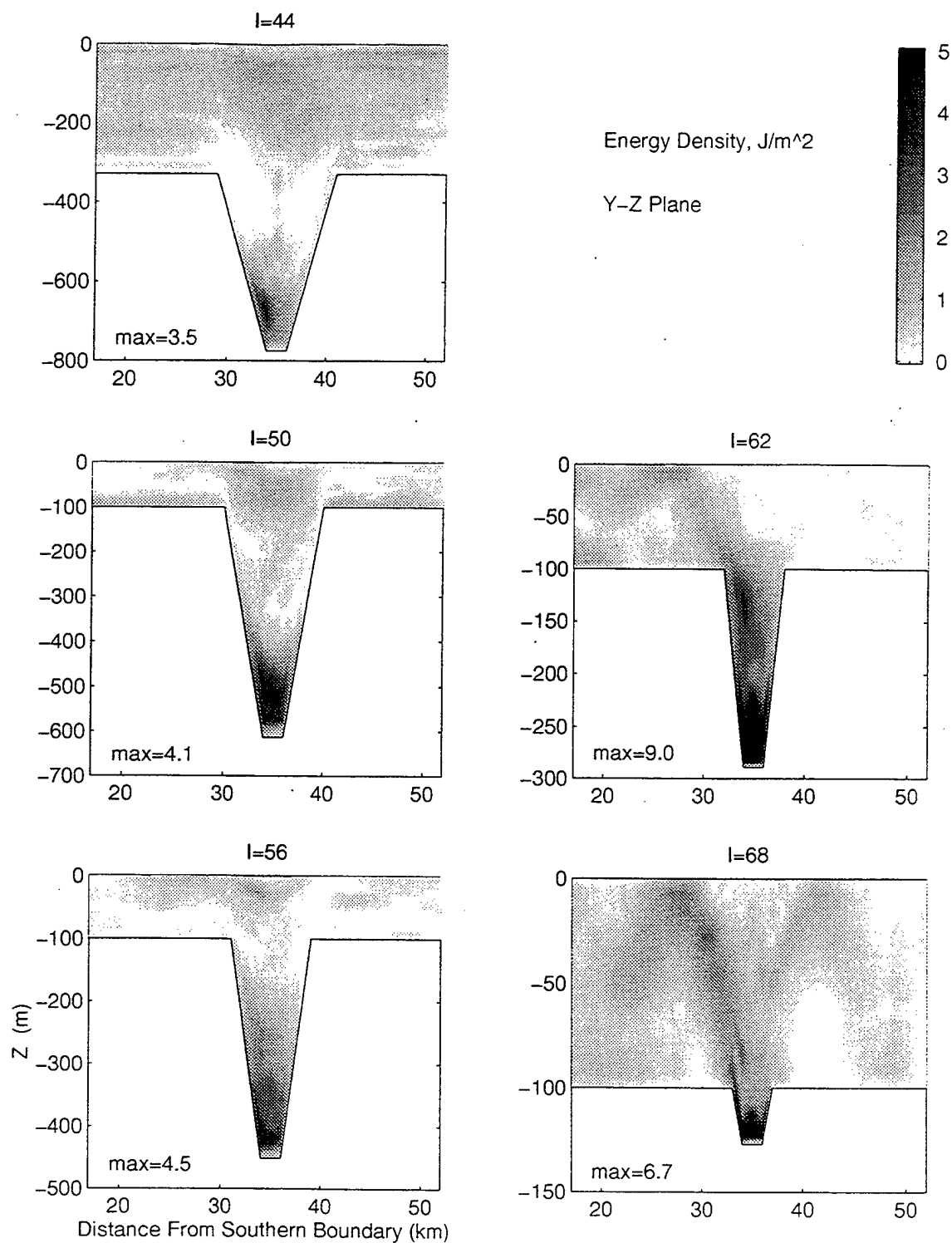
Figure 47. Energy Density Cross-Canyon. Kinetic plus potential energy density in cross-canyon sections. Locations (I) are in kilometers east of the western boundary. Note that a different vertical scale is used for each section.

147
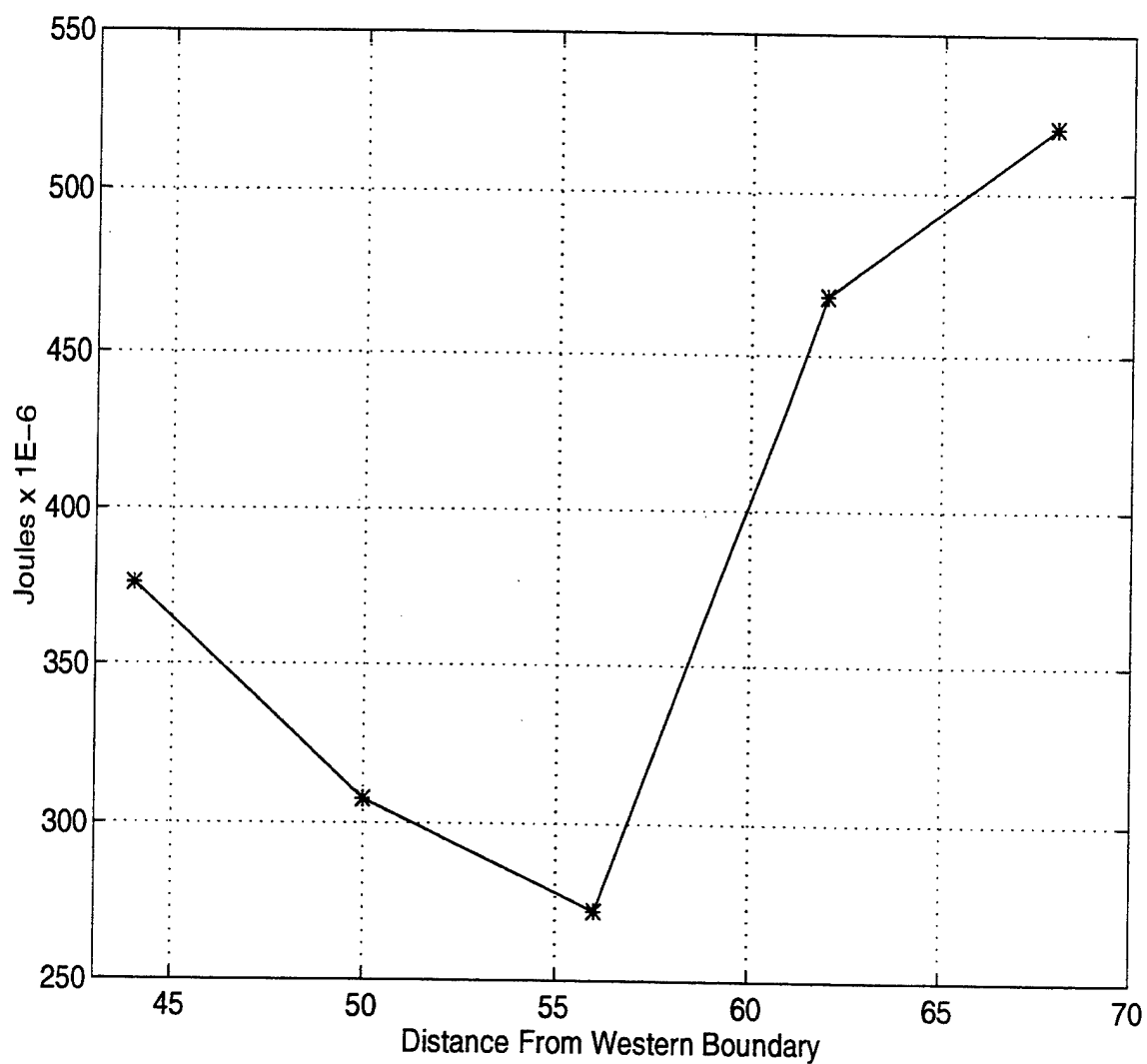
Figure 48. Total Energy in Cross-Canyon Sections. Integrated energy density for cross-canyon sections shown in Figure 47.

148
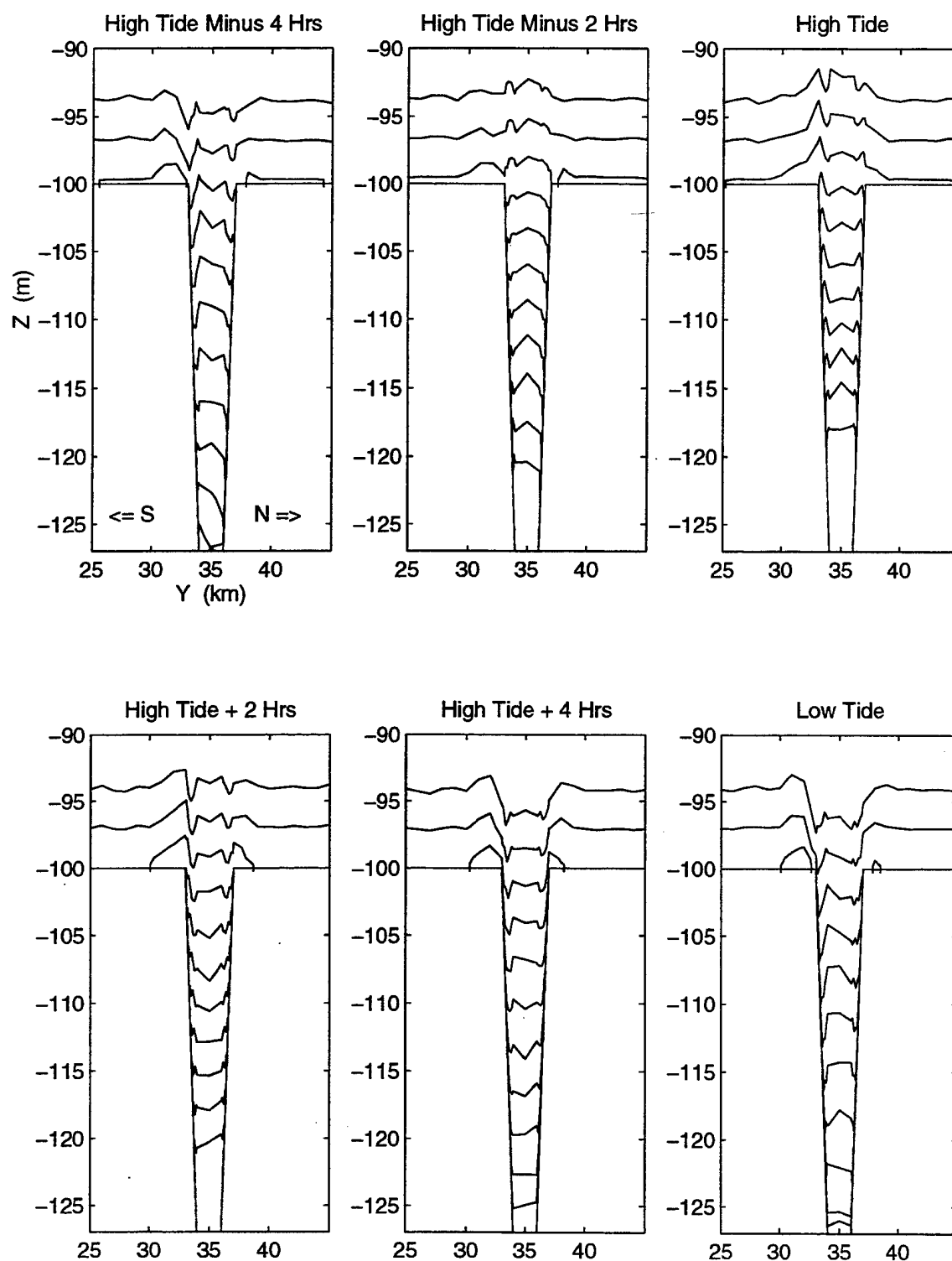
Figure 49. Cross-Canyon Density Sections throughout the Tidal Cycle. Isopycnals contoured at intervals of 0.05 kg m^{-3} across the model canyon at I = 68 (2 km from the eastern boundary) during several phases of M2 sea level.

149
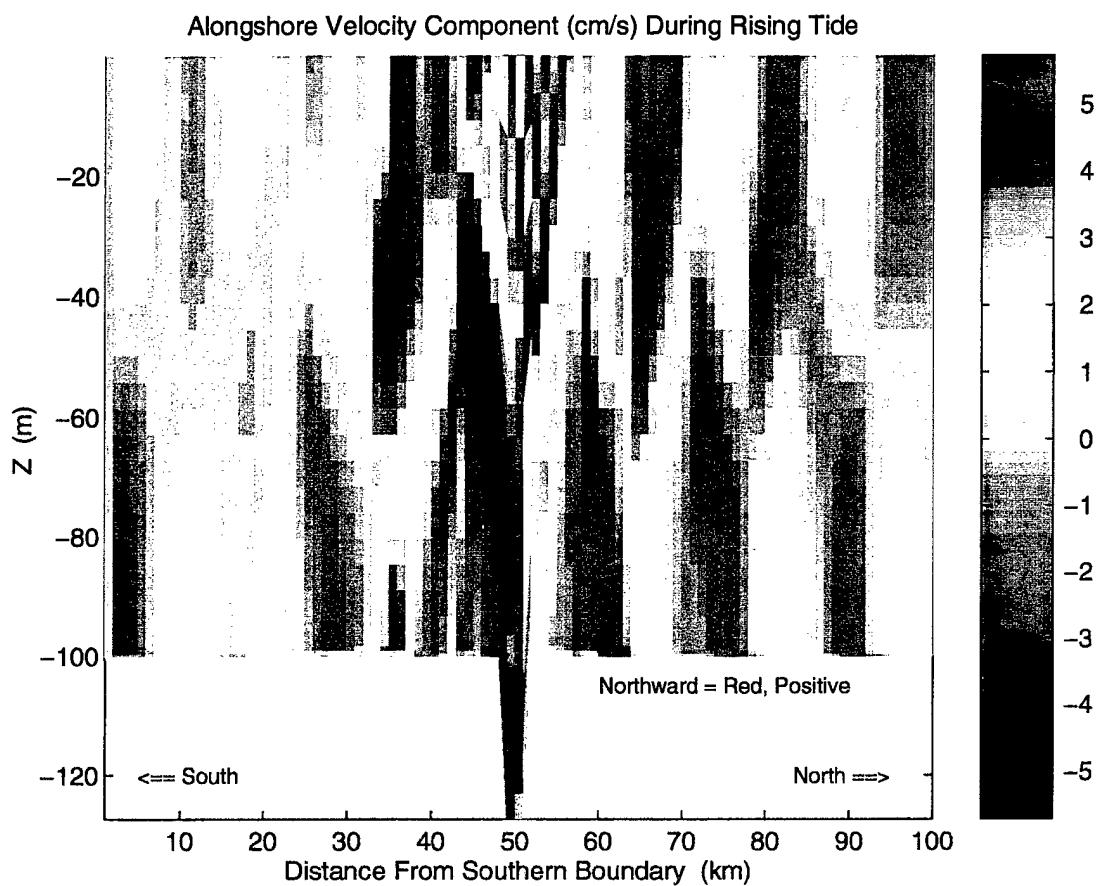
Figure 50. North-South Velocity Along the Continental Shelf. Along-shelf section of north-south velocity 2 km from model eastern boundary showing internal tide generation along the canyon rims.
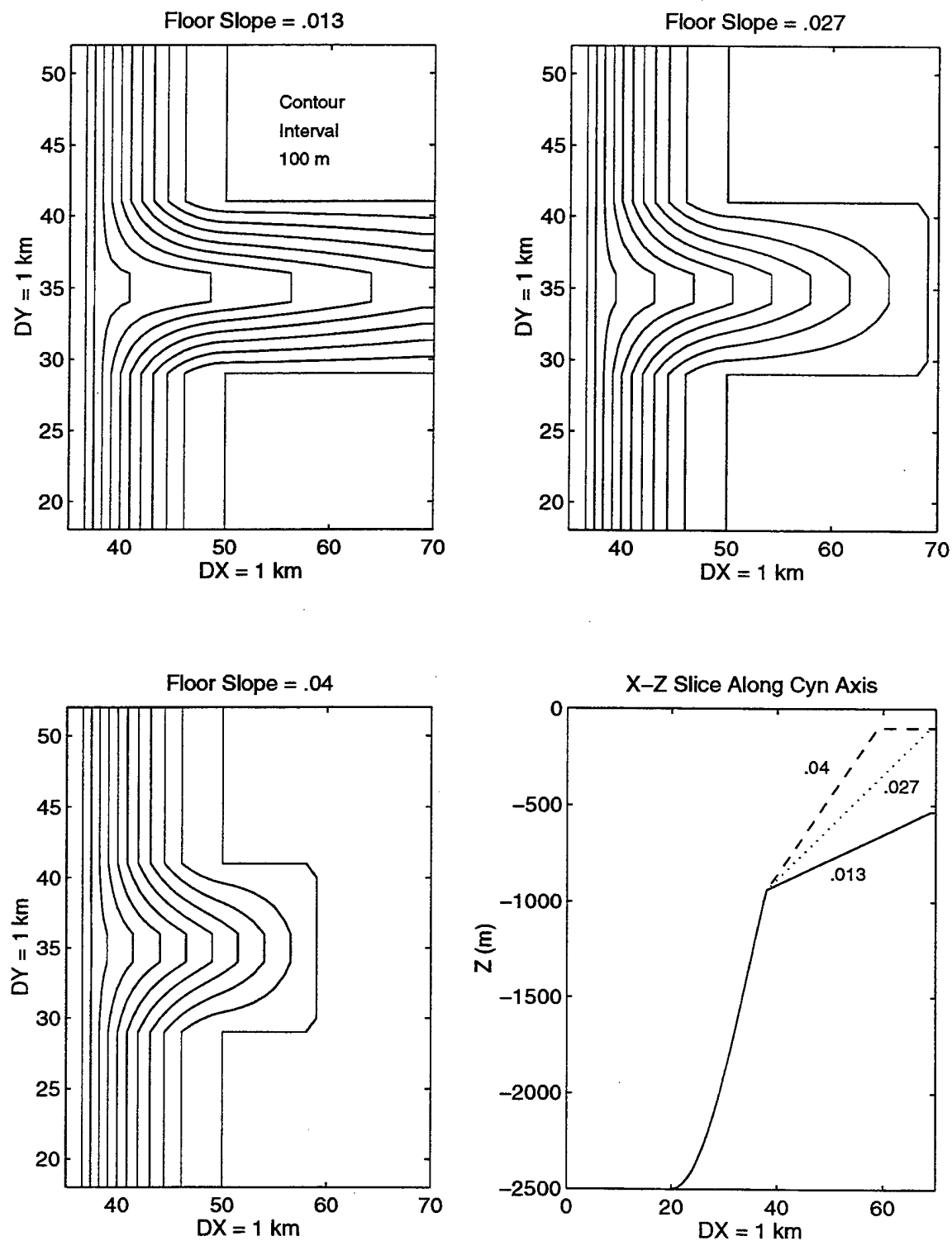
150
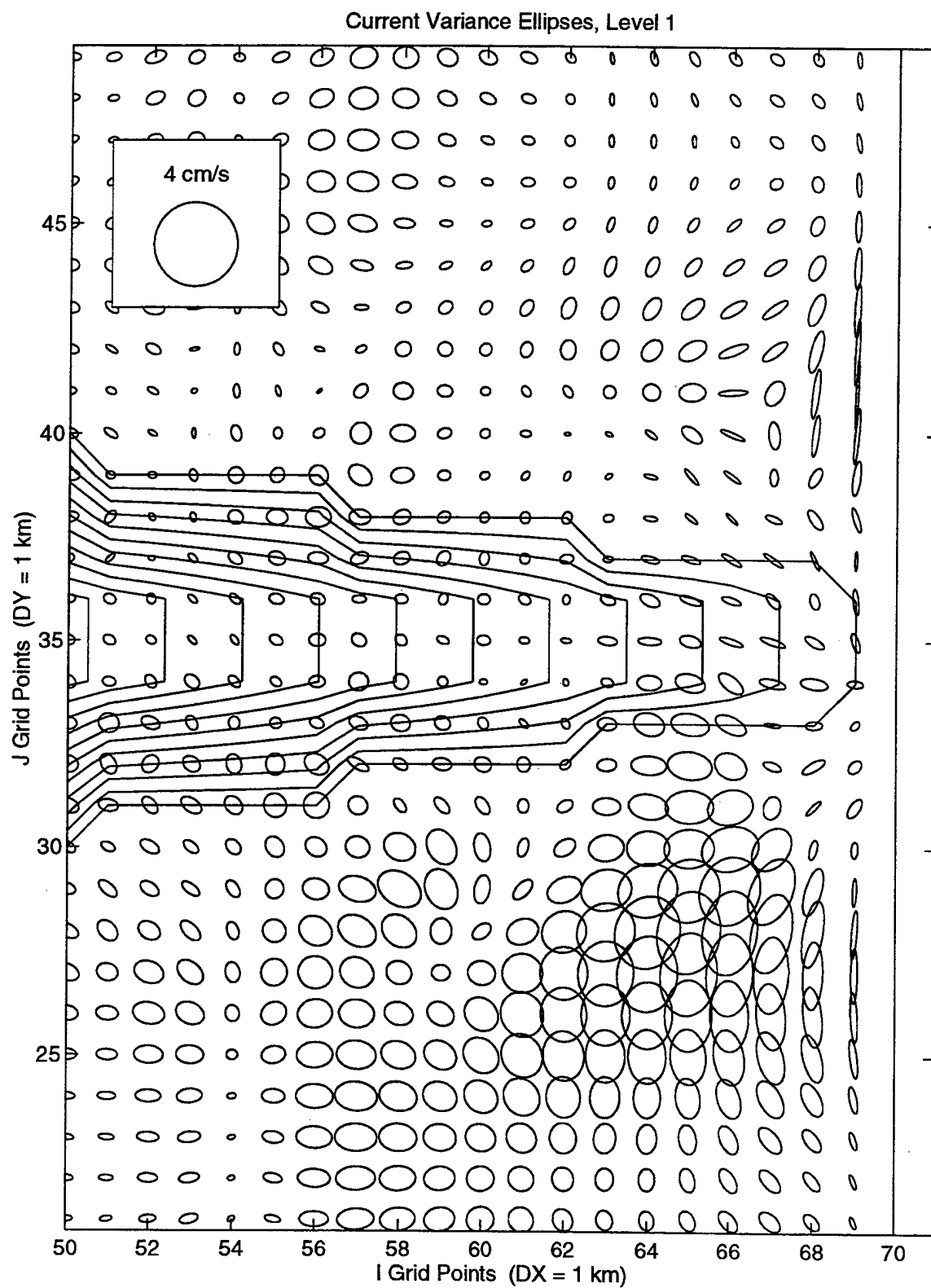
**Figure 51**. Near-Surface (Shallowest) Current Variance Ellipses.

151
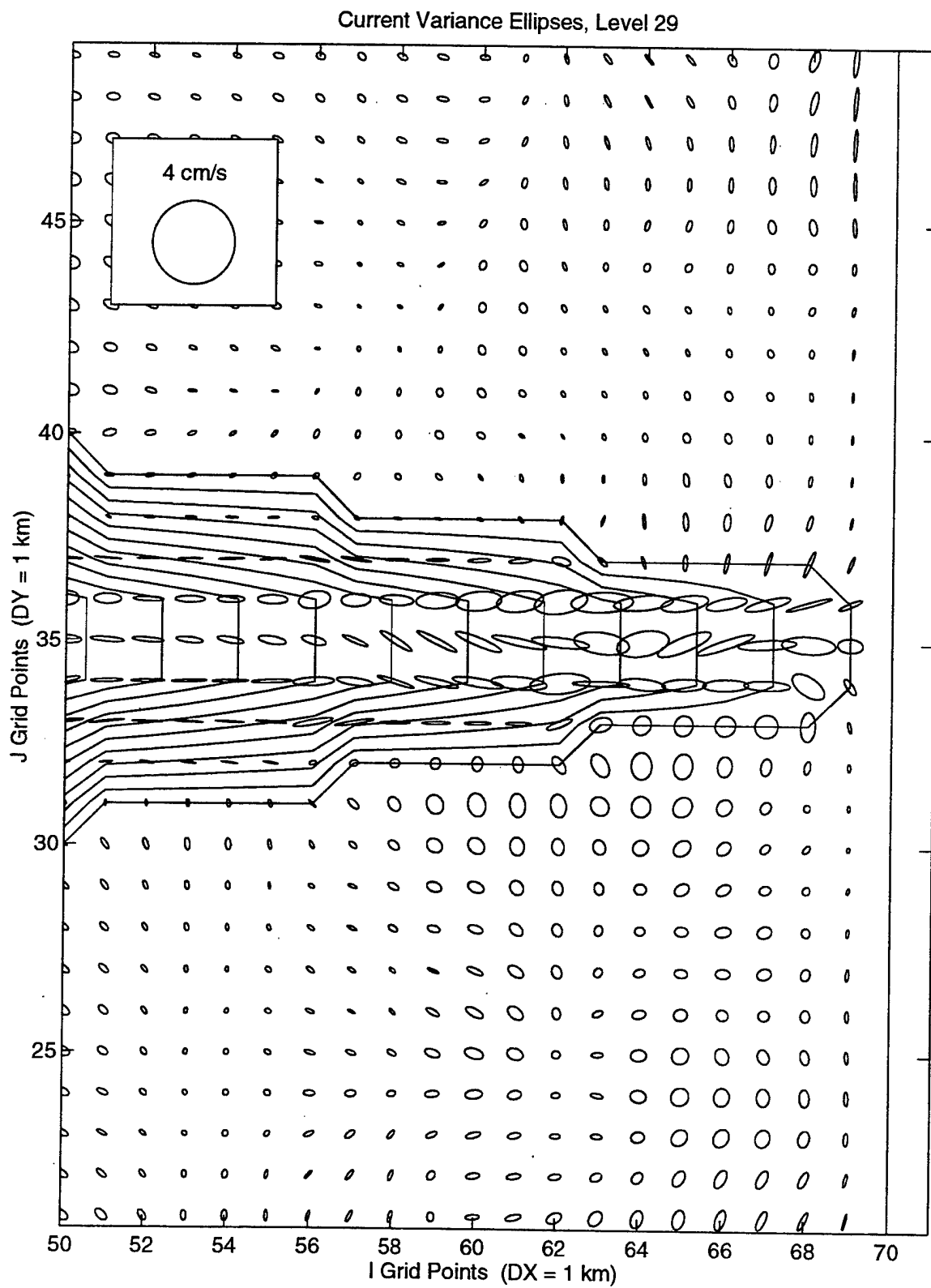
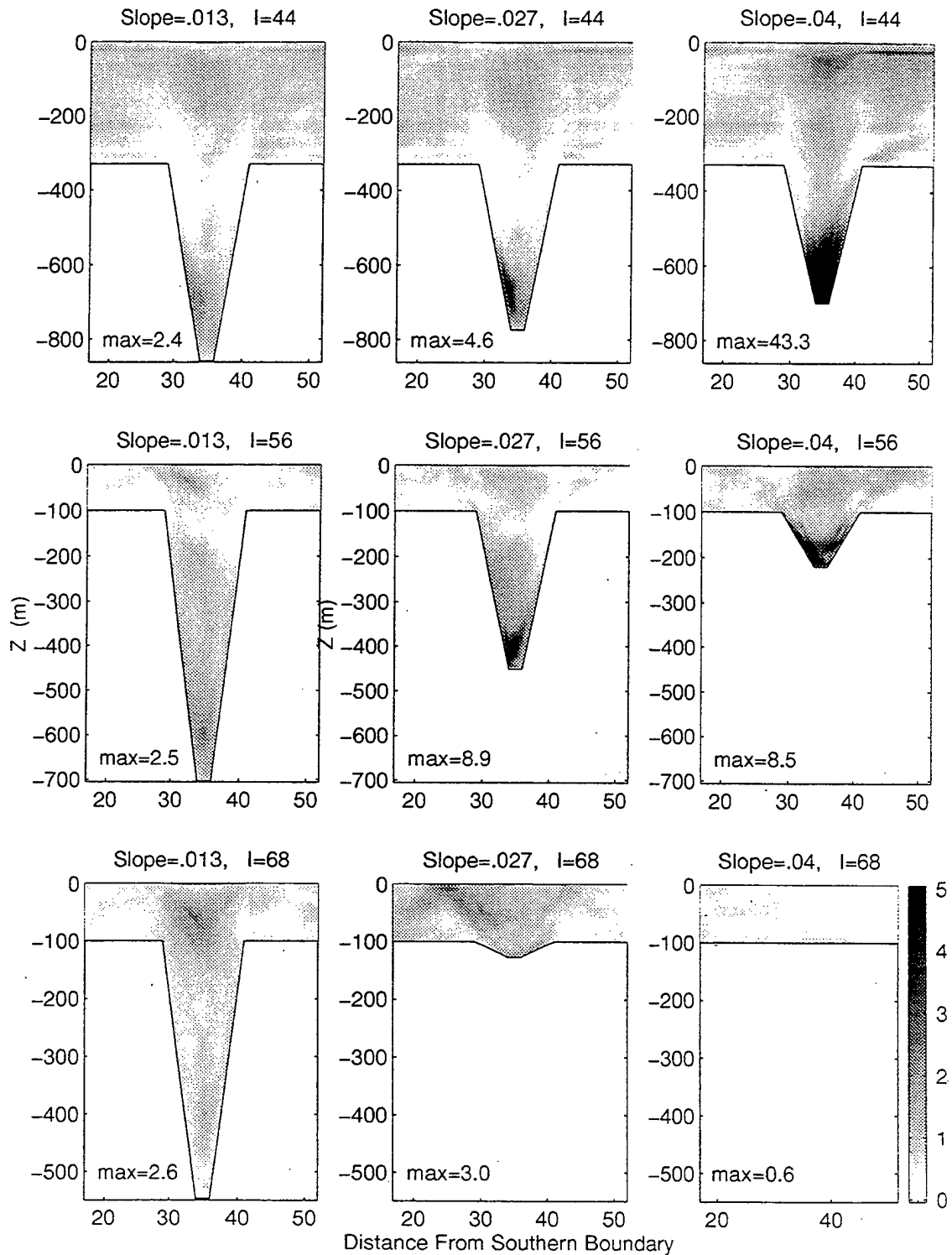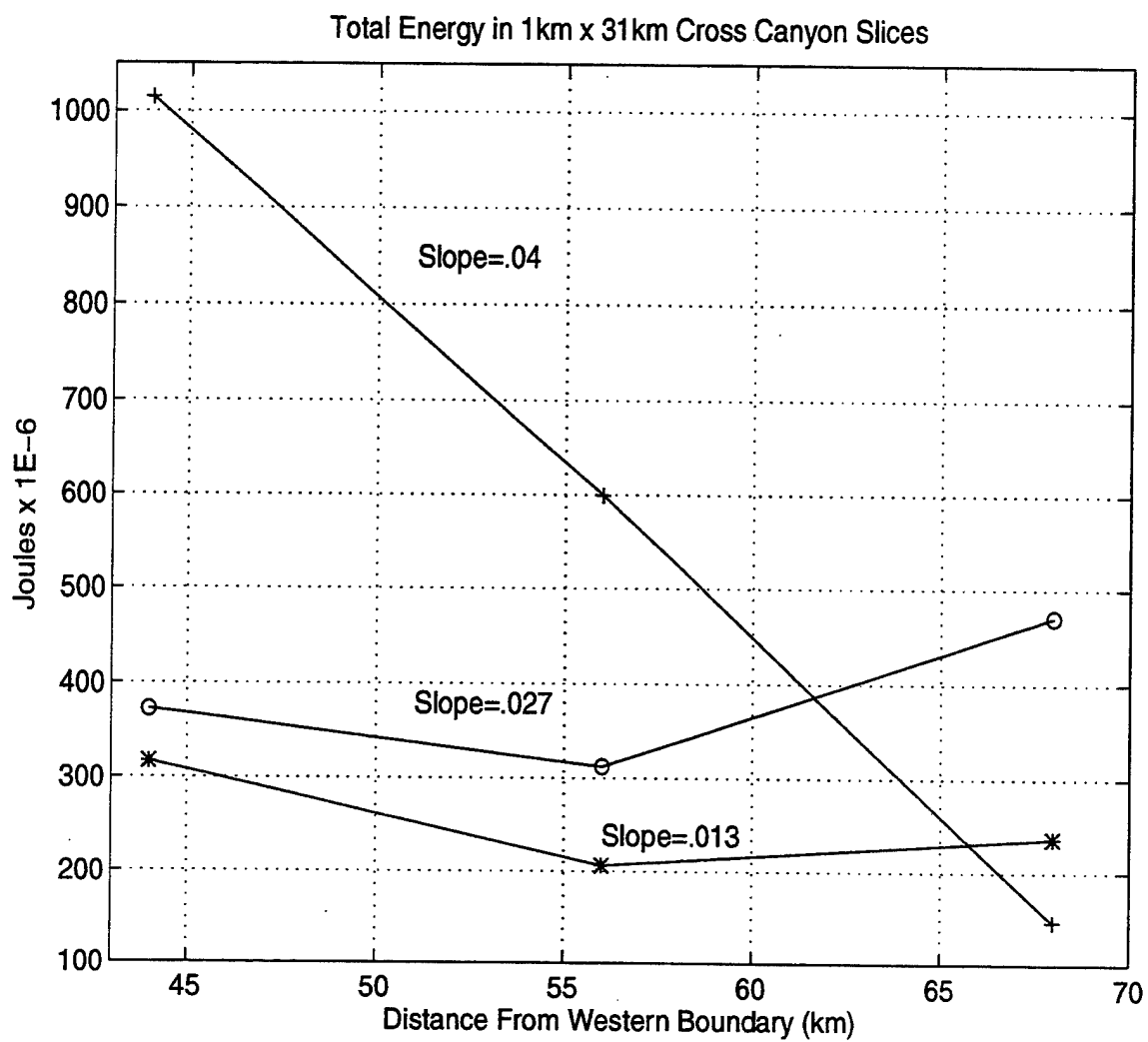**Figure 52**. Near-Bottom (Deepest) Current Variance Ellipses.

152

Figure 53. Model Canyon Topographies with Various Floor Slopes. Canyon shapes used to investigate the sensitivity of internal tide propagation to floor slope. Rim and floor widths, and the depth of the canyon foot, are the same in all three cases.
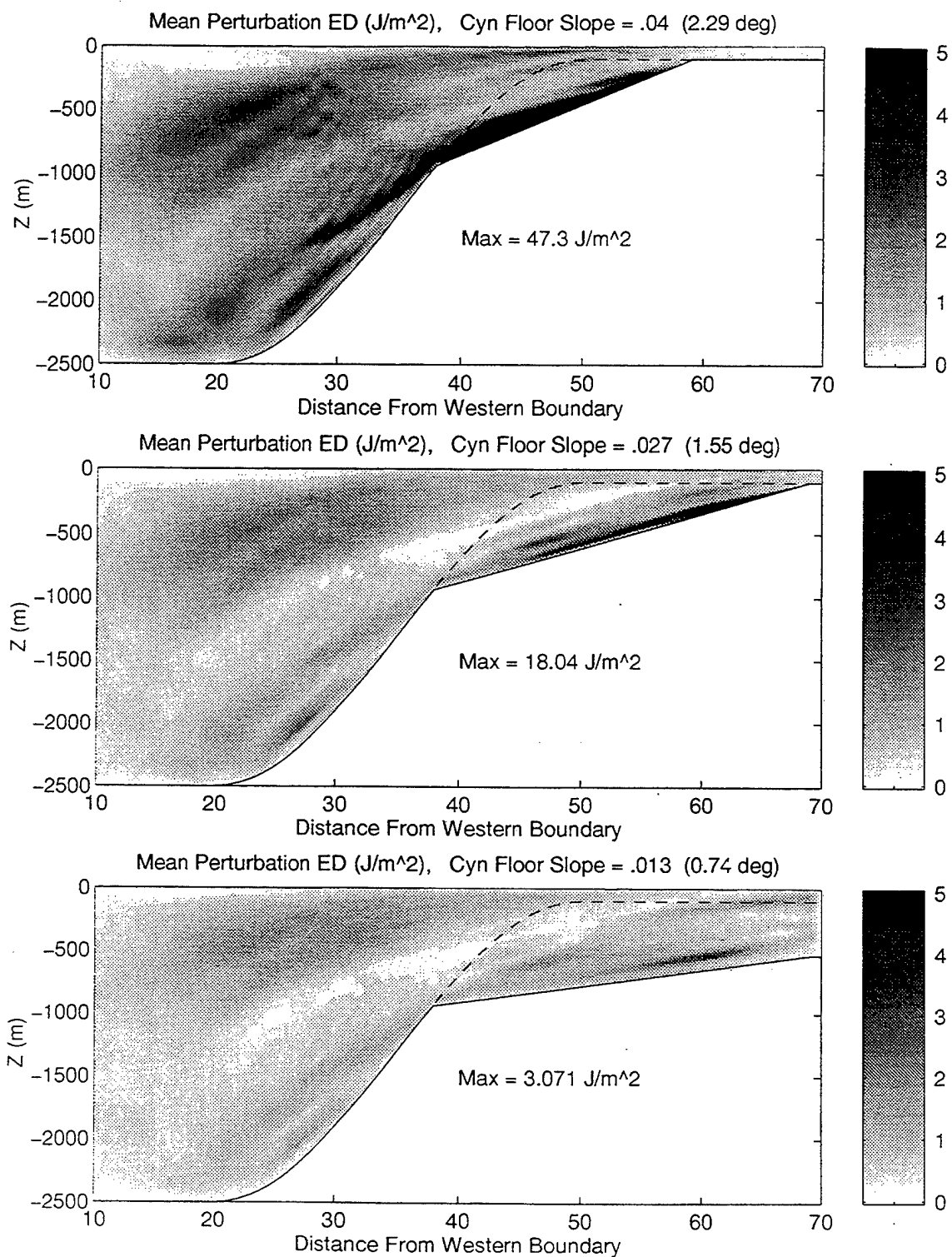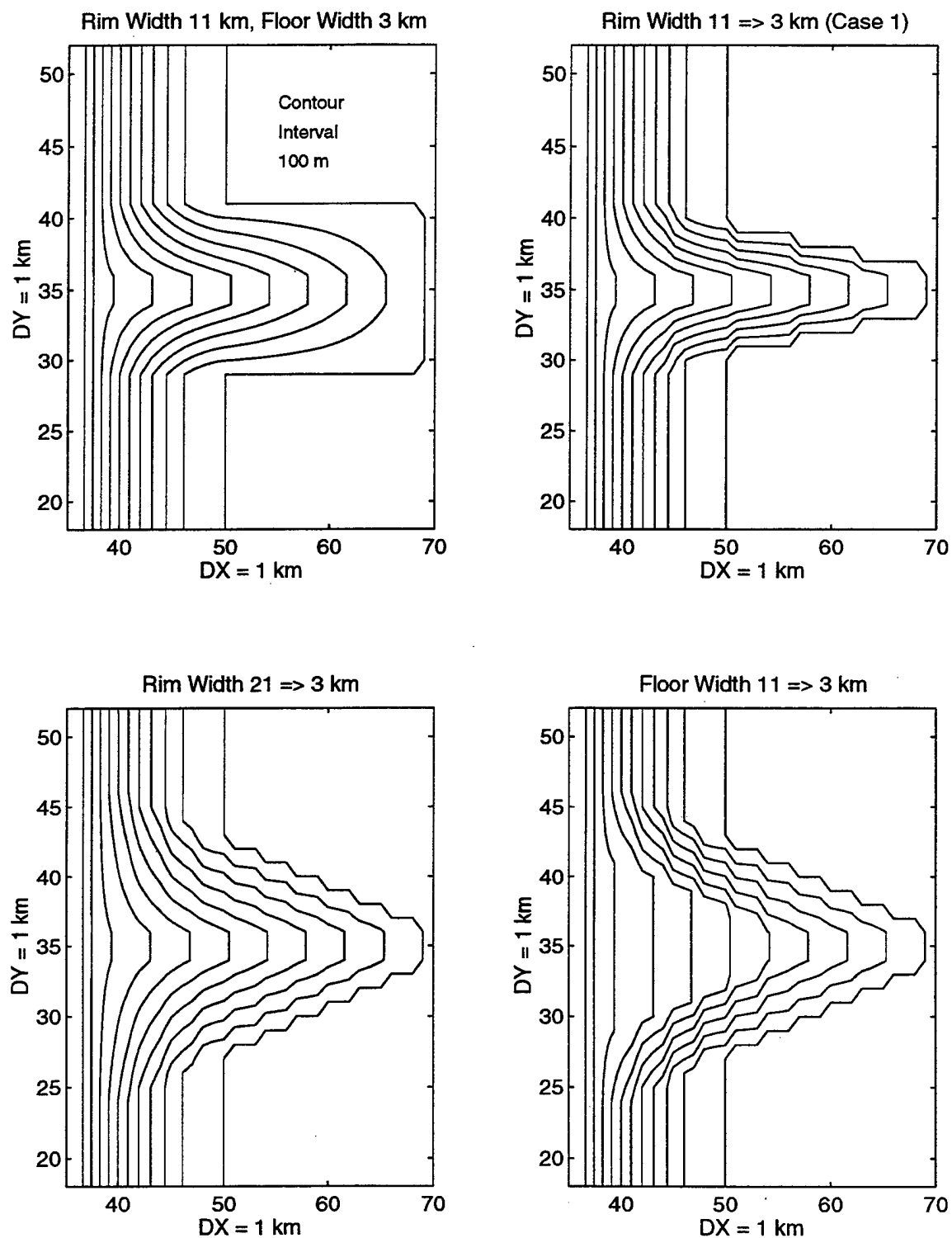
Figure 54. Energy Density Along-Canyon for Various Floor Slopes. Kinetic plus potential M2 energy density for along-canyon sections with various floor slopes. Bottom profiles for the continental shelf and slope adjacent to the canyon (dashed lines) are also shown.
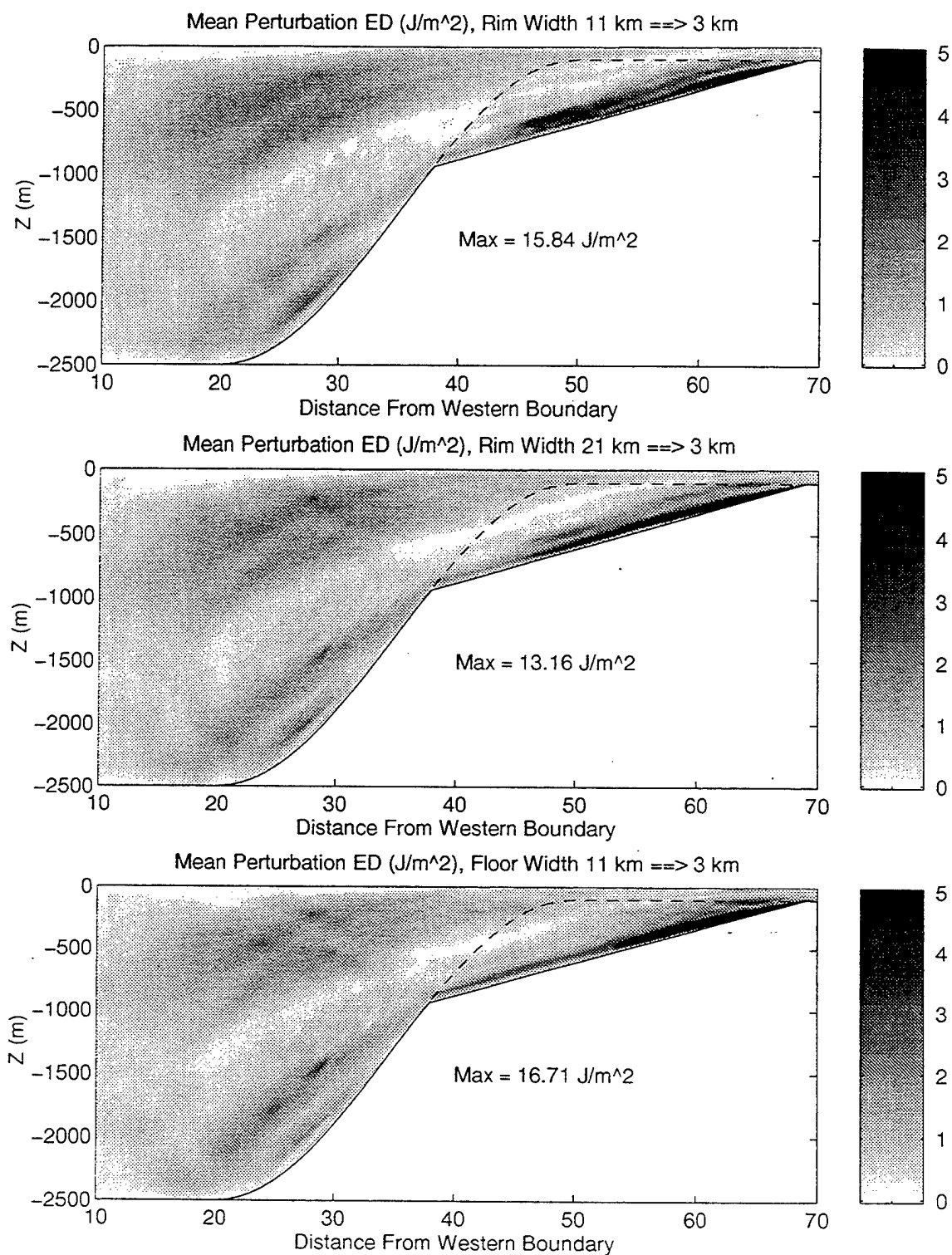
154

Figure 55. Energy Density Cross-Canyon for Various Floor Slopes. Kinetic plus potential energy density in cross-canyon sections 44 km (upper), 56 km (middle), and 68 km (lower) east of the western boundary with various floor slopes.
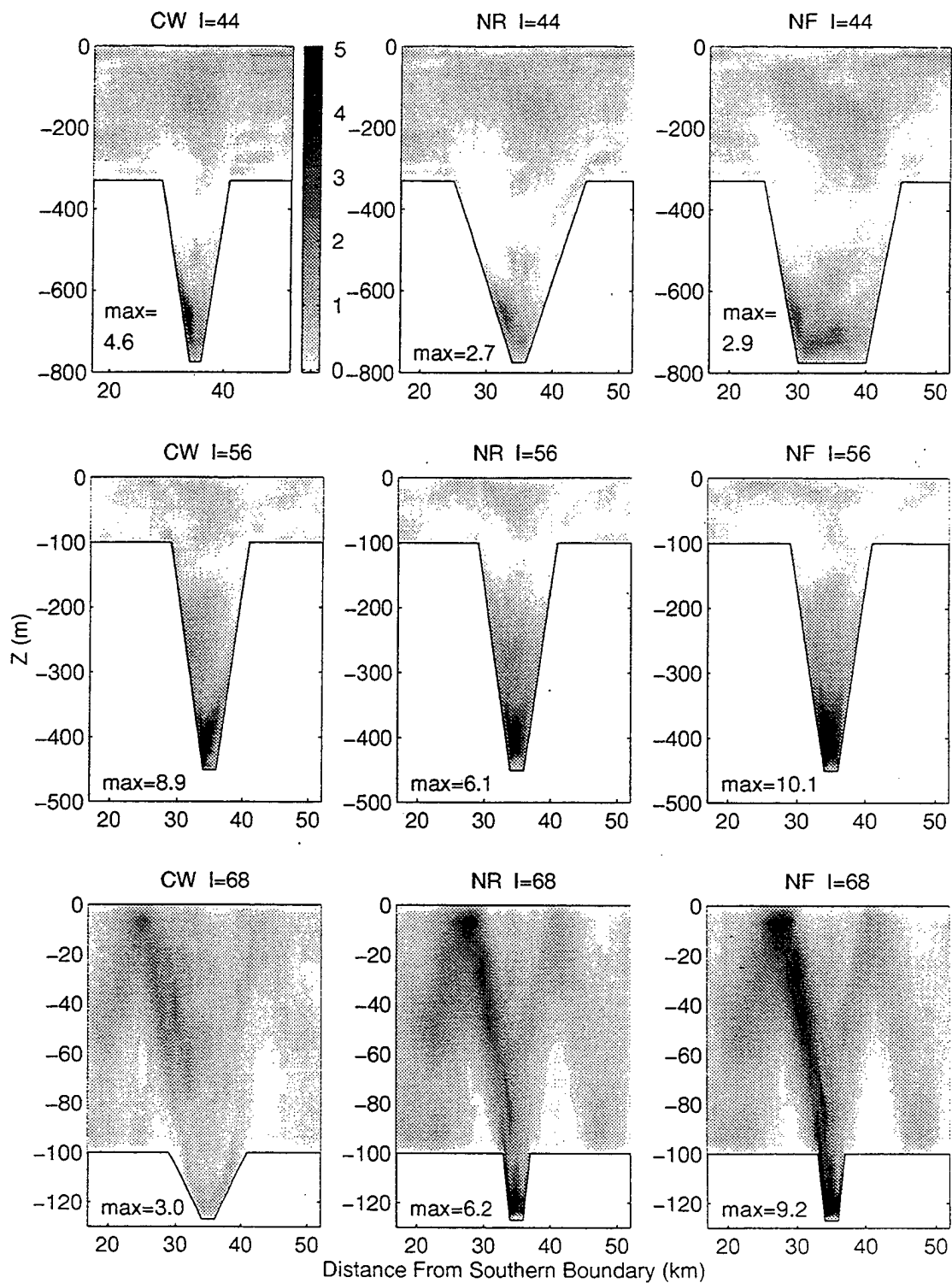
155

Figure 56. Total Energy in Cross-Canyon Sections for Various Floor Slopes. Integrated energy density for cross-canyon sections shown in Figure 55.

156

Figure 57. Model Canyon Topographies with Various Floor and/or Rim Widths. Canyon shapes used to investigate the sensitivity of internal tide propagation to floor and rim width. The same floor slope ($\gamma = 0.027$, $\tan^{-1} \gamma = 1.55°$) was used in each case.

157

Figure 58. Energy Density Along-Canyon for Various Floor and/or Rim Widths. As in Figure 54 with various floor and/or rim width.

158

Figure 59. Energy Density Cross-Canyon for Various Floor and/or Rim Widths. Kinetic plus potential energy density in cross-canyon sections (as in Figure 55) with various floor and/or rim width. CW = constant 11 km rim width, NR = narrowing rim (21-3 km), NF = narrowing floor (11-3 km) and rim (21-3 km).

159
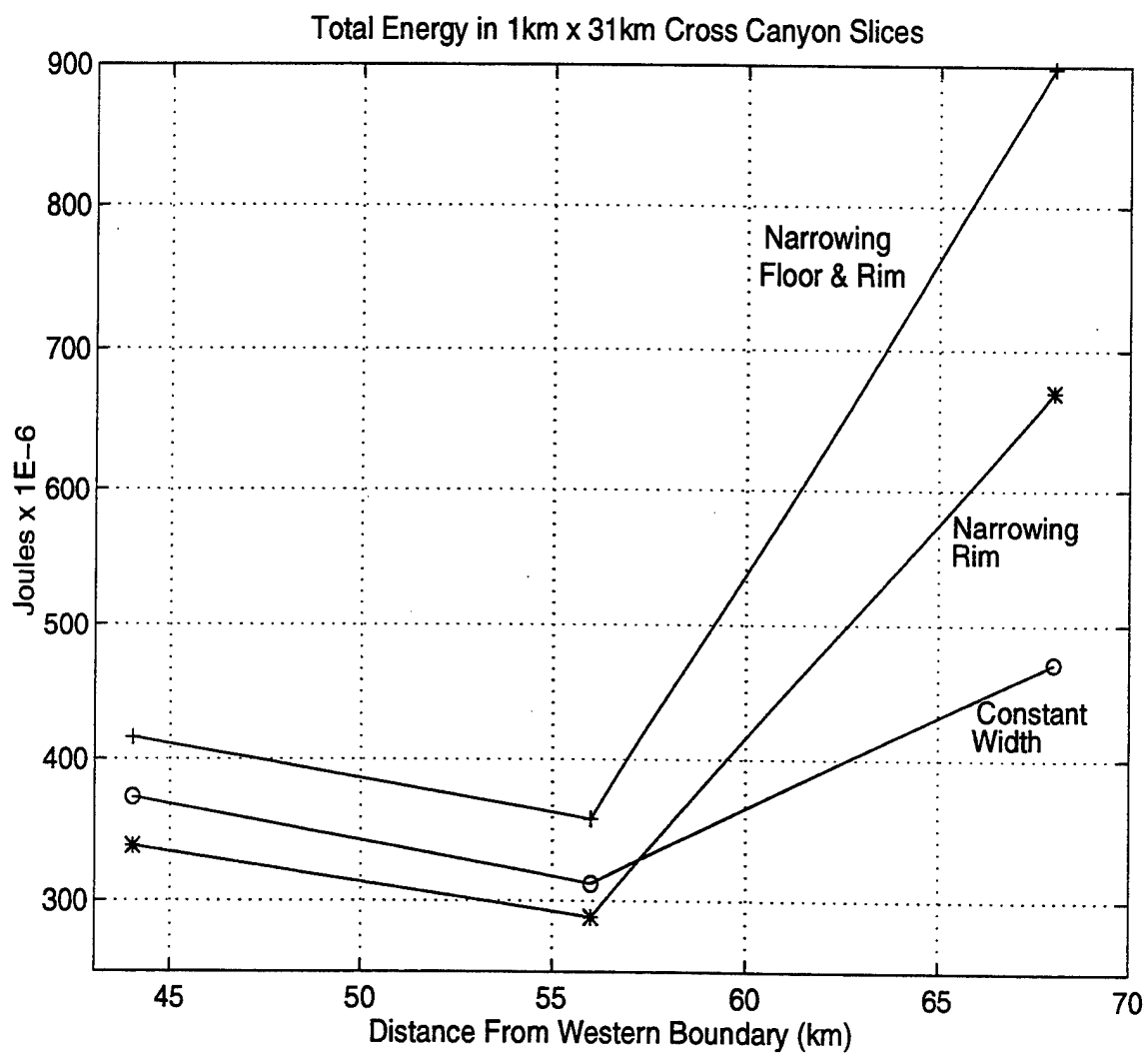
Figure 60. Total Energy in Cross-Canyon Sections for Various Floor and/or Rim Widths. Integrated energy density for cross-canyon sections shown in Figure 59.

APPENDIX A

HARMONIC ANALYSIS

In the case of sea level, the harmonic representation of the tidal constituents is:

$$A(t) = A_o + \sum_{i=1}^{N} A_i \cos(\sigma_i t - \phi_i) \tag{A1}$$

where $A(t)$ is the total sea level, A_o is the mean sea level, A_i is the amplitude of the ith constituent, σ_i is the frequency, and ϕ_i is the phase lag (or epoch). The phase lag, which is expressed in angular measure, may be expressed more fully as $\phi_i = G_i - V_i$, where V_i is the phase of the Equilibrium tide of the ith constituent at the start of the record (relative to the Greenwich Meridian), and G_i is the angle by which the ith constituent in the observed tide lags the corresponding Equilibrium tide response. By convention, G is expressed relative to Greenwich Mean Time (GMT), and is referred to as the "Greenwich Phase". Although Greenwich Phases may be expressed relative to the local time zone, they would require subsequent conversion to GMT if comparison with phases obtained in other time zones was desired. In this study, the Greenwich Phases of the various constituents in sea level variations are expressed in degrees relative to GMT. The phases of isopycnal oscillations are expressed in hours ahead of or behind sea level.

Currents are represented in a similar fashion, the main difference being that two components of flow (usually the u-component, positive in the eastward direction, and v-component, positive northward) are analyzed. The harmonic decomposition produces amplitude and phase information for each component of flow which is used to reconstruct u and v as a function of time for that particular constituent. The harmonic representation of currents is as follows:

$$U(t) = u_o(t) + \sum_{i=1}^{N} u_i \cos(\sigma_i t - \phi_{u_i}) + i[v_o(t) + \sum_{i=1}^{N} v_i \cos(\sigma_i t - \phi_{v_i})] \tag{A2}$$

The first two terms on the right side of the equation are the aperiodic (low frequency, non-tidal) and periodic (tidal) parts of the east-west component of flow, and the final two terms are the aperiodic and periodic parts of the north-south component. Setting $A_1 = u_i \cos\phi_{u_i}$, $B_1 = u_i \sin\phi_{u_i}$, $A_2 = v_i \cos\phi_{v_i}$, and $B_2 = v_i \sin\phi_{v_i}$, then dropping the constituent numbering suffix i and setting:

$$a^+ = [(\frac{A_1 + B_2}{2})^2 + (\frac{A_2 - B_1}{2})^2]^{1/2}, \qquad a^- = [(\frac{A_1 - B_2}{2})^2 + (\frac{A_2 + B_1}{2})^2]^{1/2},$$

161

$$\varepsilon^+ = \arctan(\frac{A_2 - B_1}{A_1 + B_2}), \quad \text{and} \quad \varepsilon^- = \arctan(\frac{A_2 + B_1}{A_1 - B_2}),$$

and applying some algebra (Godin, 1972), the tidal currents contribution for any constituent is then seen to be

$$U(t) = U^+(t) + U^-(t) = a^+ \exp i(\varepsilon^+ + \sigma t) + a^- \exp i(\varepsilon^- - \sigma t) \qquad \text{(A3)}$$

$$= \exp[i(\frac{\varepsilon^+ + \varepsilon^-}{2})][(U_{maj})\cos((\frac{\varepsilon^+ - \varepsilon^-}{2}) + \sigma t) + i(U_{min})\sin((\frac{\varepsilon^+ - \varepsilon^-}{2}) + \sigma t)] \qquad \text{(A4)}$$

Equation A3 reveals that this contribution consists of two vectors, $U^+(t)$ and $U^-(t)$, each rotating at the angular speed of σ cycles per hour. The former vector has length a^+, rotates counterclockwise, and is at ε^+ radians counterclockwise from the positive x (east/west) axis at time t = 0; while the latter has length a^-, rotates clockwise, and is at ε^- radians counterclockwise from the positive x axis at t = 0. The net rotational effect is that the composite vector U(t) moves counterclockwise if $a^+ > a^-$, clockwise if $a^+ < a^-$, and linearly if $a^+ = a^-$. Equation A4 shows that over a time period of $1/\sigma$ hours, the path of the composite vector traces out an ellipse (or a line segment, if moving linearly) whose respective semimajor (U_{maj}) and semiminor axis (U_{min}) lengths are $a^+ + a^-$ and $a^+ - a^-$, and whose angle of inclination (in the counterclockwise direction) from the positive x axis is $(\varepsilon^+ + \varepsilon^-)/2$ radians.

In this study, the phase difference between the maximum current and the maximum sea level deflection for a given constituent is depicted by offsetting the composite vector from the semi-major axis by an appropriate angle. For example, if the tidal current exhibits clockwise rotation and reaches maximum strength one quarter of a cycle before the occurrence of high tide for the same constituent (i.e., the current *leads* sea level by 90°), then the vector is plotted by offsetting it 90° in the clockwise direction from the semi-major axis. Conversely, if the current lags sea level by a quarter cycle, the vector is plotted by offsetting it 90° *counterclockwise* (in the opposite direction of current rotation) from the semi-major axis.

APPENDIX B

ERROR ESTIMATION OF THE TIDAL HEIGHTS ANALYSIS

Residual sea level, the difference between the observed and calculated sea level changes, can be used to calculate the expected error of the tidal heights analysis. The residual signal can be attributed to errors in the coefficients of the sine and cosine terms chosen as the best fit in the least squares matrix (Godin, 1972). The errors in the sine and cosine coefficients are propagated in the subsequent calculations of the amplitudes and phases of the various tidal constituents. In order to find the errors associated with each analyzed tidal height constituent then, the variance of the residual energy in each tidal band (low frequency, diurnal, semidiurnal, etc...) must be determined and then related to the standard deviation (or expected error) of the amplitudes and phases of the tidal constituents (Filloux and Snyder, 1979, and Tee, 1982).

The variance of some variable x is defined as

$$\sigma_x^{\,2} = \frac{1}{N} \sum_{n=1}^{N} (x_n - \bar{x})^2$$

where σ_x is the standard deviation of x, N is the total number of observations of x, and $x_n - \bar{x}$ is the difference between the nth observed signal and the mean. Similarly, the variance of the residual tidal heights, H', may be expressed as:

$$\sigma_H^{\,2} = \frac{1}{N} \sum_{n=1}^{N} (H'_n - \overline{H'})^2 .$$

Godin (1972) and Foreman (1978) assume the variance of the residual signal to be constant across the spectrum (i.e., "white noise"). Filloux and Snyder (1979) and Tee (1982) take a more rigorous approach in describing the residual signal by finding the variance of the noise in each of the major tidal bands. This more detailed method was also used in this study. In practice, σ_H was calculated for a given frequency band as follows. The residual sea level signal was determined by subtracting the calculated tidal contribution (the time varying signal resulting from the sum of the analyzed tidal constituents) from the measured sea level. A one-sided power spectrum of this residual signal was then computed, and the average variances in the various tidal bands (low frequency, diurnal, semidiurnal, terdiurnal, etc...) were determined. The average variances were calculated by integrating the spectral density in each band, dividing by the number of spectral estimates in the given band, and multiplying by two to account for the use of a one-

sided spectrum. The standard deviation (or expected error) of the amplitude for each major tidal constituent was then defined as the square root of the average variance of the noise in the appropriate frequency band.

A.   TIDAL CONSTITUENT AMPLITUDE ERROR.

The variance can be shown to depend on the errors in the sine and cosine coefficients (A and B) as follows. If x is a function of two variables, r and s, (i.e., $x = f(r,s)$) the following approximation can be made (Bevington, 1969):

$$x_n - \overline{x} \cong \frac{\partial f}{\partial r}(r_n - \overline{r}) + \frac{\partial f}{\partial s}(s_n - \overline{s}).$$

In the above expression, the partial derivatives are evaluated with the other variable (either r or s) fixed at its mean value. The variance of x can then be expressed as:

$$\sigma_x^{\,2} = (\frac{\partial f}{\partial r})^2 \sigma_r^{\,2} + (\frac{\partial f}{\partial s})^2 \sigma_s^{\,2} + 2\frac{\partial f}{\partial r}\frac{\partial f}{\partial s}\sigma_{rs}^{\,2}. \tag{B1}$$

As was stated in Appendix A, the harmonic representation of the sea level response to forcing by the ith constituent can be expressed as $H_i(t) = Z_i \cos(\sigma_i t - \phi_i)$. Expansion of this equation yields (dropping the i subscript):

$$H(t) = Z(\cos\sigma t \cos\phi + \sin\sigma t \sin\phi).$$

Letting $A = Z\cos\phi$ and $B = Z\sin\phi$, we have

$$H(t) = A\cos\sigma t + B\sin\sigma t$$

and

$$Z = \sqrt{A^2 + B^2}.$$

Since we are looking for the error in the calculated tidal amplitude, we substitute z for x in Equation B1, obtaining:

$$\sigma_z^{\,2} = (\frac{A}{Z})^2 \sigma_A^{\,2} + (\frac{B}{Z})^2 \sigma_B^{\,2} + 2(\frac{A}{Z})(\frac{B}{Z})\sigma_{AB}^{\,2}. \tag{B2}$$

164

For gap free records of sufficient length to separate the major constituents (29 days, using a Rayleigh Factor equal to 1) the following two assumptions can be made (Tee, 1982):

- The covariance of the sine and cosine terms is equal to zero ($\sigma_{AB}{}^2 = 0$).

- The variances of the sine and cosine terms are equal ($\sigma_A{}^2 = \sigma_B{}^2 = \sigma_H{}^2$).

We can then simplify Equation B2 as follows: $\sigma_Z = \sqrt{\dfrac{\sigma_H{}^2}{Z^2}(A^2 + B^2)}$, or since $Z = \sqrt{A^2 + B^2}$,

$$\sigma_Z = \sigma_H. \tag{B3}$$

Equation B3 simply states that the expected error of the calculated tidal amplitude is equal to the standard deviation (the square root of the average variance) of the residual sea level amplitude (noise) in the specified frequency band.

B.   TIDAL CONSTITUENT PHASE ERROR

Using the definition of A and B given above, the phase (ϕ) of the tidal constituent can be expressed as $\phi = \tan^{-1}\dfrac{B}{A}$. Substituting ϕ for x in Equation B1, we obtain:

$$\sigma_\phi^2 = (-\frac{B}{Z^2})^2 \sigma_A^2 + (\frac{A}{Z^2})^2 \sigma_B^2 + 2(-\frac{B}{Z^2})(\frac{A}{Z^2})\sigma_{AB}^2$$

which, after applying our two assumptions from above, simplifies to

$$\sigma_\phi = \frac{\sigma_H}{Z^2}\sqrt{(A^2 + B^2)} = \frac{\sigma_H}{Z}.$$

Thus the expected error of the calculated phase for a given constituent in the tidal heights record is easily found by dividing the standard deviation of the residual sea level in that band by the calculated amplitude of the constituent.

165

APPENDIX C

ERROR ESTIMATION OF THE TIDAL CURRENTS ANALYSIS

The determination of the errors associated with the calculated tidal current ellipse parameters employs the same basic method used to find the errors of the amplitudes and phases of the tidal heights constituents. The residual currents (the "noise" in the signal) contribute to errors in the coefficients of the sine and cosine terms chosen as the best fit in the least squares matrix, and these errors are propagated in the subsequent calculations of the lengths of the semimajor and semiminor axes, the phase, and the inclination of the tidal current ellipse.

In Appendix B the amplitude and phase for a given constituent in the tidal heights were shown to be functions of two variables, the coefficients of the sine and cosine terms. In the case of tidal currents, there are sine and cosine terms for both the east-west and north-south components of flow. Thus, the tidal current ellipse parameters are functions of four variables: two cosine coefficients (A_1 and A_2) and two sine coefficients (B_1 and B_2). The variance of a quantity which is a function of four variables ($x = f(A_1, B_1, A_2, B_2)$) is approximated by:

$$\sigma_x^2 = (\frac{\partial f}{\partial A_1})^2 \sigma_{A_1}^2 + (\frac{\partial f}{\partial B_1})^2 \sigma_{B_1}^2 + (\frac{\partial f}{\partial A_2^2})\sigma_{A_2}^2 + (\frac{\partial f}{\partial B_2^2})^2 \sigma_{B_2}^2 + \text{higher order terms} \quad (C1).$$

The higher order terms are associated with the covariances of A_1, B_1, A_2, and B_2.

As in Appendix A, the magnitude of the semimajor axis can be expressed as

$$U_{maj} = a^+ + a^- = \frac{1}{2}[(A_1 + B_2)^2 + (A_2 - B_1)^2]^{\frac{1}{2}} + \frac{1}{2}[(A_1 - B_2)^2 + (A_2 + B_1)^2]^{\frac{1}{2}}.$$

An expression for the variance of the calculated semimajor axis is obtained by substituting U_{maj} for x in Equation C1. As in the tidal heights error analysis (Appendix B), we can assume that the higher order terms in Equation C1 are negligible, and that $\sigma_{A_1}^2 = \sigma_{B_1}^2 = \sigma_u^2$ and $\sigma_{A_2}^2 = \sigma_{B_2}^2 = \sigma_v^2$. The variance of the calculated semimajor axis then simplifies to:

$$\sigma_{U_{MAJ}}^2 = \sigma_u^2[(\frac{\partial U_{maj}}{\partial A_1})^2 + (\frac{\partial U_{maj}}{\partial B_1})^2] + \sigma_v^2[(\frac{\partial U_{maj}}{\partial A_2})^2 + (\frac{\partial U_{maj}}{\partial B_2})^2].$$

The partial derivatives of U_{maj} with respect to A_1, B_1, A_2, and B_2 are then determined, and the calculated values of the sine and cosine coefficients (determined during the

least squares analysis) are plugged into these expressions. The standard deviation of the noise in the u and v components of flow (σ_u and σ_v) were determined as follows. The residual currents were determined by subtracting the time series representing the u and v components of the total tidal current (resulting from the summation of all analyzed tidal constituents) from the time series representing the u and v components of the measured currents. As in the tidal heights error analysis, one-sided power spectra of these residual signals were computed, and the average variances in each tidal band were found by integrating the power spectrum in each band, dividing by the number of spectral estimates in the band, and multiplying by two to account for the use of one-sided spectra. The standard deviation of the residual u and v signals in each tidal band were then obtained by taking the square root of the variance in the appropriate band.

The procedures to determine the errors in the semiminor axis length (U_{min}), the ellipse orientation (*INC*), and the phase (*G*) are similar. The expressions for U_{min}, *INC*, and *G* were substituted for x in Equation C1, the values of A_1, A_2, B_1, and B_2 and the appropriate σ_u and σ_v were plugged into the resulting expressions, and the variances of these parameters were calculated for each of the major tidal constituents. The standard deviation (expected error) for each parameter was obtained by taking the square root of the calculated variance.

LIST OF REFERENCES

Baines, P.G., The generation of internal tides over steep continental slopes, *Phil. Trans. Roy. Soc. London, 227*, 27-58, 1974.

Baines, P.G., On internal tide generation models, *Deep Sea Res., 21*, 307-338, 1982.

Baines, P.G., Tidal motion in submarine canyons - a laboratory experiment. *J. Phys. Oceanogr., 13*, 310-328, 1983.

Baines, P.G., Internal tides, internal waves, and near-inertial motions, in *Baroclinic Processes on Continental Shelves*, edited by C.N.K. Mooers, pp. 19-31, American Geophysical Union, Washington, DC, 1986.

Barbee, W.B., J.G. Dworski, J.D. Irish, L.H. Larsen, and M. Rattray, Measurements of internal waves of tidal frequency near a continental boundary, *J.Geophys. Res., 80*, 1965-1974, 1975.

Battisti, D.S., and Clarke, A.J., A simple method for estimating barotropic tidal currents on continental margins with specific application to the M2 tide off the Atlantic and Pacific Coasts of the United States, *J. Phys. Oceanogr., 12*, 8-16, 1982.

Bevington, P.R., *Data Reduction and Error Analysis for the Physical Sciences*, McGraw-Hill, New York, 1969.

Blumberg, A.F., and G.L. Mellor, A description of a three-dimensional coastal ocean circulation model, in *Three-Dimensional Coastal Ocean Models*, Vol. 4, edited by N. Heaps, pp. 1-16, American Geophysical Union, Washington, D.C., 1987.

Bowden, K.F., Turbulence, in *The Sea*, Vol 1, edited by M.N. Hill, pp. 802-825, John Wiley and Sons, New York, 1962.

Breaker, L.C., and W.W. Broenkow, The circulation of Monterey Bay and related processes, in *Oceanography and Marine Biology: an Annual Review, 32*, 1-64, edited by A.D. Ansell, R.N. Gibson, and M. Barnes, UCL Press, 1994.

Brink, K.H., On the effect of bottom friction on internal waves, *Cont. Shelf Res., 8*, 397-403, 1988.

Broenkow, W.W., and S. J. McKain, Tidal oscillations at the head of Monterey Submarine Canyon and their relation to oceanographic sampling and the circulation of water in Monterey Bay, Moss Landing Marine Laboratories, Moss Landing, California, Technical Publication 72-05, 1972.

Cacchione, D., and C. Wunsch, Experimental study of internal waves over a slope, *J. Fluid Mech., 66*, 223-239, 1974.

Caster, W.A., Near-bottom currents in Monterey Submarine Canyon and on the adjacent shelf, Master's Thesis, Naval Postgraduate School, Monterey, California, 1969.

Chapman, D.C., Numerical treatment of cross-shelf open boundaries in a barotropic coastal ocean model, *J. Phys. Oceanogr.*, 15, 1060-1075, 1985.

Chapman, D.C., Nearly trapped internal edge waves in a geophysical ocean, *Deep Sea Res.*, 29, 525-533, 1982.

Clarke, A.J., The dynamics of barotropic tides over the continental shelf and slope, in *Tidal Hydrodynamics*, edited by B.B. Parker, pp. 79-107, John Wiley and Sons, Inc., New York, 1991.

Coelho, E.F., Tidal dynamics and mixing over steep topography, PhD Dissertation, Naval Postgraduate School, Monterey, California, 1994.

Courant, R., K.O. Friedrichs, and H. Lewy, Uber die partiellen differenzengleichurgen der mathematischen physik, *Mathematische Annalen*, 100, 32-74, 1928.

DeWitt, L.M., M.D. Levine, C.A. Paulson, and W.V. Burt, Semidiurnal internal tide in JASIN: observations and simulation, *J. Geophys. Res.*, 91(C2), 2581-2592, 1986.

Dooley, J.J., An investigation of near-bottom currents in the Monterey Submarine Canyon, Master's Thesis, Naval Postgraduate School, Monterey, California, 1968.

Drakopolous, P., and R.F. Marsden, The internal tide off the west coast of Vancouver Island, *J. Phys. Oceanogr.*, 23, 758-775, 1993.

Durham, D.L., United States Navy operational oceanographic nowcast/forecast system, *OCEANS 94 Proceedings*, III, 45-50, 1994.

Eriksen, C.C., Observations of internal wave reflection off sloping bottoms, *J. Geophys. Res.*, 87(C1), 525-538, 1982.

Eriksen, C.C., Implications of ocean bottom reflection for internal wave spectra and mixing, *J. Phys. Oceanogr.*, 15, 1145-1156, 1985.

Filloux, J.H., and R.L. Snyder, A study of tides, set up, and bottom friction in a shallow semi-enclosed basin. Part I: Field experiment and harmonic analysis, *J. Phys. Oceanogr.,9*, 158-169, 1979.

Foreman, M.G.G., Manual for tidal heights analysis and prediction, Pac. Mar. Sci. Rep. 77-10, Inst. Of Ocean Sciences, Patricia Bay, Sydney, B.C., 1977.

Foreman, M.G.G., Manual for tidal currents analysis and prediction, Pac. Mar. Sci. Rep. 78-6, Inst. Of Ocean Sciences, Patricia Bay, Sydney, B.C., 1978.

Foreman, M.G.G., Tide removal requiring a dynamical interpretation, in *Quantitative Skill Assessment for Coastal Ocean Models*, edited by D.R. Lynch and A.M. Davies, pp. 224-239, American Geophysical Union, Washington DC, 1995.

Galperin, B., and G.L. Mellor, A time-dependent, three-dimensional model of the Delaware Bay and River system, part 1: description of the model and tidal analysis, *Estuarine, Coastal, and Shelf Sci*, 31, 231-253, 1990.

Gardner, W.D., Periodic resuspension in Baltimore Canyon by focusing of internal waves, *J. Geophys. Res.*, *94*(C12), 18,185-18,194, 1989.

Garrett, C.J.R., and D. Gilbert, Estimates of vertical mixing by internal waves reflected off a sloping bottom, in *Small-scale Turbulence and Mixing in the Ocean*, edited by J.C.J. Nihoul and b.M. Jamart, Elsevier, pp. 405-423, 1988.

Garrett, C.J.R., and W.H. Munk., Space-time scales of internal waves: a progress report, *J. Geophys. Res.*, *80*, 291-97, 1975.

Garrett, C.J.R., and W.H. Munk., Internal waves in the ocean, *Ann. Rev. Fluid Mech.*, *11*, 339-69, 1979.

Gary, J.M., Estimate of truncation error in transformed coordinate, primitive equation atmospheric models, *J. Atmos. Sci*, 30, 223-233, 1973.

Gatje, P.H., and D.D. Pizinger, Bottom current measurements in the head of Monterey Submarine Canyon, Master's Thesis, Naval Postgraduate School, Monterey, California, 1965.

Gilbert, D., A search for evidence of critical internal wave reflection on the continental rise and slope off Nova Scotia, *Atmos-Ocean*, *31*, 99-122, 1993.

Gilbert, D., and C.J.R. Garrett, Implications for ocean mixing of internal waves scattering off irregular topography, *J. Phys. Oceanogr.*, *19*, 1716-1729, 1989.

Gill, A.E., *Atmosphere-Ocean Dynamics*, Academic Press, Inc., Orlando, 1982.

Godin, G., *The Analysis of Tides*, Univ. of Toronto Press, Toronto, 1972.

Godin, G., The analysis of tides and currents, in *Tidal Hydrodynamics*, edited by B.B. Parker, pp. 675-709, John Wiley and Sons, Inc., New York, 1991.

Gordon, R.L., and N.F. Marshall, Submarine canyons: internal wave traps?, *Geophys. Res. Ltrs.*, *10*, 622-624, 1976.

Griffin, D.A., and J.H. Middleton, Upwelling and internal tides over the inner New South Wales Continental Shelf, *J. Geophys. Res.*, *97*(C9), 14,389-14,405, 1992.

Haney, R.L., On the pressure gradient force over steep topography in sigma coordinate ocean models, *J. Phys. Oceanogr.*, 21, 610-619, 1991.

Heard, J.A., A kinematic model of baroclinic tidal currents at the head of Monterey Submarine Canyon, Master's Thesis, Moss Landing Marine Laboratories, San Jose State University, Moss Landing, California, 1992.

Hickey, B.M., Coastal submarine canyons, in *Topographic Effects in the Ocean*, pp. 95-110, Proceedings, Hawaiian Winter Workshop, University of Hawaii at Manoa, 17-20 January, 1995.

Hollister, J.E., Currents in Monterey Submarine Canyon, Master's Thesis, Naval Postgraduate School, Monterey, California, 1975.

Holloway, P.E., On the semidiurnal internal tide at a shelf-break region on the Australian North West Shelf, *J. Phys. Oceanogr., 14*, 1787-1799, 1984.

Holloway, P.E., A comparison of semidiurnal internal tides from different bathymetric locations on the Australian North West Shelf, *J. Phys. Oceanogr., 15*, 240-251, 1985.

Holloway, P.E., On the dissipation of internal tides, in *Tidal Hydrodynamics*, edited by B.B. Parker, pp. 449-468, John Wiley and Sons, Inc., New York, 1991.

Holloway, P.E., Observations of internal tide propagation on the Australian North West Shelf, *J. Phys. Oceanogr, 24*, 1706-1716, 1994.

Holloway, P.E., A numerical model of internal tides with application to the Australian North West Shelf, J. Phys. Oceanogr., 26, 21-36, 1996.

Hotchkiss, F.S., and C.H. Wunsch., Internal waves in Hudson Canyon with possible geological implications, *Deep Sea Res., 29*, 415-442, 1982.

Hunkins, K., Mean and tidal currents in Baltimore Canyon, *J. Geophys. Res., 93*(C6), 6917-6929, 1988.

Huthnance, J.M., Internal tides and waves near the continental shelf edge, *Geophys. Astrophys. Fluid Dyn., 48*, 81-106, 1989.

Huthnance, J.M., Circulation, exchange, and mixing at the ocean-shelf boundary, in *Topographic Effects in the Ocean*, pp. 85-93, Proceedings, Hawaiian Winter Workshop, University of Hawaii at Manoa, 17-20 January, 1995.

Huthnance, J.M., and P.G. Baines, Tidal currents in the Northwest African upwelling region, *Deep Sea Res., 29*, 285-306, 1982.

Ivey, G.N., and R.I. Nokes, Mixing driven by breaking of internal waves against sloping boundaries, *J. Fluid Mech., 204*, 479-500, 1989.

Joyce, T.M., On in-situ calibration of shipboard ADCPs, *J. Atmos. Oceanic Technol., 6*, 169-172, 1989.

Konyaev, K.V., K.D. Sabinin, and A.N. Serebryany, Large-amplitude internal waves at the Mascarene Ridge in the Indian Ocean, *Deep Sea Res., 42*, 2075-2091, 1995.

Kowalik, Z., and T.S. Murty, *Numerical Modeling of Ocean Dynamics*, World Scientific, River Edge, New Jersey, 1993.

Largier, J.L., The internal tide over the shelf inshore of Cape Point Valley, South Africa, *J. Geophys. Res., 99*(C5), 10,023-10,034, 1994.

Lazanoff, S.M., An evaluation of a numerical water elevation and tidal current prediction model applied to Monterey Bay, Master's Thesis, Naval Postgraduate School, Monterey, California, 1971.

Lentz, S.J., The accuracy of tide gauge measurements at sub-tidal frequencies, *J. Atmos. Ocean. Tech., 10*, 238-245, 1993.

Lewis, J.K., Y.L. Hsu, and A.F. Blumberg, Boundary forcing and a dual mode calculation scheme for coastal tidal models using step-wise bathymetry, in *Coastal Modeling III*, pp, 422-431, Proceedings of the 3rd International Conference Sponsored by the Waterway, Port, Coastal and Ocean Division / ASCE, September 8-10, 1993.

Maas, L.R.M., and F.A. Lam, Geometric focusing of internal waves, *J. Fluid Mech., 300*, 1-41, 1995.

Maixner, H.V., Comparison of predicted and observed tides at Monterey California, Master's Thesis, Naval Postgraduate School, Monterey, California, 1973.

Martinsen, E.A., and H. Engedahl, Implementation and testing of a lateral boundary scheme as an open boundary condition in a barotropic ocean model., *Coastal Eng.*, 11, 603-627, 1987.

McKay, D.A., A determination of surface currents in the vicinity of the Monterey Submarine Canyon by the electromagnetic method, Master's Thesis, Naval Postgraduate School, Monterey, California, 1970.

Mellor, G.L., User's guide for a three-dimensional, primitive equation, numerical ocean model, Unpublished Report, Atmospheric and Ocean Sciences Program, Princeton Univ., Princeton, New Jersey, 1996.

Mellor, G.L., An equation of state for numerical models of oceans and estuaries, *J. Atmos. Oceanic Technol.*, 8, 609-611, 1991.

Mellor, G.L., and A.F. Blumberg, Modeling vertical and horizontal diffusivities with the sigma coordinate system, *Mon. Wea. Rev.*, 113, 1379-1383, 1985.

Mellor, G.L., T. Ezer, and L.-Y. Oey, The pressure gradient conundrum of sigma coordinate ocean models, *J. Atmos. Oceanic Technol.*, 11, 1126-1134, 1994.

Mellor, G.L., and T. Yamada, Development of a turbulence closure model for geophysical fluid problems, *Rev. Geophys. Space Phys.*, 20, 851-875, 1982.

Mesinger, F., and Z.I. Janjic, Problems and numerical methods of the incorporation of mountains in atmospheric models., Lect. Appl. Math., 22, 81-120, 1985.

Miles, J.W., Kelvin waves on oceanic boundaries, *J. Fluid Mech.*, 55, 113-127, 1972.

Munk, W., F. Snodgrass, and M. Wimbush, Tides offshore: transition from California coastal to deep-sea waters, *Geophys. Fluid Dyn., 1*, 161-235, 1970.

Münnich, M., The influence of bottom topography on internal seiches in stratified media, *Dyn. Atmos. and Oceans, 23*, 257-266, 1996.

National Ocean Service, *Tidal Current Tables 1995, Pacific Coast of North America and Asia North*, National Oceanic and Atmospheric Administration, 1991.

Niiler, P.P., On the internal tidal motions in the Florida Straits, *Deep Sea Res., 15*, 113-123, 1968.

Noble, M., Beardsley, R.C., Gardner, J.V., Rosenfeld, L.K., and Smith, R.L., Tidal currents seaward of the Northern California Continental Shelf, *J. Geophys. Res.*, 92, 1655-1681, 1987.

Njus, I.J., An investigation of the environmental factors affecting the near-bottom currents in Monterey Submarine Canyon, Master's Thesis, Naval Postgraduate School, Monterey, California, 1968.

O'Connor, W.P., A numerical model of tides and storm surges in the Rio de la Plata Estuary, *Cont. Shelf Res.*, 11, 1491-1508, 1991.

Oey, L.-Y., G.L. Mellor, and R.I. Hires (1985) A three-dimensional simulation of the Hudson-Raritan Estuary, part I: description of the model and model simulations. *J. Phys. Ocean.* 15, 1676-1692.

Oey, L.-Y., and P. Chen, A model of circulation in the Northeast Atlantic Shelves and Seas, *J. Geophys. Res.*, 97 (C12), 20,087-20,115, 1992.

Oey, L.-Y., Y.-H. Zhang, and P. Chen, Simulation of the Norwegian Coastal Current in the vicinity of the Halten Bank: comparison with observations and process study of bank-induced meanders, *J. Mar. Sys.*, 3, 391-416, 1992.

Orlanski, I., A simple boundary condition for unbounded hyperbolic flows, *J. Comp. Phys.*, 21, 251-269, 1976.

Paduan, J.D., D.E. Barrick, B.J. Lipa, and E.T. Petruncio, Surface currents within and offshore of Monterey Bay as mapped by a multiple-site HF Radar (CODAR) network, in *Proceedings, IEEE Fifth Working Conference on Current Measurement*, St. Petersburg, FL, 7-9 February, 1995.

Park, Y., Semidiurnal internal tides on the continental shelf off Abidjan, *J. Phys. Oceanogr.*, *16*, 1585-1592, 1986.

Parker, B.B., The relative importance of the various nonlinear mechanisms in a wide range of tidal interactions (Review), in *Tidal Hydrodynamics*, edited by B.B. Parker, pp. 237-268, John Wiley and Sons, Inc., New York, 1991.

Petrie, B., M2 surface and internal tides on the Scotian shelf and slope, *J. Mar. Res.*, *33*, 303-323, 1975.

Petruncio, E.T., Characterization of tidal currents in Monterey Bay from remote and in-situ measurements, Master's Thesis Naval Postgraduate School, Monterey, California, 1993.

Phillips, O.M., *The Dynamics of the Upper Ocean*, 2nd ed., Cambridge Univ. Press, 1977.

Pineda, J., An internal tidal bore regime at nearshore stations along western U.S.A.: predictable upwelling within the lunar cycle, *Cont. Shelf Res.*, 15, 1023-1041, 1995.

Pingree, R.D. and A.L. New, Downward propagation of internal tidal energy into the Bay of Biscay, *Deep Sea Res.*, *36*, 735-758, 1989.

Pingree, R.D. and A.L. New, Abyssal penetration and bottom reflection of internal tidal energy in the Bay of Biscay, *J. Phys., Oceanogr.*, *21*, 28-39, 1991.

Prandle, D., The vertical structure of tidal currents, *Geophys. Astrophys Fluid Dyn.*, *22*, 29-49, 1982.

Prinsenberg, S.J., W.L. Wilmot, and M. Rattray, Jr., Generation and dissipation of coastal internal tides, *Deep Sea Res.*, *21*, 263-281, 1974.

Prinsenberg, S.J., and M. Rattray, Jr., Effects of continental slope and variable Brünt-Väisälä frequency on the coastal generation of internal tides, *Deep Sea Res.*, *22*, 251-263, 1975.

Regal, R., and C.H. Wunsch, M2 tidal currents in the western North Atlantic, *Deep Sea Res.*, *20*, 493-502, 1973.

Rhines, P., Edge-, bottom-, and Rossby waves in a rotating stratified fluid, *Geophys. Fluid Dyn.*, 1, 273-302, 1970.

Roache, P.J., *Computational Fluid Dynamics*, Hermosa Publishers, Albuquerque, New Mexico, 1972.

Roed, L.P. and C.K. Cooper, Open boundary conditions in numerical ocean models, in *Advanced Physical Oceanographic Numerical Modelling*, edited by J. J. O'Brien, D. Reidel Publishing, Boston, pp. 411-436, 1986.

Rosenfeld, L.K., Baroclinic semidiurnal tidal currents over the continental shelf off Northern California, *J. Geophys. Res.*, *95*, 22,153-22,172, 1990.

Rosenfeld, L.K., T. Anderson, G. Hatcher, J. Roughgarden, Y. Shkedy, Upwelling fronts and barnacle recruitment in Central California, Monterey Bay Aquarium Research Institute Technical Report 95-19, 1995.

Rosenfeld, L.K., and R.C. Beardsley, Barotropic semidiurnal tidal currents off Northern California during the Coastal Ocean Dynamics Experiment (CODE), *J. Geophys. Res.*, *92*, 1721-1732 1987.

Rosenfeld, L.K., R.E. Schramm, J.B. Paduan, G.A. Hatcher, Jr., T. Anderson, Hydrographic data collected in Monterey Bay during 1 September 1988 to 16 December 1992, Monterey Bay Aquarium Research Institute Technical Report 94-15, 1994.

Sandstrom, H., The origin of internal tides (a revisit), in *Tidal Hydrodynamics*, edited by B.B. Parker, pp. 437-447, John Wiley and Sons, Inc., New York, 1991.

Schomaker, C.W., A model for tidal circulation adapted to Monterey Bay, California, Master's Thesis Naval Postgraduate School, Monterey, California, 1983.

Shulman, I., and J. K. Lewis, Optimized boundary conditions for coastal modeling, in *Estuarine and Coastal Modeling*, pp. 268-282, Proceedings of the ASCE 4th International Estuarine and Coastal Modeling Conference, 1995, Sponsored by the Waterway, Ports, Coastal, Ocean and Hydraulics Divisions/ASCE, October 26-28, 1995, San Diego, CA.

Schwab, D.J., W.P. O'Connor, and G.L. Mellor, On the net cyclonic circulation in large stratified lakes, *J. Phys. Oceanogr.*, 25, 1516-1520, 1995.

Schwiderski, E.W., Global ocean tides, part II: the semidiurnal principal lunar tide (M2), atlas of tidal charts and maps, NSWC TR 79-414, Naval Surface Weapons Center, Dahlgren, Virginia, 1979.

Shea, R.E., and W.W. Broenkow, The role of internal tides in the nutrient enrichment of Monterey Bay, California, *Estuarine, Coastal, and Shelf Sci.*, *15*, 57-66, 1982.

Shepard, F.P., N.F. Marshall, P.A. McLoughlin, and G.G. Sullivan, *Currents in Submarine Canyons and Other Sea Valleys*, AAPG Studies in Geology No. 8, American Assoc. of Petroleum Geologists, 1979.

Sherwin, T.J., Analysis of an internal tide observed on the Malin Shelf, north of Ireland, *J. Phys Oceanogr.*, *18*, 1035-1054, 1988.

Shih, H.H., and L. Baer, Some errors in tide measurement caused by the dynamic environment, in *Tidal Hydrodynamics*, edited by B.B. Parker, pp. 641-671, John Wiley and Sons, Inc., New York, 1991.

Slinn, D.N., and J.J. Riley, Turbulent mixing in the oceanic boundary layer caused by internal wave reflection from sloping terrain, *Dyn. Atmos. and Oceans*, *24*, 51-62, 1996.

Smagorinsky, J., General circulation experiments with the primitive equations, I: the basic experiment. *Mon. Wea. Rev.*, 91, 99-164, 1963.

Sundqvist, H., On truncation errors in sigma-system models, *Atmosphere*, 13, 81-95, 1975.

Tee, K., The structure of three-dimensional tide-generating currents: experimental verification of a theoretical model, *Estuarine, Coastal and Shelf Sci.*, 14, 27-48, 1982.

Tisch, T.D., Seasonal variability of the geostrophic velocity and water mass structure off Point Sur, California, Master's Thesis, Naval Postgraduate School, Monterey, California, 1990.

Torgrimson, G.M., and B.M. Hickey, Barotropic and baroclinic tides over the continental slope and shelf off Oregon, *J. Phys. Oceanogr.*, 9, 945-961, 1979.

Werner, F.E., Tidal hydrodyamics, quantitative aspects, in *Encyclopedia of Earth System Science*, 4, pp. 351-367, Academic Press, Inc., 1992.

White, M., Tidal and subtidal variability in the sloping benthic boundary layer, *J. Geophys. Res.*, 99(C4), 7851-7864, 1994.

Winant, C.D., and A.W. Bratkovich, Temperature and currents on the Southern California Shelf: a description of the variability, *J. Phys. Oceanogr.*, 11, 71-86, 1981.

Wunsch, C.H., On the propagation of internal waves up a slope, *Deep Sea Res.*, 15, 251-258, 1968.

Wunsch, C.H., Progressive internal waves on slopes, *J. Fluid Mech.*, 35, 131-144, 1969.

Wunsch, C.H., Internal tides in the ocean, *Rev. Geophys.*, 13, 167-182, 1975.

Wunsch, C.H., and R. Hendry, Array measurements of the bottom boundary layer and the internal wave field on the continental slope, *Geophys. Fluid Dyn.*, 4, 101-145, 1972.

Wunsch, C.H., and S. Webb, The climatology of deep ocean internal waves, *J.Phys. Oceanogr.*, 9, 235-242, 1979.

INITIAL DISTRIBUTION LIST

1. Defense Technical Information Center   2
   8725 John J. Kingman Rd., STE 0944
   Ft. Belvoir, Virginia 22060-6218

2. Dudley Knox Library   2
   Naval Postgraduate School
   411 Dyer Rd.
   Monterey, California 93943-5101

3. Dr. Jeffrey D. Paduan   1
   Department of Oceanography, Code OC/Pd
   833 Dyer Rd Room 328
   Monterey, CA 93943-5000

4. Dr. Leslie K. Rosenfeld   1
   Department of Oceanography, Code OC/Ro
   833 Dyer Rd Room 328
   Monterey, CA 93943-5000

5. Dr. Edward B. Thornton   1
   Department of Oceanography, Code OC/Tm
   833 Dyer Rd Room 328
   Monterey, CA 93943-5000

6. Dr. Robert L. Haney   1
   Department of Meteorology, Code MR/He
   Naval Postgraduate School
   Monterey, CA 93943-5000

7. Dr. Anthony Healey   1
   Department of Mechanical Engineering, Code ME/He
   Naval Postgraduate School
   Monterey, CA 93943-5000

8. Commander   1
   Naval Meteorology and Oceanography Command
   1020 Balch Blvd
   Stennis Space Center, MS 39529-5005

9. Dr. Melbourne G. Briscoe   1
   Office of Naval Research Code 322
   800 North Quincy Street
   Arlington, VA 22217-5660

10. Dr. Carl H. Wunsch   1
     Dept. of Earth & Planetary Sciences
     Mail Stop 54-1522
     MIT
     Cambridge, MA 02139

11. LCDR Tim Tisch, NOAA   1
     National Sea Grant College Program
     1315 East-West Highway - R/OR1
     Silver Spring, Maryland 20910

12. Dr. Martha Head   1
     N53, Director, Modeling and Techniques Department
     Naval Oceanographic Office
     1002 Balch Blvd
     Bldg 1002, Rm 179
     Stennis Space Center, MS 39522-5001

13. Dr. Dave Cacchione   1
     U.S. Geological Survey
     345 Middlefield Rd.
     MS 999
     Menlo Park, CA 94025

14. Commanding Officer   1
     U.S. Coast Guard Station
     100 Lighthouse Ave.
     Monterey, CA 93940

15. Dr. Eivind A. Martinsen   1
     Norwegian Meteorological Institute
     P.O. Box 43   Blindern,
     N-0313 Oslo, Norway

16. Dr. James K. Lewis   1
     207 So. Seashore Ave.
     Long Beach, MS 39560

17. Dr. Stephen K. Gill   1
     N-OES 22
     SSMC 4 Rm 7109
     1304 East West Highway
     Silver Spring, MD 20910

18.	Dr. W.W. Broenkow	1
	Moss Landing Marine Laboratory
	P.O. Box 223
	Moss Landing, CA 95039

19.	Library	1
	Moss Landing Marine Laboratory
	P.O. Box 223
	Moss Landing, CA 95039

20.	Harold A. Miller Library	1
	Hopkins Marine Station
	Stanford University
	Cabrillo Point
	Pacific Grove, CA 93950

21.	Library	1
	Scripps Institute of Oceanography
	Code C-075
	University of California, San Diego
	La Jolla, CA 92093

22.	Research Coordinator	1
	Monterey Bay National Marine Sanctuary
	299 Foam St.
	Suite D
	Monterey, CA 93940

23.	LCDR Emil Petruncio	2
	N-541, Naval Meteorology and Oceanography Command
	1020 Balch Blvd
	Stennis Space Center, MS 39529-5005

24.	Dr. George L. Mellor	1
	Atmospheric and Ocean Sciences Program
	Princeton University
	Princeton, NJ 08540

25.	Dr. Alan F. Blumberg	1
	Dynalysis of Princeton
	Princeton, NJ 08540

26.	Dr. Paul Martin	1
	Naval Research Laboratory
	Code 7322
	Stennis Space Center, MS 39529-5004